

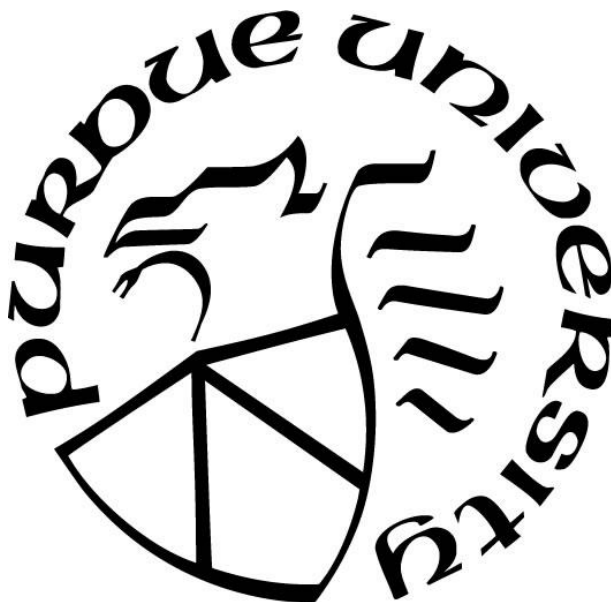
**JET-COOLED MOLECULAR SPECTROSCOPY FROM THE
MICROWAVE TO THE ULTRAVIOLET**

by
Piyush Mishra

A Dissertation

*Submitted to the Faculty of Purdue University
In Partial Fulfillment of the Requirements for the degree of*

Doctor of Philosophy



Department of Chemistry
West Lafayette, Indiana
December 2019

THE PURDUE UNIVERSITY GRADUATE SCHOOL
STATEMENT OF COMMITTEE APPROVAL

Dr. Timothy S. Zwier, Chair

Department of Chemistry

Dr. Paul G. Wenthold

Department of Chemistry

Dr. Lyudmila Slipchenko

Department of Chemistry

Dr. Scott A. McLuckey

Department of Chemistry

Approved by:

Dr. Christine A. Hrycyna

I dedicate this thesis to my family

ACKNOWLEDGMENTS

First, I would like to thank my family for their constant support and patience with me. I am extremely fortunate to be part of a family where education was very important. I would like to thank my father Prof. Ashok Kumar Mishra who instilled the passion of science in me and inspired me to pursue a career in science. He is my role model and without his wisdom and guidance, I would not be where I am. Going on long walks, discussing philosophy and academics with him, has been life changing. I would like to thank my mother Mrs. Sunita Choudhury for her love, immense patience and the sacrifices she did for me and my brother. I would like to thank my brother, Sambit Mishra (Subun dushto) for being a friend and my partner in crime. We had a wonderful time as kids and I will always cherish the memories we created. I am very thankful to my wife, Dr. Kanupriya Verma for her endless patience and support throughout this journey. If it wasn't for her love and care, this experience would have been difficult. We had a lot of fun working together, going on adventures around USA, and stalking Labho racoon. The long midnight walks we often took is the most memorable time I spent at Nobb Hill. She is more than I could ever hope for. I also want to sincerely thank my grandparents and everyone else in my extended family for all their love and support.

I am extremely grateful to my thesis supervisor Prof. Timothy S. Zwier for his guidance throughout my graduate school. I applied to Purdue University because I was impressed by the research carried out in the Zwier lab. I learnt a great deal about spectroscopy through my interactions with Tim. The way Tim thinks about spectroscopy and the way he sees through the complicated spectra, extracting the physical picture, has always dazzled me. I have immense respect for Tim as a guide and mentor. I am trained to be a very good physical chemist under his supervision and I will never forget what I learnt here.

I want to sincerely thank all the teachers since my early schooling days, in particular, my high school chemistry teacher Mr. N. Mohanasundaram (NMS) and my masters thesis supervisor Prof. K. S. Viswanathan (KSV). Their dedication towards teaching is unparalleled. Mr. NMS's down to earth demeanor and willingness to help all his students has been a source of inspiration. Apart from having learnt chemistry, I also learnt the characteristics a good teacher should possess from him. Prof. KSV is a great teacher of physical chemistry, who introduced me to the fascinating

world of quantum mechanics and spectroscopy. He could bring physical meaning to complicated equations and processes with ease. I will never forget the research practices I learnt from him. Moreover, the Vish lab will remain close to my heart as this was where I met my wife and borazine companion, Kanupriya for the first time. I also want to thank my mathematics teacher Menaka ma'am, for being a great teacher and for being very patient through my struggles.

I want to thank my lab members for the fun times we had as a group. I made some great friends and will always cherish the times we spent together. I want to thank Sean and Chris; for being there through the ups and downs. I thank Sven and Brian to have taught me a lot about Rotational spectroscopy. I thank Karl and Josh for the very useful and involved discussions on a variety of topics. I thank Alicia and Chamra for the useful discussions on instrumentation and chemical dynamics. I also want to thank Paul Fugazzi from Sandia to make our collaboration memorable and fun.

I would like to thank my committee members Prof. Paul Wenthold, Prof. Scott McLuckey, and Prof. Lyudmila Slipchenko for taking out their precious time to review my thesis and giving their valuable suggestions. Discussions I had with Tim and Paul have been very helpful in my research.

I want to thank all my friends for being a crucial part of my journey. I want to thank Bharat and his family, Aditya and his family, Vallabh and Billure (Winter), Harshal, and Manish from Purdue. I want to thank friends from KVIITM, Vicky Baba (Vignesh), Sudharsan, Prince, Shashi, Bhargav, and Prakash. I want to thank my IISER buddies Anuj, Aniket, Akshay, Ankur, Nitish (CM), Musa bhai (Upakul), Chachu (Nitin), Debi Bhaina, and Vidyanshu. They have always had my back.

I want to thank the members of JAFICI for the in-house technical expertise they offer. In particular I would like to thank Erick Norwood, Randy Replogle, Konrad Kliewer, and Jim Zimmerman. I want to thank Betty Dexter, Debra Packer, Lisa Wilson, Suzy Gustafson, Lynn Rider, Rob Reason, Darci DeCamp, Ned Gangwer, and Trisha Herrera, for their willingness to help and to make the lives of grad students so much easier.

I thank Einstein Bros. Bagels (French fry) and Brother's Bar and Grill. The short trips here with my wife were the much needed distractions during my hectic final year as a grad student. I thank UBS for their Thirsty Thursdays, which would remind us of the nearing weekend. Last but not the least, I am grateful to the silent guardian, the watchful protector, The Dark Knight.

TABLE OF CONTENTS

LIST OF TABLES	9
LIST OF FIGURES	11
ABSTRACT.....	19
CHAPTER 1. INTRODUCTION	20
1.1 Small Organic Molecular Systems.....	20
1.2 Spectroscopic Information over Microwave, Infrared and Ultraviolet ranges	25
1.3 Organization of the thesis	26
1.4 References.....	28
CHAPTER 2. METHODS	30
2.1 Introduction.....	30
2.2 Supersonic Jet Expansion and Sample Handling.....	30
2.2.1 Supersonic Jet Expansion	30
2.2.2 Sample Handling	31
2.3 Laser Spectroscopic Instruments	35
2.3.1 Lasers.....	35
2.3.2 Laser Induced Fluorescence Chamber:.....	36
2.3.3 Molecular Beam TOF Chamber	37
2.4 Chirped-Pulse Spectroscopy Instrument.....	39
2.4.1 Chirped-Pulse Fourier Transform Microwave Spectrometer	41
2.4.2 Vacuum Ultraviolet Time-of-Flight Mass Spectrometer.....	42
2.5 Species Specific Schemes	43
2.5.1 Laser-Based Schemes	43
2.5.2 Chirped-Pulse Based Schemes	45
2.6 Theoretical	46
2.7 References.....	48
CHAPTER 3. CONFORMATIONAL EXPLOSION: UNDERSTANDING THE COMPLEXITY OF <i>PARA</i> -DIALKYL BENZENE POTENTIAL ENERGY SURFACES	50
3.1 Introduction.....	50

3.2	Methods.....	51
3.2.1	Experimental and Theoretical.....	51
3.2.2	Nomenclature.....	53
3.3	Results and Discussion	54
3.3.1	Calculations	54
3.3.2	LIF excitation spectra	57
3.3.3	Conformer-specific spectroscopy: <i>p</i> -dEthB	61
3.3.4	Conformer-specific spectroscopy: <i>p</i> -dPropB	68
3.3.5	Conformer-specific spectroscopy: <i>p</i> -dButB	70
3.3.6	Torsional PES and isomerization pathways	73
3.3.7	Extrapolation to longer dialkylbenzenes: <i>p</i> -dOctB.....	77
3.4	Conclusion	80
3.5	References.....	81
CHAPTER 4. BROADBAND ROTATIONAL SPECTROSCOPY OF <i>TRANS</i> 3-PENTENENITRILE AND 4-PENTENENITRILE.....		83
4.1	Introduction.....	83
4.2	Methods.....	86
4.2.1	Experimental.....	86
4.2.2	Theoretical	87
4.3	Results.....	89
4.3.1	3-Pentenenitrile.....	89
4.3.2	Methyl internal rotation	99
4.3.3	4-Pentenenitrile.....	108
4.4	Discussion	121
4.4.1	3-PN and 4-PN as Structural Isomers.....	121
4.4.2	Conformational Preferences of 3-PN and 4-PN	122
4.5	Conclusion	126
4.6	References.....	128
CHAPTER 5. INTERDEPENDENCE BETWEEN THE ALKYL CHAIN AND π H-BOND IN PROPYLBENZENE(WATER) _N , N=2-4 CLUSTERS.....		130
5.1	Introduction.....	130

5.2	Experimental and Theoretical Methods	132
5.3	Results.....	134
5.3.1	Propylbenzene(H ₂ O) ₂	135
5.3.2	Propylbenzene(H ₂ O) ₃	144
5.3.3	Propylbenzene(H ₂ O) ₄	149
5.4	Discussion and Conclusion.....	153
5.5	References.....	157
CHAPTER 6. LOOKING AHEAD		159
6.1	Ethylanthracenes	159
6.1.1	Introduction.....	159
6.1.2	Methods	160
6.1.3	Theoretical Results and Discussion.....	161
6.1.3.1	Ethylanthracene	161
6.1.3.2	Dianthrylethane	162
6.1.4	Experimental Results and Discussion of 2-ethylanthracene.....	164
6.2	Phosphorescence of 4-H-pyran-4-one.....	170
6.3	Electronic Spectroscopy of Homosalate	171
6.4	Pyrolysis of <i>Trans</i> 3-Pentenenitrile	175
6.4.1	Introduction.....	175
6.4.2	Results and Discussion	176
6.4.3	Conclusion	184
6.5	References.....	185
VITA.....		187
PUBLICATIONS.....		189

LIST OF TABLES

Table 3.1: Zero-point corrected energies relative to the most stable structure at the DFT B3LYP-GD3BJ/Def2TZVP level of theory. Dashed lines mark breaks in energy between sub-groups of conformers.	55
Table 3.2: ZPE-corrected energies relative to the most stable structure at the DFT M06-2X/aug-cc-pVDZ level of theory.	56
Table 3.3: Calculated, scaled excitation energies for low-energy conformers of <i>p</i> -dEthB, <i>p</i> -dPropB, and <i>p</i> -dButB, carried out at B3LYP-GD3BJ/Def2TZVP level of theory.	58
Table 3.4: Calculated, scaled excitation energies for low-energy conformers of <i>p</i> -dEthB, <i>p</i> -dPropB, and <i>p</i> -dButB, carried out at the TD-DFT M06-2X/aug-cc-pVDZ level of theory.	60
Table 3.5: Symmetry of the irreducible representations associated with the low energy fundamental frequencies of the two ground electronic state conformers of para-diethylbenzene. Notation for mode assignment follows Mulliken numbering, notation brackets follows Varsanyi numbering.	67
Table 4.1: Zero-point corrected relative energies of the conformers of 3-pentenenitrile and 4-pentenenitrile, calculated at the DFT B3LYP-GD3BJ/Def2TZVP level of theory.	90
Table 4.2: Spectral fits to the A-state transitions of 3-PN using the SPFIT program suite compared with the values predicted by DFT calculations (Representation I' Watson S reduction).	95
Table 4.3: Linelist of <i>syn</i> 3-pentenenitrile A-states from SPFIT.	96
Table 4.4: Linelist of <i>eclipsed</i> 3-pentenenitrile A-states from SPFIT.	98
Table 4.5: Spectral fits of the hypothetical central frequencies using the XIAM program suite are shown along with the values resulting from DFT calculations at B3LYP-GD3BJ/Def2TZVP (Representation I' Watson S reduction).	100
Table 4.6: Linelist of <i>syn</i> 3-pentenenitrile from XIAM.	103
Table 4.7: Spectral fits to both A and E methyl rotor states of 3-PN using the XIAM program suite compared with the values resulting from DFT calculations (Representation I' Watson A reduction)	106
Table 4.8: Linelist of <i>eclipsed</i> 3-pentenenitrile from XIAM.	107
Table 4.9: Spectral fits using the SPFIT program suite are compared with DFT calculations (Representation I' Watson A reduction).	110
Table 4.10: Linelist of <i>eg</i> + 4-pentenenitrile from SPFIT.	113
Table 4.11: Linelist of <i>et</i> 4-pentenenitrile from SPFIT.	115
Table 4.12: Linelist of <i>eg</i> - 4-pentenenitrile from SPFIT.	117

Table 4.13: Linelist of <i>st</i> 4-pentenenitrile from SPFIT.....	119
Table 4.14: Linelist of <i>sg</i> - 4-pentenenitrile from SPFIT.	120
Table 5.1: BSSE-corrected and ZPE-corrected energies of pBz(H ₂ O) ₂ clusters carried out at B3LYP-GD3BJ/Def2TZVP level of theory. All energies are relative to the most stable structures within their respective column.....	136
Table 5.2: BSSE-corrected and ZPE-corrected energies of pBz(H ₂ O) ₃ clusters carried out at B3LYP-GD3BJ/Def2TZVP level of theory. All energies are relative to the most stable structures within their respective column.....	145
Table 5.3: BSSE-corrected and ZPE-corrected energies of pBz(H ₂ O) ₄ clusters carried out at B3LYP-GD3BJ/Def2TZVP level of theory. All energies are relative to the most stable structures within their respective column.....	150
Table 5.4: Electronic origin frequency shifts of Bz(H ₂ O) _n and pBz(H ₂ O) _n clusters from their respective conformational monomers.	154
Table 5.5: Summary of the propylbenzene-water cluster assignments.....	155
Table 6.1: List of dianthrylethane isomers and the number of unique conformations in each...	163
Table 6.2: α along with the corresponding i^{th} vibrational mode.	180
Table 6.3: SPFIT parameters of the ¹³ C isotopologues of <i>syn</i> 3-PN.	182
Table 6.4: Line list of the ¹³ C isotopologues of <i>syn</i> 3-PN.	183

LIST OF FIGURES

Figure 1.1: (a): Systems our work is based off are on the left side in black font and the molecules we study are on the right in red font. The techniques applied are (a) Laser spectroscopy and (b) chirped-pulse spectroscopy.	23
Figure 1.2: Energy level diagrams spanning the spectroscopic regimes from electronic states to hyperfine splitting in rotational states.	25
Figure 2.1: Schematic diagram of supersonic expansion.	31
Figure 2.2: Gas manifold used to study interaction between two different molecules. This allows fine control over the partial vapor pressures of each component.	33
Figure 2.3: Pyrolysis microreactor is an extension of the pulsed valve to pyrolyze the components in the gas pulse.	34
Figure 2.4: Schematic diagram of the laser induced fluorescence chamber. The top portion records the excitation spectra whereas the bottom portion is used to record dispersed fluorescence.	37
Figure 2.5: Schematic diagram of the molecular beam time-of-flight chamber.	38
Figure 2.6: Schematic diagram of mass-correlated broadband rotational spectrometer. The first part is the CP-FTMW chamber followed by the VUV-TOF chamber.	40
Figure 2.7: Schematic diagram of the electronics used to perform broadband chirped-pulse fourier transform microwave spectrometry.	41
Figure 2.8: Laser based schemes (a) LIF excitation spectrum where the molecules radiatively relax to the ground electronic state over ~10-100 ns, and (b) FDIR spectrum where the IR laser temporally precedes the UV laser by about 200 ns, hence depopulating the zero-point vibrational level.	44
Figure 2.9: Strong-field coherence breaking scheme to perform species-specific broadband microwave spectroscopy.	46
Figure 3.1: Chemical structures and key dihedral angles for para-diethylbenzene (<i>p</i> -dEthB), <i>p</i> -dipropylbenzene (<i>p</i> -dPropB), and para-dibutylbenzene (<i>p</i> -dButB).	50
Figure 3.2: Selected optimized geometries carried out at the DFT B3LYP-GD3BJ/Def2TZVP level of theory for (a) <i>p</i> -dEthB conformers: <i>syn</i> and <i>anti</i> , (b) <i>p</i> -dPropB conformers (t-S-t) where both the chains are <i>trans</i> and (t-S-g) with one <i>gauche</i> , and (c) the all- <i>trans</i> (tt-A-tt) and global minimum (tg-S-g't) conformers of <i>p</i> -dButB.	52
Figure 3.3: Small chain para-dialkylbenzene UV fluorescence excitation spectra. Experimental spectra (black traces) of (a) <i>p</i> -dEthB, (b) <i>p</i> -dPropB, and (c) <i>p</i> -dButB, with calculated vertical excitation energies in red. The experimental S ₁ ←S ₀ origin bands are labelled with an asterisk. Region I contains the S ₁ ←S ₀ origins from the (xt-X-tx) class of conformers, region II the (xt-X-gx) class, and region III the (xg-X-gx) family. See text for further discussion.	57

Figure 3.4: (a) UV excitation spectra of *p*-dEthB showing the origin and the vibronic excitation bands. (b) FDIR spectra of the two observed conformers of *p*-dEthB in the alkyl CH stretch region (2840–3000 cm^{-1} , bottom two traces). Red and gray traces: Calculated (red) and experimental (grey) FDIR spectrum of ethylbenzene from ref. 4, for comparison. The calculated spectrum uses a local mode anharmonic Hamiltonian derived from calculations at the B3LYP-D3/6-311++G(d,p) level of theory. (c) DFL spectra of the two S_0 - S_1 origin bands of *p*-dEthB. The transition at 36998 cm^{-1} is assigned to the *syn* (S) conformer, with C_{2v} symmetry, while that at 37002 cm^{-1} is due to the *anti* (A) conformer, with C_{2h} symmetry. Vibronic spectroscopy peaks are described using Mulliken notation, the notation in paranthesis follow Varsanyi numbering which is adapted from Wilson numbering..... 63

Figure 3.5: DFL spectra of *p*-dEthB showing false origins. These spectra have scaled intensities for easier comparison. From the top: *Anti* 31^1_0 transition at 37379 cm^{-1} , *syn* 32^1_0 transition at 37376 cm^{-1} , low frequency transitions at 37065 cm^{-1} is likely to belong to a *syn* *p*-dEthB transition, 37056 cm^{-1} assigned to *syn* 19^1_0 transition and 37034 cm^{-1} assigned to *anti* 33^1_0 transition. 65

Figure 3.6: DFL spectra of the (6b) vibronic mode of both the *p*-dEthB conformers (a) *anti* and (b) *syn* (trace intensity multiplied by 3). Varsanyi numbering scheme is being followed here. 66

Figure 3.7: (a) FDIR spectra of representative single conformers from regions I (t-X-t), III (g-X-g), and II (g-X-t) of *p*-dPropB in the alkyl CH stretch region (2800–3000 cm^{-1}). Red traces show the computed spectra generated by summing the results for the propylbenzene single-chain counterparts using a local mode Hamiltonian method at the B3LYP-D3/6-311++G(d,p) level of theory, taken from Tabor et. al. The specific UV transitions from region I, III, and II are at 36997, 36900, and 36946 cm^{-1} , respectively. (b) Comparison between the experimental FDIR spectra of *p*-dPropB (black) and propylbenzene (grey). (c) Top trace (Black): UV excitation spectrum of *p*-dPropB, Middle trace (Blue): IR-UV HB scan with IR holeburn laser fixed at 2964.6 cm^{-1} , exciting conformers of the type (t-X-t) and (t-X-g), and Bottom trace (Red): IR-UV HB scan with IR Holeburn laser fixed at 2975.8 cm^{-1} exciting conformers of the type (g-X-g) and (t-X-g). 69

Figure 3.8: The blue shaded region span the peak at 2858 cm^{-1} and the green shaded peak spans the peak at 2865 cm^{-1} . (a) FDIR spectra of representative single conformers from regions I (xt-X-ty, top), II (xt-X-gy, middle), and III (xg-X-gy, bottom) of *p*-dButB in the alkyl CH stretch region (2800–3000 cm^{-1}). Red traces show the computed spectra generated by summing the results for the butyllbenzene single-chain counterparts using a local mode Hamiltonian method at the B3LYP-D3/6-311++G(d,p) level of theory, taken from Tabor et. al.. Origin bands from region I, II, and III are at 36973, 36909, and 36831 cm^{-1} , respectively. (b) Comparison between the experimental FDIR spectra of *p*-dButB (black) and butylbenzene (grey). The butylbenzene conformations that were added are labelled with the first and the second letters being the first dihedral and the second dihedral angles along the chain. See text for further discussion. 71

Figure 3.9: FDIR spectra of the UV excitations of *p*-dButB indicated by asterisk in Figure 3(c). The UV excitation corresponding to the various IR spectra are mentioned on the left. The blue traces are from region I, the green traces are from region II and the red traces are from region III. 72

Figure 3.10: Relaxed potential energy curve generated by varying the dihedral angle between each of the chains and the plane of the phenyl ring (θ), mapping out the isomerization path between *syn* (S) and *anti* (A) structures of p-dEthB (black), and p-dPropB (red) and p-dButB (red). (a) 1D cuts of the torsional surface due to conformers where the chains are not sterically hindered by the ring during this isomerization. (b) Similar 1D cuts of the p-dPropB surface for conformers of the type (g-X-g), where the chains are sterically hindered by the phenyl ring, resulting in a much higher barrier. (c) 1D cut of the torsional surface due to conformers if the type (tg-X-tg), where the chains are not sterically hindered by the ring during this isomerization. (d) Similar 1D cut of the p-dButB surface for conformers of the type (tg-X-g't), where the chains are sterically hindered by the phenyl ring, resulting in a much higher barrier. 74

Figure 3.11: (a) PES of p-dPropB of the type (x-A-x) where the dihedral angles along the chains are varied. (b) Contour of the (x-A-x) p-dPropB PES shown in (a). (c) PES of p-dButB of the type (tt-A-xx) where both the dihedral angles on the same alkyl chain were varied. (d) 1D cut of the torsional mode taken from (b) marked with the arrows, where the first dihedral on the chain of p-dPropB is varied..... 76

Figure 3.12: (a) R2PI spectrum of para-dioctylbenzene (middle) compared to p-dButB (top) and octylbenzene (bottom). The star on the p-dOctB UV excitation spectra indicates the wavenumber position of the doubly folded g1g3g4 conformer of p-dOctB assuming the electronic frequency shift relative to the all-*trans* structure is additive. (b) Lowest energy conformer of p-dOctB calculated at the B3LYP-D3BJ/Def2TZVP level of theory. 79

Figure 4.1: Chemical structures of (a) 4-pentenitrile and (b) *trans* 3-pentenitrile molecules. The carbon atoms are labelled starting from the nitrile group and the flexible dihedral angles are indicated..... 84

Figure 4.2: Conformers of *trans* 3-pentenitrile geometry optimized at the dispersion corrected DFT B3LYP-GD3BJ/Def2TZVP level of theory. The lowest energy conformer (a) *syn* 3-pentenitrile has all the heavy atoms in the same plane with a C2-C3 dihedral of 0° and (b) *eclipsed* 3-pentenitrile with a C2-C3 dihedral of -120° , calculated to be 186 cm^{-1} higher in energy. The *eclipsed* conformer exists as a degenerate pair, with its second member having a dihedral angle of $+120^\circ$ (not shown). The flexible dihedral angles are shown as double headed arrows..... 87

Figure 4.3: Optimized geometries for the five unique conformers of 4-pentenitrile calculated at the dispersion corrected DFT B3LYP-GD3BJ/Def2TZVP level of theory. Structures are listed in order of increasing energy: (a) *eg+*, (b) *et*, (c) *eg-*, (d) *st*, and (e) *sg-*. See the text for further discussion of the nomenclature. The relative zero-point corrected energies in cm^{-1} are given below the labels. 88

Figure 4.4: Comparison of two broadband microwave spectra for 3-PN recorded in the rapid adiabatic passage regime with 100%, 10% and 1% power on the TWTA. The spectrum recorded while sweeping $8 \rightarrow 18\text{ GHz}$ sweep (black trace) and the corresponding spectrum with an $18 \rightarrow 8\text{ GHz}$ sweep (blue trace). Note that with 100% power of TWTA the distortions in the two spectra with intensities of transitions at the end of each scan enhanced unlike in case of 10% and 1% power of the TWTA..... 91

Figure 4.5: Strong-field coherence breaking spectra of (a) *syn* and (b) *eclipsed* conformers of 3-pentenenitrile (black traces) along with their final fit spectra going down. The intensity axes show almost a factor of 20 difference in signal intensity. The numbering on the transitions label the frequencies of the single frequency pulses of the SFCB method (see text for further discussion). 92

Figure 4.6: Broadband microwave spectrum of 3-pentenenitrile (black trace) over the 8-18 GHz range with the final fit spectra of *syn* (blue trace) and *eclipsed* (red trace) conformers below. The experimental spectrum is a 1 million average scan of 3-pentenenitrile entrained in argon carrier gas. 94

Figure 4.7: Close-up view of individual transitions of 3-pentenenitrile (black traces) along with the final fits of the A/E states of (a-c) the *syn* conformer (blue/green sticks), and (d) *eclipsed* conformer (red/green sticks). (a) The $4_{13-3_{12}}$ transition of the *syn* conformer shows collapsed hyperfine splitting with unresolved methyl rotor splittings. The $1_{11-0_{00}}$ (b) and $4_{13-4_{04}}$ (c) transitions of the *syn* conformer with both hyperfine and methyl rotor splittings. Predictions of $4_{13-4_{04}}$ (c) are convolved to Lorentzian lineshapes and are overlaid (grey trace). (d) The $6_{25-5_{24}}$ transition of the *eclipsed* conformer in which only methyl rotor splittings are resolved. The predicted fits are convolved to Lorentzian lineshapes and are overlaid (grey trace). 102

Figure 4.8: Broadband microwave spectrum in the 7.5-18.5 GHz region of 4-pentenenitrile (black trace) with the final fit spectra of the conformers *eg+* (violet), *et* (green), *eg-* (brown), *st* (blue) and *sg* (red) shown below. The rotational spectrum is a 1 million FID average of 4-PN entrained in helium carrier gas. 109

Figure 4.9: A close-up view of individual transitions of 4-pentenenitrile conformers (black traces) along with their final fit spectra (stick diagrams below). Representative transitions belonging to the (a) *et* and *eg+* conformers, (b) *eg-*, (c) *st*, and (d) *sg* conformers. 111

Figure 4.10: Relaxed potential energy scans of the dihedral angle indicated above it, calculated at the dispersion corrected DFT B3LYP-GD3BJ/Def2TZVP level of theory. (a) The C2-C3 dihedral of 3-pentenenitrile, (b) the C3-C4 dihedral of 4-PN holding C2-C3 in its trans configuration (*xt*), and (c) the C2-C3 dihedral of 4-PN with C3-C4 held as *syn* (*sx*). The flexible dihedral angle was rotated in 10° steps. The scan along *sx* includes only dihedral angles from 60 to 300 degrees because the barrier to $sg+\leftrightarrow sg-$ isomerization is too high due to steric constraints. 122

Figure 4.11: The Boltzmann plot for (a) *syn* and (b) *eclipsed* 3-pentenenitrile. The rotational temperature calculated using the equation: $W = (4\pi^3 2\omega_0^2 S \mu_i^2 g_l g_e I \epsilon N_{tot}) / (c \sqrt{\alpha} k T Q_{rot}) \exp(-E_l/kT_{rot})$, are shown in the respective plots. The errors on the rotational temperatures were derived from the best-fit plot based on the scatter in the intensities within the set of transitions rather than based on errors from multiple measurements of each rotational transition. 123

Figure 4.12: The Boltzmann plot for (a) *eg+*, (b) *et*, (c) *eg-* and (d) *sg-* 4-pentenenitrile. The rotational temperature calculated using the equation: $W = (4\pi^3 2\omega_0^2 S \mu_i^2 g_l g_e I \epsilon N_{tot}) / (c \sqrt{\alpha} k T Q_{rot}) \exp(-E_l/kT_{rot})$, are shown in the respective plots. The errors on the rotational temperatures were derived from the best-fit plot based on the scatter in the intensities within the set of transitions rather than based on errors from multiple measurements of each rotational transition. 125

Figure 5.1: Monomer precursors Propylbenzene and water. The flexible dihedral angles with their labels are shown.....	131
Figure 5.2: R2PI spectra of (a) pBz and (b-e) pBz(H ₂ O) _n clusters. The mass channels where the spectra was recorded is written in brackets. R2PI spectra of the pBz(H ₂ O) ₂ is shown in (b). With higher water vapor pressure, pBz(H ₂ O) ₃ also shows up in (c) and (d), and pBz(H ₂ O) ₄ shows up in (e). Cluster-specific spectroscopy is performed on the peaks marked with asterisk.	135
Figure 5.3: Structures of Bz(H ₂ O) ₂ and pBz(H ₂ O) ₂ clusters along with their labels. (a) Bz(H ₂ O) ₂ , (b) ‘Ag(1)’, (c) ‘Sg(1)’, (d) The double π H-bonded ‘St(3)’, and (e) ‘St(1)’	137
Figure 5.4: RIDIRS of Bz(H ₂ O) ₂ and pBz(H ₂ O) ₂ in the OH stretch region. B1, B2 and B3 are labelled along with their best match predictions. The UV frequencies where the RIDIRS were recorded are mentioned. The dotted line goes through the free OH stretch of all the spectra....	139
Figure 5.5: IR-UV HB of (a) B1, (b) B2, and (c) B3, UV excitation spectrum of (d) pBz(H ₂ O) ₂ , and (e) pBz. The IR frequencies where the IR-UV HB spectra wer recorded are mentioned. The electronic origin for each cluster is marked with a pound. RIDIRS are recorded on the peaks marked with asterisks in the UV excitation spectrum.	140
Figure 5.6: RIDIRS of pBz conformers and pBz(H ₂ O) ₂ in the CH stretch region. B1, B2 and B3 are labelled along with their best match predictions. The UV frequencies where the RIDIRS were recorded are mentioned.....	142
Figure 5.7: Structures of Bz(H ₂ O) ₃ and pBz(H ₂ O) ₃ clusters along with their labels. (a) Experimentally observed Bz(H ₂ O) ₃ structure with 1 π H-bond, (b) Bz(H ₂ O) ₃ structure with 2 π H-bonds, (c) ‘Sg(3)’, (d) ‘Sg(1)’, (e) ‘Ag (2)’, (f) ‘Ag(1)’, and (g) ‘St(1)’	147
Figure 5.8: RIDIRS of Bz(H ₂ O) ₃ and pBz(H ₂ O) ₃ in the CH and the OH stretch regions. C1, C2 and C3 are labelled along with their best match predictions. The UV frequencies where the RIDIRS were recorded are mentioned.	148
Figure 5.9: Structures of Bz(H ₂ O) ₄ and pBz(H ₂ O) ₄ clusters along with their labels. (a) Experimentally observed Bz(H ₂ O) ₄ with 1 π H-bond, (b) Bz(H ₂ O) ₄ with 2 π H-bonds, (c) ‘Sg(2)’, (d) ‘St(1)’, (e) ‘At(1)’, and (f) ‘St(2)’	151
Figure 5.10: Structures of Bz(H ₂ O) ₄ and pBz(H ₂ O) ₄ clusters along with the harmonic frequency predictions in the OH stretch region. The UV frequencies where the RIDIRS were recorded are mentioned.....	153
Figure 6.1: 2-Ethylanthracene with the unique positions on anthracyl ring rounded.	160
Figure 6.2: Structures of (a) 2-ethylanthracene, and (b)-(e) dianthrylethanes.....	162
Figure 6.3: Energy level diagram of dianthrylethanes.....	163
Figure 6.4: Electronic spectra of 2-ethylanthracene. (a) UV excitation spectrum, and (b) DFL spectra at 0 ⁰ ₀ . Long FC progressions of ethyl torsional mode are connected by tie lines.	165
Figure 6.5: DFL spectra of 2-ethylanthracene at (a) 84 ¹ ₀ (b) 84 ² ₀ (c) 83 ¹ ₀ (d) 83 ¹ ₀ 84 ¹ ₀	168
Figure 6.6: Synthetic scheme of 9- and 2-ethylanthracene.....	169

Figure 6.7: Jet-cooled LIP spectrum of the $T_1(n\pi^*) \leftarrow S_0$ origin band in 4-H-pyran-4-one, compared to a simulation generated using the STROTA program. The simulation used a rotational temperature of 20 K. The chemical structure of 4-H-pyran-4-one is in the top right corner. 170

Figure 6.8: The tautomers of homosalate 172

Figure 6.9: (a) LIF spectrum of vaporized HMS upon photoexcitation in the 29806.26 – 32786.89 cm^{-1} energy region; the same spectrum is shown in more detail in (b), with the inset showing the peak and energy corresponding to the 0^0_0 of HMS..... 173

Figure 6.10: Dispersed fluorescence plot of homosalate exciting at 30761.19 cm^{-1} . X-axis is the shift from the exciting frequency. Maximum is $\sim 5750 \text{ cm}^{-1}$ 174

Figure 6.11: Mass spectrum of pyrolysis of 3-pentenenitrile at 830°C and 685°C. 177

Figure 6.12: Broadband microwave spectrum of pyrolysis of 3-pentenenitrile at 830°C..... 178

Figure 6.13: The species with the same mass corresponding to the m/z seen in the mass spectrum. The m/z values are in the respective boxes..... 179

LIST OF ABBREVIATIONS

Abbreviation	Full Form
PES	Potential Energy Surface
PAH	Polycyclic Aromatic Hydrocarbon
<i>p</i> -dEthB	<i>Para</i> -diethylbenzene
<i>p</i> -dPropB	<i>Para</i> -dipropylbenzene
<i>p</i> -dButB	<i>Para</i> -dibutylbenzene
FR	Fermi Resonance
Bz	Benzene
3-PN	<i>Trans</i> 3-pentenenitrile
4-PN	4-pentenenitrile
VUV	Vacuum Ultraviolet
CP-FTMW	Chirped-Pulse Fourier Transform Microwave
MW	Microwave
IR	Infrared
UV	Ultraviolet
ZPE	Zero-Point Energy
TOF	Time Of Flight
LIF	Laser Induced Fluorescence
LIP	Laser Induced Phosphorescence
SCCM	Standard Cubic Centimeter per Minute
D	Diameter
T _{trans}	Translational Temperature
T _{rot}	Rotational Temperature
T _{vib}	Vibrational Temperature
pBz	Propylbenzene
OPC	Optical Parametric Converter
FWHM	Full Width at Half Maximum
KTP	Potassium Titanyl Phosphate
KTA	Potassium Titanyl Arsenate
OPO	Optical Parametric Oscillator
OPA	Optical Parametric Amplifier
BBO	Barium Borate

PMT	Photomultiplier Tube
DFL	Dispersed Fluorescence
R2PI	Resonance 2-Photon Ionization
MCP	Microchannel Plate
FID	Free Induction Decay
TWTA	Travelling Wave Tube Amplifier
FFT	Fast Fourier Transform
SFCB	Strong Field Coherence Breaking
SFP	Single Frequency Pulse
FDIR	Fluorescence Dip Infrared
RIDIR	Resonance Ion Dip Infrared
IR-UV HB	Infrared-Ultraviolet Holeburning
RAP	Rapid Adiabatic Passage
LFP	Linear Fast Passage
DFT	Density Functional Theory
TD-DFT	Time-Dependent Density Functional Theory
QST2	Quadratic Synchronous Transit
IVR	Intramolecular Vibrational energy Redistribution
<i>p</i> -dOctB	<i>Para</i> -dioctylbenzene
expt	Experimental
pred	Predicted
LAM	Large Amplitude Motion
BSSE	Basis Set Superposition Error
MMFFs	Merck Molecular Force Field static
FC	Franck-Condon
EA	Ethylanthracene
dAE	Dianthrylethane
4-HP	4-H-pyran-4-one

ABSTRACT

The present thesis shows how versatile and important the field of gas-phase spectroscopy under supersonic expansion conditions can be to understand fundamental intermolecular and intramolecular interactions. We have employed spectroscopic techniques over a very broad range spanning from microwave (2-18 GHz), through infrared (2600-4000 cm^{-1}) and ultraviolet (350-250 nm) region, studying the rotational, vibrational and electronic properties, respectively. These techniques use either chirped-pulse based (broadband rotational spectroscopy) or laser based methods (vibrational and electronic spectroscopy), and their usage depends on the types of information of particular interest and the chemical system requirements of specific techniques. The analytes are brought into the gas phase and supersonically cooled to their zero-point vibrational level to perform rotational and vibrationally resolved IR/UV spectroscopy, including conformer-specific techniques. The variety of small organic molecular systems studied include phenyl-containing hydrocarbons, water containing clusters, heteroatom containing organic molecules with and without phenyl ring, fused aromatic molecules, bichromophoric molecules and pyrolysis reaction intermediates. Apart from gaining invaluable fundamental knowledge of the various interactions, we also observe interesting quantum-physical phenomena like tunneling and large amplitude motions that provide further insight into the molecular world.

CHAPTER 1. INTRODUCTION

1.1 Small Organic Molecular Systems

Small organic molecules and molecular systems in the gas phase are very crucial to atmospheric and combustion chemistry. They are also extensively present in planetary atmospheres, interstellar media and circumstellar shells. The importance of studying the weak inter and intramolecular interactions cannot be overemphasized. Studying such systems at a molecular scale is a key step towards the identification and understanding of the chemical processes and also essential for the development of accurate modeling of combustion, atmospheric and extraterrestrial processes. Such chemical processes depend significantly on the structure of the various conformers and complexes, which is why there is a growing recognition of the importance of isomer-specific, conformer-specific and mass-resolved techniques. Apart from helping develop models, these studies also benchmark theoretical tools. To perform high resolution spectroscopy, the analytes are brought to the gas-phase and supersonically cooled to their lowest vibrational state.¹⁻⁴ We want to characterize these analytes by providing a comprehensive picture of their rotational, vibrational and electronic degrees of freedom through spectroscopic tools.

The central theme of this thesis is conformers, and their corresponding potential energy surfaces (PESs). All our studies are aimed towards understanding how the conformational preferences of prototypical molecules and clusters are perturbed under various circumstances, and hence understand their PESs. We study a diverse selection of small organic molecular systems including alkylbenzenes, alkylbenzene-water clusters, diarylalkanes, pentenenitriles and their pyrolysis products that have important applications in a number of fields as described later.

A schematic of the molecules and clusters studied in this thesis is shown in **Figure 1.1**. Some of our work on alkylaromatics are based off a previous research carried out in our lab with our theoretical collaborator Dr. Sibert on short-chain alkylbenzenes (ethylbenzene, propylbenzene and butylbenzene).⁵ We wanted to see how the conformational preferences and the torsional PES is affected in the presence of a second alkyl chain substituted at the *para*-position, which gave rise to our studies carried out on short-chain *para*-dialkylbenzenes (*para*-diethylbenzene, *para*-dipropylbenzene and *para*-dibutylbenzene). We also wanted to know if and how the

conformational preference of short-chain alkylbenzenes is altered in the presence of solvent molecules, which led to our work on propylbenzene-water clusters. The Zwier lab recently identified the smallest alkylbenzene where the folded structure starts to show up in octylbenzene by Hewett et. al.⁶ As an important extension of this work, we seek to understand the interactions between alkyl chains and larger fused-ring aromatics. My studies on diarylethanes and ethylarenes are aimed towards understanding the stacking tendency of such dimeric aryl systems. Similar studies were recently completed by a previous member of our group on dinaphthylethane. Moving in the direction of polycyclic aromatic hydrocarbons (PAHs), we studied ethylanthracenes (1-, 2-, and 9-ethylanthracene), which lays a foundation for studying dianthrylethanes later. Stacking of PAHs is considered an important first step towards soot formation.⁷ We study these topics through logical set of experiments starting from alkylaromatics and small fused aromatic molecules to larger aromatic molecules with a chemical link. More on this is discussed later.

While several groups have studied the influence of a single functional group on a pure alkyl chain, many organic molecules of importance have more than one functional group present. The over-all preferences of such multi-functional chains is determined by the nature and relative positions of the groups along the alkyl chain. We also studied functionalized organic chains and their structural isomers. This was based off work carried out in our lab by Pillsbury et. al.⁸, Fraser et. al.⁹ and Samdal et. al.¹⁰ on the conformations of 5-phenyl-1-pentene, 1-pentene and 4-isocyano-1-butene respectively. Specifically, we studied 1-pentene with a nitrile group attached on the opposite end giving us 4-pentenitrile, and a more stable structural isomer 3-pentenitrile. Our research was focused on how the conformational preferences depend on the functionality, position of the double bond and the stabilization of the conformers within the respective structural isomers due to hyperconjugation and steric effects.

The research involving conformations of hydrocarbons used laser spectroscopic techniques. Short-chain dialkylbenzenes are a class of molecules that are common components of coal and aviation fuel.¹¹ The conformational preferences of key fuel components are important to understand the reaction pathways of a combustion process. As mentioned, study builds off previous work on single-chain *n*-alkylbenzenes.⁵ We explore the extent to which the two chains interact with each other as a function of chain length. The series of molecules chosen for this study are *para*-diethylbenzene (*p*-dEthB), *para*-dipropylbenzene (*p*-dPropB) and *para*-dibutylbenzene (*p*-dButB). Due to the presence of Fermi resonances (FR), we applied an anharmonic local mode

Hamiltonian in the CH region of the IR spectra through our collaborator Dr. Edwin Sibert III from the University of Wisconsin-Madison.

Apart from studying the interaction of key fuel hydrocarbons with solvent molecules, our research on water complexes and clusters with hydrocarbons are also of fundamental interest, which we explored using laser spectroscopic techniques. Benzene(Bz)-water clusters have been thoroughly studied as a prototypical system for the π H-bond, where the smaller Bz(H₂O)_{1,2} exhibits transitions involving combination bands in the antisymmetric OH stretch region due to tumbling motions of the H₂O molecule on the aromatic ring.¹² This project is aimed towards studying the effect of short alkyl chain containing phenyl ring (propyl chain in this case) on the π H-bond between the H₂O cluster and the aromatic ring; this is another research that is built off previous work on short-chain alkylbenzenes.⁵ We also were interested to study how the presence of water molecular cluster influences the conformational preference of the propyl chain and vice-versa.

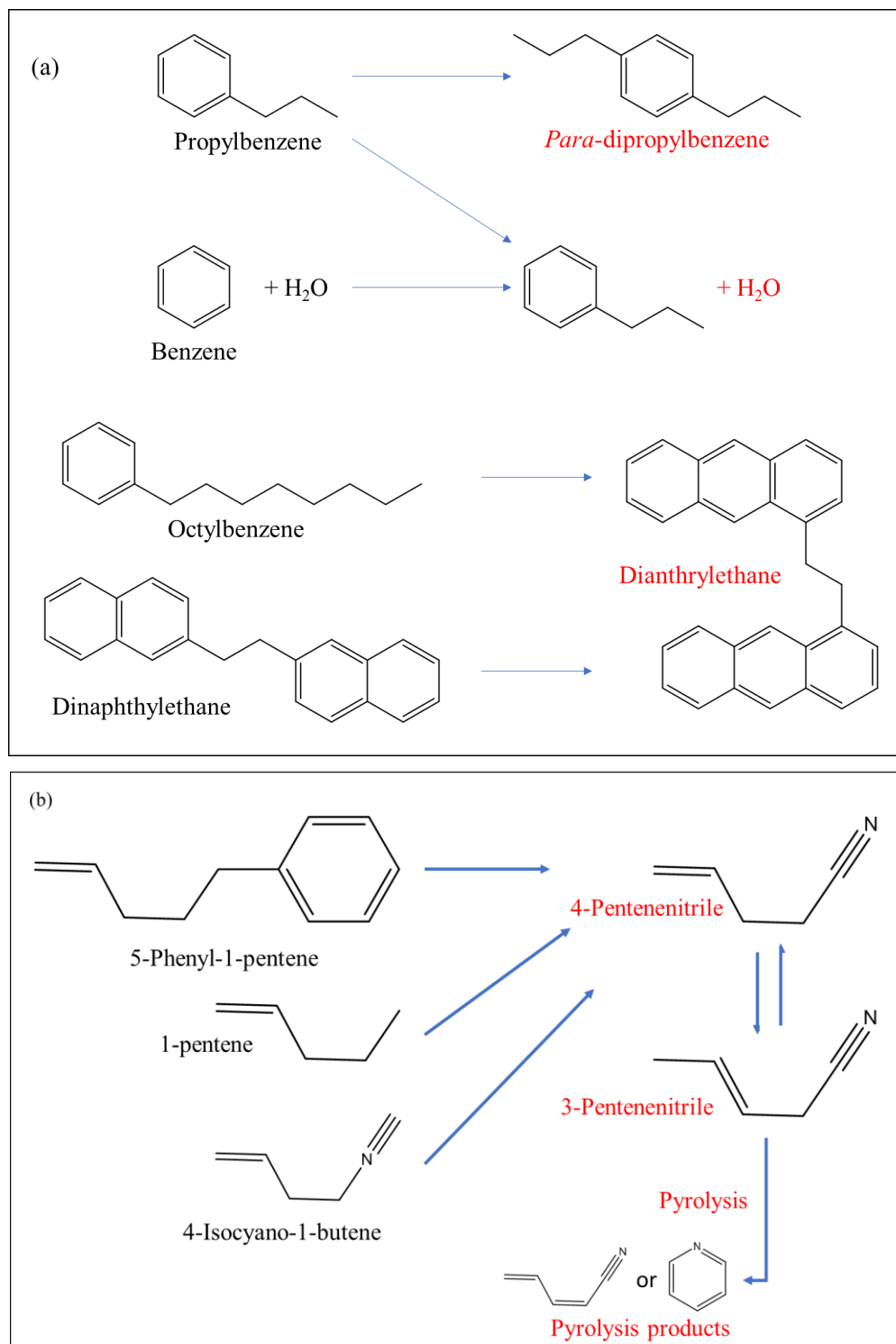


Figure 1.1: (a): Systems our work is based off are on the left side in black font and the molecules we study are on the right in red font. The techniques applied are (a) Laser spectroscopy and (b) chirped-pulse spectroscopy.

Soot formation is a field that has been an important area of research, but it still lacks in accurate modeling of the early stages of PAH and soot formation.¹³ Until recently there has been a conundrum in understanding how the first stages of soot formation occur. The current model of the inception of soot requires PAHs to come together, and stack to form dimers at sizes of pentacene, it also involves radical recombination forming PAH dimers with an ethyl linker.¹⁴ The study carried out to address this issue focuses on the stacking tendency of diarylethane molecules with the ethyl chain linking the various unique positions on the fused aromatic ring. Work carried out by Hewett in our lab was carried out on dinaphthylethane and ethyl naphthalene series. Series of dianthrylethanes would be the logical next step towards understanding stacking of PAHs. Ethyl chain substituted at unique positions on anthracene giving rise to a series of ethylanthracenes are studied as preliminary experiments to better understand the spectroscopic signatures of the stacking structures of dianthrylethanes and its stability with respect to the unstacked structures.

The research carried out with pentenenitriles using the mass-correlated broadband chirped-pulse MW techniques has astronomical relevance. Titan, a moon of Saturn, has a nitrogen- and methane-rich atmosphere that is similar to prebiotic earth, and is replete with organic nitriles. Nitriles due to their high dipole moment are about 18% of the molecules detected in interstellar and circumstellar medium.¹⁵ The structural isomers 3-pentenenitrile (3-PN) and 4-pentenenitrile (4-PN) were chosen to study using our chirped-pulse fourier transform microwave (CP-FTMW) instrument as they are products of radical recombination reactions where the photochemistry by vacuum ultraviolet (VUV) from solar radiation is what drives the chemistry in planetary atmospheres like Titan. The pentenenitriles are potential precursors to interesting hetero-aromatic compounds like pyridine. Formation of pyridine is always interesting especially towards the understanding of the origin of the building blocks of life through formation of simple amino acids.¹⁶ Apart from its relevance to astrochemistry, this work is an interesting extension of very similar molecules studied previously where the conformations of pentene chain were examined.⁸⁻¹⁰ The relative populations of conformers gave us an insight on stabilities of the various conformers within the pentenenitrile structural isomers. As an attempt to study reaction pathways to interesting nitrogen containing compounds such as pyridine, we performed pyrolysis on 3-PN and studied the reaction products.

1.2 Spectroscopic Information over Microwave, Infrared and Ultraviolet ranges

We use state-of-the-art tools to spectroscopically characterize the molecules in **Figure 1.1**. An energy level diagram is shown in **Figure 1.2** spanning the various regimes where we perform spectroscopy. A particular strength of our research lies in the multi-faceted nature of performing species-specific and mass-resolved techniques spanning the microwave to the ultraviolet regions. The experimental schemes utilized here are designed to study spectroscopically distinguishable species including isomers, complexes, conformers, reaction intermediates etc. The spectroscopic tool used depends primarily on two things: (1) What kind of information needs to be extracted, and (2) the requirements a chemical system needs to possess. Pure or mixture of inert buffer gas with a small percentage of the sample of interest is brought to the vapor phase and expanded into vacuum in a supersonic free jet or molecular beam (if skimmed). The molecules in the sample get cooled by collisions with the buffer gas, removing most of their rotational and vibrational energy.¹⁻⁴ Downstream in the expansion, the sample molecules are isolated in most cases, and when we want to study the intermolecular interactions we control the ‘isolation’ by controlling the vapor pressure of the various samples and the backing pressure of the buffer gas. Experimental parameters can be varied to achieve fine control over the propensity to form clusters, cooling conditions, etc. Under such experimental conditions, the resulting spectrum has a greatly reduced number of transitions, which makes it possible to make conformation-specific assignments.

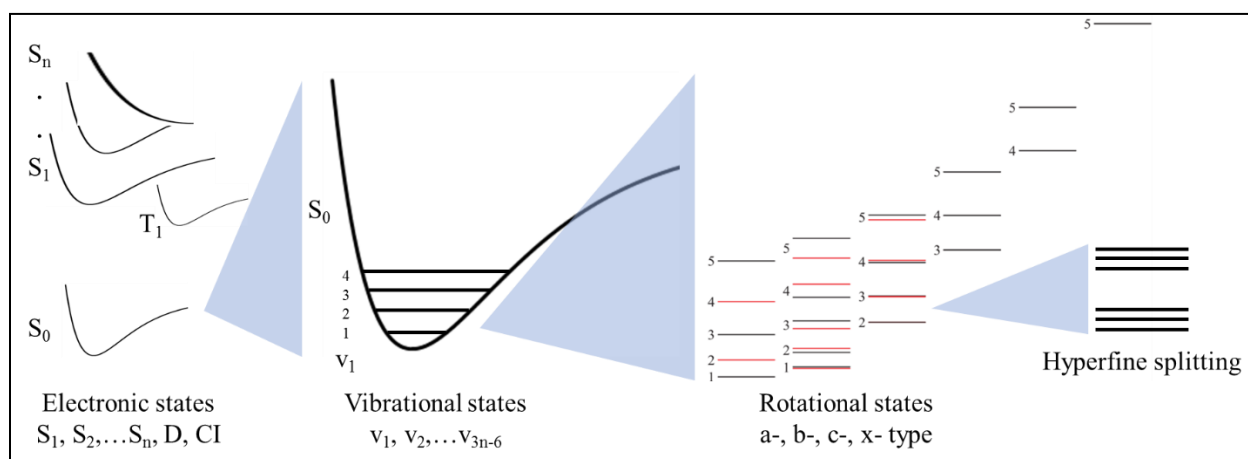


Figure 1.2: Energy level diagrams spanning the spectroscopic regimes from electronic states to hyperfine splitting in rotational states.

Broadly, we use laser based and chirped-pulse based spectroscopic techniques. The chirped-pulse technique is in the microwave (MW) region, whereas the laser based techniques are in the infrared (IR) and the ultraviolet (UV) frequency ranges.¹⁷⁻¹⁹ MW spectroscopy of a chemical system is obtained due to coherent rotational transitions. Rotational selection rules require the molecule of interest to possess a dipole moment projection along at least one of the three inertial axes. The structural information is encoded within this spectrum as the moments of inertia are very sensitive to slight structural changes. Because of the high resolution of Chirped-pulse Fourier transform microwave (CP-FTMW) spectroscopy as opposed to traditional spectroscopies in the IR and UV regions, this technique can be used to study splitting due to tunneling even at the zero-point energy (ZPE) level. A VUV Time-of flight (TOF) mass spectrometer is attached to this instrument to perform mass-correlated MW spectroscopy.¹⁹ Other angular momentum quantum phenomena could couple into rotational states and show up as hyperfine splittings such as nuclear quadrupolar coupling.

Our laser based techniques are primarily based on $\pi \rightarrow \pi^*$ transitions of an aromatic moiety due to their readily accessible well-resolved states, which is why the chemical systems that we study need such functionality. We have a photon count based detection system where the emitted fluorescence or phosphorescence is detected, and we also have a mass-resolved technique (TOF) where we count ions generated by the laser, which is very useful to study complexes, clusters or even reactions. The IR spectral shifts depend on the local environments of the vibrating bond(s), which reflect strong and weak molecular interactions. The UV spectroscopy involves electronic excitation, the shifts of which depend upon the environment of the aromatic undergoing excitation and also indicates the geometry changes between the ground and excited states.

1.3 Organization of the thesis

Chapter 1 is the introduction to this thesis and Chapter 2 discusses the various chirped-pulse and laser based spectroscopic instrumentation. The isomer-specific, conformer-specific and mass-resolved techniques are described in detail.

Chapter 3 discusses the conformation explosion in short-chain dialkylbenzenes which show how quickly the potential energy surface (PES) becomes complex with several low energy minima. This is based off work of a previous graduate student in the group on short-chain alkylbenzenes.

The studies I have carried out primarily used a vacuum chamber outfitted for laser induced fluorescence (LIF) detection. Chapter 4 discusses structural characteristics of 3-pentenenitrile and 4-pentenenitrile. Interesting effects like methyl rotor tunneling and hyperfine splitting due to the presence of N was also observed. Chapter 5 studies the fundamentals of π H-bond between water clusters of various sizes and propylbenzene. We compare the effect of the water cluster on the alkyl chain and vice-versa with comparison to the prototypical of benzene-water clusters. This work was carried out in the molecular beam TOF set-up.

Chapter 6 discusses extensions of the research in this thesis. We discuss laser spectroscopy projects followed by chirped-pulse experiments, including collaborative research. The systems we discuss are LIF studies on series of Ethylanthracene and Dianthrylethane molecules, Laser Induced Phosphorescence (LIP) studies on 4-H-pyran-4-one (Collaborator: Dr. Stephen Drucker, University of Wisconsin, Eau Claire), LIF studies on Homosalate, a sunscreen candidate (Collaborator: Dr. Vasilios Stavros, University of Warwick), and pyrolysis reactions with *trans* 3-pentenenitriles were carried out which produced species of both molecular and radical nature.

1.4 References

- ¹ D. H. Levy, *Science* **214**, 263 (1981).
- ² D. M. Lubman, C. T. Rettner, and R. N. Zare, *J. Phys. Chem.* **86**, 1129 (1982).
- ³ R. E. Smalley, L. Wharton, and D. H. Levy, *Accounts Chem. Res.* **10**, 139 (1977).
- ⁴ A. Amirav, U. Even, and J. Jortner, *Chem. Phys.*, **51**, 31 (1980).
- ⁵ D. P. Tabor, D. M. Hewett, S. Bocklitz, J. A. Korn, A. J. Tomaine, A. K. Ghosh, T. S. Zwier, and E. L. Sibert III, *J. Chem. Phys.* **144**, 224310 (2016).
- ⁶ D. M. Hewett, S. Bocklitz, D. P. Tabor, E. L. Sibert III, M. A. Suhm, and T. S. Zwier, *Chem. Sci.* **8**, 5305 (2017).
- ⁷ M. R. Kholghy, A. Veshkini, and M. J. Thomson, *Carbon* **100**, 508 (2016).
- ⁸ N. R. Pillsbury, and T. S. Zwier, *J. Phys. Chem. A.* **113**, 118 (2009).
- ⁹ G. T. Fraser, *J. Chem. Phys.* **112**, 6209 (2000).
- ¹⁰ S. Samdal, T. Grønås, H. Møllendal, and J-C Guillemin, *J. Phys. Chem. A.* **118**, 1413 (2014).
- ¹¹ V. A. Gerasimenko, A. V. Kirilenko, and V. M. Nabivach, *J. Chromatogr. A* **208**, 9 (1981); J. Chao, C. T. Lin, and T. H. Chung, *J. Phys. Chem. Ref. Data* **12**, 1033 (1983); B. G. Harvey, W. W. Merriman, and T. A. Koontz, *Energy Fuels* **29**, 2431 (2015).
- ¹² R. N. Pribble, and T. S. Zwier, *Faraday Discuss.*, 1994, **97**, 229; H. S. Gutowsky, T. Emilsson, and E. Arunan, *J. Chem. Phys.* **99**, 4883 (1993); R. N. Pribble, A. W. Garrett, K. Haber, and T. S. Zwier, *J. Chem. Phys.* **103**, 531 (1995); R. N. Pribble and T. S. Zwier, *Science*, **265**, 75 (1994); D. P. Tabor, R. Kusaka, P. S. Walsh, T. S. Zwier, and E. L. Sibert III, *J. Phys. Chem. A*, **119**, 9917 (2015).
- ¹³ C. J. Mueller, W. J. Cannella, T. J. Bruno, B. Bunting, H. D. Dettman, J. A. Franz, M. L. Huber, M. Natarajan, W. J. Pitz, M. A. Ratclif, and K. Wright, *Energy Fuels* **26**, 3284 (2012).
- ¹⁴ M. Frenklach, *Phys. Chem. Chem. Phys.* **4**, 2028 (2002). H. Sabbah, L. Biennier, S. J. Klippenstein, I. R. Sims, B. R. Rowe, *J. Phys. Chem. Lett.* **1**, 2962 (2010).
- ¹⁵ B. A. McGuire, *Astrophys. J. Suppl. Ser.*, **239**:17 (2018); B. A. McGuire, A. M. Burkhardt, S. Kalenskii, C. N. Shingledecker, A. J. Remijan, E. Herbst, and M. C. McCarthy, *Science*, **359**, 202 (2018).
- ¹⁶ N. Kitadai, and S. Maruyama, *Geosci. Front.*, **9**, 1117 (2018).

- ¹⁷ N. R. Pillsbury, J. A. Stearns, C.W.Müller, D. F. Plusquellic, and T. S. Zwier, *J. Chem. Phys.* **129**, 114301 (2008); C. A. Arrington, C. Ramos, A. D. Robinson, and T. S. Zwier, *J. Phys. Chem. A*, **102**, 3315 (1998); F. A. Ensminger, J. Plassard, T. S. Zwier, and S. Hardinger, *J. Chem. Phys.*, **102**, 5246 (1995); E. G. Buchanan, J. R. Gord, and T. S. Zwier, *J. Phys. Chem. Lett.* **4**, 1644 (2013); P. S. Walsh, E. G. Buchanan, J. R. Gord, and T. S. Zwier, *J. Chem. Phys.* **142**, 154303 (2015); D. M. Lubman, *Mass Spectrom. Rev.* **7**, 559 (1988); R. H. Page, Y. R. Shen, and Y. T. Lee, *J. Chem. Phys.* **88**, 4621 (1988); T. S. Zwier, *Annu. Rev. Phys. Chem.* **47**, 205 (1996); T. S. Zwier, *J. Phys. Chem. A* **105**, 8827 (2001); P. S. Walsh, R. Kusaka, E. G. Buchanan, W. H. James, B. F. Fisher, S. H. Gellman, and T. S. Zwier, *J. Phys. Chem. A*, **117**, 12350 (2013).
- ¹⁸ A. O. Hernandez-Castillo, C. Abeysekera, B. M. Hays and T. S. Zwier, *J. Chem. Phys.* **145**, 114203 (2016).
- ¹⁹ Sean M. Fritz, Brian M. Hays, Alicia O. Hernandez-Castillo, Chamara Abeysekera, and Timothy S. Zwier, *Rev. Sci. Instrum.* **89**, 093101 (2018).

CHAPTER 2. METHODS

2.1 Introduction

The work described in this thesis uses a combination of experimental and theoretical tools to study the spectroscopy of small organic molecular systems. Conformations and weakly bound clusters are inherent part of such systems. These conformers and clusters having the same masses cannot be ‘filtered’ out like isomers. The eigenstates are the only unique features that differentiate such components. We use conformer-specific or cluster-specific spectroscopy to study rotational, vibrational and electronic states of small organic molecular systems. All the analytes studied are brought to the vapor phase, typically by heating the sample container, mixed with an inert carrier gas, and supersonically expanded into vacuum chambers which hydrodynamically cools them to their lowest vibrational states of the different low-lying minima on the PES. The laser spectroscopies operate in the IR and the UV regions corresponding to vibrational and electronic excitations respectively, whereas rotational spectroscopy is a chirped-pulse technique operating in the microwave region. In this chapter, supersonic jet expansion, sample preparation and handling are discussed first, followed by the laser and the chirped-pulse spectroscopy instruments. After the instrumental background, we detail the various conformer-specific and complex-specific techniques that occupy a central part of the research in this thesis. Henceforth, we refer to these techniques as species-specific techniques. Theoretical tools that are also a very important backbone of the described work are detailed.

2.2 Supersonic Jet Expansion and Sample Handling

2.2.1 Supersonic Jet Expansion

To perform rotational and vibrationally resolved spectroscopy and differentiate transitions from different species intermingled with one another, the samples have to be prepared such that they have little to no excess energy, in other words, at their zero-point vibrational states. The sample system should also be isolated with no interactions/collisions. This is achieved by supersonically expanding the analytes using a pulsed supersonic nozzle (**Figure 2.1**). A small fraction of the sample to be studied in its vapor phase is seeded into inert carrier gases, which are

typically He, Ne, Ar, or a known mixture of these. This mixture containing the analyte is held in a reservoir at a stagnation pressure (p_0) of 0.3-4.1 bar, which has a very small mean free path. A solenoid based pulsed valve (Parker General Valve Series 9) operating at 10-20 Hz is utilized at a flow rate in the range 5-60 standard cubic cm/minute (SCCM). The orifice of the supersonic nozzle is 500-1000 microns in diameter (D). As the gas mixture flows through the orifice, a large number of 2-body and 3-body collisions proportional to p_0D and p_0^2D , respectively, take place.¹ This converts the temperature governed Maxwell-Boltzmann velocity distribution into directed mass flow along the expansion axis through the orifice. In other words, the relative velocity distribution is narrowed by collisions, which is equivalent to a low translational temperature ($T_{\text{trans}} \sim 1$ K) in the moving frame of reference at the terminal velocity of the expansion. The analytes are cooled via collisions isoentropically² lowering the $T_{\text{rot}} \sim 0.5-5$ K and $T_{\text{vib}} \sim 10-15$ K³. In most cases these analytes lie at their zero-point vibrational states, isolated and in gas-phase with negligible inhomogenous broadening.^{2,3}

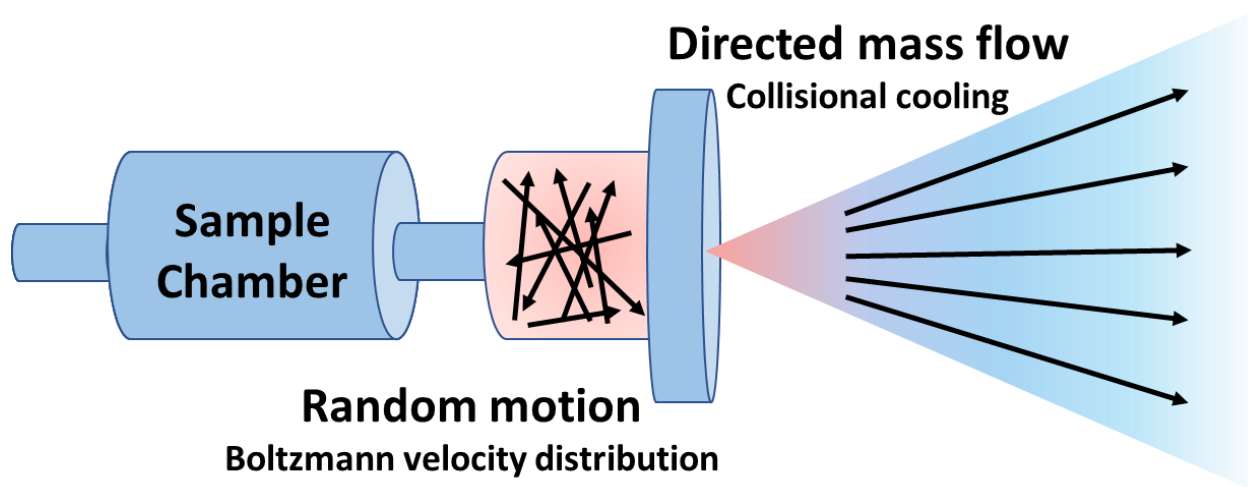


Figure 2.1: Schematic diagram of supersonic expansion.

2.2.2 Sample Handling

As mentioned before, the chemical system to be studied are brought to the vapor phase and mixed with an inert carrier gas. This is typically done by placing the sample container before the supersonic nozzle. If the sample is thermally stable, it is heated to increase its partial vapor pressure in the gas mixture if required. A resistively heated rope is wound around the valve assembly which

consists of the sample chamber and the pulsed valve. The rate of heating is proportional to the voltage applied which is controlled by a Variac. The temperature is monitored by the working end of a k-type thermocouple, which rests between the outer wall of the sample chamber and the resistively heated rope.

When the motive of the experiment is to study intermolecular interactions, we use a gas manifold which controls the relative partial vapor pressures of the individual molecules. Such a sample introduction set-up was utilized when we studied water clusters of various sizes (**Figure 2.2**). The carrier gas line splits into three lines through a cross joint. Two of these lines pass over containers with the compounds of interest, propylbenzene (pBz) and water in our case. The third is a bypass line that is used for finer control of relative partial pressures and dilution by the carrier gas. Needle valves and flow meters are connected to each of these three lines for control and monitoring the flows. These volatile samples are soaked on cotton that are placed in the containers to avoid droplets clogging the gas lines. Only those compounds with sufficient vapor pressure at room temperature can be used in this set-up, else, the sample with low vapor pressure can be taken closer to the pulsed valve and heated.

Towards pulse valve

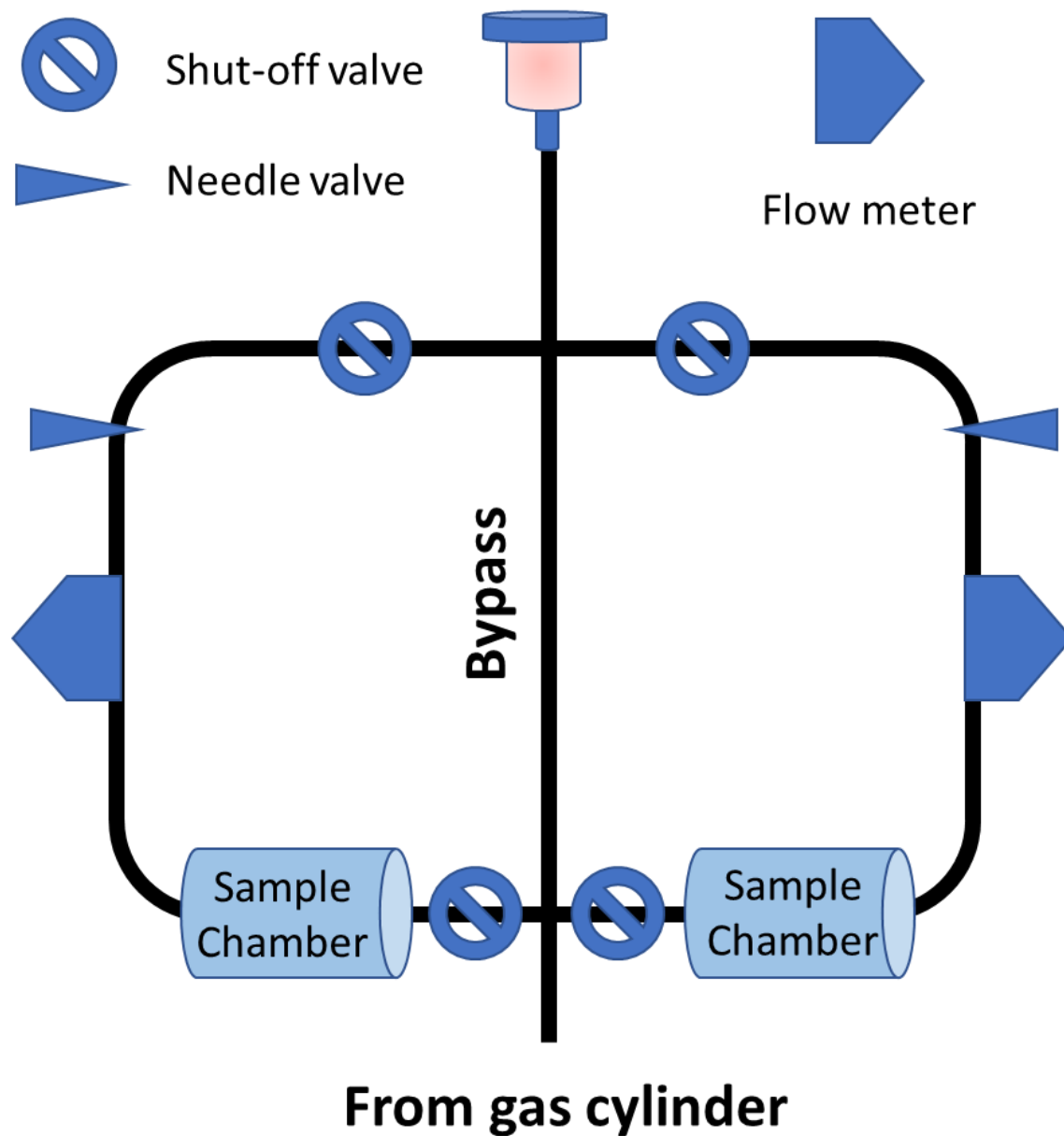


Figure 2.2: Gas manifold used to study interaction between two different molecules. This allows fine control over the partial vapor pressures of each component.

We also studied pyrolysis reaction intermediates and products where a flash pyrolysis microreactor was utilized,⁴ which is a modified version of the Chen nozzle⁵. The pyrolysis microreactor (**Figure 2.3**) is an extension of the pulsed valve. The SiC tube can be resistively heated to a maximum operable pyrolytic temperature of 1900 K while the chilled water cooled copper heat sink protects the delicate components of the pulsed general valve. SiC tube has the dimensions of 2mm ID X 5mm OD X 3.5 cm long (Saint-Gobain Ceramics, Hexoloy SE), which is mounted inside an alumina housing to avoid radiative loss. A combination of Mb clips and annular carbon rings are used to apply voltage across the SiC tube, whose optimal resistance for stable operation is 0.5-3 k Ω . The pyrolytic reaction occurs inside the SiC when the gas pulse passes through whose temperature is monitored by a W/Re type C thermocouple. The resistive heating is achieved by controlling the current flowing through the SiC tube by incorporating it into a circuit with a set of up to 6 light bulbs (250 watt) connected in parallel to each other, but in series with the SiC tube. The power provided is controlled by a Variac (120 VAC) which is in series with the SiC tube and the set of bulbs.

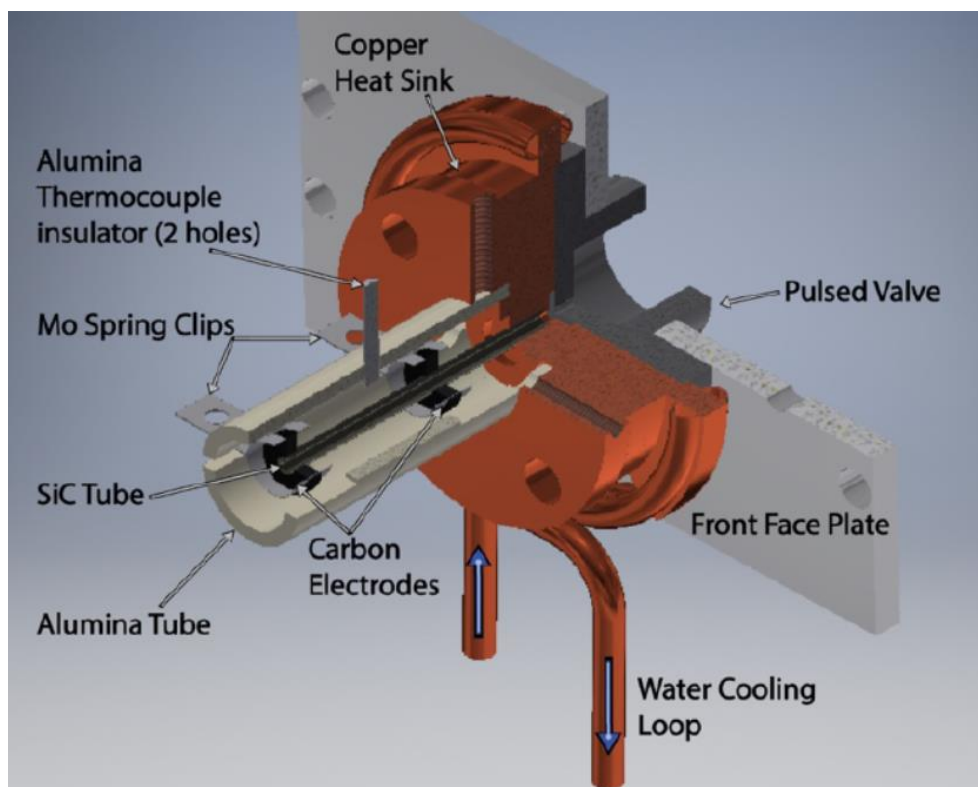


Figure 2.3: Pyrolysis microreactor is an extension of the pulsed valve to pyrolyze the components in the gas pulse.

2.3 Laser Spectroscopic Instruments

The laser spectroscopic techniques performed in the Zwier lab operate in the IR and the UV regions, and are used to study vibrational and electronic spectra respectively. Two chambers to perform laser spectroscopy used were the LIF chamber and the molecular beam TOF chamber. These chambers were used independently for most of the work in this thesis; although they can be used complementarily to obtain very useful information. Both these chambers use Nd:YAG (Qsmart 450, Quantel; YG661-20(680), Continuum) pumped tunable dye lasers to perform electronic excitation in the UV region operating at 20Hz repetition rate and Nd:YAG (Surelite II, Continuum; Precision, Continuum) pumped tunable optical parametric convertors (OPCs) in the IR region operating at 10 Hz repetition rate. These systems output laser pulses that have temporal pulse widths of about 6 ns full width at half maximum (FWHM). The fundamental of Nd:YAG is 1064 nm, which pumps the OPC, whereas the second and third harmonics which are 532 nm and 355 nm pump the dye lasers. As we are studying processes that take place within tens of nanoseconds, all the timings are controlled by timing boxes (BNC 565) and all the laser control as well as data collection is controlled by LabVIEW software (National Instruments).

2.3.1 Lasers

The IR laser (LaserVision OPC) generates tunable IR source using angle adjustment of the potassium titanyl phosphate (KTP) in the oscillator stage and potassium titanyl arsenate (KTA) crystals in the amplifier stage. 33% of the pump energy is used in the oscillator stage and the rest is used in the amplifier stage. This optical parametric oscillator (OPO) stage has an output coupler, two KTP crystals and grating to increase the resolution. These crystals split the incoming photons into lower energy ‘idler’ and higher energy ‘signal’ photons. These two beams possess opposite polarizations that can be filtered using a wedged Si polarizer. The ‘idler’ photon is mixed with 67% of 1064 nm pump at the optical parametric amplifier (OPA) stage. The OPA idler photons are tunable in the 2000-4100 cm^{-1} range. We used this laser in the 2800-3800 cm^{-1} range that includes the CH and the OH stretch regions. The UV lasers (Radiant Dyes, NarrowScan; Lambda Physik, ScanMate) are dye lasers that are excited by the second or third harmonic of Nd:YAG laser. The excited dye fluoresces over a range of lower frequencies that are selected via a grating which allows for tunable light generation in the visible region. This visible laser light is doubled in frequency by angle tuning a non-linear barium borate (BBO) crystal, which generates tunable light

in the UV region. The resultant beam is filtered and the desired light is separated out using a Pellin Broca prism, which then electronically excites the analyte.

2.3.2 Laser Induced Fluorescence Chamber:

The LIF chamber used in this thesis is a light based detection system that records fluorescence from the samples being studied (**Figure 2.4**), which is described in detail elsewhere.⁶ The valve apparatus is mounted on a ‘captain’s wheel’ and a sealed X-Y translation stage which is used to manually adjust the position of the valve in all three directions from the spectroscopic region inside the chamber. This chamber is pumped by a roots blower backed by rotary pumps (Welch). The molecules are electronically excited by a tunable UV laser, followed by radiative relaxation to the ground electronic state through a process called fluorescence. LIF excitation scans were recorded by collecting the total fluorescence emission from the jet-cooled molecules at a given laser wavelength. With a set of collection/steering optics, the emission is imaged onto a UV-enhanced photomultiplier tube (PMT). The PMT was outfitted with long-pass filters to reduce the scattered light from the laser, which depends on the analyte being studied. A sampling gate was placed around the fluorescence decay profile, digitized by an oscilloscope (Tektronix, model 3052B), and integrated. The resultant spectrum obtained is due to all the species present in the supersonic expansion.

Dispersed fluorescence (DFL) spectra are obtained by fixing the laser wavelength resonant with selected transitions in the excitation spectrum, and imaging the fluorescence onto the entrance slit of 0.1-0.5 mm of a $\frac{3}{4}$ m monochromator instead of a PMT. An intensified CCD camera (Andor SOLIS iStar) collects the dispersed emission peaks at a fixed grating position which is tuned point-by-point, every ‘point’ corresponding to a range of 14 nm. Fluorescence lifetime traces are also recorded by exciting select transitions, and directly recording the time profile of the fluorescence signal from the PMT on the digital oscilloscope. The conformer-specific schemes are detailed in section 2.5 of this chapter.

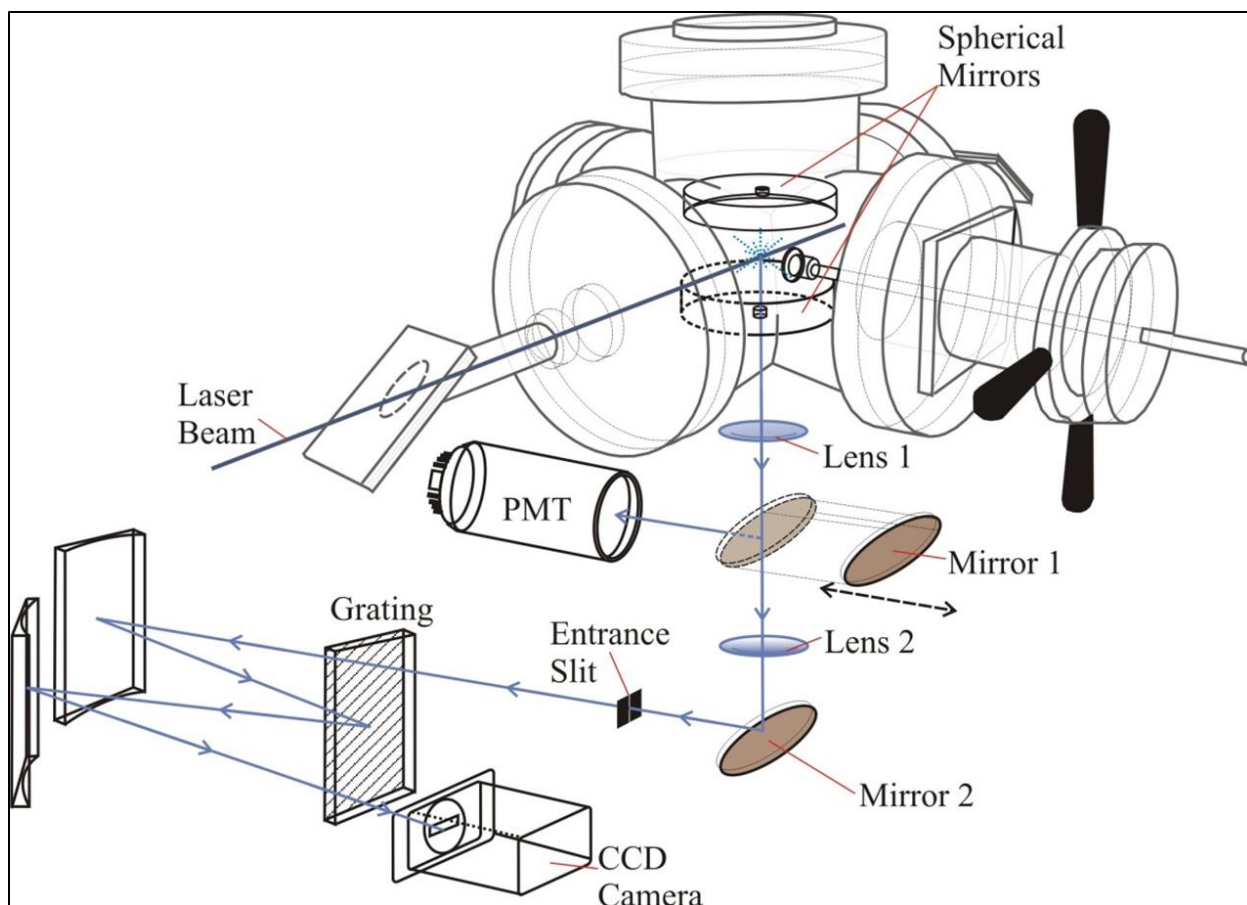


Figure 2.4: Schematic diagram of the laser induced fluorescence chamber. The top portion records the excitation spectra whereas the bottom portion is used to record dispersed fluorescence.

2.3.3 Molecular Beam TOF Chamber

The molecular beam TOF chamber is an ion detection system that records a mass resolved molecular spectrum (**Figure 2.5**), which is described in detail elsewhere.⁷ This chamber is differentially pumped which is separated by a skimmer. The molecular beam source region pumped by a water cooled turbomolecular pump (880 L/s, TMU 1001, Pfeiffer) backed by a rotary pump (Welch) reaches operating pressures of $\sim 10^{-5}$ mbar, whereas the detection region pumped by an air cooled turbomolecular pump (220 L/s, TMU 261, Pfeiffer) backed by another rotary pump (Welch) reaches operating pressures of $\sim 10^{-6}$ - 10^{-7} mbar depending on the ionization threshold of the carrier gas used. Just like in the LIF apparatus, the valve apparatus is mounted on a ‘captain’s wheel’ and a sealed X-Y translation stage for manual adjustment of the position of the

valve along all three directions. The coldest portion of the molecular beam is sampled by this skimmer to perform spectroscopy.

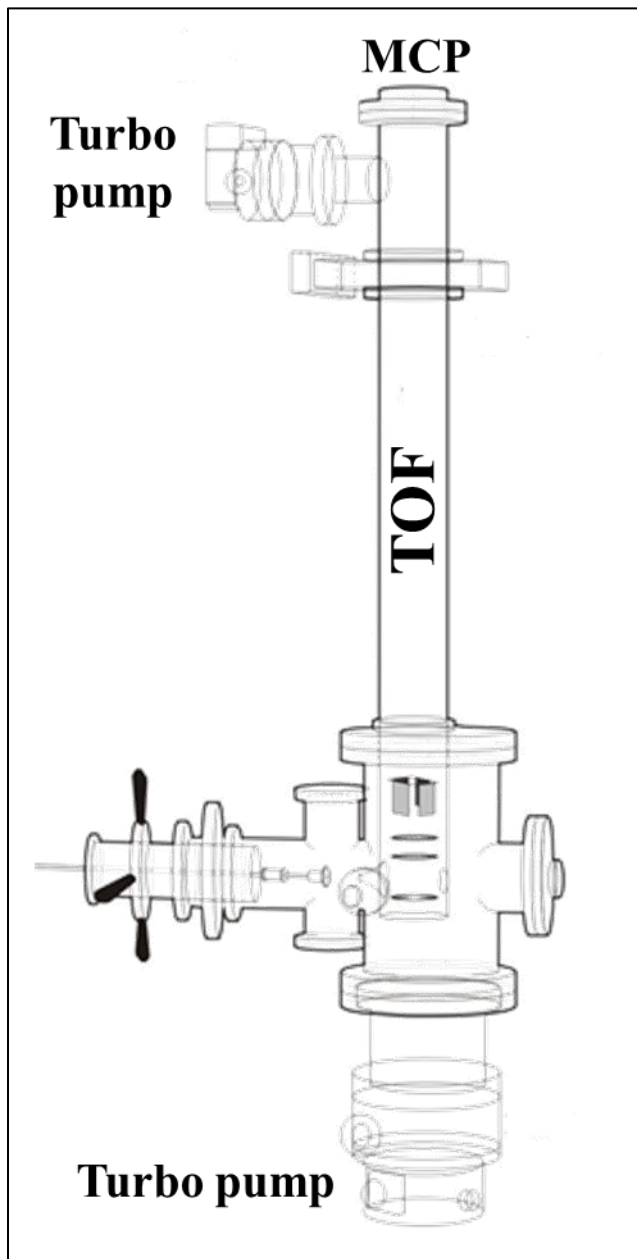


Figure 2.5: Schematic diagram of the molecular beam time-of-flight chamber.

Resonant two-photon ionization (R2PI) is used to record the excitation spectrum. The output of a tunable dye laser is focused onto the ionization region between the extraction plates of a Wiley-McLaren TOF mass spectrometer (R. M. Jordan)⁸ with a 1 m drift tube perpendicular to

the molecular beam. The repeller plate and the draw-out grid are held at constant voltages of +4220V and +3900V respectively. Ion optics are utilized to focus the resulting cations into the TOF tube producing a current after impacting the microchannel plate (MCP) detector. Raw signal from the MCP is amplified by a DC-300 MHz pre-amplifier (Stanford Research Systems, SR250). An oscilloscope is used to gate around the mass of interest and record mass resolved molecular spectrum. The species-specific schemes are explained in section 2.5 of this chapter.

2.4 Chirped-Pulse Spectroscopy Instrument

Chirped pulse Fourier transform microwave (CP-FTMW) spectroscopy pioneered by Pate and co-workers is a powerful tool to determine the structures of gas phase molecules with precision.⁹ The strong electric fields provided by the chirps polarize all rotational transitions lying in the 8-18 GHz range within 1 μ s, and the resulting free induction decay (FID) is collected which is Fourier transformed to obtain a rotational spectrum. The ingenuity of utilizing chirps lies in making the data acquisition process about 1000 times faster than previously possible. The patterns of transitions forming the spectrum provide a measurement of the geometry via the rotational constants and dipole moment projections along the three inertial axes. After the introduction of this technique, its applications are growing quickly.¹⁰

When studying reactions or multi component mixtures, analyzing a CP-FTMW spectrum becomes challenging, despite using theoretical predictions. For molecular systems which are non-polar or weakly polar ($\mu < 1$ Debye), the instrument is not sensitive enough as the microwave signal intensity scales as μ^2 . Hence, there was a need to utilize a complimentary analytical tool such as a mass spectrometer. We incorporated a TOF mass spectrometer after the spectral acquisition region of our CP-FTMW chamber for fast simultaneous measurement. Apart from online monitoring of the expansion components, the m/z can help us out by detecting components with low or no dipole moments, and also reduce the number of possible structures that need to be analyzed in the broadband rotational spectrum. We use a soft ionization technique to not cause fragmentation of the expansion components, such as a vacuum ultraviolet (VUV) laser source (118 nm) which is a single photon ionization process.

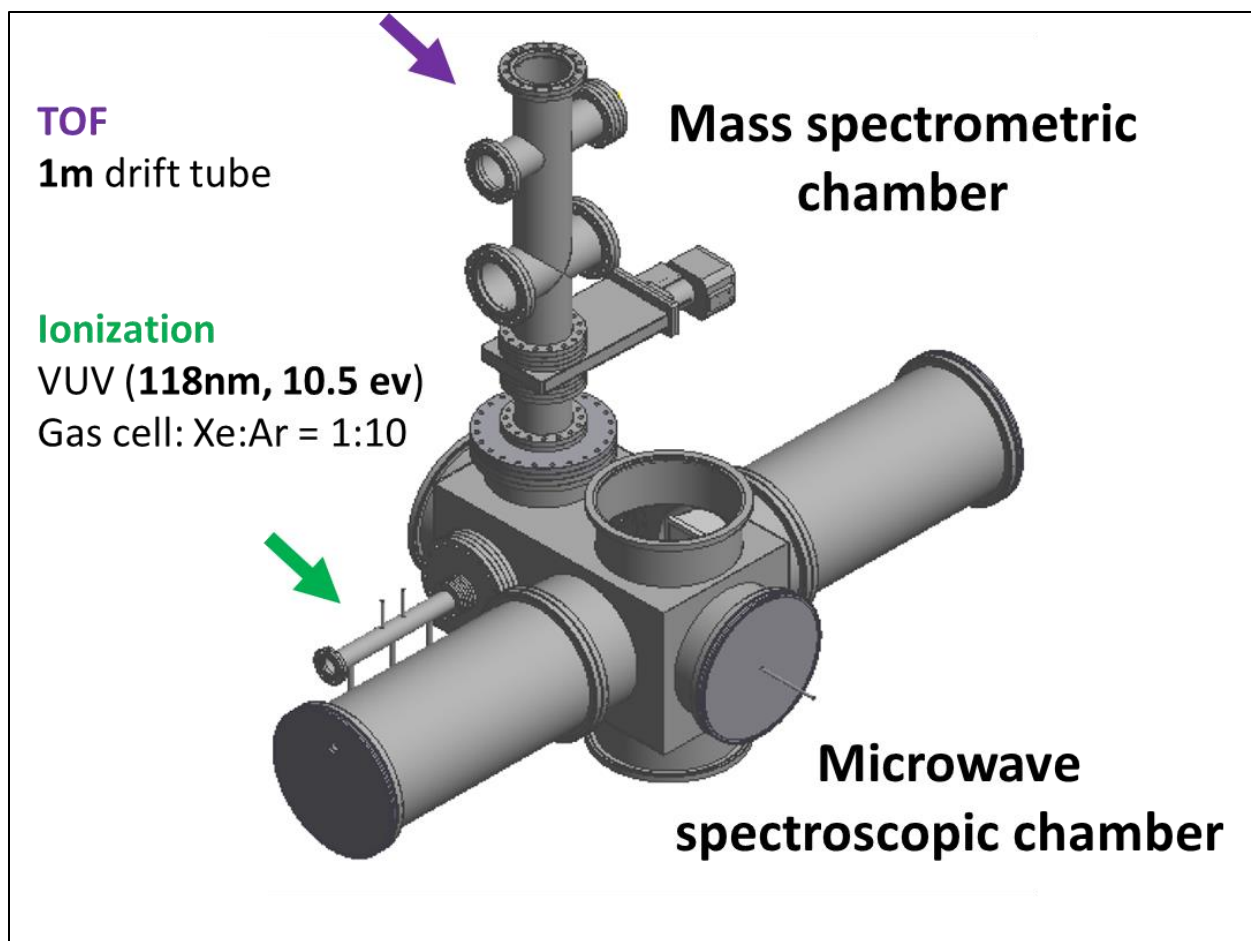


Figure 2.6: Schematic diagram of mass-correlated broadband rotational spectrometer. The first part is the CP-FTMW chamber followed by the VUV-TOF chamber.

The chamber used (**Figure 2.6**) is described in detail elsewhere.¹¹ This chamber has two parts that are differentially pumped, separated by a skimmer. The first is the cuboidal spectroscopic chamber and the second part, which is beyond the skimmer, is the mass spectrometric chamber which is cylindrical. The spectroscopic chamber located behind the skimmer is evacuated by two 25 cm diameter diffusion pumps (Varian VHS 10) backed by a roots blower (BOC Edwards EH500) and a rotary roughing pump (Alcatel 2063); this brings the operating pressure of the spectroscopic chamber down to $\sim 10^{-4}$ mbar. The interior of the microwave portion is covered with microwave absorber material (Emerson and Cuming Eccosorb HR-25/ML; LS-24) to avoid microwave resonances from being created within the walls of the chamber. The mass spectrometric portion has a Wiley-McLaren TOF with a 1 m drift tube, which is evacuated by a 350 L/s turbomolecular

pump (Osaka Vacuum TG350F) backed by a rotary pump (Alcatel 20101) with operating pressures of $\sim 5 \times 10^{-7}$ mbar. The two portions of the instrument are described here.

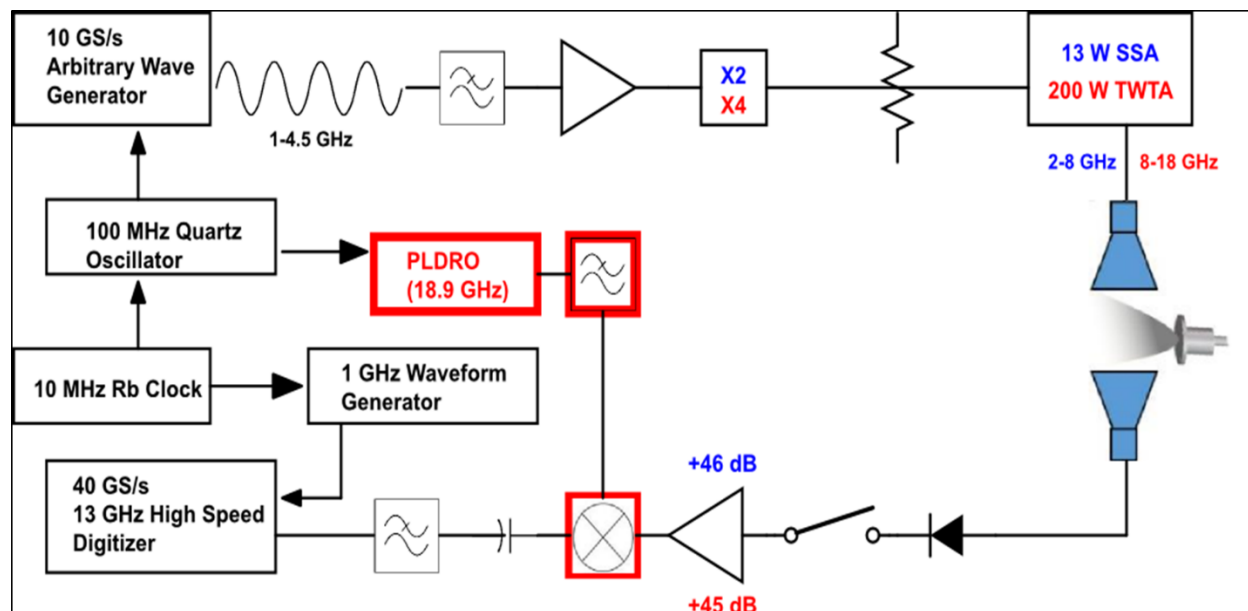


Figure 2.7: Schematic diagram of the electronics used to perform broadband chirped-pulse fourier transform microwave spectrometry.

2.4.1 Chirped-Pulse Fourier Transform Microwave Spectrometer

The microwave spectroscopic region of the chamber is composed of fast electronic circuits for creation and detection of microwaves over the 2-18 GHz region (**Figure 2.7**). The current set-up is a modified version of a previously used system in the Zwier lab.¹² A 10 gigasamples per second (GS s^{-1}) arbitrary waveform generator (Tektronix AWG7101) is used to generate broadband linear frequency chirps and/or single frequency pulses. The AWG which acts as a trigger to the other electronics, is referenced by a 100 MHz quartz oscillator driven by a 10 MHz Rb-disciplined crystal oscillator (Stanford Research Systems FS725). The output frequencies up to 5 GHz pass through a low pass filter (Lorch 10LP-5000-S) and a pre-amplifier (Mini Circuits ZX60-6031E-S+ 6000 MHz, +14.2 dB gain), which is then up-converted to 8-18 GHz range (quadrupled by Phase One PS06-0161). The power of the up-converted chirps is set manually with a step attenuator (Weinschel AF117A-69-11), followed by amplification by a 200W travelling wave-tube amplifier (TWTA; Amplifier Research 200T8G18A), which is sent to the vacuum chamber through the broadcasting horn. The microwave pulses intercept the sample molecules

about 12.5 cm from the nozzle orifice, which get polarized and then undergo free induction decay (FID).

In order to minimize interference from the microwave pulse, a switch is used to collect the FID signal after the receiving horn. This switch is timed to open after a 60 ns delay from the end of the chirp. The time-domain signal is amplified with a 45 dB low noise amplifier (Miteq AMF-6F-06001800-15-10P), which is down-converted by mixing with an 18.9 GHz PLDRO. The signal then passes through a DC block (MCL 15542 BLK-18) and a 12 GHz low pass filter (Lorch 7LA-12000-S) Finally, the FID is phase coherently averaged and digitized in the time domain with a 13 GHz, 40 GS s⁻¹ real-time digitizer (Guzik ADC6131). Twenty 16 ms long FIDs were collected within each gas pulse, resulting in a resolution of 60 kHz. A Kaiser-Bessel windowing function with a shape parameter of 11.5 was applied to the molecular FID signal before taking the Fast Fourier Transform (FFT), in order to reduce noise from the Travelling Wave Tube Amplifier (TWTA) in the early part of the FID.

2.4.2 Vacuum Ultraviolet Time-of-Flight Mass Spectrometer

After recording the rotational spectrum, the jet-cooled gas pulse travels further downstream where the coldest part of the gas pulse is sampled through a 2 mm diameter skimmer located 35 cm from the pulsed valve, where it is introduced into the ionization region of a mass spectrometer. As mentioned before, the soft ionization method is a VUV source operating at 118 nm (10.5 eV). The pump laser is the third harmonic (355 nm) of a Nd:YAG laser (Continuum YG661-20(680)) which is frequency tripled in a 31 cm long custom VUV cell with a gas mixture of Xe (10 torr)/Ar (100 torr).¹³ A MgF₂ lens is fixed at the end of the VUV cell to focus 118 nm and spatially separate the 355 nm pump beam. The laser pulse is triggered by the AWG via a digital delay generator (Berkeley Nucleonics model 577). The analyte is ionized by VUV radiation via a one-photon process in the extraction region where the repeller plate and the draw-out grid are held at constant voltages of +3000 V and +2750V respectively. The formed cations are focused by an einzel lens held at +1700 V onto the surface of an MCP (Jordan TOF Products, Inc., C0701) located 100 cm away. The ion current is amplified by a fast amplifier (Stanford Research Systems SR445) and displayed on a 3.5 GHz, 40 GS/s oscilloscope (Tektronix DPO 7354C).

2.5 Species Specific Schemes

The strength of our lab lies in performing conformer-specific and complex-specific spectroscopy via double-resonance or multiple-resonance schemes. We utilize laser based double resonance schemes and a combination of chirp and single frequency pulses (SFP) based multiple resonance schemes.

2.5.1 Laser-Based Schemes

All the experiments reported in this thesis used double resonance schemes involving one IR and one UV laser. First, a UV excitation spectrum is obtained which is a result of all the species present in the expansion, hence making it non species-specific (**Figure 2.8 (a)**). Next we perform conformer-specific IR spectroscopy called Fluorescence-dip infrared (FDIR) spectroscopy, when carried out in the LIF chamber, or Resonance ion-dip infrared (RIDIR) spectroscopy, when performing conformer or complex-specific IR spectroscopy in the Molecular beam TOF chamber. After obtaining unique IR spectra corresponding to selected peaks in the excitation spectrum, we perform IR-UV holeburning (IR-UVHB) spectroscopy to identify all the peaks in the excitation spectrum that share a known IR transition. The schemes across both the laser spectrometers are very similar to each other. The only difference is that in the LIF chamber, we monitor the emitted photon intensity whereas in the molecular beam TOF chamber, we monitor the ion signal upon R2PI. The schemes described below correspond to the schemes carried out only in the LIF chamber for ease.

FDIR spectroscopy (**Figure 2.8 (b)**) was utilized to obtain ground-state IR spectra associated with individual transitions in the excitation spectrum, tuning the IR over the 2800-3800 cm^{-1} spanning the CH stretch and the OH stretch regions. This IR-UV double resonance technique was performed by fixing the UV laser at a particular excitation frequency with a repetition rate of 20 Hz and scanning a spatially overlapped IR laser beam, operating at 10 Hz, which temporally preceded the UV laser by 200 ns. The active baseline subtraction mode of a gated integrator was used to record the difference signal with and without the IR laser present, to produce a decrease (or dip) in fluorescence signal, whenever the IR frequency of the laser was in resonance with the vibration of the particular conformer, whose signal was being monitored by the UV LIF. The active baseline subtraction is crucial as the largest noise introduced to the spectrum is the shot-to-shot

noise. In this way, single-conformation IR spectra were recorded for each of the conformations of the three molecules.

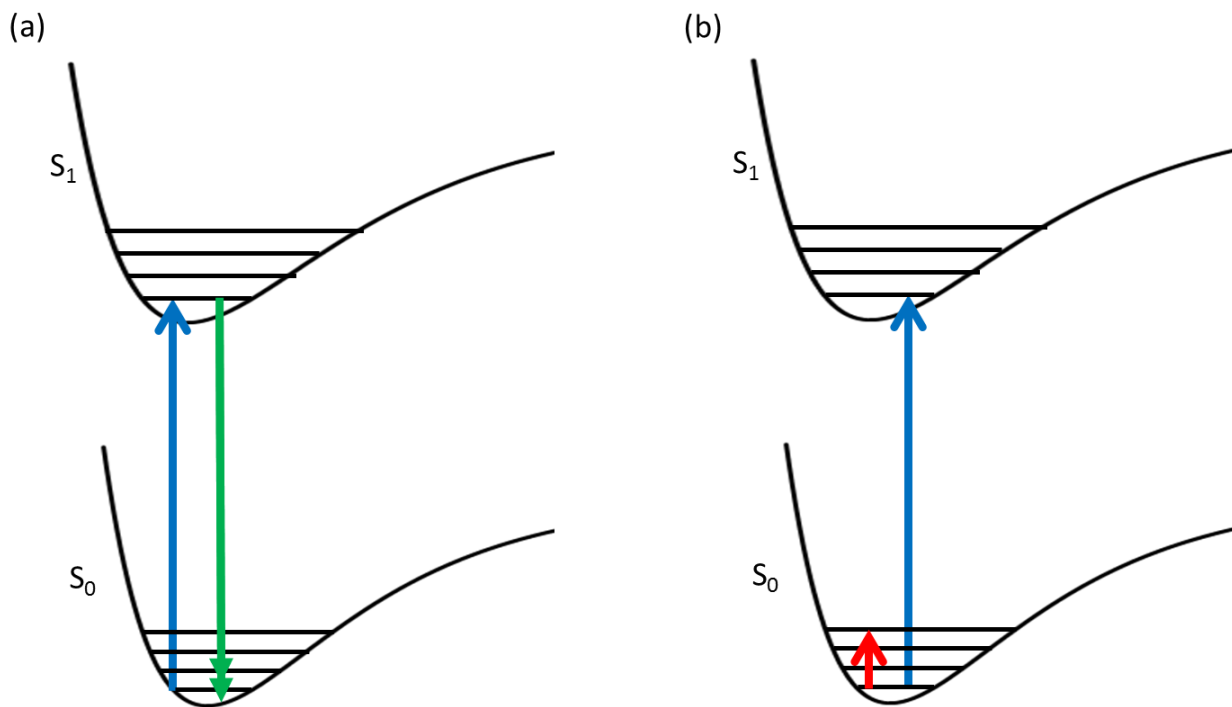


Figure 2.8: Laser based schemes (a) LIF excitation spectrum where the molecules radiatively relax to the ground electronic state over ~ 10 - 100 ns, and (b) FDIR spectrum where the IR laser temporally precedes the UV laser by about 200 ns, hence depopulating the zero-point vibrational level.

After obtaining unique IR spectra corresponding to different types of conformers, we employed IR-UV holeburning (IR-UV HB) to record conformer-specific UV spectra. This technique was used for the identification of excitation peaks corresponding to a common IR frequency. Just like in the case of FDIR spectroscopy, the spatial overlap and the 200 ns temporal delay of the UV and IR laser beams were retained. In the IR-UV HB scheme, the IR laser is fixed at a unique IR transition of a particular type of conformer and the UV laser is scanned. The active baseline subtraction mode of the gated integrator records a dip in the fluorescence signal when the IR probe laser is in resonance with an electronic transition sharing the same ground state as the UV excitation laser, hence showing the UV transitions corresponding to particular IR bands.

2.5.2 Chirped-Pulse Based Schemes

Multiple resonance schemes using series of chirp and SFPs are utilized to perform conformer-specific spectroscopy in the microwave spectral region (8-18 GHz). For molecules with large dipole moments, chirps from a high power source can operate in the rapid adiabatic passage (RAP) regime where significant population changes are induced by the chirp compared to the weak field limit of linear fast passage (LFP).¹⁴ In order to determine when these conditions were achieved, we recorded preliminary broadband spectra following polarization sweeps from 8 GHz to 18 GHz and from 18 GHz to 8 GHz and collected molecular FIDs at 100%, 10% and 1% of full TWTA power. If the frequency sweep is operating in the RAP regime, population will be moved up or down the rotational ladder by the sweep, producing spectra with different intensities when swept in the two directions.

A modified line picking scheme was utilized for 3-PN which is described elsewhere.¹⁵ Initially, an 8-18 GHz chirp followed by a “coherence-breaking” single-frequency pulse (SFP) resonant with the most intense transition in the broadband microwave spectrum was used. A difference spectrum is obtained by subtracting the broadband spectrum from a second broadband spectrum recorded with the SFP present, and plotting the magnitude of the difference between them. Those transitions whose intensities are modulated by the SFP belong to the same conformer as the one targeted by the SFP. Based on those transitions that appear in this difference spectrum, a second transition with a high percent modulation is selected for SFP excitation. The difference spectrum so acquired contains new modulated lines, which are used to choose a third SFP and follow the same procedure to obtain a conformer specific difference spectrum with a sufficient number of intensity-modulated transitions to obtain a preliminary fit to the conformer-specific spectrum. The broadband chirp is 1 μ s long and the SFPs are each 150 ns long. A gap of 50 ns between the chirp and the first SFP is maintained, while 5 ns gaps between the individual single-frequency pulses is used to avoid beats between them (**Figure 2.9**).

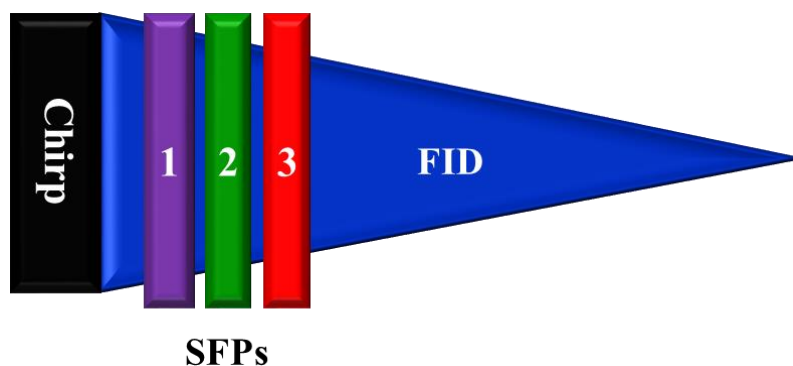


Figure 2.9: Strong-field coherence breaking scheme to perform species-specific broadband microwave spectroscopy.

2.6 Theoretical

Computational tools for prediction of energetics and spectra are crucial for the analysis of all the spectroscopy carried out in the Zwier lab. Development of dispersion corrected theoretical techniques aid in more accurate predictions of spectra and stabilities, especially for the molecular systems we study, as the conformations and intermolecular interactions are primarily governed by weak molecular interactions such as hydrogen bonds and dispersion.¹⁵⁻¹⁷ The chemical systems studied in this thesis typically have several conformers or possible clusters that range from just 2 to >1000 possible structures. Which is why we perform a quick search of starting geometries using MACROMODEL suite of program¹⁸ carried out using a molecular mechanics force field, as this process is computationally inexpensive. We then treat these starting geometries at higher levels of theory using the Gaussian 09 suite of programs¹⁹ for accuracy in the predictions.

After obtaining the starting structures, the first step would be performing geometry optimizations that are carried out to arrive at stable minima followed by harmonic vibrational frequency calculations. Apart from providing us with the vibrational frequencies, these calculations also are a check to ensure that no imaginary frequencies are obtained. The relative energies of the conformations are affected by weak interactions such as dispersive interactions; hence, we used dispersion corrected functionals and suitable basis sets to get accurately calculated relative energies. Calculations are typically done at B3LYP-GD3BJ/Def2TZVP level of theory since our past experience indicates that they are able to give reliable predictions.¹⁵⁻¹⁷ The rotational constants are also obtained from these calculations to predict and assign rotational spectra.

In order to compare the observed $S_1 \leftarrow S_0$ origin transitions with the predicted of calculations, time-dependent density functional theory (TD-DFT) calculations were carried out at the same level of theory to obtain vertical excitation energies. After scaling, they provided predictions of the frequency ordering of origin bands in the UV excitation spectra. Excited state geometry optimizations were also carried out to help assign the vibronic peaks with more accuracy than frequency calculations at the S_0 level.

Torsional potential energy surface of the molecules were studied computationally by performing relaxed potential energy surface (PES) scans which optimize the geometry at fixed values for the dihedral angles regularly spaced on the PES array. This is used to locate all the minima on a PES and to study isomerization pathways by taking one dimensional cuts of the PES linking specific potential energy minima. Calculations using the Quadratic Synchronous Transit (QST2) method²⁰ were performed on specific systems to estimate the zero-point energy (ZPE)-corrected barrier height to methyl rotation as rotational spectroscopy has sufficient resolution to record internal rotation splitting.

Harmonic vibrational frequencies in the alkyl CH stretch region do not match well with the experiment due to the pervasive presence of Fermi resonance between the stretch fundamentals and even overtones of the CH_n bends. We used anharmonic calculations using local mode Hamiltonian developed by our collaborator Dr. Sibert from UW Madison to predict and assign the IR spectra in the CH stretch region.

The rotational constants obtained from calculations are used as starting ‘guesses’ for the microwave spectral fitting using programs such as SPFIT/SPCAT²¹ and XIAM²². These are widely used fitting programs in the microwave spectroscopy community, while SPFIT/SPCAT has the capability to fit hyperfine splittings due to the presence of multiple quadrupolar nuclei such as nitrogen, XIAM has the capability to fit multiple internal rotation tunneling splitting along with one quadrupolar nucleus. Fitting is done such that the error in the fits are well below the experimental resolution of 60 kHz.

2.7 References

- ¹ M. D. Morse, *Experimental Methods in the Physical Sciences*, **29**, 21 (1996).
- ² D. M. Lubman, C. T. Rettner, and R. N. Zare, *J. Phys. Chem.* **86**, 1129 (1982).
- ³ R. E. Smalley, L. Wharton, and D. H. Levy, *Acc. Chem. Res.* **10**, 139 (1977).
- ⁴ C. Abeysekera, A. O. Hernandez-Castillo, J. F. Stanton, and T. S. Zwier, *J. Phys. Chem. A.* **122**, 6879 (2018).
- ⁵ P. Chen, S. D. Colson, W. A. Chupka, and J. A. Berson, *J. Phys. Chem.* **90**, 2319 (1986).
- ⁶ N. R. Pillsbury, J. A. Stearns, C.W.Müller, D. F. Plusquellic, and T. S. Zwier, *J. Chem. Phys.* **129**, 114301 (2008); C. A. Arrington, C. Ramos, A. D. Robinson, and T. S. Zwier, *J. Phys. Chem. A* **102**, 3315 (1998); F. A. Ensminger, J. Plassard, T. S. Zwier, and S. Hardinger, *J. Chem. Phys.* **102**, 5246 (1995).
- ⁷ E. G. Buchanan, J. R. Gord, and T. S. Zwier, *J. Phys. Chem. Lett.* , **4**, 1644 (2013); P. S. Walsh, E. G. Buchanan, J. R. Gord, and T. S. Zwier, *J. Chem. Phys.*, **142**, 154303 (2015); D. M. Lubman, *Mass Spectrom. Rev.*, **7**, 559 (1988); R. H. Page, Y. R. Shen, and Y. T. Lee, *J. Chem. Phys.*, **88**, 4621 (1988); T. S. Zwier, *Annu. Rev. Phys. Chem.*, **47**, 205 (1996); T. S. Zwier, *J. Phys. Chem. A*, **105**, 8827 (2001); P. S. Walsh, R. Kusaka, E. G. Buchanan, W. H. James, B. F. Fisher, S. H.Gellman, and T. S. Zwier, *J. Phys. Chem. A*, **117**, 12350 (2013).
- ⁸ W. C. Wiley, I. H. McLaren, *Rev. Sci. Instrum.* **26**, 1150 (1955).
- ⁹ G. G. Brown, B. C. Dian, K. O. Douglass, S. M. Geyer, S. T. Shipman, and B. H. Pate, *Rev. Sci. Instrum.* **79**, 053103 (2008).
- ¹⁰ J. M. Oldham, C. Abeysekera, B. Joalland, L. N. Zack, K. Prozumet, I. R. Sims, G. B. Park, R.W. Field, and A. G. Suits, *J. Chem. Phys.* **141**, 154202 (2014); C. Abeysekera, B. Joalland, N. Ariyasingha, L. N. Zack, I. R. Sims, R. W. Field, and A. G. Suits, *J. Phys. Chem. Lett.* **6**, 1599 (2015); C. Abeysekera, L. N. Zack, G. B. Park, B. Joalland, J. M. Oldham, K. Prozumet, N. M. Ariyasingha, I. R. Sims, R.W. Field, and A. G. Suits, *J. Chem. Phys.* **141**, 214203 (2014); K. Prozumet, Y. V. Suleimanov, B. Buesser, J. M. Oldham, W. H. Green, A. G. Suits, and R. W. Field, *J. Phys. Chem. Lett.* **5**, 3641 (2014); B. C. Dian, G. G. Brown, K. O. Douglass, and B. H. Pate, *Science* **320**, 924 (2008); N. M. Kidwell, V. Vaquero-Vara, T. K. Ormond, G. T. Buckingham, D. Zhang, D. N. Mehta-Hurt, L. McCaslin, M. R. Nimlos, J. W. Daily, B. C. Dian, J. F. Stanton, G. B. Ellison, and T. S. Zwier, *J. Phys. Chem. Lett.* **5**, 2201 (2014).
- ¹¹ S. M. Fritz, B. M. Hays, A. O. Hernandez-Castillo, C. Abeysekera, and T. S. Zwier, *Rev. Sci. Instrum.* **89**, 093101 (2018).
- ¹² A. O. Hernandez-Castillo, C. Abeysekera, B. M. Hays, and T. S. Zwier, *J. Chem. Phys.*, **145**, 114203 (2016).

- ¹³ J. Yang, X. B. Wang, X. P. Xing, and L. S. Wang, *J. Chem. Phys.* **128**, 201102 (2008).
- ¹⁴ D. Schmitz, V. A. Shubert, T. Betz, and M. Schnell, *J. Mol. Spectrosc.* **280**, 77 (2012).
- ¹⁵ S. M. Fritz, A. O. Hernandez-Castillo, C. Abeysekera, B. M. Hays, and T. S. Zwier, *J. Mol. Spectrosc.* **349**, 10 (2018).
- ¹⁶ P. Mishra, D. M. Hewett, and T. S. Zwier, *J. Chem. Phys.* **148**, 184304 (2018).
- ¹⁷ D. P. Tabor, D. M. Hewett, S. Bocklitz, J. A. Korn, A. J. Tomaine, A. K. Ghosh, T. S. Zwier, and E. L. Sibert III, *J. Chem. Phys.* **144**, 224310 (2016).
- ¹⁸ F. Mohamadi, N. G. J. Richards, W. C. Guida, R. Liskamp, M. Lipton, C. Caufield, G. Chang, T. Hendrickson, and W. C. Still, *J. Comput. Chem.* **11**, 440 (1990).
- ¹⁹ M. J. Frisch, G. W. Trucks, H. B. Schlegel, G. E. Scuseria, M. A. Robb, J. R. Cheeseman, G. Scalmani, V. Barone, B. Mennucci, G. A. Petersson, H. Nakatsuji, M. Caricato, X. Li, H. P. Hratchian, A. F. Izmaylov, J. Bloino, G. Zheng, J. L. Sonnenberg, M. Hada, M. Ehara, K. Toyota, R. Fukuda, J. Hasegawa, M. Ishida, T. Nakajima, Y. Honda, O. Kitao, H. Nakai, T. Vreven, J. A. Montgomery, Jr., J. E. Peralta, F. Ogliaro, M. Bearpark, J. J. Heyd, E. Brothers, K. N. Kudin, V. N. Staroverov, T. Keith, R. Kobayashi, J. Normand, K. Raghavachari, A. Rendell, J. C. Burant, S. S. Iyengar, J. Tomasi, M. Cossi, N. Rega, J. M. Millam, M. Klene, J. E. Knox, J. B. Cross, V. Bakken, C. Adamo, J. Jaramillo, R. Gomperts, R. E. Stratmann, O. Yazyev, A. J. Austin, R. Cammi, C. Pomelli, J. W. Ochterski, R. L. Martin, K. Morokuma, V. G. Zakrzewski, G. A. Voth, P. Salvador, J. J. Dannenberg, S. Dapprich, A. D. Daniels, O. Farkas, J. B. Foresman, J. V. Ortiz, J. Cioslowski, and D. J. Fox, gaussian 09, Revision C.01, Gaussian, Inc., Wallingford, CT, 2010.
- ²⁰ C. Peng and H. B. Schlegel, *Isr. J. Chem.*, **33**, 449 (1993).
- ²¹ M. Pickett, *J. Mol. Spectrosc.*, **148**, 371 (1991).
- ²² H. Hartwig and H. Dreizler, *Z. Naturforsch.*, **51a**, 923 (1996).

CHAPTER 3. CONFORMATIONAL EXPLOSION: UNDERSTANDING THE COMPLEXITY OF *PARA*-DIALKYL BENZENE POTENTIAL ENERGY SURFACES

3.1 Introduction

Short-chain dialkylbenzenes are a class of molecules that are common components of coal and aviation fuel.¹⁻³ While the conformation-specific spectroscopy of the single-chain alkylbenzenes has been studied for chain lengths up to ten carbon atoms long,^{4,5} the conformational preferences of the diethylbenzenes have only been explored in cursory fashion previously.⁶ Fundamental questions arise such as to what extent the two chains interact with each other as a function of chain length. What is the threshold chain length at which the conformational preferences of the individual chains are clearly distorted from the single chains analogs? Do the two chains tend to lie in the same side of the aromatic ring, or do they prefer to lie on opposite sides? How are the conformational preferences affected by the relative positions of substitution on the aromatic ring (*ortho*-, *meta*-, and *para*-)?

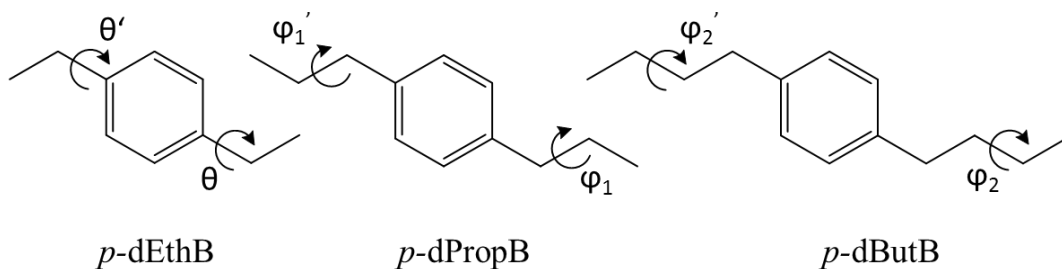


Figure 3.1: Chemical structures and key dihedral angles for *para*-diethylbenzene (*p*-dEthB), *p*-dipropylbenzene (*p*-dPropB), and *para*-dibutylbenzene (*p*-dButB).

The present work is aimed at addressing these questions on the symmetric chain, *para*-substituted series (**Figure 3.1**): *para*-diethylbenzene (*p*-dEthB), *para*-dipropylbenzene (*p*-dPropB), and *para*-dibutylbenzene (*p*-dButB). This work is an extension of previous studies on the single-chain analogs ethylbenzene, propylbenzene, and butylbenzene, where an anharmonic local mode Hamiltonian was developed for the modeling of the alkyl CH stretch region, especially to address the stretch-bend Fermi resonances (FRs) that appear in the IR spectra of the alkyl CH stretch

region.⁴ A major goal of the single-chain alkylbenzene work was to identify the chain length at which ‘stacked’ structures begin to form, where the chain is folded over the π cloud, the first evidence of which appeared in octylbenzene, at a size about half the length ($n = 17-18$) that the straight alkane chains begin to compete with their all-*trans* counterparts.^{5,7}

One of the main take home messages about the double-chain molecules is that the number of low-energy conformations exponentially increases with size relative to their single-chain analogs as the number of flexible coordinates grows from two (θ, θ') in *p*-dEthB to four ($\theta, \theta', \phi_1, \phi_1'$) in *p*-dPropB and then six ($\theta, \theta', \phi_1, \phi_1', \phi_2, \phi_2'$) in *p*-dButB (**Figure 3.1**). Moreover, the relative orientations of the chains produce unique conformations with *gauche* dihedrals (g_+ or g_-) and with the two chains on the same (*syn*) or opposite (*anti*) sides of the phenyl ring. We shall see that the single-chain UV and IR⁴ spectra play a crucial role in identifying key conformational families in the dialkyl substituted analogs. The effects of disubstitution are quite subtle in these molecules, leading to an exponential growth in the number of low-energy conformers with significant population, contributing to the spectra even after cooling in a supersonic expansion. In case of *p*-dButB, tentative identification of electronic origin peaks due to 19 conformers is made, setting a record in the number of distinguishable conformers in the UV excitation spectrum. The close energies of these conformers and the similar potential barriers computed lead to a torsional PES that looks like an “egg carton”.

3.2 Methods

3.2.1 Experimental and Theoretical

The LIF apparatus used is described in more detail elsewhere.⁸⁻¹⁰ LIF excitation, FDIR and DFL spectroscopies are carried out on the *para*-dialkylbenzenes. Helium was used in the 1.0-2.8 bar pressure range flowing over liquid samples of *p*-dEthB (18°C), *p*-dPropB (18°C), and *p*-dButB (42°C). Orifice of the pulsed valve was 500-800 μm , operating at 20 Hz. LIF excitation spectrum of *p*-dEthB was recorded over the origin and vibronic bands, whereas for the other two compounds, our focus was on the origin region, all of which were in the $S_1 \leftarrow S_0$ region. DFL spectra was recorded for multiple peaks of *p*-dEthB and not for *p*-dPropB and *p*-dButB due to lower fluorescence quantum yield. FDIR spectra was recorded for all three molecules. IR-UVHB spectra

was recorded only for *p*-dPropB as the IR spectra obtained for the other molecules had no unique peaks.

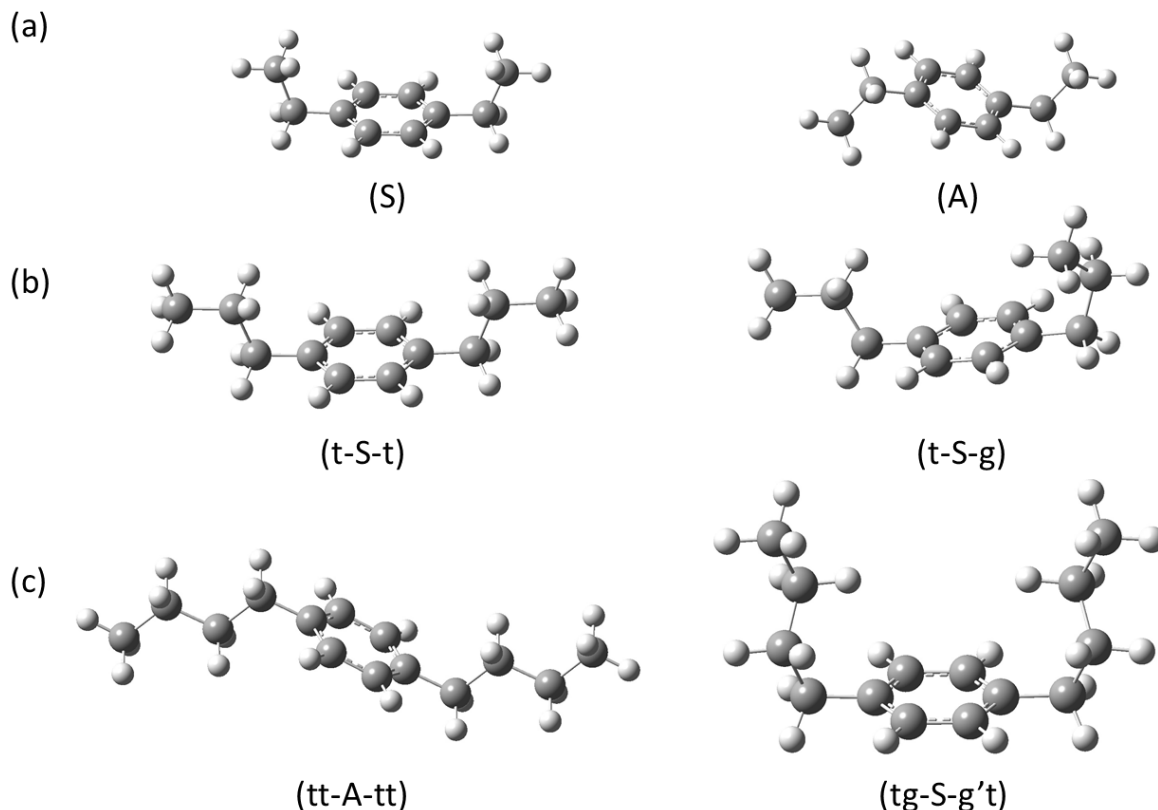


Figure 3.2: Selected optimized geometries carried out at the DFT B3LYP-GD3BJ/Def2TZVP level of theory for (a) *p*-dEthB conformers: *syn* and *anti*, (b) *p*-dPropB conformers (t-S-t) where both the chains are *trans* and (t-S-g) with one *gauche*, and (c) the all-*trans* (tt-A-tt) and global minimum (tg-S-g't) conformers of *p*-dButB.

All the conformers of the short-chain *para*-dialkylbenzenes can be obtained by rotating torsional angles θ , ϕ_1 , and ϕ_2 . Calculations were carried out using Gaussian 09 suite of programs to corroborate with our experiments.¹¹ TDDFT and S_1 electronic state optimizations were carried out to assign the UV excitation and the DFL spectra. As the harmonic vibrational calculations in the CH stretch region do not match with the experiment due to the pervasive presence of FR, we used local mode anharmonic model of the CH stretch region developed for the single-chain alkylbenzenes by the Sibert group from UW-Madison. This calculation carried out at the DFT B3LYP/6-311++G(d,p) was used to predict the IR spectra for the double-chain *para*-

dialkylbenzene molecules without modification via simple extrapolation. The assumption followed was that for lengths of upto four carbon atoms, there is no interaction between the chains in *para* position, hence the vibrational spectra can be predicted by additivity of the IR spectra of the single chain alkylbenzenes. Finally, torsional PES was performed and isomerization pathways were studied linking specific conformers.

3.2.2 Nomenclature

The nomenclature used for labeling the conformers prescribes the orientation of the two chains with respect to each other and the torsional dihedral angles along the carbon chain. When the chains are positioned on the same side of the aromatic ring, the conformer is labeled “*syn*” (designated “S”) whereas for opposite sides, it is labelled “*anti*” (designated “A”) (**Figure 3.2 (a)**). The torsional dihedral angles along a chain are denoted as *trans* (designated as “t”) for values near 180°, *gauche* (+) when near +60° (designated as g), and *gauche* (-) when near -60° (designated as g’). The full *para*-dialkylbenzene configuration is then stipulated by labeling the chain orientations with respect to each other in upper case at the centre and the local dihedrals along the chain listed radially outward in lower case on either side (**Figures 3.2 (b) and (c)**).

In pure alkyl chains, the presence of a *gauche* dihedral comes at an energetic cost of about 2.5 kJ/mol relative to a *trans* dihedral.^{4,5} Every *gauche* dihedral angle will have a double degeneracy, as *gauche* (+) is the mirror image of *gauche* (-). For example, a conformer of *p*-dButB which is (tg-A-g’g) is a mirror image of (tg’-A-gg’) where the g is replaced by g’. Some of these are non-superimposable mirror images or enantiomers, while others are identical. For example, (tg-S-g’t) has a mirror image identical to itself. Such conformers have even number of *gauche* dihedrals, with an equal number of g and g’ dihedrals. Moreover, these opposite signed *gauche* dihedrals should occur on equivalent positions on the two chains. When referring to a generic conformer type, we have used an ‘X’ or ‘x’ in place of letters. For example, (xg-X-tx) refers to all the conformers with one *gauche* (+) configuration at the first dihedral on one of the chains, while the other chain is *trans* at the first dihedral. In further discussion of regions I, II, and III, we will use ‘g’ generically when referring to a class of conformers that contain both *gauche* (+) and *gauche* (-) type of conformers.

3.3 Results and Discussion

3.3.1 Calculations

The laser spectroscopic techniques in the Zwier lab operating in the IR and the UV regions, are used to study vibrational and electronic spectra, respectively. Two chambers used to perform laser spectroscopy were the LIF chamber and the molecular beam TOF chamber. These chambers were used independently for most of the work in this thesis. Operation and data collection is controlled by LabVIEW software (National Instruments).

In *p*-dEthB, the preference of the β -carbon for a perpendicular configuration relative to the phenyl ring leads to just low-energy conformations, *syn* (S) and *anti* (A). A third high energy conformer with a very shallow minima exists in which one of the ethyl chains was in the plane of the phenyl ring. Such conformations are predicted to be high energy local minima for all three molecules with no experimental evidence for population being trapped in them, hence are not studied. For *p*-dPropB, eight unique conformers were found in the conformational search, while for *p*-dButB, fifty conformers were obtained. As we shall see shortly, a similar ‘explosion’ in the number of conformers with distinct $S_1 \leftarrow S_0$ origins is also observed experimentally. Due to indistinguishable spectroscopic signatures, only the non-mirror image conformations are explicitly considered. **Table 3.1** displays the relative ZPE (kJ/mol) of stable conformations within 5 kJ/mol of the global minimum for each of the molecules at B3LYP-GD3BJ/Def2TZVP level of theory. For the smallest two molecules *p*-dEthB and *p*-dPropB, all the conformers lie within 1 kJ/mol of one another, while *p*-dButB has 28 of its conformers spread over 4.5 kJ/mol. In *p*-dButB, the different conformations are separated by dashed lines differentiating different energy regimes. From these energy calculations, it is evident that the number of low energy conformations increases exponentially with the increase in the length of the chains. Geometry optimizations were also carried out at the DFT M06-2X/aug-cc-pVDZ (**Table 3.2**) giving relative energies similar to those at the B3LYP-GD3BJ/Def2TZVP level of theory despite some minor re-ordering of relative energies.

Table 3.1: Zero-point corrected energies relative to the most stable structure at the DFT B3LYP-GD3BJ/Def2TZVP level of theory. Dashed lines mark breaks in energy between sub-groups of conformers.

Conformer	Relative energy (kJ mol ⁻¹)
Para-diethylbenzene	
A	0
S	0.02
Para-dipropylbenzene	
t-A-t	0
t-S-t	0.09
g'-A-t	0.38
g-S-t	0.39
g'-S-g	0.61
g'-A-g'	0.63
g'-S-g'	0.64
g'-A-g	0.80
Para-dibutylbenzene ^a	
tg-S-g't	0
tt-S-tt	0.07
tg-S-gt	0.08
tt-S-gt	0.15
tt-A-tt	0.16
tt-A-gt	0.19
tg-A-g't	0.31
tg-A-gt	0.43
tg-S-g'g'	1.86
gg-S-gt	1.86
tt-A-g'g'	1.94
tt-S-g'g'	1.96
tg'-A-g'g'	1.99
tg-A-g'g'	2.04
tt-S-tg'	2.60
g't-A-tt	2.61
gt-S-gt	2.69
g't-A-gt	2.70
tg'-S-tg	2.71
g't-A-g't	2.75
g'g'-S-gg	3.52
g'g'-S-g'g'	3.70
g'g'-A-g'g'	3.71
g'g'-A-gg	3.85
g'g'-S-tg'	4.40
g'g'-A-tg	4.48
g'g'-S-tg	4.52
g'g'-A-tg'	4.52

^aThe 28 most stable conformers of p-dButB (<5 kJ mol⁻¹) out of a total of 50 structures.

Table 3.2: ZPE-corrected energies relative to the most stable structure at the DFT M06-2X/aug-cc-pVDZ level of theory.

Conformer	Relative energy (kJ mol ⁻¹)
p-dEthB	
S	0
A	0.20
p-dPropB	
g'-s-g'	0
g'-a-g'	0.02
g-a-g'	0.04
g'-s-g	0.11
g'-a-t	0.56
t-s-g	0.62
t-s-t	0.77
t-a-t	1.00
p-dButB ^a	
tg-A-g't	0
tg-S-g't	0.12
tg-A-gt	0.21
tg-S-gt	0.39
tt-A-gt	0.57
tt-S-gt	0.88
tt-S-tt	0.98
tt-A-tt	0.98
tg-S-g'g'	1.17
tg'-A-g'g'	1.31
tg-A-g'g'	1.33
gg-S-gt	1.51
tt-A-g'g'	1.87
tt-S-g'g'	1.92
g'g'-A-g'g'	2.36
g'g'-A-gg	2.44
g't-A-gt	2.70
gt-S-gt	2.71
g't-A-g't	2.76
g'g'-S-gg	2.89
g'g'-S-g'g'	3.01
tg'-S-tg	3.01
g't-A-tt	3.15
tt-S-tg'	3.27
g'g'-S-tg'	3.58
g'g'-A-tg'	3.74
g'g'-A-tg	3.95
g'g'-S-tg	4.20

^a The 28 most stable conformers of p-dButB (<5 kJ mol⁻¹) out of a total of 50 structures.

3.3.2 LIF excitation spectra

UV excitation spectra in the $S_1 \leftarrow S_0$ origin region ($36\,800\text{--}37\,070\text{ cm}^{-1}$) of *p*-dEthB, *p*-dPropB, and *p*-dButB are shown in black traces in **Figure 3.3**. The red traces going up correspond to the relative vertical excitation frequencies of the conformers calculated at the DFT B3LYP-GD3BJ/Def2TZVP. The computed spectra are scaled such that the highest calculated $S_1 \leftarrow S_0$ vertical excitation frequency, corresponding to the *anti* all-*trans* structure, is set to the highest experimental frequency. The intensities of the calculated spectra are the computed oscillator strengths. **Figure 3.3** is segmented into three regions (I-III) identified by the vertical excitation calculations. Regions I, II, and III encompass the origin bands for classes of conformers that have a *trans* dihedral in the first dihedral angles of both chains, a single *gauche* first dihedral and two *gauche* dihedrals, respectively. The LIF excitation peaks marked with asterisk represent the origin transitions of unique conformers. The computed vertical excitation frequencies of the different conformers are listed in **Table 3.3**.

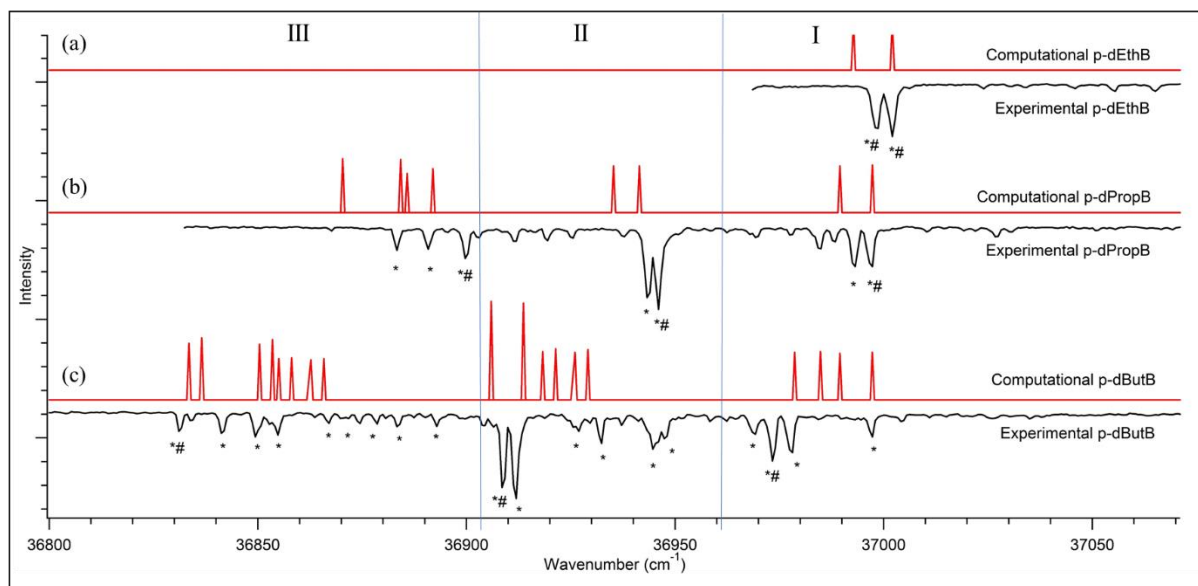


Figure 3.3: Small chain para-dialkylbenzene UV fluorescence excitation spectra. Experimental spectra (black traces) of (a) *p*-dEthB, (b) *p*-dPropB, and (c) *p*-dButB, with calculated vertical excitation energies in red. The experimental $S_1 \leftarrow S_0$ origin bands are labelled with an asterisk. Region I contains the $S_1 \leftarrow S_0$ origins from the (xt-X-tx) class of conformers, region II the (xt-X-gx) class, and region III the (xg-X-gx) family. See text for further discussion.

Table 3.3: Calculated, scaled excitation energies for low-energy conformers of *p*-dEthB, *p*-dPropB, and *p*-dButB, carried out at B3LYP-GD3BJ/Def2TZVP level of theory.

Conformer	Computational UV excitation (cm ⁻¹)
• Para-diethylbenzene	•
• A	• 37002 ^b
• S	• 36993
• Para-dipropylbenzene	•
Region 1	•
• t-A-t	• 36997 ^b
• t-S-t	• 36990
Region 2	•
• g-A-t	• 36941
• g-S-t	• 36935
• g-A-g	• 36892
Region 3	•
• g-S-g'	• 36886
• g-A-g'	• 36884
• g-S-g	• 36870
• Para-dibutylbenzene ^a	•
• tt-A-tt	• 36997 ^b
Region 1	•
• tt-S-tt	• 36990
• g't-A-tt	• 36985
• tt-S-tg'	• 36979
• tt-A-g'g'	• 36929
• tt-A-gt	• 36926
• tt-S-g'g'	• 36921
Region 2	•
• tt-S-gt	• 36918
• g't-A-gt	• 36914
• g't-A-g't	• 36914
• gt-S-gt	• 36906
• tg'-S-tg	• 36906
• g'g'-A-g'g'	• 36869
• tg'-A-g'g'	• 36866
• tg-A-gt	• 36863
• g'g'-S-gg	• 36863
Region 3	•
• tg-S-g'g'	• 36858
• g'g'-A-gg	• 36857
• tg-S-g't	• 36855
• tg-A-g'g'	• 36853
• tg-A-g't	• 36850
• g'g'-S-g'g'	• 36843
• tg-S-gg	• 36837
• tg-S-gt	• 36833

^a The 28 most stable conformers of *p*-dButB (<5 kJ mol⁻¹) out of a total of 50 structures. Dashed lines mark divide the structures into three groups, as xt-X-tx (region I), xg-X-tx (region II), and xg-X-gx (region III).

^b Highest frequency transition used as a reference for each molecule. The scaling factors are 1.136385 for *p*-dEthB, for 1.134957 *p*-dPropB and 1.134005 for *p*-dButB.

In the case of *p*-dEthB (**Figure 3.3(a)**), two origin bands are observed experimentally at 36998 and 37002 cm⁻¹. Previous work by Breen *et al.* tentatively assigned the peak at 37002 cm⁻¹ to the *anti* conformer and the one at 36998 cm⁻¹ to the *syn* conformer based on the trend seen for the *ortho*-, *meta*-, and *para*-substituted diethylbenzenes.⁶ The same frequency ordering is predicted by the calculations (**Table 3.3**). The excitation spectrum of *p*-dEthB extending out to 37600 cm⁻¹ with mode assignments is shown in **Figure 3.4**. Apart from just the Franck-Condon activity involving totally symmetric modes, non-totally symmetric fundamentals gaining intensity via vibronic coupling from the S₂ state are also observed.

In the origin region, the *p*-dPropB LIF spectrum in (**Figure 3.3(b)**) divides itself into three regions. Based on the assignments for small chain alkylbenzenes, the *gauche* propyl chain conformation has its S₁←S₀ origin shifted to lower frequency in UV excitation by about 50 cm⁻¹ relative to *trans*.^{4,12} As a result, we anticipate region I containing two all-*trans* chain conformations (t-A-t and t-S-t), region II with one *gauche* and one *trans* (g-A-t and g-S-t), and region III with two *gauche* alkyl chains (g-A-g, g-S-g', g-A-g', and g-S-g). Consistent with this idea, there are two origin bands in region I corresponding to the *syn* and *anti* all-*trans* conformers of the molecule, as predicted by the vertical excitation frequencies (**Table 3.3**). The intense peaks in region II correspond to conformers with one propyl chain in a *trans* configuration and the other *gauche* (region II, **Table 3.3**). These conformers possess enantiomers due to the two distinct *gauche* conformations (g and g') of the propyl chain that are mirror images of one another. Region III is anticipated to contain S₁←S₀ origin peaks due to four conformers in which both the alkyl chains are in a *gauche* conformation. This class of conformers has higher energies than the others; hence, their intensities are weaker despite two of them having enantiomers. The calculations predict four such conformations as shown in region III, but experimentally, we see only observe three origin peaks in that region, probably because two of the transitions are unresolved. Another lesser possibility is that one of the conformers has too little population to be observable. All the smaller unmarked peaks in the spectrum of **Figure 3.3(b)** are due to the low frequency vibronic activity.

Table 3.4: Calculated, scaled excitation energies for low-energy conformers of *p*-dEthB, *p*-dPropB, and *p*-dButB, carried out at the TD-DFT M06-2X/aug-cc-pVDZ level of theory.

• Conformer	• Computational UV
• Para-diethylbenzene	
• A	• 37002 ^a
• S	• 37000
• Para-dipropylbenzene	
• t-S-t	• 36997 ^a
• t-A-t	• 36996
• g-S-t	• 36931
• g-A-t	• 36929
• g'-S-g	• 36874
• g'-A-g'	• 36872
• g-A-g'	• 36864
• g'-S-g'	• 36852
• Para-dibutylbenzene ^b	
• tt-S-tt	• 36997 ^a
• tt-A-tt	• 36997
• g't-A-tt	• 36985
tt-S-tg'	• 36980
tt-A-gt	• 36912
tt-S-gt	• 36906
g't-A-gt	• 36902
tg'-S-tg	• 36901
gt-S-gt	• 36899
g't-A-g't	• 36899
tt-A-g'g'	• 36895
tt-S-g'g'	• 36895
tg-S-g't	• 36835
tg-A-gt	• 36833
tg-A-g't	• 36825
tg-S-g'g'	• 36824
tg'-A-g'g'	• 36821
g'g'-S-gg	• 36814
tg-S-gt	• 36811
g'g'-A-g'g'	• 36808
tg-A-g'g'	• 36805
gg-S-gt	• 36799
g'g'-A-gg	• 36773
g'g'-S-g'g'	• 36767

^a Highest frequency transition used as a reference for each molecule. The scaling factors are 0.86200 for *p*-dEthB, for 0.86233 *p*-dPropB and 0.86289 for *p*-dButB.

^b The 28 most stable conformers of *p*dButB (<5 kJ mol⁻¹) are listed out of a total of 50 conformational minima.

Finally, the $S_1 \leftarrow S_0$ origin region of *p*-dButB (**Figure 3.3(c)**) has far more resolved transitions than the previous two molecules. This rise in complexity is due to the fast increase in the number of low energy conformations associated with the presence of two butyl chains. The calculations (**Table 3.3**, Fig. 3.3 (c)) predict a clear spacing between different classes of conformations. However, unlike in case of *p*-dPropB, the experimental spectrum of *p*-dButB does not divide cleanly into three regions, hindering the same straight-forward classification of conformers. Thus, it was difficult to make unambiguous assignments relying on the UV excitation spectrum alone. Based on the calculated excitation energy ordering of the different conformers, we have segmented the spectrum into different regions, using the strongest pair of transitions in region II as a reference point. According to **Table 3.3**, this pair of transitions is actually a set of four unresolved transitions belonging to ($g't$ -X- gt) and ($g't$ - X- $g't$), which are two conformers where the sign of the *gauche* dihedral is the same or opposite to that in the opposing chain.

TDDFT calculations of vertical excitation energies were also carried out at the DFT M06-2X/aug-cc-pVDZ for all three molecules, which also suggested the UV excitation based on the different classes of conformers still holds, despite re-ordering of the relative energies of individual conformers (**Table 3.4**). Conformer specific spectroscopy is hence imperative for further classification of conformers and for any reliable assignment.

FDIR spectroscopy is an IR-UV double resonance method that produces single-conformation IR spectra. Depending on the local geometry, different CH bonds will be in unique environments which affect their frequencies and the way in which they couple with other CH bonds. These signature IR peaks can be used to identify, assign, and study different conformations. The labeling of the IR transitions is adopted from the early work of Strauss and co-workers:¹³ CH_2 symmetric stretch/scissor overtone Fermi resonant pairs (d^+ FR), CH_2 antisymmetric stretch (d^-), CH_3 symmetric stretch/scissor overtone Fermi resonance pairs (r^+ FR), CH_3 in-plane antisymmetric stretch (r_a^-), and CH_3 out-of-plane antisymmetric stretch (r_b^-).

3.3.3 Conformer-specific spectroscopy: *p*-dEthB

p-dEthB showed two distinct origin bands in its excitation spectrum. The FDIR spectra (**Figure 4(b)**) were taken with the UV laser fixed on the two origin transitions (marked with a pound sign in **Figure 3(a)**). Anticipating a close correspondence of the *p*-dEthB spectrum with that of ethylbenzene, we have included the experimental spectrum of ethylbenzene along with the

predictions of the anharmonic local mode theory for ethylbenzene from Tabor *et al.*⁴ Our hypothesis is that if the two chains interact only weakly, the infrared spectrum of the two conformers will be nearly identical and also nearly identical to that of the single chain counterpart ethylbenzene, which is indeed the case (**Figure 4(b)**). In this case, the anharmonic model for ethylbenzene fits the experimental spectra for *p*-dEthB in the 2900-2960 cm⁻¹ region somewhat better than it did for ethylbenzene itself. Like in case of ethylbenzene, the model predicts a splitting of the CH₃ antisymmetric stretch doublet, but experimentally, the two bands are not resolved but shows up as a broadened band.

As expected, FDIR spectra of the *syn* and *anti* electronic origins had no characteristic differences, hence, identifying the corresponding conformations based on the IR spectrum is not possible. However, DFL spectra of the two electronic origins were recorded to look for conformational specificity in the Franck-Condon activity. The DFL spectra are also conformer-specific, with the absorbed frequency of the photon serving to select the emission from a single conformer and the emitted photon characteristic of the S₁ origin of that conformer. Symmetry suggests that DFL may aid in the assignment process since the *syn* conformer has the C_{2v} symmetry while the *anti* conformer belongs to the C_{2h} point group. **Figure 3.4 (c)** shows the two DFL spectra and the observed low frequency vibrations of the two conformers with their associated assignments and symmetries are listed in **Table 3.5**. Beyond -600 cm⁻¹, both the conformers have very similar observed transitions; hence, we focus on the transitions in the low-frequency region of the spectra. The origin transition in the UV excitation spectrum and its resonance fluorescence counterpart in the DFL spectra are the most intense peaks observed, keeping with the small geometry change accompanying the ππ* excitation in phenyl derivatives. We follow Mulliken numbering¹⁴ for our assignments and mention Varsanyi labeling¹⁵ whenever used, which is adapted from Wilson numbering¹⁶.

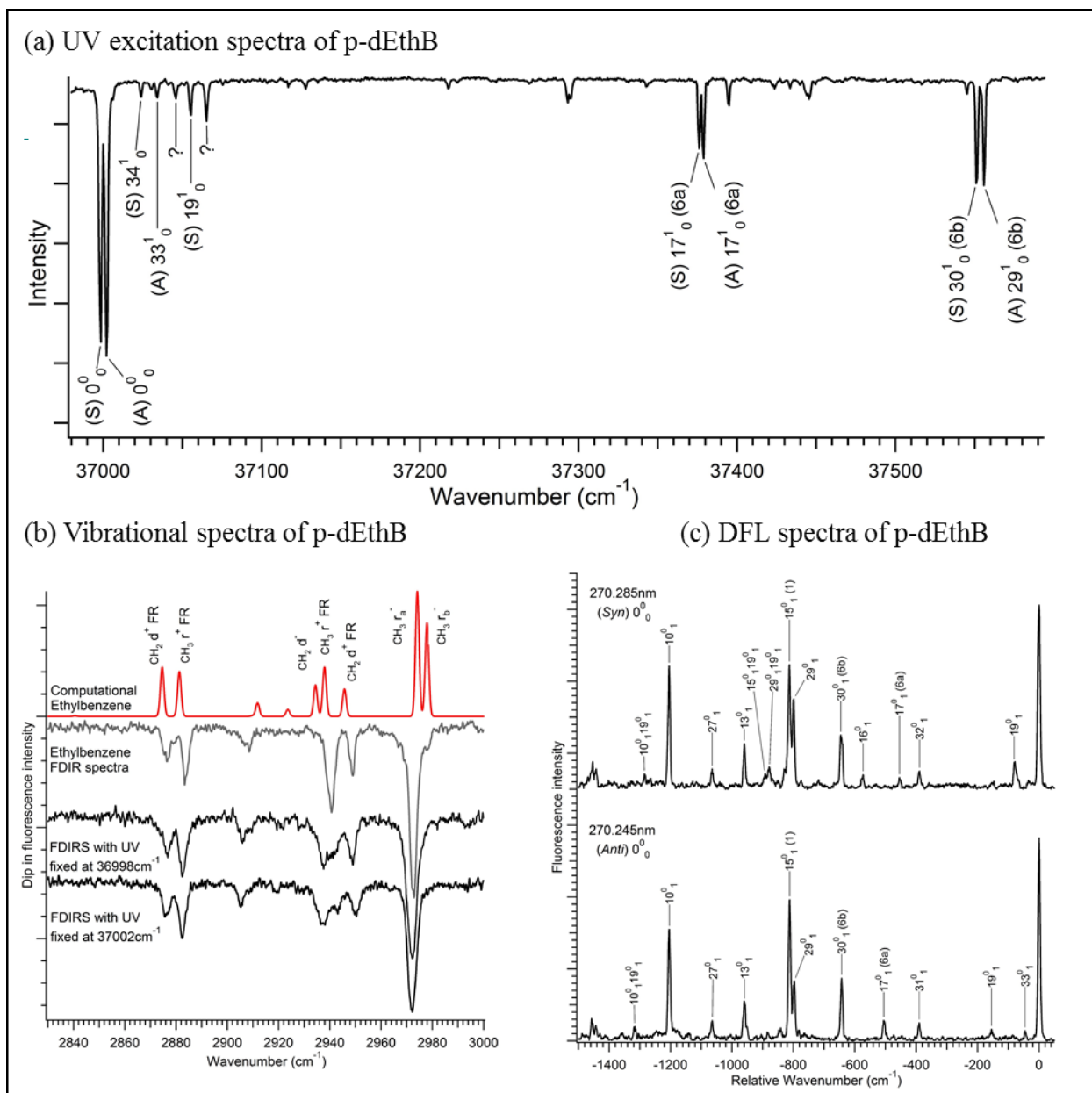


Figure 3.4: **(a)** UV excitation spectra of *p*-dEthB showing the origin and the vibronic excitation bands. **(b)** FDIR spectra of the two observed conformers of *p*-dEthB in the alkyl CH stretch region (2840–3000 cm⁻¹, bottom two traces). Red and gray traces: Calculated (red) and experimental (grey) FDIR spectrum of ethylbenzene from ref. 4, for comparison. The calculated spectrum uses a local mode anharmonic Hamiltonian derived from calculations at the B3LYP-D3/6-311++G(d,p) level of theory. **(c)** DFL spectra of the two S₀-S₁ origin bands of *p*-dEthB. The transition at 36998 cm⁻¹ is assigned to the *syn* (S) conformer, with C_{2v} symmetry, while that at 37002 cm⁻¹ is due to the *anti* (A) conformer, with C_{2h} symmetry. Vibronic spectroscopy peaks are described using Mulliken notation¹⁴, the notation in paranthesis follow Varsanyi numbering¹⁵ which is adapted from Wilson numbering¹⁶.

As with most phenyl derivatives, intensity is seen in both the spectra. (6a) and (6b) vibrational fundamentals (using the Varsanyi¹⁵ labeling scheme), which correspond to in-plane ring distortion either along (6a) or perpendicular to (6b) to the sites of ring substitution. In the *syn* and *anti* conformers of *p*-dEthB, these vibrations correspond to ν_{17} (6a) and ν_{30} (6b). Since ν_{30} does not involve displacement of the chains at the *para* positions, the 30^0_1 (6b) fundamental appears near 642 cm^{-1} for both the conformers. By contrast, the 17^0_1 6a mode involves displacement of the chains, leading to frequency shifts that are unique to the two conformers, appearing at 454 cm^{-1} for the *syn* conformer and 504 cm^{-1} for the *anti* conformer. As a result, the low frequency vibrations involving chain displacements as seen in DFL spectra were successful; while the FDIR spectra in the CH stretch region had failed.

There are other aspects of the two S_1 origin DFL spectra that confirm this assignment. The bottom trace in **Figure 3.4 (c)** has a transition at -45 cm^{-1} that can only arise from 33^0_1 , a vibronically induced transition of *bg* symmetry in the *anti* conformer. The transition at -154 cm^{-1} also matches well with the *Ag* fundamental of the same conformer (19^0_1), whereas the 19^0_1 transition of the *syn* conformer lies at -79 cm^{-1} . The other assigned transitions with relative frequencies up to -1400 cm^{-1} are associated with in-plane ring modes commonly seen for a $\pi\pi^*$ transition. The DFL spectra thus confirm and strengthen the assignment of the transition at $36\,998\text{ cm}^{-1}$ to the $S_1 \leftarrow S_0$ origin of the *syn* conformer and the $37\,002\text{ cm}^{-1}$ transition to the *anti* conformer. DFL spectra were also recorded for several vibronic transitions of both conformers of *p*-dEthB, all of which show an intense “false origin” appearing due to strong $\Delta v = 0$ Franck-Condon factors (**Figure 3.5**). Evidence for conformer-specific intramolecular vibrational energy redistribution (IVR) is present in the DFL of the $6b^1_0$ transitions of the two conformers.

The DFL spectra of the $6b^1$ levels are very different for the *syn* and the *anti* conformers of *p*-dEthB (**Figure 3.6**). In case of *anti* *p*-dEthB, the DFL spectra show a set of sharp transitions, with a false origin shifted 647 cm^{-1} from the resonance fluorescence peak as its most intense peak, associated with the $6b^1_1$ transition. By contrast, the $6b^1_0$ transition of *syn* *p*-dEthB has a DFL spectrum with a mixture of sharp transitions appearing in the midst of a set of closely spaced or unresolved transitions that appear as broadened lumps with maxima slightly red-shifted from the sharp transitions (e.g., $6b^1_1$). These observations are reminiscent of the effects of intramolecular vibrational energy redistribution (IVR). From **Table 3.5**, we see that the ground state low frequency vibrational modes have slightly higher frequencies than their excited state counterparts,

which would produce red shifts in the $6b^1_1$ transitions, as observed. Calculations of the total vibrational density of states were carried out for the *syn* and *anti* conformers, which showed no appreciable difference ($\rho(E) \sim 2$ states/cm⁻¹) that could explain the occurrence of IVR in the *syn* conformer as opposed to the *anti* conformer of *p*-dEthB. A possible explanation could be that the density of states with A₂ symmetry corresponding to the (6b) mode of *anti* *p*-dEthB is much higher than the (6b) mode of *syn* *p*-dEthB which has a B_g symmetry. Alternatively, the coupling matrix elements of the *syn* conformer could be much larger than the *anti* conformer. This physically pleasing possibility would be consistent with the two alkyl chains being on the same side of the ring in the *syn* conformer, and hence more strongly coupled to one another than if they were on opposite sides of the ring plane, as they are in the *anti* conformer. However, further exploration both experimentally and theoretically is needed before any strong conclusions can be drawn.

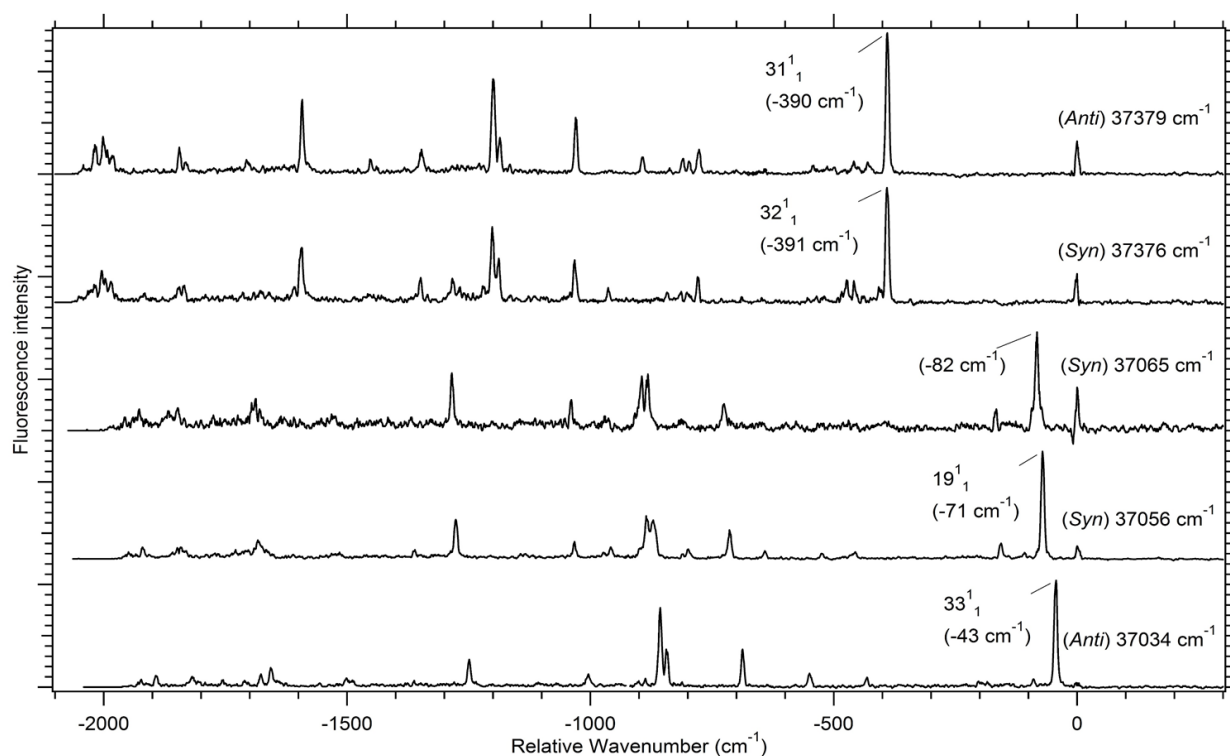


Figure 3.5: DFL spectra of *p*-dEthB showing false origins. These spectra have scaled intensities for easier comparison. From the top: *Anti* 31^1_0 transition at 37379 cm⁻¹, *syn* 32^1_0 transition at 37376 cm⁻¹, low frequency transitions at 37065 cm⁻¹ is likely to belong to a *syn* *p*-dEthB transition, 37056 cm⁻¹ assigned to *syn* 19^1_0 transition and 37034 cm⁻¹ assigned to *anti* 33^1_0 transition.

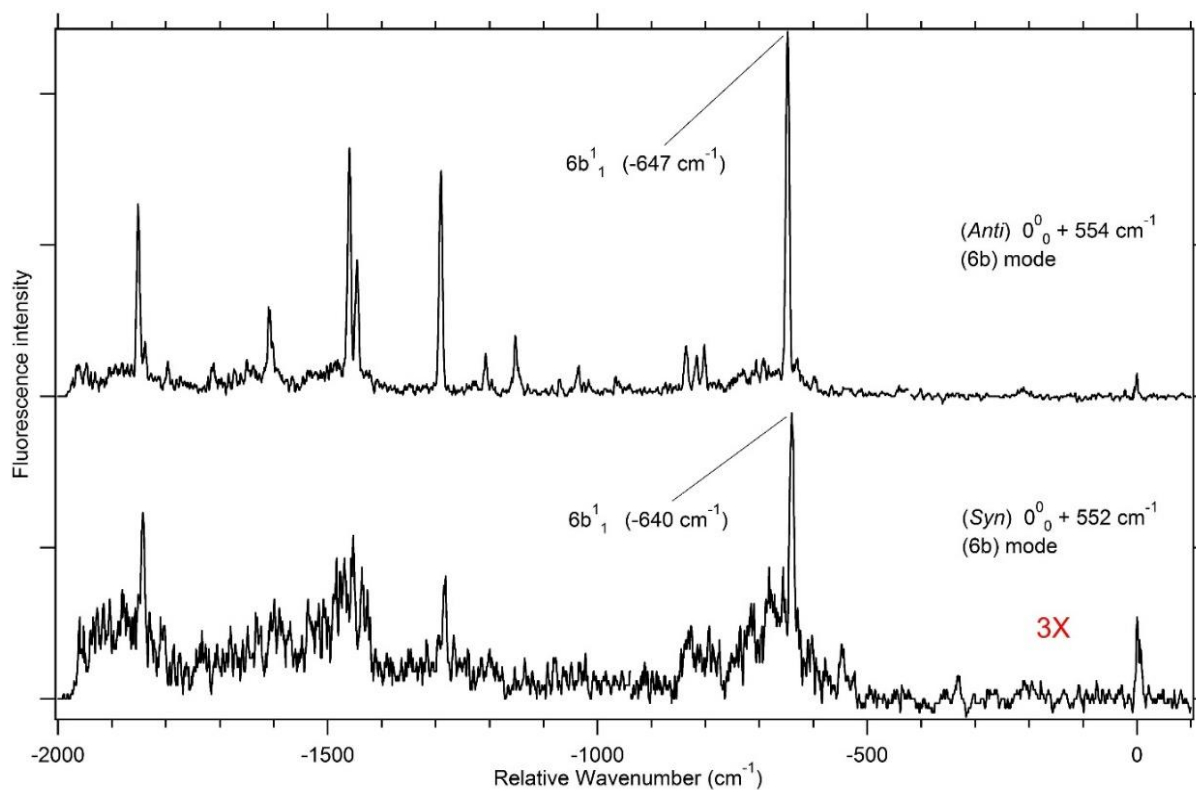


Figure 3.6: DFL spectra of the (6b) vibronic mode of both the *p*-dEthB conformers (a) *anti* and (b) *syn* (trace intensity multiplied by 3). Varsanyi numbering scheme is being followed here.¹⁵

Table 3.5: Symmetry of the irreducible representations associated with the low energy fundamental frequencies of the two ground electronic state conformers of para-diethylbenzene. Notation for mode assignment follows Mulliken numbering¹⁴, notation brackets follows Varsanyi numbering¹⁵.

<i>Syn</i> p-dEthB					
Ground state frequency (cm ⁻¹)		Excited state frequency (cm ⁻¹)		Mode	Symmetry
expt	calc ^a	expt ^b	calc ^a		
34 (weak band)	33	25	27	34	a ₂ ^c
79	72	57	58	19	a ₁
390	394	378	384	32	a ₂
454	463		419	17 (6a)	a ₁
573	589		353	16	a ₁
645	661	552	569	30 (6b)	a ₂
799	798			29	a ₂
813	823			15	a ₁
960	973			13	a ₁
1064	1090			27	a ₂
1204	1229			10	a ₁
<i>Anti</i> p-dEthB					
Ground state frequency (cm ⁻¹)		Excited state frequency (cm ⁻¹)		Mode	Symmetry
expt	calc ^a	expt ^b	calc ^a		
45	46	32	35	33	b _g ^c
154	158	126 (tentative)	125	19	a _g
390	396	376	384	31	b _g
504	514		424	17 (6a)	a _g
642	661	553	568	30/29 ^d (6b)	b _g
798	797			29	b _g
812	825			15	a _g
960	973			13	a _g
1065	1090			27	b _g
1205	1229			10	a _g

^a Computations were carried out at B3LYP-GD3BJ/Def2TZVP level of theory.

^b UV excitation peak shifts from the corresponding origin frequencies.

^c Vibronic bands with non-totally symmetric modes have b_g for *anti* conformer and a₂ *syn* conformer.

^d 6b mode is 30 in ground state and 29 in excited state of *anti* p-dEthB

3.3.4 Conformer-specific spectroscopy: *p*-dPropB

A preliminary partial assignment of the UV excitation spectrum of *p*-dPropB was made on the basis of the shifts in the electronic origins of the conformers compared to calculations. To confirm these assignments and look for potential effects of interaction between the chains, FDIR spectra were recorded for each of the origin bands of the conformers. **Figure 3.7(a)** shows these FDIR spectra for three UV transitions marked with a pound sign in Fig. 3.3(b), that are representative of the three regions, located at 36 997 cm⁻¹ (region I, t-X-t), 36 946 cm⁻¹ (region II, t-X-g), and 36 900 cm⁻¹ (region III, g-X-g). FDIR spectra performed on other origin transitions in the same region are very similar to one another.

The transitions in the CH₃ stretch region confirm our tentative assignments for the chain conformations. Inspection of the experimental spectra in the CH₃ asymmetric stretch region (ν , 2960–2980 cm⁻¹) shows doublets due to the identical pairs of transitions present in the (t-X-t) and (g-X-g) conformations in regions I and III, which resolves into a triplet in region II. The calculated spectra correctly predict the experimental shifts in the wavenumber positions of the methyl doublets in (g-X-g) relative to (t-X-t). Furthermore, the CH₃ asymmetric stretch transitions recorded while monitoring peaks in region II of the LIF spectrum (**Figure 3.7(a)**, bottom trace) comprise a triplet, with the lowest wavenumber member broadened. This suggests that the (g-X-t) FDIR spectrum can be obtained by co-addition of the FDIR spectra due to *trans* and *gauche* propylbenzene. This is demonstrated in **Figure 3.7(b)**, where the FDIR spectra of *trans* and *gauche* propylbenzene are compared with the transitions in regions I and III tentatively assigned as (t-X-t) and (g-X-g), respectively. The dual-chain spectra bear a close resemblance to their single-chain counterparts in all respects. Furthermore, the spectrum for transitions in region II, tentatively assigned to (t-X-g), is reproduced very well by simply co-adding the spectra from *trans* and *gauche* propylbenzene (**Figure 3.7(b)**, bottom trace). Apart from confirming the assignments in the LIF spectrum, this also implies that the chains on either side of the ring are non-interacting and essentially independent of each other.

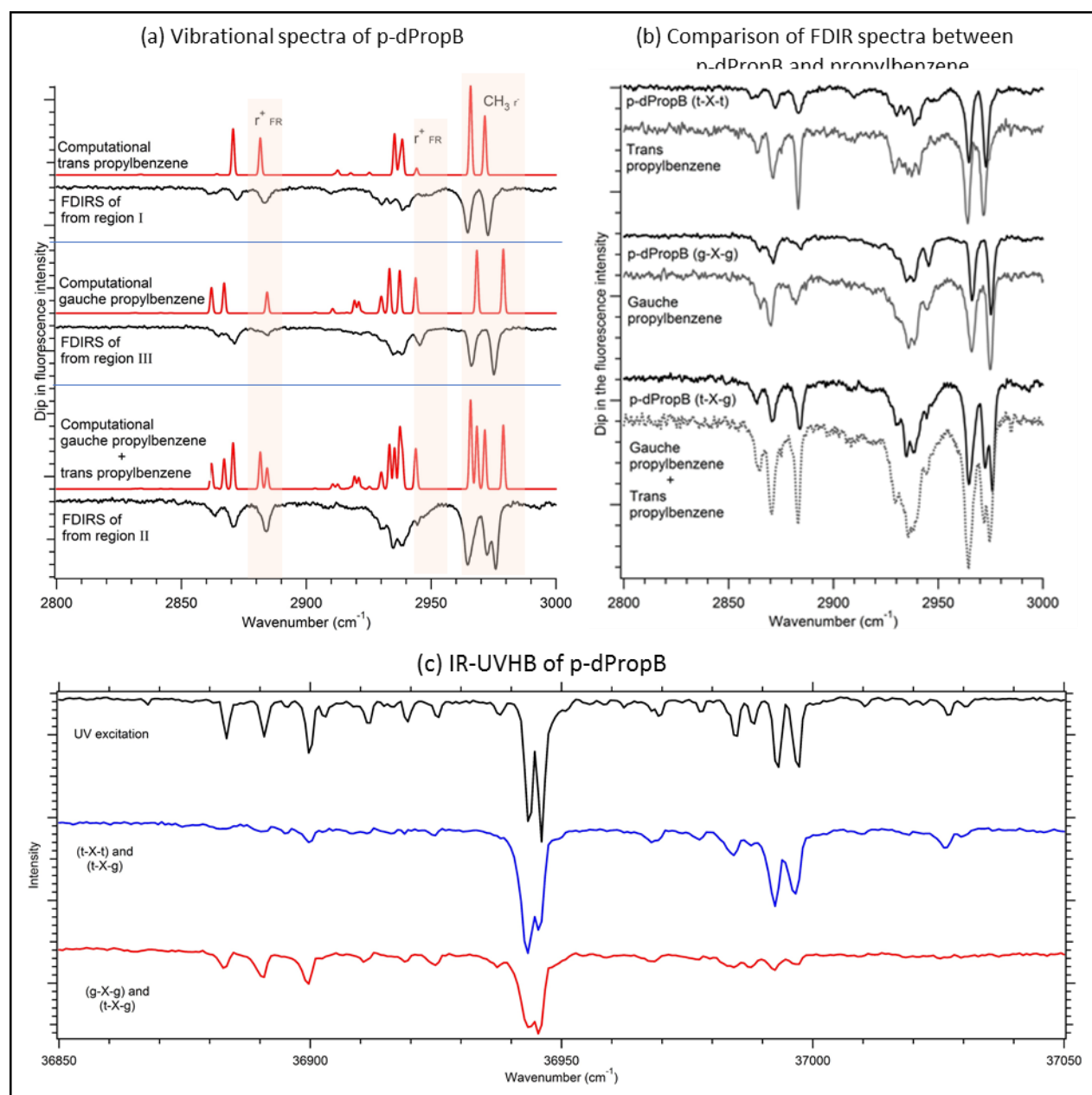


Figure 3.7: **(a)** FDIR spectra of representative single conformers from regions I (t-X-t), III (g-X-g), and II (g-X-t) of *p*-dPropB in the alkyl CH stretch region (2800–3000 cm⁻¹). Red traces show the computed spectra generated by summing the results for the propylbenzene single-chain counterparts using a local mode Hamiltonian method at the B3LYP-D3/6-311++G(d,p) level of theory, taken from Tabor et. al.⁶ The specific UV transitions from region I, III, and II are at 36997, 36900, and 36946 cm⁻¹, respectively. **(b)** Comparison between the experimental FDIR spectra of *p*-dPropB (black) and propylbenzene (grey). **(c)** Top trace (Black): UV excitation spectrum of *p*-dPropB, Middle trace (Blue): IR-UV HB scan with IR holeburn laser fixed at 2964.6 cm⁻¹, exciting conformers of the type (t-X-t) and (t-X-g), and Bottom trace (Red): IR-UV HB scan with IR Holeburn laser fixed at 2975.8 cm⁻¹ exciting conformers of the type (g-X-g) and (t-X-g).

IR-UV HB scans were also carried out to obtain conformer-specific excitation spectra and to identify low-frequency vibronic activity corresponding to the origin peaks in the different regions (**Figure 3.7(c)**). Due to the IR spectral similarity, it was not possible to obtain hole-burning scans that eliminated contributions due to the (t-X-g) conformer entirely (which has IR absorptions due to both *trans* and *gauche* propyl chains). Through these experiments, we conclude that the division of the UV spectra into three regions due to conformational classes with zero, one, or two *gauche* chains is indeed correct.

3.3.5 Conformer-specific spectroscopy: *p*-dButB

In *p*-dButB, the LIF excitation spectrum (**Figure 3.3**) provides strong evidence for a further ‘explosion’ in the number of observed conformers, leading to a large increase in the number of electronic origin peaks. Nineteen such transitions were observed experimentally. In an attempt to distinguish electronic origins from hot bands, several mixtures of helium, neon, and argon were used as carrier gases, but in no case were we able to reduce the number of observed peaks. Since the low energy conformers have very similar energies and torsional barriers between them, cooling population out of local minima does not occur significantly.

FDIR spectra (**Figure 3.8**) are recorded for three representative UV transitions marked with a pound sign in **Figure 3.3(c)**, one from each of the three regions I-III, at 36973 cm^{-1} (region I, xt-X-tx), 36909 cm^{-1} (region II, xt-X-gx), and 36831 cm^{-1} (region III, xg-X-gx). While performing FDIR spectroscopy on the small features in region III, we had to subtract the gain due to the IR-induced fluorescence at the wavelengths used for the FDIR spectra. This was done by taking a second IR scan with UV shifted just off-resonance from the cold origin transition used in the FDIR spectrum. To generate the model-based spectra in (**Figure 3.8(a)**) (red traces)), we added the appropriate butylbenzene computed IR spectra assuming the chains to be independent of each other, just like in case of *p*-dPropB. Calculated spectra of the most stable conformers in each class are plotted in **Figure 3.8(a)**. The figure also compares the *p*-dButB FDIR spectra with butylbenzene scans (**Figure 3.8(b)**, grey traces) that are co-added appropriately. The close correspondence between the single-chain and double-chain analogs confirms that, as with the propyl chains, the two butyl chains can be viewed as independent of each other. FDIR spectra recorded for all nineteen peaks are marked with an asterisk (**Figure 3.9**). Interestingly, only one of the observed

alkyl CH stretch spectra of *p*-dButB shows a quartet in the asymmetric CH₃ stretch region, with all other spectra exhibiting a doublet.

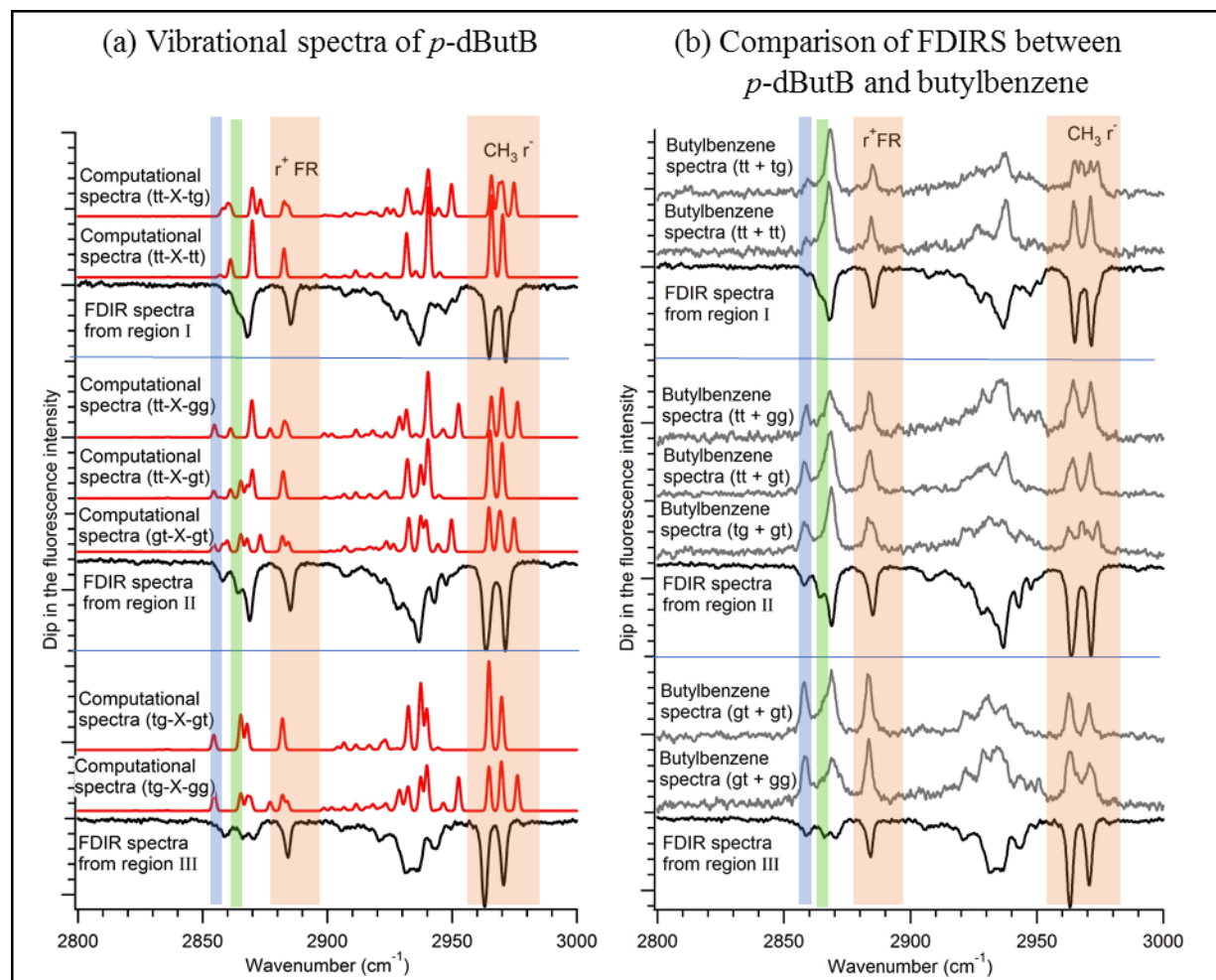


Figure 3.8: The blue shaded region span the peak at 2858 cm^{-1} and the green shaded peak spans the peak at 2865 cm^{-1} . **(a)** FDIR spectra of representative single conformers from regions I (xt-X-ty, top), II (xt-X-gy, middle), and III (xg-X-gy, bottom) of *p*-dButB in the alkyl CH stretch region ($2800\text{--}3000\text{ cm}^{-1}$). Red traces show the computed spectra generated by summing the results for the butylbenzene single-chain counterparts using a local mode Hamiltonian method at the B3LYP-D3/6-311++G(d,p) level of theory, taken from Tabor et. al.⁶ Origin bands from region I, II, and III are at 36973 , 36909 , and 36831 cm^{-1} , respectively. **(b)** Comparison between the experimental FDIR spectra of *p*-dButB (black) and butylbenzene (grey). The butylbenzene conformations that were added are labelled with the first and the second letters being the first dihedral and the second dihedral angles along the chain. See text for further discussion.

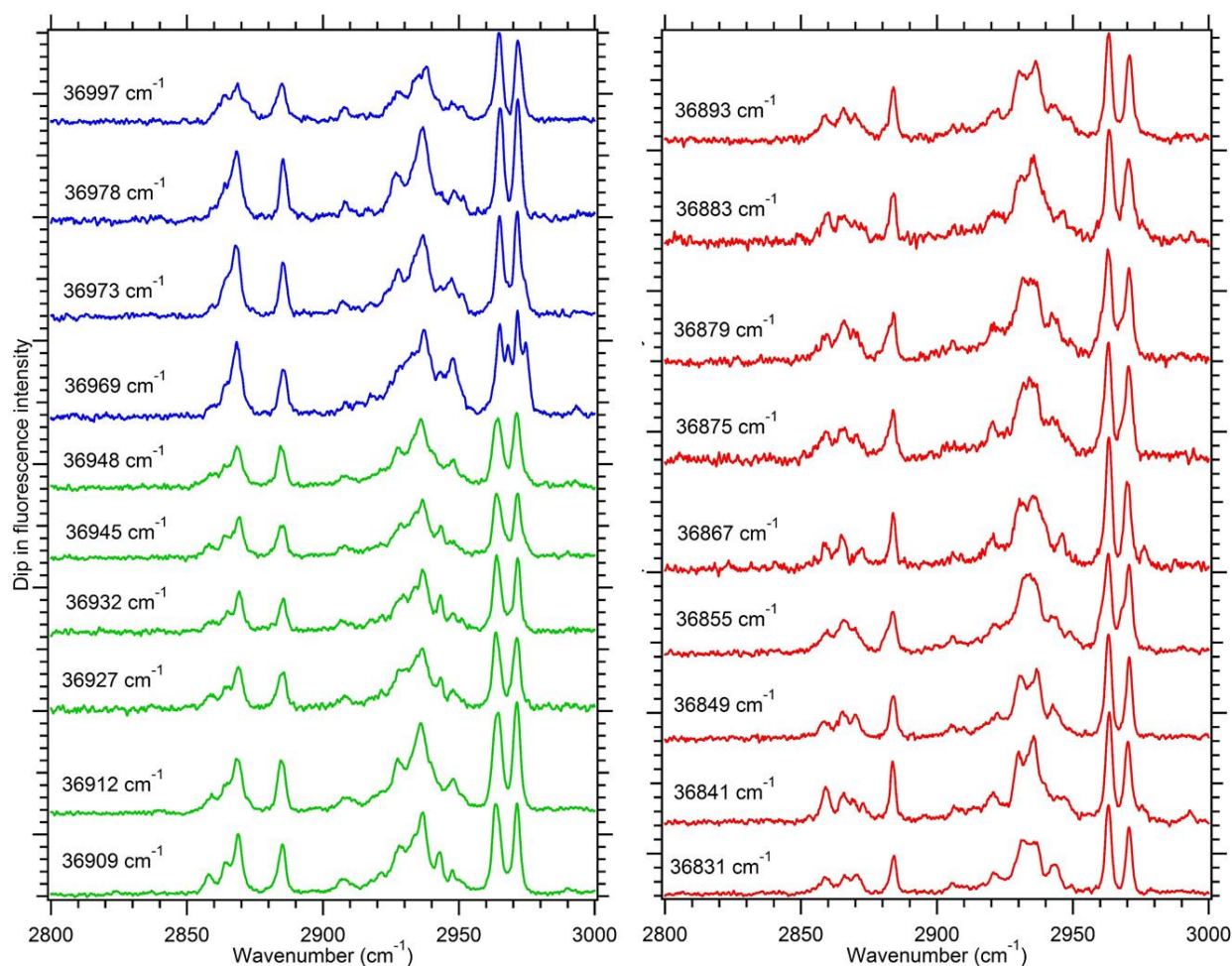


Figure 3.9: FDIR spectra of the UV excitations of p-dButB indicated by asterisk in **Figure 3(c)**. The UV excitation corresponding to the various IR spectra are mentioned on the left. The blue traces are from region I, the green traces are from region II and the red traces are from region III.

The only feature that is clearly distinct between the three regions arises in the presence of a gauche defect in the first dihedral of a given alkyl chain, which occurs at around 2858 cm^{-1} (shaded in blue and marked on the black trace with an asterisk in **Figure 3.8**). The ratio of the peak height of this feature with respect to its neighboring band at around 2865 cm^{-1} (shaded in green and marked on the black trace with an asterisk in **Figure 3.8**) tells us about the number of gauche defects present in the first dihedral angle on either chain. When the ratio is close to $\frac{1}{4}$, there are no gauche defects in the first dihedral angles. When the ratio is about $\frac{1}{2}$, one of the first dihedral angles has a gauche defect. The ratio is close to 1 when both the first dihedrals have gauche defects. This observation also holds true for both calculated and experimental spectra of *n*-butylbenzene.⁴ Although our experimental UV excitation frequencies and intensities do not match with their

calculated values with quantitative accuracy, based on the above analysis of the IR spectra, we can say that the segmentation of the UV excitation spectrum into the three regions is still valid for *p*-dButB.

3.3.6 Torsional PES and isomerization pathways

One of the obvious conclusions to be drawn from the present work is the explosion in the number of conformational minima associated with the presence of two largely independent chains. This ‘explosion’ is a natural consequence of the doubling of the number of torsional degrees of freedom and the relative orientations of the two chains with respect to each other, when comparing with the single-chain counterparts. The minima on the PES that were equivalent by symmetry can have that symmetry broken by the presence of the second chain. Thus, while ethylbenzene has a single electronic origin due to a single conformer with torsional dihedral θ , there, nevertheless, are two equivalent minima (above and below the plane of the ring), which are spectroscopically indistinguishable. In *p*-dEthB, the presence of the two chains produces *syn* and *anti* conformers that are now unique and have resolved $S_1 \leftarrow S_0$ electronic origins (**Table 3.1** and **3.2**). In propylbenzene, the two dihedrals θ and ϕ_1 lead to a set of 6 conformational minima (2 in coordinate θ and 3 in ϕ_1), 3 of which are unique, while the full set of $6^2 = 36$ minima in *p*-dPropB (with 2 sets of two identical conformers) lead to 8 spectroscopically distinguishable conformers (**Table 3.1** and **3.2**). Finally, the butyl chain in butylbenzene possesses 3 torsional degrees of freedom (θ , ϕ_1 , ϕ_2) with $2 \times 3 \times 3 = 18$ minima, four of which are unique. In *p*-dButB, $18^2 = 324$ conformational minima exist (with 8 sets of two identical conformers), with 50 spectroscopically distinguishable and 28 with energies within 5 kJ/mol of the global minimum (**Table 3.1** and **3.2**).

To better understand the rise in conformational complexity and the chain interdependence, we generated PESs for the torsional degrees of freedom of the alkyl chains in this series of molecules. We focused on the effect of the configuration of one chain on the PES of the other to test whether our inference of the experiment holds and where it breaks down. Appropriate surfaces were generated by varying particular torsional dihedral angles under relaxed optimization conditions in which all other degrees of freedom were optimized. Because the molecules are symmetric in their alkyl chain substitution, the PES will also be symmetric with respect to the exchange of the labels of the alkyl chains.

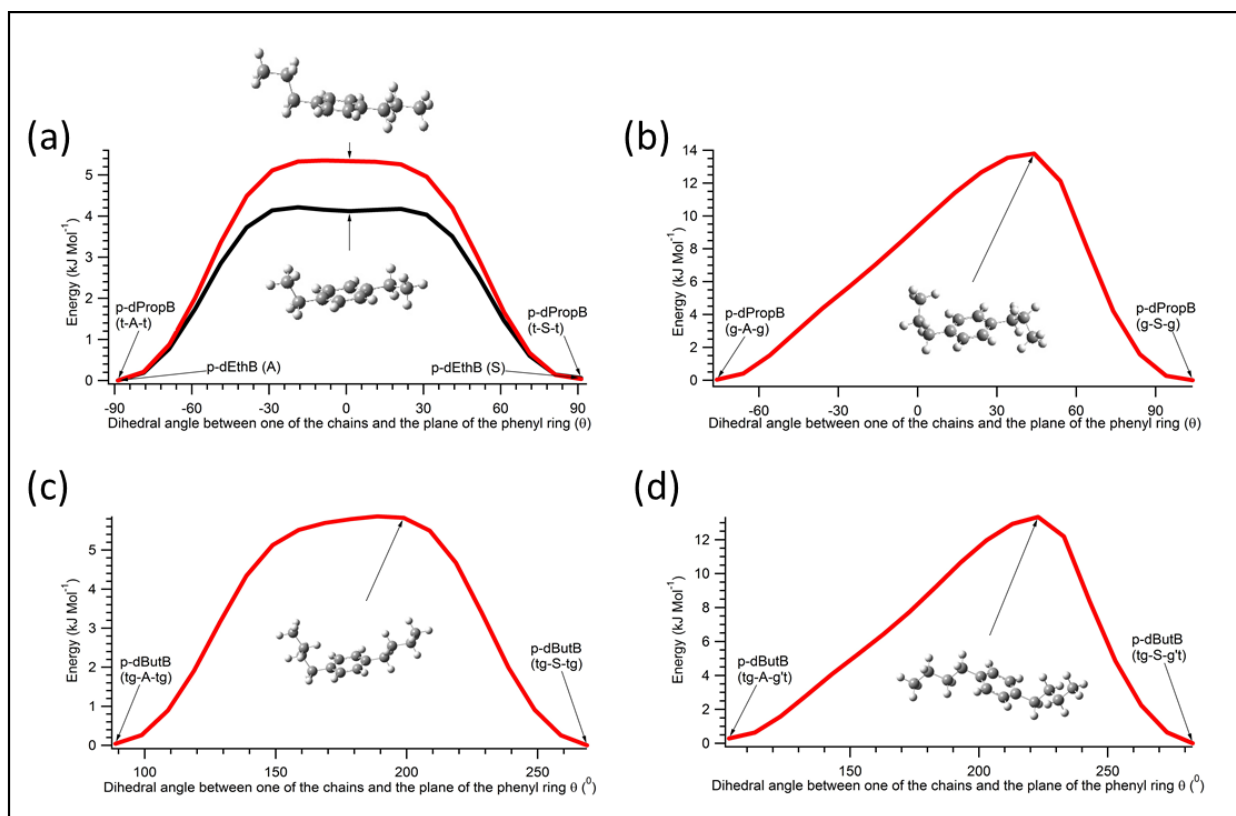


Figure 3.10: Relaxed potential energy curve generated by varying the dihedral angle between each of the chains and the plane of the phenyl ring (θ), mapping out the isomerization path between *syn* (S) and *anti* (A) structures of *p*-dEthB (black), and *p*-dPropB (red) and *p*-dButB (red). **(a)** 1D cuts of the torsional surface due to conformers where the chains are not sterically hindered by the ring during this isomerization. **(b)** Similar 1D cuts of the *p*-dPropB surface for conformers of the type (g-X-g), where the chains are sterically hindered by the phenyl ring, resulting in a much higher barrier. **(c)** 1D cut of the torsional surface due to conformers if the type (tg-X-tg), where the chains are not sterically hindered by the ring during this isomerization. **(d)** Similar 1D cut of the *p*-dButB surface for conformers of the type (tg-X-g't), where the chains are sterically hindered by the phenyl ring, resulting in a much higher barrier.

Isomerization between *syn* and *anti* conformers involves hindered rotation of one of the chains from the same to the opposite side of the aromatic ring plane as the other chain. In *p*-dEthB (**Figure 3.10 (a)**, in black), this isomerization involves motion along a potential energy curve involving the dihedral θ or θ' that one of the chains makes with the plane of the phenyl ring. The barrier for isomerization between *syn* and *anti* conformers is rather modest at 4.2 kJ/mol (350 cm^{-1}). The analogous isomerization between (t-A-t) and (t-S-t) conformers of *p*-dPropB is also shown (**Figure 3.10 (a)**, in red). When the propyl chain is extended in its *trans* conformation, the (A) \leftrightarrow (S) isomerization barrier is similar to that in *p*-dEthB (5.4 kJ/mol = 450 cm^{-1}). This implies that

when the first dihedral on the chain of *p*-dPropB is *trans*, the propyl chain can isomerize with very similar energy requirements to that for the ethyl chain.

By contrast, the isomerization pathway between (g-A-g) and (g-S-g) conformers of *p*-dPropB shown in **Figure 3.10 (b)**, has a potential barrier more than twice (13.8 kJ/mol) that of the *trans* propyl chain. The higher barrier associated with (A) \leftrightarrow (S) interconversion of a *gauche* propyl chain arises from steric hindrance between the chain and the phenyl ring. The analogous 1D PES in *p*-dButB yields similar results. Isomerization between (tg-A-tg) and (tg-S-tg) (**Figure 3.10 (c)**) has a barrier of about 5.8 kJ/mol when the interconverting chain is *trans* in ϕ_1 , while the corresponding isomerization between (tg-A-g't) and (tg-Sg't) conformations is more than twice as high (13.3 kJ/mol) (**Figure 3.10 (d)**).

In order to gain a more global view of the torsional surfaces for *p*-dPropB and *p*-dButB, we generated 2D PESs by varying suitable dihedral angles along the chains. **Figure 3.11(a)** shows the surface generated for *p*-dPropB in the *anti* configuration represented by (x-A-x), where the dihedrals (ϕ_1 and ϕ_1') along the chain are rotated. **Figure 3.11(b)** shows a contour plot representation of **Figure 3.11 (a)**, where the number of minima and their relative energies of the minima and barriers are clear. As hypothesized, this PES is shaped much like an egg carton, signifying the presence of several similar-energy pathways for isomerization between any conformer pair.

There is, however, some level of preference for certain isomerization pathways. This is evident by taking 1D slice of the 2D PES along a line connecting the two arrowheads in **Figure 3.11(b)**. Here ϕ_1' was fixed at -180° and ϕ_1 was rotated, producing the potential energy curve shown in **Figure 3.11(d)**. On this basis, it is clear that conformer (t-A-g') can isomerize to (t-A-g) in two ways: (i) by passing through a single transition state where the chain sweeps through an eclipsed geometry over the top of the ring or (ii) by surmounting two lower-energy barriers in which the chain passes through the (t-A-t) minimum as an intermediate state. The minimum energy pathway for the isomerization is the second route where the steric hindrance due to the phenyl ring on the chain is the least. The barrier heights for the torsional degrees of freedom of the propyl chain in *p*-dPropB are nearly identical to those in propylbenzene. Similar results hold in *p*-dButB where the minimum energy pathway involves motions of the chain that also avoid the phenyl ring. Even the barrier heights for the torsional degrees of freedom of the butyl chain in *p*-dButB are nearly identical to those in butylbenzene. This implies that the presence of a second chain in the

para position does not affect torsional isomerization on the first chain for the short-chain *para*-dialkylbenzenes.

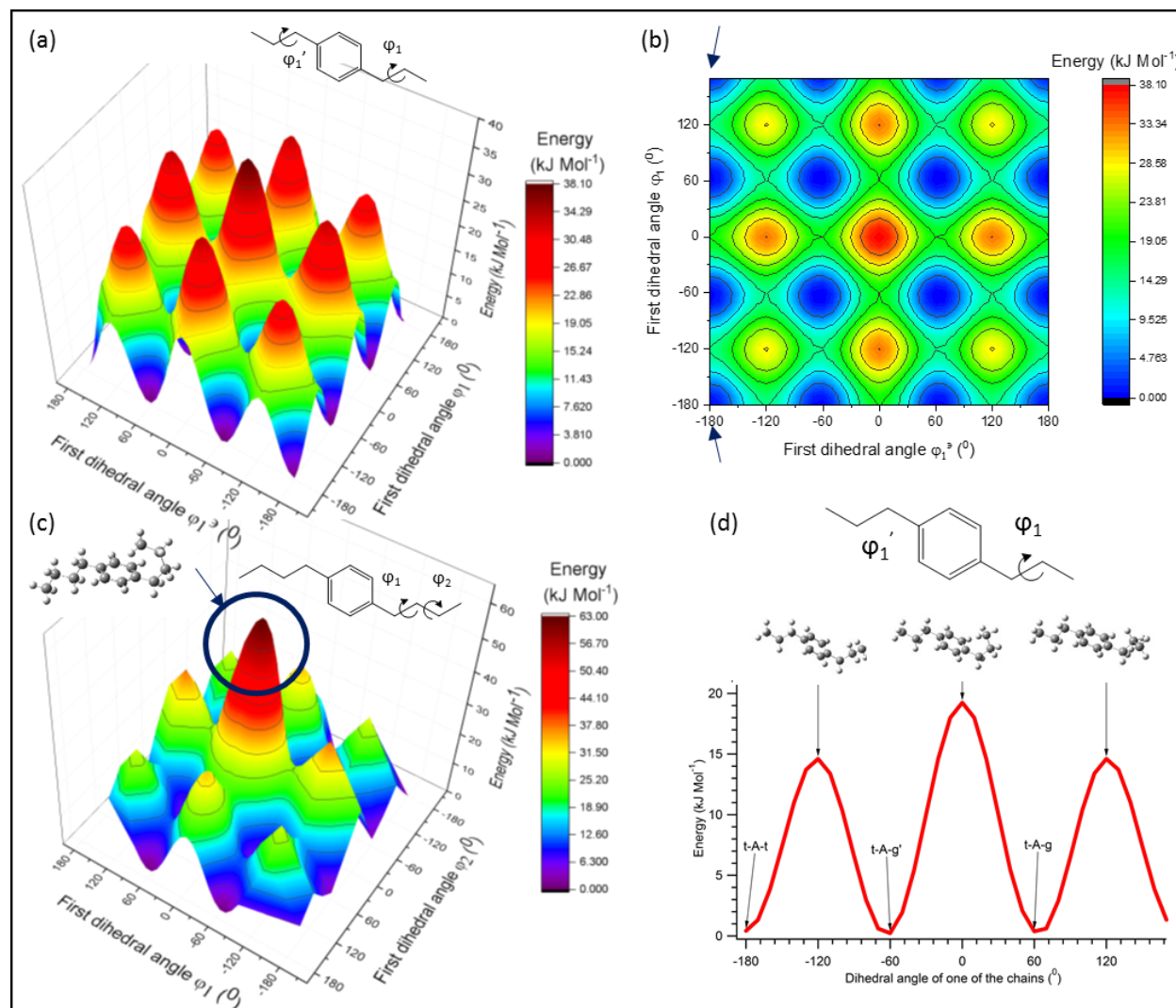


Figure 3.11: **(a)** PES of *p*-dPropB of the type (x-A-x) where the dihedral angles along the chains are varied. **(b)** Contour of the (x-A-x) *p*-dPropB PES shown in (a). **(c)** PES of *p*-dButB of the type (tt-A-xx) where both the dihedral angles on the same alkyl chain were varied. **(d)** 1D cut of the torsional mode taken from (b) marked with the arrows, where the first dihedral on the chain of *p*-dPropB is varied.

The PES for the *syn* set of conformers of *p*-dPropB (i.e., x-S-x) looks very similar to **Figure 3.11 (a)**, as it should, if the two propyl chains are not interacting with one another. Conformers on the edge of the 2D surface in **Figure 3.11 (a)** are those with at least one *trans* propyl chain configuration. As discussed in **Figure 3.10**, such conformers have a lower potential barrier to

isomerize to their *syn* counterparts, so they can more easily isomerize between the (x-A-x) PES and the (x-S-x) PES than conformers involving a *gauche* propyl chain.

Figure 3.11 (c) shows the two-dimensional PES for all conformers of *p*-dButB of the type (tt-A-xx), where both the alkyl chain dihedral angles ϕ_1 and ϕ_2 were varied on one of the chains. This 2D surface also has an egg carton shape but with a significantly larger second-order transition state in the center. While a typical barrier along the alkyl chain is 15-20 kJ/mol (1250-1670 cm^{-1}), the central barrier is about three times this height (63 kJ/mol). The geometry of *p*-dButB at $\phi_1 = \phi_2 = 0^\circ$ places the butyl chain in a doubly-eclipsed geometry, raising its energy. Note that this geometry also places the butyl chain such that it is maximally folded back over the phenyl ring. Conformational minima of type (xx-X-gg') are very high in energy. This destabilization due to adjacent *gauche* (+) and *gauche* (-) defects is called the “pentane effect,” studied previously by Klauda *et al.*,¹⁷ applied here with the phenyl ring carbon playing the role of the fifth carbon in an alkyl chain. The 2D PES for conformers of the type (tg-S-xx) showed very similar results, implying that the configuration of one chain and the conformational preferences of the other are still largely independent of each other for the two butyl chains. The only conformers in which the two chains interact significantly are (g'g-S-gg') or (g'g-S-g'g), but these have extremely high energies due to the presence of two “pentane effects.” As a result, torsional surfaces were not calculated for conformers of the type (g'g-S-xx).

The molecules *n*-octylbenzene and *p*-dButB have the same number of atoms, suggesting a comparison between the two: one long chain versus two shorter ones of half the length. As mentioned previously, the first folded structure in *n*-alkylbenzenes was found in *n*-octylbenzene, where the chain had three *gauche* defects in order to facilitate folding over the phenyl ring.⁵ In this conformer, dispersive interactions between the alkyl chain and the phenyl ring π cloud were sufficient to overcome the destabilization due to the three *gauche* defects. By contrast, in *p*-dButB, with two short chains, steric strain associated with the two “pentane effects” of the conformer and the double eclipsed butyl chain in the transition state greatly destabilizes folding back over the phenyl ring by a butyl chain.

3.3.7 Extrapolation to longer dialkylbenzenes: *p*-dOctB

The exponential growth in the number of low-energy conformers along the series *p*-dEthB, *p*-dPropB, and *p*-dButB begs the question as to how the LIF excitation spectrum will appear in a

longer member of this series. While not the primary focus of the present study, we did record a Resonant two photon Ionization (R2PI) spectrum of *para*-dioctylbenzene (*p*-dOctB), shown as the bottom trace in **Figure 3.12 (a)**, where the excitation intensity is recorded as a function of the ion signal. This mass resolved technique was utilized for this molecule to ensure we are recording a spectrum solely of the monomer. Our choice of this length chain was dictated at least in part by the fact that its single-chain analog, octylbenzene, was identified in our earlier study as the shortest *n*-alkyl chain for which significant population is observed in a structure in which the octyl chain is folded back over the phenyl ring.⁵ This g1g3g4 conformer (in which only the gauche “defect” sites are indicated starting from the ring, with all others *trans*) had a calculated energy of only 0.98 kJ/mol above the all-*trans* global minimum.

The excitation spectrum over the origin region (36 575-37 025 cm⁻¹) is extremely congested, as one would anticipate given the presence of a greatly increased number of low-energy conformers. This is made obvious by the comparison with the spectrum of *p*-dButB, reproduced above it in **Figure 3.12 (a)**, where nineteen S₁←S₀ origin transitions due to distinct conformations were tentatively identified. This *p*-dOctB excitation spectrum obtained was still vibrationally cold as confirmed by the fact that three small, sharp transitions at the low frequency edge of the spectrum were identified (see inset) at 36 584, 36 601, and 36 626 cm⁻¹. Apart from these three transitions, the spectrum is generally so congested that it is a lumpy near-continuum, with a pile-up in intensity at certain wavenumber positions, that are suggestive of the same subclasses of structures as in the smaller dialkylbenzenes. As it can be seen in **Figure 3.12 (a)**, maxima in regions I and II appear near the previously ascribed to (xt-X-tx) and (xt-X-gx) conformers in *p*-dButB, respectively. In *p*-dOctB, these labels would be (x₅t-X-tx₅) and (x₅t-X-gx₅) given the six unique dihedrals along the octyl chains.

As indicated in the figure, much of the intensity in the excitation spectrum of *p*-dOctB is below 36 900 cm⁻¹, where S₀←S₁ origin transitions for structures with two *gauche* defects in the φ₁ position would reside. More importantly, the maximum in intensity in this region (at 36 781 cm⁻¹) is redshifted even from the g1g3g4 origin of octylbenzene, shown for comparison in the bottom trace of **Figure 3.12 (a)**. This suggests the presence of many conformers, in which the pair of octyl chains are interacting strongly with the phenyl ring.

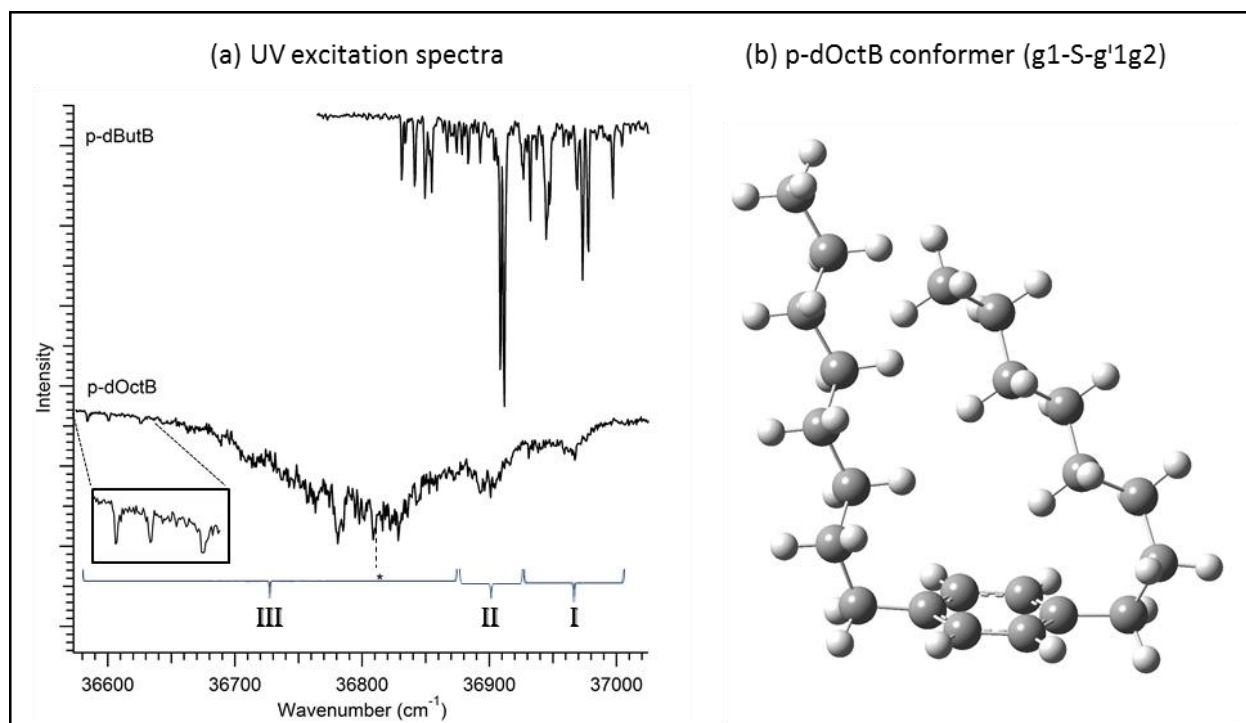


Figure 3.12: **(a)** R2PI spectrum of para-dioctylbenzene (middle) compared to p-dButB (top) and octylbenzene (bottom). The star on the p-dOctB UV excitation spectra indicates the wavenumber position of the doubly folded g1g3g4 conformer of p-dOctB assuming the electronic frequency shift relative to the all-*trans* structure is additive. **(b)** Lowest energy conformer of p-dOctB calculated at the B3LYP-D3BJ/Def2TZVP level of theory.

In order to gain a general understanding of these possibilities, the MacroModel suite of programs¹⁸ was used to carry out a force field search of the conformational potential energy surface followed by energy minimization of 100 structures, using the Merck Molecular Force Field static (MMFFs). The 10 lowest-energy structures from the search, supplemented by those incorporating g1g3g4 folds, were submitted to optimization at B3LYP-GD3BJ/Def2TZVP, the same level of theory as in the shorter dialkylbenzenes, in order to get a qualitative feel for the likely low-energy structures, in light of the large number of conformations possible. **Figure 3.12 (b)** presents a representative example of the lowest energy of these DFT optimized structures, which has structural aspects common to most of the lowest-energy dioctylbenzene structures. In particular, most of these structures had both the octyl chains on the same side of the ring interacting with each other. This implies that the conformational space preferred by one chain is affected by the presence of the other. Indeed, one would anticipate that the alkyl CH stretch spectra of octylbenzene could not be used to generate possible structures for *p*-dOctB.

We have indicated the wavenumber position that a doubly folded g1g3g4 structure would have if the electronic frequency shift relative to its all-*trans* counterpart is additive, as shown in **Figure 3.12 (a)**. The double chain g1g3g4 fold in which the two alkyl chains are on the opposite sides of the phenyl ring has a calculated energy of about 4 kJ/mol higher than the lowest energy conformer, as shown in **Figure 3.12 (b)**. Finally, the three sharp transitions shifted farthest to the red in the *p*-dOctB LIF excitation spectrum have conformational structures that are tantalizing to consider. Further exploration of these longer dialkylbenzenes is certainly warranted. The R2PI was scanned upto 37800 cm⁻¹ and similar congested features were seen with maxima anticipated to be due to (6a) and (6b) vibronic modes, following Varsanyi labelling¹⁵.

3.4 Conclusion

The conformations of short-chain symmetric *para*-dialkylbenzenes were studied by employing a set of conformation specific techniques, enabling the acquisition of single-conformer UV and IR spectra. As the size of the chains on the molecule increases, there is an exponential increase in the number of experimentally observed conformations in the UV excitation spectrum. This gives rise to a very rich and complex PES, whose two-dimensional cuts look much like an egg carton, with several similar energy minima separated by barriers of sufficient size such that the conformer population can be trapped in them during collisional cooling in the expansion. While it was not possible to make specific assignments of all electronic origin transitions to specific conformers, we were able to classify different types of conformers based on their excitation frequencies with a fair amount of certainty. Both experimental and computational evidences point to these short chains not interacting with one another significantly, with torsional surfaces for each chain that bear a close resemblance to their single-chain counterparts. For the short alkyl chains, the lowest energy isomerization pathway between any two conformers involves unfolding the alkyl chain such that the interaction of the chain with the phenyl ring is minimized. An electronic excitation scan of *p*-dOctB showed a highly congested spectrum, further substantiating our claim of conformational explosion with the increase in chain length in *para*-dialkylbenzenes.

3.5 References

- ¹ V. A. Gerasimenko, A. V. Kirilenko and V. M. Nabivach, *J. Chromatogr.* **208**, 9 (1981).
- ² J. Chao, C. T. Lin, and T. H. Chung, *J. Phys. Chem. Ref. Data*, **12**, 1033 (1983).
- ³ B. G. Harvey, W.W. Merriman, and T. A. Koontz, *Energy & Fuels*, **29**, 2431 (2015).
- ⁴ D. P. Tabor, D. M. Hewett, S. Bocklitz, J. A. Korn, A. J. Tomaine, A. K. Ghosh, T. S. Zwier, and E. L. Sibert III, *J. Chem. Phys.* **144**, 224310 (2016).
- ⁵ D. M. Hewett, S. Bocklitz, D. P. Tabor, E. L. Sibert III, M. A. Suhm, and T. S. Zwier, *Chem. Sci.*, **8**, 5305 (2017).
- ⁶ P. J. Breen, E. R. Bernstein, and J. I. Seeman, *J. Chem. Phys.* **87**, 3269 (1987).
- ⁷ N. O. B. Lüttschwager, T. N. Wassermann, R. A. Mata, and M. A. Suhm, *Angew. Chem. Int. Ed.* **52**, 463 (2013).
- ⁸ N. R. Pillsbury, J. A. Stearns, C. W. Müller, D. F. Plusquellic, and T. S. Zwier, *J. Chem. Phys.* **129**, 114301 (2008).
- ⁹ C. A. Arrington, C. Ramos, A. D. Robinson, and T. S. Zwier, *J. Phys. Chem. A* **102**, 3315 (1998).
- ¹⁰ F. A. Ensminger, J. Plassard, T. S. Zwier, and S. Hardinger, *J. Chem. Phys.* **102**, 5246 (1995).
- ¹¹ M. J. Frisch, G. W. Trucks, H. B. Schlegel, G. E. Scuseria, M. A. Robb, J. R. Cheeseman, G. Scalmani, V. Barone, B. Mennucci, G. A. Petersson, H. Nakatsuji, M. Caricato, X. Li, H. P. Hratchian, A. F. Izmaylov, J. Bloino, G. Zheng, J. L. Sonnenberg, M. Hada, M. Ehara, K. Toyota, R. Fukuda, J. Hasegawa, M. Ishida, T. Nakajima, Y. Honda, O. Kitao, H. Nakai, T. Vreven, J. A. Montgomery, Jr., J. E. Peralta, F. Ogliaro, M. Bearpark, J. J. Heyd, E. Brothers, K. N. Kudin, V. N. Staroverov, T. Keith, R. Kobayashi, J. Normand, K. Raghavachari, A. Rendell, J. C. Burant, S. S. Iyengar, J. Tomasi, M. Cossi, N. Rega, J. M. Millam, M. Klene, J. E. Knox, J. B. Cross, V. Bakken, C. Adamo, J. Jaramillo, R. Gomperts, R. E. Stratmann, O. Yazyev, A. J. Austin, R. Cammi, C. Pomelli, J. W. Ochterski, R. L. Martin, K. Morokuma, V. G. Zakrzewski, G. A. Voth, P. Salvador, J. J. Dannenberg, S. Dapprich, A. D. Daniels, O. Farkas, J. B. Foresman, J. V. Ortiz, J. Cioslowski, and D. J. Fox, *Gaussian 09, Revision C.01 Gaussian, Inc, Wallingford, CT, 2010.*
- ¹² J. A. Dickinson, P. W. Joireman, R. T. Kroemer, E. G. Robertson, and J. P. Simons, *J. Chem. Soc., Faraday Trans.*, **93**, 1467 (1997).
- ¹³ R. G. Snyder, A. L. Aljibury, H. L. Strauss, H. L. Casal, K. M. Gough, and W. F. Murphy, *J. Chem. Phys.*, **81**, 5352 (1984).
- ¹⁴ R. S. Mulliken, *J. Chem. Phys.* **23**, 1997 (1955).

- ¹⁵ G. Varsanyi, Assignments for Vibrational Spectra of 700 Benzene Derivatives (Wiley, New York, 1974).
- ¹⁶ E. B. Wilson, Physical Review, **45**,706 (1934).
- ¹⁷ J. B. Klauda, B. R. Brooks, A. D. MacKerell, R. M. Venable, and R. W. Pastor, J. Phys. Chem. B, **109**,5300 (2005).
- ¹⁸ F. Mohamadi, N.G.J. Richards, W. C. Guida, R. Liskamp, M. Lipton, C. Caufield, G. Chang, T. Hendrickson, and W. C. Still, J. Comput. Chem. **11**, 440 (1990).

CHAPTER 4. BROADBAND ROTATIONAL SPECTROSCOPY OF *TRANS* 3-PENTENENITRILE AND 4-PENTENENITRILE

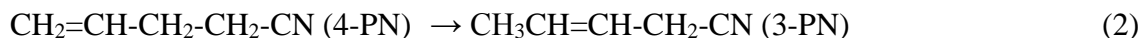
4.1 Introduction

The list of molecules detected in the interstellar and circumstellar medium continues to grow at an impressive rate of about 4 per year, with some 204 listed in the recent review by McGuire as of late 2018.¹ Among these, $\text{-C}\equiv\text{N}$ containing compounds comprise an impressively large fraction (18%), due in part to their large dipole moments and distinctive ^{14}N nuclear quadrupole splittings that make them prime targets for astronomical searches for rotational transitions occurring in the microwave to mm wave regions. Among these are a number of unsaturated nitriles, including long-chain poly-yne (HC_{2n+1}N), $\text{CH}_2=\text{CH-CN}$, $\text{CH}_2=\text{C}=\text{CH-CN}$, and most recently, the aromatic benzonitrile ($\text{c-C}_6\text{H}_5\text{CN}$).² As searches are carried out for even more complicated molecules, it is important to target particular molecules anticipated as likely candidates based on simple reaction sequences.

One logical possibility is that resonance-stabilized radicals, by virtue of their unusual stability, may build up in concentration and subsequently be lost via barrierless radical-radical recombination reactions, which thereby could occur efficiently even at low temperatures. One such recombination reaction of note is that between allyl radical ($\cdot\text{CH}_2\text{-CH}=\text{CH}_2$) and cyanomethyl radical ($\cdot\text{CH}_2\text{-CN}$) to form 4-pentenenitrile (4-PN) (**Figure 4.1 (a)**).



Furthermore, given the energetic preference of secondary over primary alkenes, isomerization to 3-pentenenitrile (3-PN) (**Figure 4.1 (b)**) is exothermic.



As a result, 4-PN and 3-PN are good candidates to submit to future astronomical searches. However, a first prerequisite for radioastronomy searches are high resolution rotational spectra that can be used to target the search.

Nitriles also play an important role in planetary science, most notably in the chemistry of Titan, one of the moons of Saturn. Titan has attracted much attention, as its atmosphere is similar to prebiotic earth.³ It has a nitrogen abundant atmosphere (>95%), significant methane (3%), and only trace oxygen, rendering it a reducing atmosphere in which organic photochemistry driven by

solar radiation plays a dominant role. This photochemistry is initiated by absorption of solar radiation in the vacuum ultraviolet (VUV) region with wavelengths around Lyman α (121 nm) or shorter.³ This region is energetic enough to break N_2 in the upper atmosphere. CH_4 occurs a little lower in the atmosphere which also photodissociates at VUV wavelengths and reacts with N atoms.³ Further photochemistry leads to an atmosphere and surface rich in organics (hydrocarbons, aromatics) and especially in nitriles as the principal means of incorporating nitrogen. While the Cassini-Huygens mission provided a remarkable opportunity to characterize the chemical composition of the atmosphere, the recently approved Dragonfly drone mission will characterize the surface composition of Titan in even greater detail, probing the dissolved organics and nitriles that are likely to be abundant there. In laboratory experiments, aerosols thought to be similar to those on Titan (called ‘tholins’) have been studied in depth and pentenenitriles have been detected by gas chromatography mass spectrometry.⁴

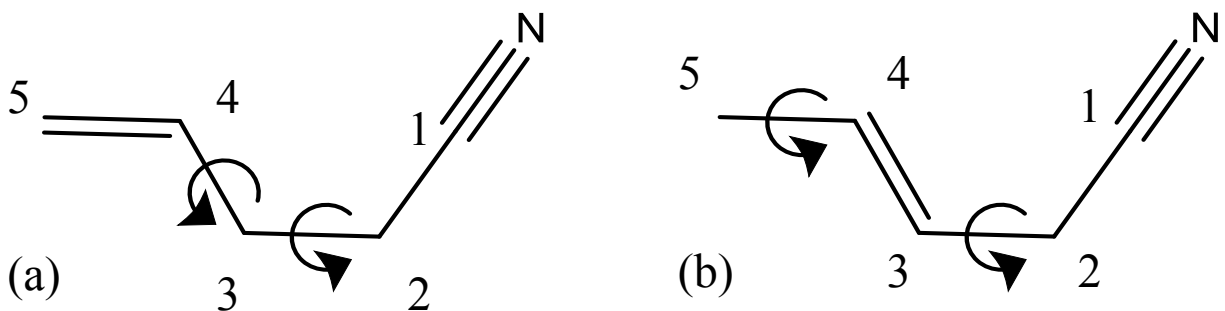


Figure 4.1: Chemical structures of (a) 4-pentenenitrile and (b) *trans* 3-pentenenitrile molecules. The carbon atoms are labelled starting from the nitrile group and the flexible dihedral angles are indicated.

Apart from establishing a database to detect nitrogenous compounds in space, the pentenenitriles are also worthy of attention as potential intermediates along the pathway to heteroaromatics such as pyridine (C_5H_5N). Absorption in the deep UV could provide the energy needed to dissociate them by loss of $2H$ or H_2 , rearrange its backbone, and cyclize to pyridine, either in a single step or in sequence. As the prototypical nitrogen heteroaromatic, establishing pathways to its formation could be important for understanding initial steps along the pathway to nitrogen-rich aromatics present in the nucleic acid bases that are among the fundamental building blocks of life.⁵

Finally, the conformational preferences of 3-PN and 4-PN are interesting in their own right. Both isomers have two C-C single bonds about which torsional motion is possible (**Figure 4.1**). In 4-PN, these two bonds are adjacent to one another, with torsional motion about the central C2-C3 bond and along C3-C4 due to the non-linear vinyl group. The infrared spectroscopy of 4-PN has been studied under matrix isolated conditions, in the gas phase⁶ and the liquid phase⁷, and as part of a larger study aimed at understanding the effect of various substituents on the observed vibrational frequencies.

The interior position of the double bond in 3-PN separates the two torsional degrees of freedom, so that the second hindered rotation is that of a methyl group. Furthermore, both *trans* and *cis* isomers are in principle possible, although calculations presented later confirm that the *trans* isomer is significantly more stable. Using Raman and infrared spectroscopy, Durig and co-workers studied the conformational populations of *trans*-3-PN as a function of temperature (-100 to -55°C) in liquid Xe.⁸ They concluded that the *syn* conformer (**Figure 4.2 (a)**) is the global minimum, with the *eclipsed* conformer (**Figure 4.2(b)**, labeled ‘gauche’ by these authors) higher in energy by 205 ± 7 cm⁻¹.

The present work reports the broadband chirped pulse-Fourier transform microwave (CP-FTMW) spectrum of jet-cooled *trans* 3-pentenenitrile and 4-pentenenitrile over the 8-18 GHz range. In order to identify rotational transitions due to individual conformational isomers, the strong-field coherence breaking (SFCB) technique was applied to 3-PN to selectively modulate conformer-specific microwave transitions. Spectra due to the two lowest-energy conformers of 3-PN (*syn* and *eclipsed*) and five of 4-PN were all identified and assigned. Due to the presence of a terminal methyl group adjacent to an *sp*² hybridized carbon in 3-PN, we observed typically small A/E splittings (<1 MHz) due to the two lowest energy methyl internal rotor states. The barriers to internal rotation were experimentally determined for the two conformers of 3-PN. Finally, we compare the conformational landscapes of the two molecules, reflecting on how the conformational complexity will affect searches for rotational transitions of these two nitriles in space.

4.2 Methods

4.2.1 Experimental

The CP-FTMW spectrometer used in this study has been described previously^{9,10}, hence only the essential aspects will be described here. Commercially available 3-PN (95%, Sigma Aldrich), predominantly the *trans* isomer, or 4-PN (97%, Sigma Aldrich) was loaded into a sample reservoir placed immediately before the pulsed valve. 3-PN required no heating, while 4-PN was heated to 70°C to obtain sufficient vapor pressure, and was entrained in helium or argon as backing gases at pressures in the 1.4-3.3 bar range. The gas mixtures were pulsed into a chamber through a pulsed valve (Parker General Valve Series 9) with an orifice of 1 mm diameter operating at 10 Hz. This produced supersonically cooled and isolated molecules in the zero-point levels of the low-lying conformational minima. No evidence for vibrational hot bands was observed in the microwave spectra. In 3-PN, the different nuclear spin symmetries of the lowest A and E methyl rotor states prevented collisional cooling between them, trapping population in the lowest A and E state.

The CP-FTMW instrument used to record the MW spectra is described in chapter 2. A Kaiser-Bessel windowing function with a shape parameter of 11.5 was applied to the molecular FID signal before taking the Fast Fourier Transform (FFT), in order to reduce noise from the TWTA in the early part of the FID. Our experimental resolution limited the internal rotation and the nuclear quadrupolar coupling analysis discussed in the results section; hence, we interpolated the rotational spectra using cubic splines with four times the number of experimental data points (interpolating with three points between consecutive data points) to smooth the spectrum before determining peak splittings. The maximum intensity of the interpolated lineshapes were used as the line center frequencies of the experimental transitions. This peak picking method led to a reduced average error in the fits of 15 kHz. Anticipating that more than one conformation may be present in the spectrum, we utilized the method of strong-field coherence breaking (SFCB)^{Error! Bookmark not defined.} to identify a set of transitions due to a single conformational isomer. The SFCB method works best when operating in the RAP regime¹¹ with strong coupling between the electric field and the molecular dipole moment. SFCB was used systematically only on 3-PN, since the data for this molecule was obtained after the method was more fully developed.

Fitting of the 3-PN spectra was complicated by the fact that the magnitude of the nuclear hyperfine and methyl rotor splittings were similar, leading to overlapping transitions that were

difficult to deconvolve. As a result, both SPCAT/SPFIT¹² and XIAM¹³ program suites were employed in the fitting process. Preliminary fits to the ‘A’ methyl rotor states were first carried out using SPFIT with a Watson S reduced Hamiltonian which incorporated the nuclear hyperfine splitting, whereas both A and E states along with the hyperfine splittings were fit using XIAM, again with the Watson S reduced Hamiltonian. The best fit rotational parameters and errors from SPFIT were obtained from the PIFORM program available from the PROSPE website.¹⁴

4.2.2 Theoretical

Calculations were performed using Gaussian 09 suite of programs¹⁵. Geometry optimizations of all conformational minima of 3-PN and 4-PN were carried out using dispersion-corrected density functional theory with the B3LYP functional (B3LYP-GD3BJ) and the Def2TZVP basis set. This level of theory has been shown in previous studies to give relative energies in good correspondence with experiment for medium-sized molecules.^{9, 16, 17} Harmonic vibrational frequency calculations were used to obtain zero-point corrected relative energies.

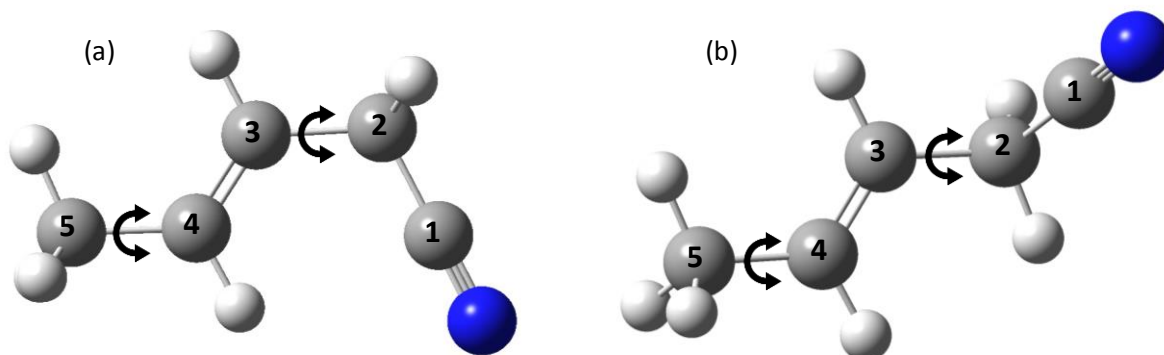


Figure 4.2: Conformers of *trans* 3-pentenenitrile geometry optimized at the dispersion corrected DFT B3LYP-GD3BJ/Def2TZVP level of theory. The lowest energy conformer (a) *syn* 3-pentenenitrile has all the heavy atoms in the same plane with a C2-C3 dihedral of 0° and (b) *eclipsed* 3-pentenenitrile with a C2-C3 dihedral of -120° , calculated to be 186 cm^{-1} higher in energy. The *eclipsed* conformer exists as a degenerate pair, with its second member having a dihedral angle of $+120^\circ$ (not shown). The flexible dihedral angles are shown as double headed arrows.

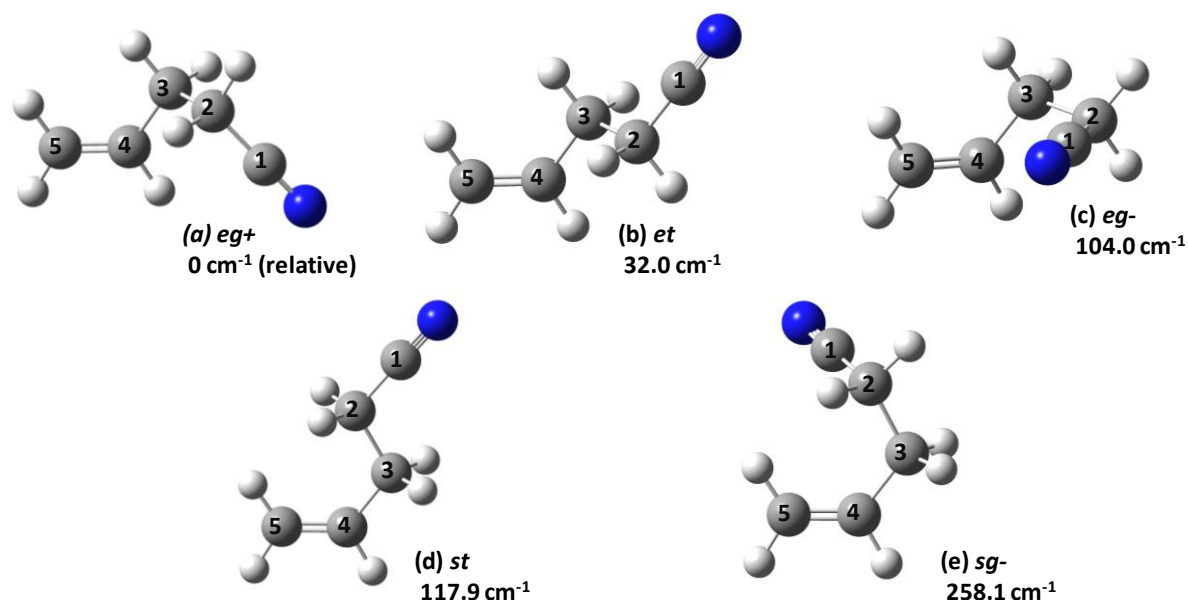


Figure 4.3: Optimized geometries for the five unique conformers of 4-pentenitrile calculated at the dispersion corrected DFT B3LYP-GD3BJ/Def2TZVP level of theory. Structures are listed in order of increasing energy: (a) *eg+*, (b) *et*, (c) *eg-*, (d) *st*, and (e) *sg-*. See the text for further discussion of the nomenclature. The relative zero-point corrected energies in cm^{-1} are given below the labels.

The nomenclature followed for 3-PN is based on the C2-C3 dihedral angle, shown in **Figure 4.2**. The conformer is labelled *syn* when the C2-C3 dihedral θ_{23} has an angle around 0° and *eclipsed* when $\theta_{23} \sim 120^\circ$. Previous studies by Durig and co-workers labelled this second conformer as *gauche* rather than *eclipsed*.⁸ Strictly speaking based on IUPAC nomenclature, both the conformers of 3-PN are ‘*eclipsed*’ between the C=C and C-H or C-C(N) bond.¹⁸ However, we distinguish the conformers by the orientation of these groups using ‘*syn*’, a term that denotes that the C=C and C-C(N) bonds are on the same side as opposed to ‘*eclipsed*’ where the C-H bond rotates into that position.

4-PN has two flexible dihedral angles between C2-C3 and C3-C4 as labelled in **Figure 4.1** (a), producing a conformational landscape richer than 3-PN. The Macromodel suite of programs¹⁹ with the generalized AMBER force field was used to identify five conformations for subsequent optimization via DFT. The nomenclature of the 4-PN conformers follows the configuration of the two flexible dihedral angles. For simplicity, the structures are labeled by *e*, *s*, *t*, and *g*, representing

eclipsed, *syn*, *trans*, and *gauche*, respectively. The *e/s* designations follow those in 3-PN, while the C2-C3 dihedral angle is either near 180° (*trans*, *t*) or $\pm 60^\circ$ (*gauche*, *g+* or *g-*). Note that *eclipsed* configurations can also take values near $\pm 120^\circ$, but these are not differentiated here, as such structures result in mirror images. Further details are in the section where PES analysis is discussed. The nomenclature of the 4-PN conformers labels the C3-C4 dihedral first, followed by the C2-C3 label, as shown in **Figure 4.3**.

Relaxed torsional potential energy curves were calculated along C2-C3 and C4-C5 dihedrals (3-PN) or C2-C3/C3-C4 dihedrals (4-PN) at the same level of theory, in 10° steps. Through this process, we also made sure all possible conformers were obtained along with their degeneracies. In 3-PN, transition state calculations using the quadratic synchronous transit (QST2) method²⁰ were performed to estimate the zero-point energy (ZPE)-corrected barrier height to methyl rotation.

4.3 Results

4.3.1 3-Pentenenitrile

The DFT calculations of the zero-point corrected relative energies of 3-PN predict that the *syn* conformer (**Figure 4.2 (a)**) is the most stable, with the *eclipsed* conformer (**Figure 4.2 (b)**) 186 cm^{-1} (2.23 kJ/mol) higher in energy (**Table 4.1**). Both conformers are near-prolate asymmetric tops. Broadband microwave spectra of 3-PN were recorded with 1%, 10% and 100% of full microwave power on the TWTA. 3-PN shows clear evidence for distortion of the intensities at full power, as shown in **Figure 4.4**, and these conditions were used for carrying out SFCB to identify sets of transitions due to conformational isomers. Using the SFCB scheme outlined in Sec. II, we chose transitions at 16773.9375 MHz, 12956.3125 MHz and 10090.0000 MHz as the three single-frequency “coherence-breaking” pulses. These SFPs were subsequently assigned to $5_{1,5}-4_{1,4}$, $2_{1,2}-1_{0,1}$ and $3_{1,3}-2_{1,2}$ transitions of *syn* 3-PN. The final difference spectrum obtained via SFCB exhibited eight peaks whose intensities were modulated by more than 25% by the single-frequency pulses. This difference spectrum, which consisted of a-type and b-type R-branch transitions, is plotted against the simulated fit spectrum of the *syn* conformer in **Figure 4.4 (a)**. Each of the modulated lines was in fact composed of a set of transitions due to ^{14}N hyperfine and methyl rotor splittings, since the 150 ns SFP pulses had widths that subtended these splittings. Based on these transitions, a preliminary fit was achieved that had rotational constants consistent with those

calculated for the *syn* conformer of 3-PN, and transition intensities that reflected its in-plane dipole moment.

Table 4.1: Zero-point corrected relative energies of the conformers of 3-pentenenitrile and 4-pentenenitrile, calculated at the DFT B3LYP-GD3BJ/Def2TZVP level of theory.

Species	Relative energy (cm ⁻¹)
3-Pentenenitrile	
<i>Syn</i>	0
<i>Eclipsed</i>	186.3
4-Pentenenitrile	
<i>eg+</i>	0
<i>et</i>	32.0
<i>eg-</i>	104.0
<i>st</i>	117.9
<i>sg-</i>	258.1

Remaining unassigned transitions, presumably belonging to *eclipsed* 3-PN, were about a factor of 10 weaker than those due to the *syn* conformer. SFCB was performed by choosing transitions at 14380.3750 MHz, 17503.0000 MHz and 17023.5000 MHz in subsequent SFCB scans, which were later assigned to the $5_{0,5}-4_{0,4}$, $6_{1,5}-5_{1,4}$ and $6_{1,6}-5_{1,5}$ transitions respectively. In this case, only two additional transitions were identified at a modulation threshold of 35%. A higher percent modulation was required to avoid interference, as the *eclipsed* conformer had transitions that were much weaker than the *syn* conformer. The final SFCB spectrum of the *eclipsed* conformer is plotted against the simulated fit in **Figure 4.5 (b)**. The transition used for the third SFP was modulated in the previous difference spectrum but its' percent modulation dropped below 35% in the final difference spectrum.

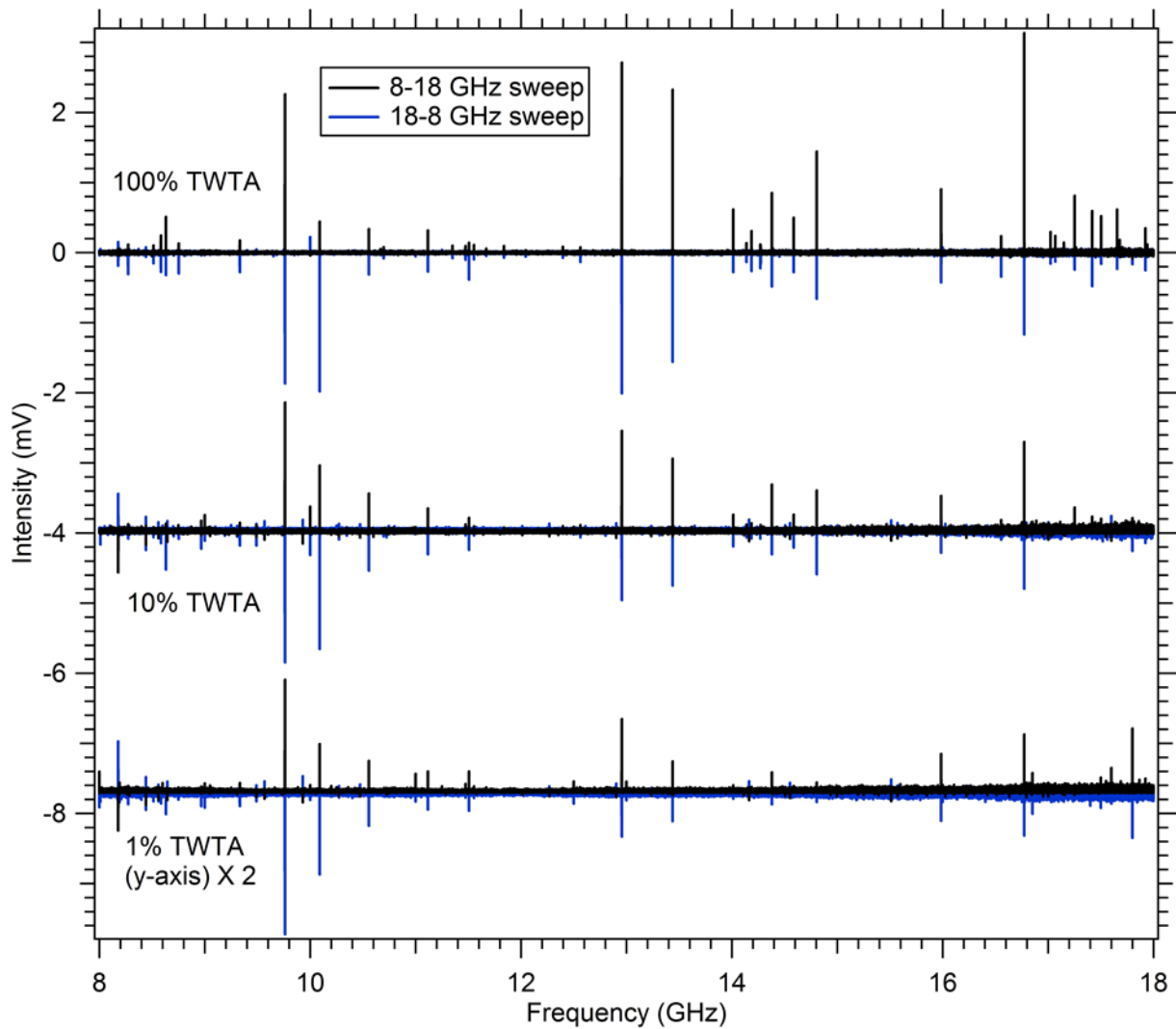


Figure 4.4: Comparison of two broadband microwave spectra for 3-PN recorded in the rapid adiabatic passage regime with 100%, 10% and 1% power on the TWTA. The spectrum recorded while sweeping 8 \rightarrow 18 GHz sweep (black trace) and the corresponding spectrum with an 18 \rightarrow 8 GHz sweep (blue trace). Note that with 100% power of TWTA the distortions in the two spectra with intensities of transitions at the end of each scan enhanced unlike in case of 10% and 1% power of the TWTA.

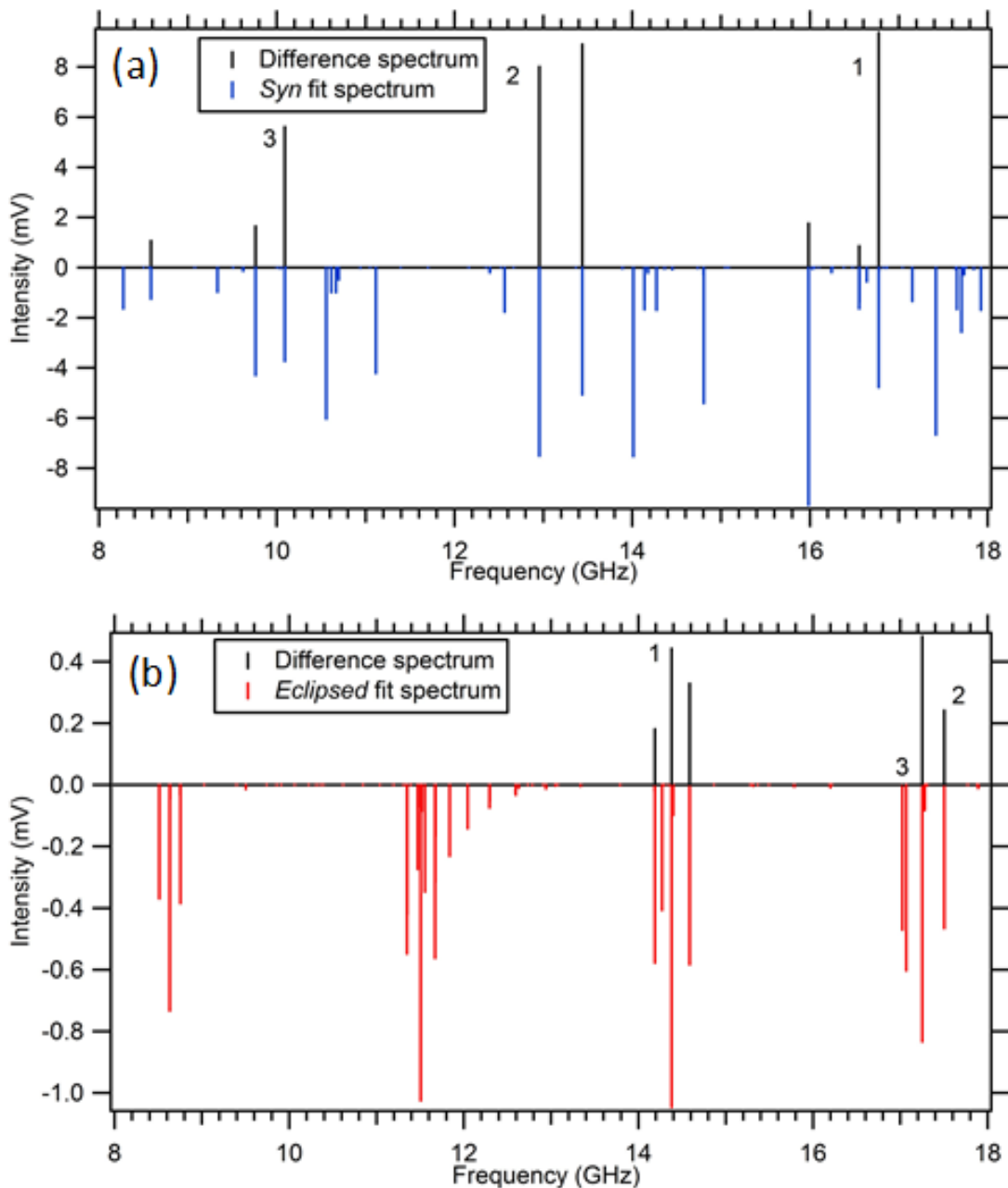


Figure 4.5: Strong-field coherence breaking spectra of (a) *syn* and (b) *eclipsed* conformers of 3-pentenenitrile (black traces) along with their final fit spectra going down. The intensity axes show almost a factor of 20 difference in signal intensity. The numbering on the transitions label the frequencies of the single frequency pulses of the SFCB method (see text for further discussion).

The broadband microwave spectrum along with the final fit simulation of both the 3-PN conformers is shown in **Figure 4.6**. The experimental spectrum is a 1M FID average recorded at full TWTA power, with argon as carrier gas at 1.4 bar backing pressure. Final fits were carried out

using SPFIT with a Watson-S reduced Hamiltonian. Both these conformers have very low dipole moments along the c axis ($\mu_c \leq 0.1$ D), so only a- and b-type transitions were observed in the spectrum. The final fit is shown in blue. The strong transitions belong to the R branch, and includes both a-type and b-type transitions with similar intensities ($\mu_A \approx \mu_B$).

Figure 4.7 (a)-(c) shows three examples of the splittings of individual rotational transitions due to ^{14}N hyperfine and methyl rotor splittings in *syn* 3-PN. The strong a-type lines (e.g., **Figure 4.7 (a)**) have generally collapsed hyperfine structures with weak side bands, while several of the less-intense a-type transitions have a doublet splitting due to internal rotation. The position of the ^{14}N -atom on the 'a' inertial axis is responsible for collapsing the major hyperfine transitions. By contrast, the b-type lines exhibit hyperfine splittings which are especially clear in the strong transitions (**Figure 4.7 (b)**). Relatively weaker transitions belonging to Q branch (**Figure 4.7 (c)**) are also seen consisting of only b-type lines that are broadened doublets with some partially resolved features.

The *eclipsed* conformer of 3-PN (**Figure 4.2 (b)**) has a structure in which the nitrile group rotates out-of-plane of the other four carbon atoms. In this case, $\mu_b \sim -0.58\mu_a$, so the R-branch consists of a-type transitions that are more intense than the assigned b-type transitions. The pattern of hyperfine transitions are much like that in the *syn* conformer, with collapsed structure in the a-type transitions and doublets in the b-type transitions. Weak Q-branch transitions composed only of b-type transitions are also observed. The fit parameters obtained from SPFIT along with the DFT predicted values are listed in **Table 4.2**. 82 lines of the *syn* conformer were fit (**Table 4.3**), while 26 were assigned to the *eclipsed* conformer (**Table 4.4**), due to its smaller population and hence weaker transitions.

The conformational population distribution downstream in the supersonic free jet was determined by fitting the rotational transition intensities to Boltzmann plots²¹ based on a broadband spectrum taken in the LFP regime with 10% TWTA power with helium backing gas at 1.4 bar. The best-fit plots have $T_{\text{rot}} = 0.7$ K (**Figure 4.5**) and the population ratio of [eclipsed]/[syn] = 18(10)/82(10) favoring a greater population in the global minimum. Efforts were made to look for the *cis* 3-PN conformer, with calculated energy 631 cm^{-1} (7.55 kJ/mol) above *syn* 3-PN, but no transitions due to this conformer were detected in our spectrum.

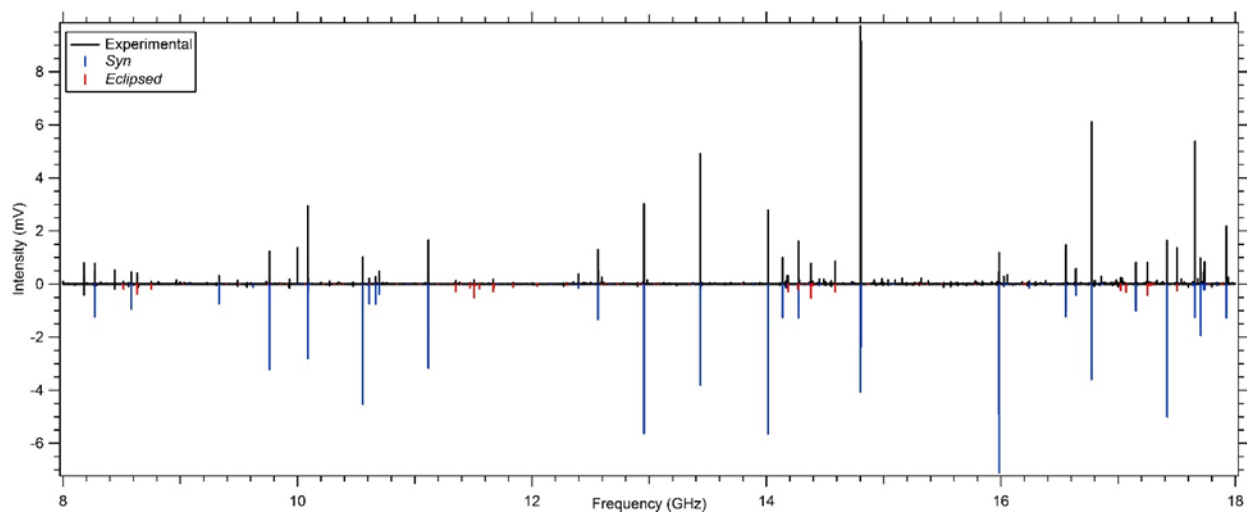


Figure 4.6: Broadband microwave spectrum of 3-pentenenitrile (black trace) over the 8-18 GHz range with the final fit spectra of *syn* (blue trace) and *eclipsed* (red trace) conformers below. The experimental spectrum is a 1 million average scan of 3-pentenenitrile entrained in argon carrier gas.

Table 4.2: Spectral fits to the A-state transitions of 3-PN using the SPFIT program suite compared with the values predicted by DFT calculations (Representation I' Watson S reduction).

3-Pentenitrile	<i>Syn</i>	<i>Eclipsed</i>
A (MHz) (pred^a/expt^b)	8312.7855 / 8163.5900(93)	12901.0547 / 12871.430(23)
B (MHz) (pred/expt)	1926.6016 / 1939.7050(23)	1484.7483 / 1478.8720(47)
C (MHz) (pred/expt)	1594.5939 / 1597.5310(18)	1406.0122 / 1398.9380(34)
μ_A (pred)	2.7	3.8
μ_B (pred)	2.9	-2.2
μ_C (pred)	0.000	0.1
D_J (kHz) (expt)	-0.630(43)	-0.610(60)
D_{JK} (kHz) (expt)	4.40(33)	27.0(19)
χ_{AA} (MHz) (pred/expt)	0.227 / -0.333(07)	-1.934 / 0.73(11)
$\chi_{BB}-\chi_{CC}$ (MHz) (pred/expt)	-4.810 / -4.760(56)	-2.735 / 2.56(14)
rms (kHz)	25	36
N^c	82	26
Relative energy (cm⁻¹) (pred)	0	186.3

^a pred: predicted values at the B3LYP-GD3BJ/Def2TZVP level of theory.

^b expt: experimental fit values

^cNumber of transitions fit, including individual hyperfine transitions.

Table 4.3: Linelist of *syn* 3-pentenitrile A-states from SPFIT.

J up	Ka up	Kc up	F up	J low	Ka low	Kc low	F low	Observed (MHz)	Calculated (MHz)
4	1	3	3	4	0	4	3	8272.76563	8272.72159
4	1	3	5	4	0	4	5	8272.9375	8272.94668
4	1	3	4	4	0	4	4	8273.8125	8273.81765
4	0	4	3	3	1	3	2	8583.92188	8583.93456
4	0	4	5	3	1	3	4	8584.14063	8584.14642
4	0	4	4	3	1	3	3	8584.71875	8584.72988
5	1	4	4	5	0	5	4	9332.48438	9332.47528
5	1	4	6	5	0	5	6	9332.65625	9332.66721
5	1	4	5	5	0	5	5	9333.625	9333.62475
1	1	1	1	0	0	0	1	9760.53125	9760.54345
1	1	1	2	0	0	0	1	9761.23438	9761.23561
1	1	1	0	0	0	0	1	9762.26563	9762.26571
3	1	3	3	2	1	2	3	10089.32812	10089.32285
3	1	3	4	2	1	2	3	10089.98438	10089.99676
3	1	3	2	2	1	2	2	10090.89062	10090.89169
3	0	3	4	2	0	2	3	10556.92188	10556.88851
6	1	5	5	6	0	6	5	10696.98438	10696.98168
6	1	5	7	6	0	6	7	10697.14062	10697.1569
6	1	5	6	6	0	6	6	10698.1875	10698.19737
3	1	2	2	2	1	1	2	11115.14062	11115.15336
3	1	2	4	2	1	1	3	11116.1875	11116.16284
3	1	2	3	2	1	1	3	11116.9375	11116.93749
7	1	6	6	7	0	7	6	12397.42188	12397.3995
7	1	6	8	7	0	7	8	12397.5625	12397.56058
7	1	6	7	7	0	7	7	12398.67188	12398.67941
5	0	5	4	4	1	4	3	12563.76562	12563.80637
5	0	5	6	4	1	4	5	12563.9375	12563.94755
5	0	5	5	4	1	4	4	12564.4375	12564.45977
2	1	2	2	1	0	1	1	12955.57812	12955.59097
2	1	2	3	1	0	1	2	12956.32812	12956.32469
2	1	2	1	1	0	1	0	12956.8125	12956.80477
4	1	4	4	3	1	3	4	13437.32812	13437.34127
4	1	4	5	3	1	3	4	13438.04688	13438.03963
4	0	4	5	3	0	3	4	14012.85938	14012.8557
4	2	3	5	3	2	2	4	14138.32812	14138.28485
4	2	2	5	3	2	1	4	14274.14062	14274.18248
8	1	7	8	8	0	8	8	14452.51562	14452.53513
4	1	3	3	3	1	2	3	14803.65625	14803.66981

Table 4.3 continued

4	1	3	5	3	1	2	4	14804.625	14804.64533
4	1	3	4	3	1	2	4	14805.42188	14805.42585
3	1	3	3	2	0	2	2	15984.89062	15984.87807
3	1	3	4	2	0	2	3	15985.60938	15985.59778
3	1	3	2	2	0	2	1	15985.875	15985.84377
6	0	6	5	5	1	5	4	16555.125	16555.07582
6	0	6	7	5	1	5	6	16555.17188	16555.17361
6	0	6	6	5	1	5	5	16555.60938	16555.60591
5	1	5	5	4	1	4	5	16773.25	16773.26171
5	1	5	6	4	1	4	5	16773.96875	16773.98868
5	1	5	4	4	1	4	4	16774.82812	16774.83507
5	0	5	6	4	0	4	5	17417.82812	17417.84075
5	2	4	6	4	2	3	5	17655.60938	17655.60292
6	2	4	6	6	1	5	6	16639.89062	16639.87288
6	2	4	7	6	1	5	7	16640.1875	16640.21723
5	2	3	5	5	1	4	5	17150.6875	17150.63439
5	2	3	6	5	1	4	6	17151.125	17151.10498
7	2	5	7	7	1	6	7	16242.90625	16242.92825
7	2	5	8	7	1	6	8	16243.125	16243.13829
4	2	2	4	4	1	3	4	17704.53125	17704.54747
4	2	2	5	4	1	3	5	17705.125	17705.12794
4	2	2	3	4	1	3	3	17705.26562	17705.27867
3	3	1	3	4	2	2	4	17638.78125	17638.7748
3	3	1	4	4	2	2	5	17639.07812	17639.06678
3	2	2	4	2	2	1	3	10611.8125	10611.76489
3	2	1	4	2	2	0	3	10666.51562	10666.50276
3	2	1	3	2	2	0	2	10666.64062	10666.64256
8	2	6	9	8	1	7	9	16028.25	16028.22027
9	2	7	10	9	1	8	10	16056.625	16056.6611
9	2	7	9	9	1	8	9	16056.78125	16056.72799
9	1	8	10	9	0	9	10	16856	16856.00781
9	1	8	9	9	0	9	9	16857.26562	16857.21759
5	3	3	6	4	3	2	5	17730.01562	17730.04856
5	3	2	6	4	3	1	5	17737.21875	17737.2546
5	3	2	5	4	3	1	4	17737.375	17737.31347
3	3	0	4	4	2	3	5	17843.70312	17843.76525
4	3	2	5	3	3	1	4	14175.65625	14175.64385
4	3	1	5	3	3	0	4	14177.71875	14177.70579
4	3	1	5	5	2	4	6	14365.89062	14365.86812
8	1	7	9	7	2	6	8	14737.25	14737.25512

Table 4.3 continued

8	1	7	8	7	2	6	7	14737.89062	14737.91451
3	3	1	3	4	2	2	4	17638.78125	17638.7748
3	3	1	4	4	2	2	5	17639.07812	17639.06678
5	4	1	6	4	4	0	5	17717.375	17717.37928

Table 4.4: Linelist of *eclipsed* 3-pentenitrile A-states from SPFIT.

J up	Ka up	Kc up	F up	J low	Ka low	Kc low	F low	Observed (MHz)	Calculated (MHz)
3	1	3	4	2	1	2	3	8513.25	8513.32845
3	1	3	3	2	1	2	2	8513.4375	8513.4095
3	0	3	4	2	0	2	3	8631.6875	8631.67795
3	1	2	4	2	1	1	3	8753.125	8753.15824
4	1	4	5	3	1	3	4	11350.5625	11350.57581
4	1	4	4	3	1	3	3	11350.6875	11350.61586
4	0	4	5	3	0	3	4	11506.875	11506.88577
4	0	4	3	3	0	3	2	11506.9375	11506.90593
2	1	1	3	2	0	2	3	11553.125	11553.12047
4	1	3	5	3	1	2	4	11670.3125	11670.32123
4	1	3	4	3	1	2	3	11670.375	11670.34193
5	1	5	6	4	1	4	5	14187.375	14187.34475
1	1	1	1	0	0	0	1	14270.6875	14270.64562
5	0	5	6	4	0	4	5	14380.375	14380.3591
5	1	4	6	4	1	3	5	14586.9375	14586.99718
5	1	4	5	4	1	3	4	14587	14587.00824
6	1	6	7	5	1	5	6	17023.5	17023.52687
2	1	2	3	1	0	1	2	17068.25	17068.30248
2	1	2	2	1	0	1	1	17068.625	17068.61222
6	0	6	7	5	0	5	6	17251.6875	17251.66943
6	1	5	7	5	1	4	6	17503.0625	17503.06122
1	1	0	1	1	0	1	1	11471.9375	11471.95046
1	1	0	2	1	0	1	2	11472.625	11472.66113
1	1	0	0	1	0	1	1	11473.1875	11473.18202
4	1	3	4	4	0	4	4	11837.625	11837.55188
4	1	3	5	4	0	4	5	11838	11838.03622

4.3.2 Methyl internal rotation

The splittings shown in **Figure 4.7** due to nuclear hyperfine and methyl rotor states were of similar magnitude and led to patterns that were sensitively dependent on the rotational states involved. As a result, fitting both methyl rotor and hyperfine splittings simultaneously was challenging. Moreover, both these types of splittings collapsed at higher J levels for the intense transitions. Since the methyl rotor splittings were just above the experimental resolution of 60 kHz, the error in the derived barrier height is raised.^{22,23} Interpolation of the broadband spectra aided in acquiring a better estimation of the frequency of the transitions. In early stages of the fit, we followed previous work, where the hyperfine splitting and internal rotation were treated separately, since the ¹⁴N atom responsible for nuclear hyperfine coupling was not in the spatial vicinity of the methyl group.^{23,24} The results from these fits were very similar to the final fits (see **Table 4.5**).

Table 4.5: Spectral fits of the hypothetical central frequencies using the XIAM program suite are shown along with the values resulting from DFT calculationsn at B3LYP-GD3BJ/Def2TZVP (Representation I' Watson S reduction).

3-Pentenitrile	<i>Syn</i>	<i>Eclipsed</i>
A (MHz) (pred/expt^a)	8312.7855 / 8163.609(18)	12901.0547 / 12.878(17)
B (MHz) (pred/expt)	1926.6016 / 1939.7349(30)	1484.7483 / 1478.8851(63)
C (MHz) (pred/expt)	1594.5939 / 1597.5068(32)	1406.0122 / 1398.9110(83)
F₀ (fixed)	158.0	158.0
D_J (kHz) (expt)	0.757(38)	0.502(37)
D_{JK} (kHz) (expt)	5.25(18)	-27.39(51)
D_K (kHz) (expt)	30.1(18)	-
d₁ (kHz) (expt)	0.219(10)	-0.105(58)
Dpi2J (expt)	0.00141(57)	-
Dpi2K (expt)	-0.0185(29)	-
Dpi2- (expt)	0.00144(33)	-
δ (fixed)	2.099929695	0.544274057
ε (fixed)	2.612459285	1.090581459
rms (kHz)	64	22
N^b	60	18
V₃ (cm⁻¹) (pred/expt)	609.3 / 553.8±2.4	588.6 / 619.9±0.9

^a expt: experimental fit values

^b N is the number of hypothetical central transitions (not counting individual hyperfine transitions) fit.

As our fits improved, we iteratively alternated between SPFIT to determine A-state hyperfine splittings and XIAM to fit both methyl rotor and hyperfine splittings. This helped ensure that the A and E state transitions were identified properly. After confidently identifying the A and the E states, SPFIT was used to successfully fit the A states, providing high-accuracy rotational constants. Final fits of both nuclear hyperfine and methyl rotor splittings were carried out with XIAM. Representative examples of the fits are shown in **Figure 4.7 (a)-(d)**. The XIAM program was used solely to fit the frequencies and not the intensities of the transitions. As a result, in the predicted stick spectra, the intensity of the E state transitions is taken to be the same as its A state counterpart. The best-fit prediction shown as a stick spectrum in **Figure 4.7 (c)** are convolved to a Lorentzian lineshape that are overlaid on the stick spectra. With 131 lines fit using XIAM, the lowest energy *syn* conformer of 3-PN has a barrier to methyl internal rotation of $552.9 \pm 1.1 \text{ cm}^{-1}$ with an average fitting error of 33 kHz. 86 A methyl rotor state transitions and 45 E states were used in the final fit (**Table 4.6**). The fit parameters from XIAM for *syn* 3-PN are listed in **Table 4.7**.

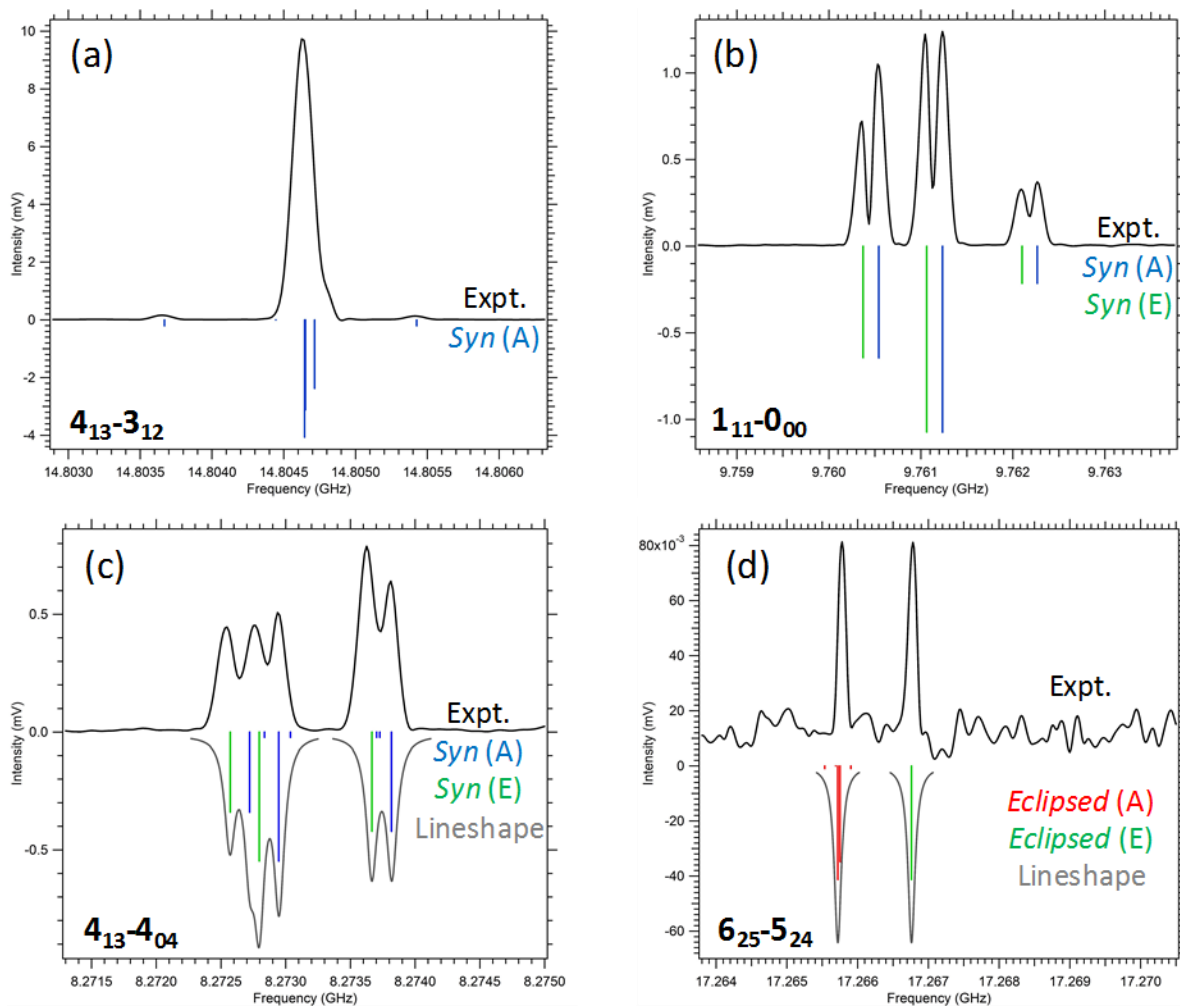


Figure 4.7: Close-up view of individual transitions of 3-pentenitrile (black traces) along with the final fits of the A/E states of (a-c) the *syn* conformer (blue/green sticks), and (d) *eclipsed* conformer (red/green sticks). (a) The $4_{13}-3_{12}$ transition of the *syn* conformer shows collapsed hyperfine splitting with unresolved methyl rotor splittings. The $1_{11}-0_{00}$ (b) and $4_{13}-4_{04}$ (c) transitions of the *syn* conformer with both hyperfine and methyl rotor splittings. Predictions of $4_{13}-4_{04}$ (c) are convoluted to Lorentzian lineshapes and are overlaid (grey trace). (d) The $6_{25}-5_{24}$ transition of the *eclipsed* conformer in which only methyl rotor splittings are resolved. The predicted fits are convoluted to Lorentzian lineshapes and are overlaid (grey trace).

Table 4.6: Linelist of *syn* 3-pentenitrile from XIAM.

J up	Ka up	Kc up	F up	J low	Ka low	Kc low	F low	A state (MHz)		E state (MHz)	
								Calc.	Obs.	Calc.	Obs.
4	1	3	3	4	0	4	3	8272.719 4	8272.765 6	8272.572 3	8272.562 5
4	1	3	5	4	0	4	5	8272.943 2	8272.937 5	8272.796 1	8272.734 4
4	1	3	4	4	0	4	4	8273.813 7	8273.812 5	8273.666 6	8273.609 4
4	0	4	3	3	1	3	2	8583.938 5	8583.921 9	8584.093 6	8584.109 4
4	0	4	5	3	1	3	4	8584.150 9	8584.140 7	8584.306	8584.328 2
4	0	4	4	3	1	3	3	8584.734 7	8584.718 8	8584.889 8	8584.906 3
5	1	4	4	5	0	5	4	9332.468 7	9332.484 4	9332.332 1	9332.296 9
5	1	4	6	5	0	5	6	9332.663 3	9332.656 3	9332.526 7	9332.468 8
5	1	4	5	5	0	5	5	9333.618 4	9333.625	9333.481 8	9333.437 5
1	1	1	1	0	0	0	1	9760.546	9760.531 2	9760.372 1	9760.359 4
1	1	1	2	0	0	0	1	9761.237 2	9761.234 3	9761.063 3	9761.062 5
1	1	1	0	0	0	0	1	9762.274 1	9762.265 6	9762.100 1	9762.093 8
7	1	6	7	6	2	5	6	10045.13 9	10045.21 58		
3	1	3	3	2	1	2	3	10089.32 97	10089.32 81		
3	1	3	4	2	1	2	3	10090	10089.98 44		
3	1	3	2	2	1	2	2	10090.89 08	10090.89 06		
3	0	3	4	2	0	2	3	10556.89 23	10556.92 19		
3	2	2	4	2	2	1	3	10611.76 53	10611.81 25	10612.40 04	10612.43 75
3	2	1	4	2	2	0	3	10666.50 35	10666.51 56	10665.86 13	10665.88 28
3	2	1	3	2	2	0	2	10666.64 71	10666.64 06	10666.00 67	10666.00 78

Table 4.6 continued.

6	1	5	5	6	0	6	5	10696.978	10696.9844	10696.8563	10696.8125
6	1	5	7	6	0	6	7	10697.1535	10697.1406	10697.0318	10696.9687
6	1	5	6	6	0	6	6	10698.1929	10698.1875	10698.0712	10698.0156
3	1	2	2	2	1	1	2	11115.1526	11115.1406		
3	1	2	4	2	1	1	3	11116.1653	11116.1875		
3	1	2	3	2	1	1	3	11116.9427	11116.9375		
7	1	6	6	7	0	7	6	12397.3983	12397.4219	12397.2954	12397.3125
7	1	6	8	7	0	7	8	12397.5595	12397.5625	12397.4566	12397.4531
7	1	6	7	7	0	7	7	12398.6774	12398.6719	12398.5745	12398.5625
5	0	5	4	4	1	4	3	12563.81	12563.7656	12563.9575	12563.9375
5	0	5	6	4	1	4	5	12563.9515	12563.9375	12564.099	12564.1094
2	1	2	2	1	0	1	1	12955.5923	12955.5781	12955.4211	12955.3906
2	1	2	3	1	0	1	2	12956.3273	12956.3281	12956.1561	12956.1406
2	1	2	1	1	0	1	0	12956.81	12956.8125	12956.6388	12956.625
4	1	4	4	3	1	3	4	13437.3484	13437.3281		
4	1	4	5	3	1	3	4	13438.0427	13438.0469		
4	0	4	5	3	0	3	4	14012.8595	14012.8594		
4	2	3	5	3	2	2	4	14138.2848	14138.3281		
4	3	2	5	3	3	1	4	14175.6396	14175.6562	14176.5316	14176.5625
4	3	1	5	3	3	0	4	14177.7031	14177.7188	14176.8018	14176.8437
4	2	2	5	3	2	1	4	14274.1851	14274.1406		
4	2	2	4	3	2	1	3	14274.2911	14274.1719		
4	3	1	5	5	2	4	6	14365.8667	14365.8906		
8	1	7	8	8	0	8	8	14452.5382	14452.5156	14452.4566	14452.4844
8	1	7	9	7	2	6	8	14737.2703	14737.25		
8	1	7	8	7	2	6	7	14737.9294	14737.8906		
4	1	3	3	3	1	2	3	14803.6691	14803.6562		
4	1	3	5	3	1	2	4	14804.6481	14804.625		
4	1	3	4	3	1	2	4	14805.432	14805.4218		
3	1	3	3	2	0	2	2	15984.8836	15984.8906	15984.7102	15984.7188
3	1	3	4	2	0	2	3	15985.6009	15985.6094	15985.4275	15985.4376
3	1	3	2	2	0	2	1	15985.8617	15985.875		
9	2	7	10	9	1	8	10	16056.6661	16056.625	16056.287	16056.2656
9	2	7	9	9	1	8	9	16056.7323	16056.7812	16056.3532	16056.4218
7	2	5	7	7	1	6	7	16242.9213	16242.9063	16242.4812	16242.4922
7	2	5	8	7	1	6	8	16243.1315	16243.125	16242.6914	16242.711
10	2	8	10	10	1	9	10	16380.5129	16380.5156		
6	0	6	5	5	1	5	4	16555.0775	16555.125	16555.2135	16555.1875
6	0	6	7	5	1	5	6	16555.1757	16555.1719	16555.3117	16555.2344
6	0	6	6	5	1	5	5	16555.6078	16555.6094	16555.7438	16555.6719

Table 4.6 continued.

6	2	4	6	6	1	5	6	16639.8649	16639.8906		
6	2	4	7	6	1	5	7	16640.2098	16640.1875		
5	1	5	5	4	1	4	5	16773.2674	16773.25		
5	1	5	6	4	1	4	5	16773.99	16773.9688		
5	1	5	4	4	1	4	4	16774.8315	16774.8281		
9	1	8	10	9	0	9	10	16856.0179	16856		
9	1	8	9	9	0	9	9	16857.247	16857.2656		
11	2	9	11	11	1	10	11	17042.6835	17042.6875	17042.3989	17042.4062
5	2	3	5	5	1	4	5	17150.6294	17150.6875		
5	2	3	6	5	1	4	6	17151.0993	17151.125		
5	0	5	6	4	0	4	5	17417.8433	17417.8281		
3	3	1	3	4	2	2	4	17638.763	17638.7813		
3	3	1	3	4	2	2	4	17638.763	17638.7813		
3	3	1	4	4	2	2	5	17639.0633	17639.0782		
3	3	1	4	4	2	2	5	17639.0633	17639.0782		
5	2	4	6	4	2	3	5	17655.5999	17655.6094		
4	2	2	4	4	1	3	4	17704.5439	17704.5312	17704.1137	17704.1172
4	2	2	5	4	1	3	5	17705.1252	17705.125	17704.695	17704.7109
4	2	2	3	4	1	3	3	17705.2747	17705.2656	17704.8446	17704.8516
5	4	1	6	4	4	0	5	17717.3666	17717.375		
5	3	3	6	4	3	2	5	17730.0423	17730.0156	17731.8734	17731.8437
5	3	2	6	4	3	1	5	17737.2486	17737.2188	17735.4064	17735.3906
5	3	2	5	4	3	1	4	17737.3094	17737.375	17735.4671	17735.5468
3	3	0	4	4	2	3	5	17843.7635	17843.7031		
5	2	3	6	4	2	2	5	17923.5373	17923.5		
5	2	3	5	4	2	2	4	17923.6379	17923.5469		

Table 4.7: Spectral fits to both A and E methyl rotor states of 3-PN using the XIAM program suite compared with the values resulting from DFT calculations (Representation I' Watson A reduction)

3-Pentenitrile	<i>Syn</i>	<i>Eclipsed</i>
A (MHz) (pred^a/expt^b)	8312.7855 / 8163.5733(81)	12901.0547 / 12871.163(16)
B (MHz) (pred/expt)	1926.6016 / 1939.7216(19)	1484.7483 / 1478.8795(32)
C (MHz) (pred/expt)	1594.5939 / 1597.5056(16)	1406.0122 / 1398.9152(29)
F₀ (fixed)	158.0	158.0
D_J (kHz) (expt)	0.663(24)	0.512(42)
D_{JK} (kHz) (expt)	-6.19(12)	-27.87(42)
D_K (kHz) (expt)	33.14(65)	-
d₁ (kHz) (expt)	-0.2075(53)	-
d₂ (kHz) (expt)	-0.0070(18)	-
D_{pi2J} (expt)	0.00114(28)	-
D_{pi2K} (expt)	-0.0185(14)	-
D_{pi2-} (expt)	0.00159(16)	-
δ (fixed)	2.099929695	0.544274057
ε (fixed)	2.612459285	1.090581459
χ_{AA} (MHz) (pred/expt)	0.227 / 0.263(15)	-1.934 / 0.655(57)
χ_{BB}-χ_{CC} (MHz) (pred/expt)	-4.810 / -4.346(20)	-2.735 / 2.707(81)
rms (kHz)	33	37
No. of lines fit (A/E)^c	86/45	28/4
V₃ (cm⁻¹) (pred/expt^d)	609.3 / 552.9±1.1	588.6 / 619.4±1.0

^a pred: predicted values at B3LYP-GD3BJ/Def2TZVP

^b expt: experimental fit values

^c A/E refers to number of A state lines/number of E state lines fit, including individual hyperfine transitions.

^dThe stated error bars are statistical errors from the fit. Due to the small number of assigned transitions in the *eclipsed* conformer, there is a greater risk of systematic error in the fit.

Table 4.8: Linelist of *eclipsed* 3-pentenitrile from XIAM.

J up	Ka up	Kc up	F up	J low	Ka low	Kc low	F low	State	Calculated (MHz)	Observed (MHz)
3	1	3	4	2	1	2	3	A	8513.2989	8513.25
3	0	3	4	2	0	2	3	A	8631.6466	8631.6875
3	1	2	4	2	1	1	3	A	8753.1405	8753.125
4	1	4	5	3	1	3	4	A	11350.547	11350.5625
4	1	4	4	3	1	3	3	A	11350.5849	11350.6875
4	0	4	5	3	0	3	4	A	11506.8547	11506.875
4	0	4	3	3	0	3	2	A	11506.8727	11506.9375
2	1	1	3	2	0	2	3	A	11553.1391	11553.125
4	1	3	5	3	1	2	4	A	11670.3069	11670.3125
4	1	3	4	3	1	2	3	A	11670.3243	11670.375
5	1	5	6	4	1	4	5	A	14187.3267	14187.375
1	1	1	1	0	0	0	1	A	14270.6641	14270.6875
5	0	5	6	4	0	4	5	A	14380.3381	14380.375
5	1	4	6	4	1	3	5	A	14586.9966	14586.9375
5	1	4	5	4	1	3	4	A	14587.0058	14587
6	1	6	7	5	1	5	6	A	17023.532	17023.5
2	1	2	3	1	0	1	2	A	17068.2765	17068.25
2	1	2	2	1	0	1	1	A	17068.6202	17068.625
6	0	6	7	5	0	5	6	A	17251.6706	17251.6875
6	1	5	7	5	1	4	6	A	17503.0869	17503.0625
1	1	0	1	1	0	1	1	A	11471.9668	11471.9375
1	1	0	2	1	0	1	2	A	11472.6677	11472.625
1	1	0	0	1	0	1	1	A	11473.2275	11473.1875
4	1	3	4	4	0	4	4	A	11837.5784	11837.625
6	2	5	7	5	2	4	6	A	17265.7751	17265.7812
6	2	5	7	5	2	4	6	E	17266.7624	17266.7813
6	2	4	7	5	2	3	6	A	17280.435	17280.4375
6	2	4	7	5	2	3	6	E	17279.4283	17279.4375
5	2	4	6	4	2	3	5	A	14388.8923	14388.9062
5	2	4	6	4	2	3	5	E	14390.4082	14390.3906
5	2	3	6	4	2	2	5	A	14397.2743	14397.25
5	2	3	6	4	2	2	5	E	14395.7421	14395.7344

A similar fitting procedure was used to obtain final best-fit rotational parameters in *eclipsed* 3-PN (**Table 4.7**). The higher energy *eclipsed* conformer of 3-PN has a barrier of $619.4 \pm 1.0 \text{ cm}^{-1}$ with an average error in the fit of 37 kHz. A total of 32 lines were included in the fit, of which 28 were A states and 4 were E states (**Table 4.8**). The transitions due to *eclipsed* 3-PN were much weaker than *syn* 3-PN, moreover, the transitions with easily resolved methyl rotor splittings were even weaker, as shown in **Figure 4.7 (d)**. The best-fit predictions and the convolved Lorentzian lineshape are also shown in **Figure 4.7 (d)**. Furthermore, all four E states in the fit belonged to R branch a-type transitions with $J=4-6$ and similar nuclear hyperfine splitting patterns. As a result, while the statistical error in the fits for the two conformers are similar, the extracted methyl rotor barrier height in *eclipsed* 3-PN has a greater risk of systematic error.

4.3.3 4-Pentenenitrile

The conformational search for 4-PN identified five unique conformers, all of which have relative energies within 300 cm^{-1} of the global minimum (**Table 4.1**), and therefore may be present in the expansion. All five structures are near-prolate asymmetric tops. The broadband spectrum of **Figure 4.8** was a 1M scan average recorded at 5% TWTA, which is in the LFP regime. SFCB was not applied to 4-PN, hence, we did not record the microwave spectrum in the RAP regime. The spectrum was recorded with helium as backing gas ($P_0 = 1.4 \text{ bar}$) in order to retain population in higher-energy conformers in the expansion, which could be cooled away with heavier bath gases such as Ar.²⁵ As anticipated, the 4-PN spectrum is more complicated than the 3-PN spectrum, indicative of the presence of transitions due to additional conformers.

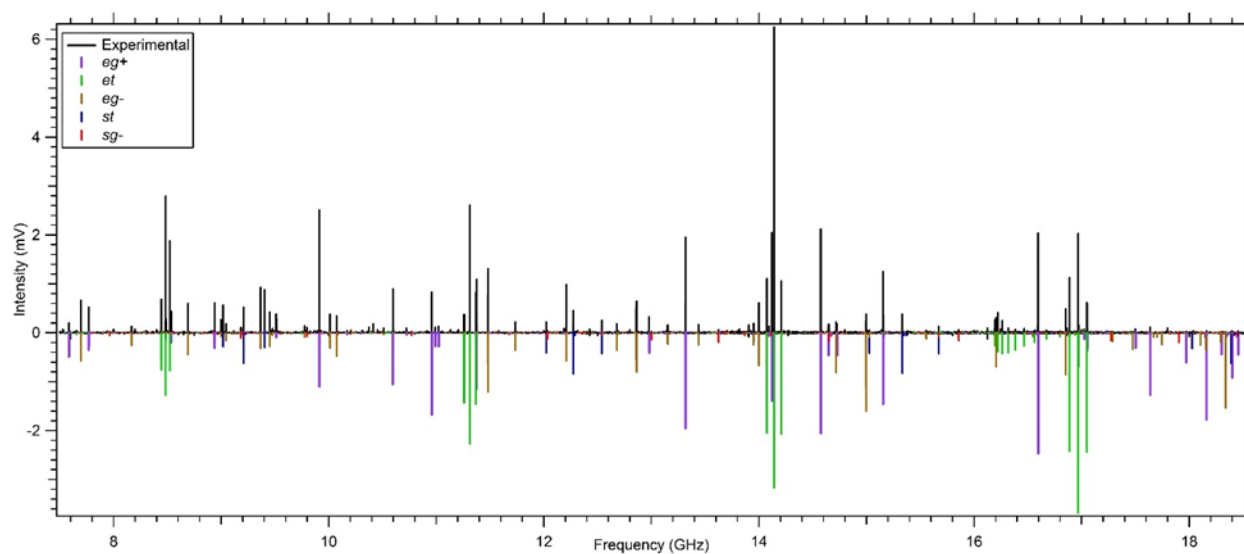


Figure 4.8: Broadband microwave spectrum in the 7.5-18.5 GHz region of 4-pentenitrile (black trace) with the final fit spectra of the conformers *eg+* (violet), *et* (green), *eg-* (brown), *st* (blue) and *sg-* (red) shown below. The rotational spectrum is a 1 million FID average of 4-PN entrained in helium carrier gas.

Table 4.9: Spectral fits using the SPFIT program suite are compared with DFT calculations (Representation I' Watson A reduction).

4-Pentenenitrile	<i>eg+</i>	<i>et</i>	<i>eg-</i>	<i>st</i>	<i>sg-</i>
A (MHz) (pred ^a /expt ^b)	8297.6034 / 8210.3675(54)	17849.6284 / 17595.7813(56)	5908.6477 / 5804.3411(58)	15041.200 / 14816.7(54)	6008.2593 / 5927.995(11)
B (MHz) (pred/expt)	1952.8733 / 1961.2611(52)	1428.8795 / 1427.6418(13)	2445.7686 / 2491.5640(19)	1600.4804 / 1599.9324(16)	2566.0147 / 2587.2440(34)
C (MHz) (pred/expt)	1700.4463 / 1702.3928(53)	1402.3176 / 1400.6661(15)	1878.9817/ 1892.2972(17)	1472.5354 / 1470.7745(14)	2026.4610 / 2035.7256(51)
μ_A (pred)	2.8	3.9	2.3	4.0	-2.9
μ_B (pred)	2.9	1.3	3.4	0.4	2.8
μ_C (pred)	0.5	0.1	-0.2	0.0	1.1
Δ_J (kHz) (expt)	1.690(47)	0.253(20)	5.001(56)	-	1.77(25)
Δ_{JK} (kHz) (expt)	-21.85(34)	-12.65(30)	-23.38(20)	-	-7.26(63)
Δ_K (kHz) (expt)	102.2(14)	-	40.1(13)	-	-
δ_J (kHz) (expt)	0.3748(94)	-0.0308(76)	1.801(12)	-	-
δ_K (kHz) (expt)	10.9(25)	-	5.58(51)	-	-
χ_{AA} (MHz) (pred/expt)	-0.786 / - 0.669(11)	-3.678 / - 3.256(11)	0.546 / 0.553 (11)	-4.384 / - 3.920(23)	-0.777 / - 0.672(25)
χ_{BB} - χ_{CC} (MHz) (pred/expt)	-3.481 / - 3.137(20)	-0.930 / - 0.863(22)	-5.125 / - 4.639(19)	-0.234 / - 0.220(48)	-2.402 / - 2.208(48)
rms (kHz)	17	19	15	17	17
N^c	70	70	70	26	24
Relative energy (cm⁻¹) (pred)	0	32.0	104.0	117.9	258.1

^a pred: predicted values at B3LYP-GD3BJ/Def2TZVP

^b expt: experimental fit values

^c N is the number of transitions (including individual hyperfine transitions) in the fit.

Essentially all significant transitions in the spectrum in **Figure 4.8** could be fit to one of the five lowest-energy conformers of 4-PN shown in **Figure 4.3**, *eg+* (purple), *et* (green), *eg-* (brown), *st* (blue), and *sg-* (red). The rotational parameters from the best fits are summarized in **Table 4.9**, where they are compared with the predictions of calculation. **Figure 4.9** shows close-up views of the hyperfine structure present in the five observed conformers.

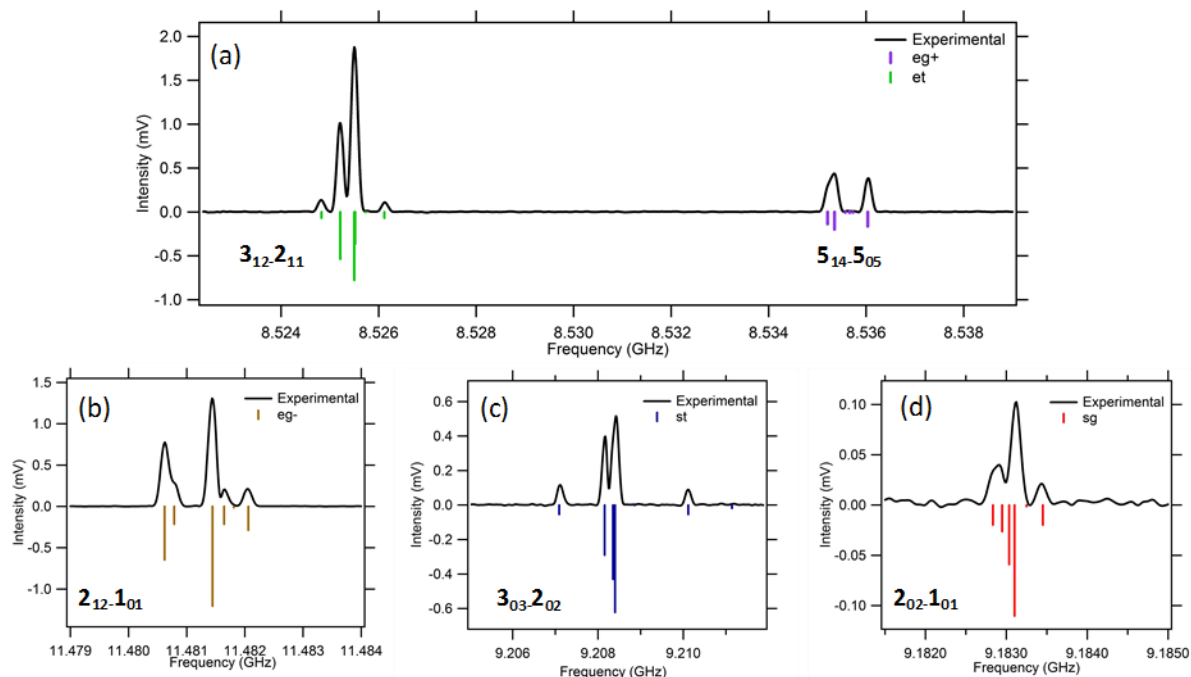


Figure 4.9: A close-up view of individual transitions of 4-pentenitrile conformers (black traces) along with their final fit spectra (stick diagrams below). Representative transitions belonging to the (a) *et* and *eg+* conformers, (b) *eg-*, (c) *st*, and (d) *sg* conformers.

The spectrum of the *et* conformer (green) is dominated by triplets of a-type transitions within an R branch, due to a near-prolate asymmetric top. These were the most intense transitions within our spectrum. The transitions display some hyperfine structure, but this structure was largely collapsed, as the ^{14}N atom falls along the a-axis. In addition, a relatively strong Q branch containing b-type transitions was observed in the 16-16.5 GHz range. This Q branch greatly reduced the uncertainty in fitting the A rotation constant, and had well-resolved hyperfine structure, aiding the assignment. Within the Q branch, the hyperfine structure starts to collapse around $J=4$ at our experimental resolution. As a result, only the Δ_J , Δ_{JK} , and δ_J (kHz) centrifugal distortion terms could be fit reliably.

Transitions due to the *eg+* conformer, shown in purple, were assigned using patterns resulting from a- and b-type R-branch transitions, but also included a few weak c-type transitions, despite the small value calculated for μ_c (0.5 D). This conformer had the second most intense transitions within the spectrum and several transitions displayed well-resolved hyperfine structure. The fit of the transitions due to the *eg-* conformer, shown in brown, followed similar methods to that for *eg+*; however, in this case, no c-type transitions were observed, likely due to its low predicted dipole moment along this axis. The hyperfine structure was readily apparent in several transitions of this conformer, enabling straight forward assignment of the hyperfine constants. The fits to both these *eg* conformers included Watson-A reduced centrifugal distortion constants.

The *st* conformer, with simulation shown in blue, could be assigned despite its transitions being relatively weak compared to those of the other conformers. Only a-type transitions within an R-branch could be assigned. This branch displayed a largely collapsed hyperfine structure with small hyperfine transitions observable to the sides of each large transition. The assignment of only a-type transitions resulted in a larger uncertainty in the A rotational constant and no centrifugal distortion constants. Searches were conducted for weak b-type transitions but none were observed. This is likely the combined consequence of low population and a weak dipole component along the b-axis (0.4 D).

Finally, the *sg-* conformer, shown in red, was barely observable within the spectrum. As a result, the assignment of the *sg-* conformer could only be accomplished after the assignment of the rest of the spectrum. Accurate predictions of the transition frequencies and hyperfine splittings involving the lowest rotational levels from the DFT calculations played an important role in discerning the transitions in the experimental spectrum. In the final fit, several a- and b-type R-branch transitions could be assigned, including hyperfine splittings that enabled extraction of hyperfine coupling constants (**Table 4.9**). However, only the Δ_J and Δ_{JK} centrifugal distortion terms could be fit reliably. The linelists of the five 4-PN conformers are in the **Tables 4.10-4.14**.

Table 4.10: Linelist of *eg*+ 4-pentenenitrile from SPFIT.

J up	Ka up	Kc up	F up	J low	Ka low	Kc low	F low	Observed (MHz)	Calculated (MHz)
2	1	1	1	1	1	0	1	7585.375	7585.36953
2	1	1	2	1	1	0	1	7585.984	7585.98653
2	1	1	3	1	1	0	2	7586.156	7586.16076
2	1	1	2	1	1	0	2	7586.547	7586.55744
2	1	1	1	1	1	0	0	7586.781	7586.7968
4	1	3	3	4	0	4	3	7768.891	7768.89758
4	1	3	5	4	0	4	5	7769.078	7769.06568
4	1	3	4	4	0	4	4	7769.719	7769.71316
5	1	4	6	5	0	5	6	8535.344	8535.34971
5	1	4	5	5	0	5	5	8536.031	8536.03363
2	2	0	1	3	1	3	2	8932.109	8932.10427
2	2	0	3	3	1	3	4	8932.469	8932.47713
2	2	0	2	3	1	3	3	8933.406	8933.41064
4	0	4	4	3	1	3	4	8938.75	8938.76864
4	0	4	3	3	1	3	2	8938.938	8938.93404
4	0	4	5	3	1	3	4	8939.098	8939.09284
4	0	4	4	3	1	3	3	8939.469	8939.46517
4	0	4	3	3	1	3	3	8939.875	8939.87437
6	1	5	7	6	0	6	7	9512.188	9512.21414
6	1	5	6	6	0	6	6	9512.953	9512.94163
1	1	1	1	0	0	0	1	9912.406	9912.4098
1	1	1	2	0	0	0	1	9912.781	9912.78006
1	1	1	0	0	0	0	1	9913.328	9913.33541
1	1	0	0	0	0	0	1	10170.609	10170.58848
1	1	0	2	0	0	0	1	10171.453	10171.44483
1	1	0	1	0	0	0	1	10172.016	10172.01575
3	1	3	3	2	1	2	3	10597.203	10597.21336
3	1	3	3	2	1	2	2	10597.813	10597.82506
3	1	3	4	2	1	2	3	10597.906	10597.90988
3	1	3	2	2	1	2	2	10598.766	10598.76538
7	1	6	8	7	0	7	8	10723.484	10723.49438
7	1	6	7	7	0	7	7	10724.281	10724.26828
3	0	3	3	2	0	2	3	10959.094	10959.08609
3	0	3	4	2	0	2	3	10959.344	10959.3616
3	0	3	2	2	0	2	2	10959.688	10959.69336
3	2	2	3	2	2	1	2	10991.125	10991.13626
3	2	2	4	2	2	1	3	10991.359	10991.35128
3	2	1	3	2	2	0	2	11022.594	11022.59403

Table 4.10 continued

3	2	1	4	2	2	0	3	11022.781	11022.77848
3	1	2	2	2	1	1	2	11373.609	11373.59715
3	1	2	4	2	1	1	3	11374.125	11374.11591
3	1	2	3	2	1	1	3	11374.469	11374.4648
5	0	5	6	4	1	4	5	12979.797	12979.7954
5	0	5	5	4	1	4	4	12980.172	12980.15856
2	1	2	2	1	0	1	2	13317.094	13317.09048
2	1	2	2	1	0	1	1	13317.297	13317.29117
2	1	2	3	1	0	1	2	13317.703	13317.70218
2	1	2	1	1	0	1	1	13318.25	13318.24271
2	1	1	3	1	0	1	2	14093.922	14093.92498
2	1	1	2	1	0	1	1	14094.516	14094.52236
4	1	4	4	3	1	3	4	14120.813	14120.79864
4	1	4	5	3	1	3	4	14121.516	14121.54355
4	1	4	3	3	1	3	3	14122.438	14122.43164
4	0	4	4	3	0	3	4	14575.625	14575.61805
4	0	4	5	3	0	3	4	14575.938	14575.94224
4	0	4	3	3	0	3	3	14576.297	14576.30276
4	1	3	3	3	1	2	3	15155.313	15155.2977
4	1	3	5	3	1	2	4	15155.719	15155.7297
4	1	3	4	3	1	2	4	15156.063	15156.05298
3	1	3	3	2	0	2	3	16595.5	16595.51448
3	1	3	3	2	0	2	2	16595.75	16595.74981
3	1	3	4	2	0	2	3	16596.219	16596.211
3	1	3	2	2	0	2	2	16596.688	16596.69014
5	1	5	6	4	1	4	5	17637.906	17637.93217
7	2	5	8	7	1	6	8	16591	16591.02159
4	2	3	4	3	2	2	3	14648.672	14648.70397
4	2	3	5	3	2	2	4	14648.813	14648.80021
4	2	2	5	3	2	1	4	14727.094	14727.04361
6	2	4	6	6	1	5	6	17025.328	17025.37952
6	2	4	7	6	1	5	7	17025.719	17025.63788

Table 4.11: Linelist of *et* 4-pentenenitrile from SPFIT.

J up	Ka up	Kc up	F up	J low	Ka low	Kc low	F low	Observed (MHz)	Calculated (MHz)
2	1	2	3	3	0	3	4	7656.359	7656.38675
2	1	2	2	3	0	3	3	7656.828	7656.81065
3	1	3	3	2	1	2	3	8443.625	8443.6188
3	1	3	3	2	1	2	2	8444.281	8444.28069
3	1	3	4	2	1	2	3	8444.578	8444.5766
3	1	3	2	2	1	2	2	8445.563	8445.57391
3	0	3	3	2	0	2	3	8483.703	8483.71437
3	0	3	2	2	0	2	1	8484.594	8484.59862
3	0	3	4	2	0	2	3	8484.797	8484.80016
3	0	3	2	2	0	2	2	8486.219	8486.22701
3	1	2	3	2	1	1	3	8524.813	8524.82988
3	1	2	3	2	1	1	2	8525.203	8525.21433
3	1	2	4	2	1	1	3	8525.5	8525.49998
3	1	2	2	2	1	1	2	8526.125	8526.11921
1	1	1	0	2	0	2	1	10510.172	10510.17842
1	1	1	1	2	0	2	1	10511.063	10511.07539
1	1	1	2	2	0	2	3	10511.297	10511.29841
1	1	1	1	2	0	2	2	10512.703	10512.70378
4	1	4	4	3	1	3	4	11258.234	11258.20191
4	1	4	4	3	1	3	3	11259.203	11259.15971
4	1	4	5	3	1	3	4	11259.297	11259.29259
4	1	4	3	3	1	3	3	11260.531	11260.53098
4	0	4	4	3	0	3	4	11311.734	11311.7431
4	0	4	5	3	0	3	4	11312.844	11312.85407
4	0	4	3	3	0	3	3	11314.234	11314.22567
4	1	3	4	3	1	2	4	11366.406	11366.40791
4	1	3	5	3	1	2	4	11367.172	11367.20437
4	1	3	3	3	1	2	3	11368.094	11368.07945
5	1	5	5	4	1	4	5	14072.797	14072.80579
5	1	5	6	4	1	4	5	14073.922	14073.96975
5	1	5	4	4	1	4	4	14075.328	14075.29764
5	0	5	5	4	0	4	5	14139.625	14139.6265
5	0	5	6	4	0	4	5	14140.766	14140.75519
5	1	4	5	4	1	3	5	14208	14208.00863
5	1	4	6	4	1	3	5	14208.875	14208.87385
5	1	4	4	4	1	3	4	14209.844	14209.84669
6	1	6	7	5	1	5	6	16888.578	16888.57964
6	0	6	7	5	0	5	6	16968.438	16968.46017

Table 4.11 continued

6	1	5	6	5	1	4	6	17049.625	17049.57452
6	1	5	7	5	1	4	6	17050.469	17050.48211
1	1	0	1	1	0	1	0	16194.016	16194.02742
1	1	0	2	1	0	1	2	16194.875	16194.8749
1	1	0	1	1	0	1	2	16195.484	16195.49261
1	1	0	2	1	0	1	1	16195.843	16195.85153
1	1	0	1	1	0	1	1	16196.453	16196.46924
2	1	1	2	2	0	2	1	16221.078	16221.08833
2	1	1	1	2	0	2	1	16221.688	16221.68681
2	1	1	3	2	0	2	3	16222.063	16222.05452
2	1	1	2	2	0	2	2	16222.719	16222.71672
2	1	1	3	2	0	2	2	16223.094	16223.10117
2	1	1	1	2	0	2	2	16223.328	16223.3152
3	1	2	3	3	0	3	2	16261.75	16261.70404
3	1	2	3	3	0	3	4	16262.094	16262.08424
3	1	2	4	3	0	3	4	16262.75	16262.75434
3	1	2	3	3	0	3	3	16263.188	16263.17003
3	1	2	4	3	0	3	3	16263.859	16263.84013
4	1	3	5	4	0	4	5	16317.141	16317.10465
4	1	3	4	4	0	4	4	16317.422	16317.41916
5	1	4	6	5	0	5	6	16385.203	16385.22332
5	1	4	5	5	0	5	5	16385.437	16385.48678
6	1	5	7	6	0	6	7	16467.219	16467.24526
6	1	5	6	6	0	6	6	16467.516	16467.47965
7	1	6	8	7	0	7	8	16563.313	16563.32845
7	1	6	7	7	0	7	7	16563.563	16563.54496
8	1	7	9	8	0	8	9	16673.656	16673.65561
8	1	7	8	8	0	8	8	16673.859	16673.86053
5	2	3	5	4	2	2	4	14142.344	14142.35614
5	2	3	6	4	2	2	5	14142.593	14142.58783
6	2	5	7	5	2	4	6	16970.109	16970.1286
6	2	4	7	5	2	3	6	16971.313	16971.3093

Table 4.12: Linelist of *eg*- 4-pentenitrile from SPFIT.

J up	Ka up	Kc up	F up	J low	Ka low	Kc low	F low	Observed (MHz)	Calculated (MHz)
4	0	4	5	3	1	4	4	14717.58	14717.59
4	0	4	4	3	1	4	3	14717.94	14717.92
3	1	3	3	2	0	4	2	14996.05	14996.05
3	1	3	4	2	0	3	3	14996.77	14996.78
3	1	3	2	2	0	3	1	14997.08	14997.04
4	1	4	4	3	1	3	4	16203.2	16203.2
4	1	4	5	3	1	5	4	16203.89	16203.92
4	1	4	3	3	1	5	3	16204.8	16204.78
4	0	4	4	3	0	5	3	16852.39	16852.39
4	0	4	5	3	0	0	4	16852.61	16852.6
1	1	1	1	0	0	0	1	7696	7695.994
1	1	1	2	0	0	0	1	7696.766	7696.774
1	1	1	0	0	0	2	1	7697.938	7697.945
2	1	2	1	1	1	2	0	8167.703	8167.679
2	1	2	3	1	1	2	2	8168.5	8168.484
2	1	2	1	1	1	2	1	8169.641	8169.63
2	0	2	3	1	0	6	2	8693.391	8693.42
2	0	2	1	1	0	6	0	8693.641	8693.639
2	1	1	1	1	1	6	1	9365.688	9365.682
2	1	1	3	1	1	1	2	9366.766	9366.76
2	1	1	2	1	1	1	1	9366.984	9366.982
2	1	1	1	1	1	1	0	9367.219	9367.217
2	1	1	2	1	1	7	2	9367.594	9367.596
5	1	4	4	5	0	7	4	9776	9775.99
5	1	4	6	5	0	7	6	9776.25	9776.252
5	1	4	5	5	0	4	5	9777.531	9777.535
3	0	3	2	2	1	4	1	10073.42	10073.42
3	0	3	4	2	1	4	3	10073.73	10073.74
3	0	3	3	2	1	1	2	10074.27	10074.27
2	1	2	2	1	0	1	1	11480.63	11480.62
2	1	2	3	1	0	1	2	11481.44	11481.44
2	1	2	1	1	0	3	1	11481.64	11481.64
2	1	2	1	1	0	3	0	11482.05	11482.06
3	1	3	3	2	1	3	3	12208.08	12208.08
3	1	3	4	2	1	2	3	12208.73	12208.75
3	1	3	2	2	1	1	2	12209.63	12209.65
3	0	3	3	2	0	8	2	12861.56	12861.58
3	0	3	4	2	0	2	3	12861.75	12861.76

Table 4.12 continued

3	1	2	4	2	1	2	3	14000.27	14000.26
3	2	2	2	3	1	2	2	12678.34	12678.33
3	2	2	4	3	1	2	4	12678.56	12678.56
3	2	2	3	3	1	2	3	12679.23	12679.23
5	2	4	6	5	1	2	6	15554.75	15554.81
5	2	4	5	5	1	5	5	15555.67	15555.62
3	2	2	4	2	2	5	3	13151.59	13151.57
3	2	2	3	2	2	5	2	13151.75	13151.74
3	2	1	4	2	2	4	3	13440.83	13440.84
3	2	1	3	2	2	4	2	13441.2	13441.2
4	2	3	3	4	1	4	3	13951.48	13951.5
4	2	3	5	4	1	4	5	13951.7	13951.69
4	2	3	4	4	1	3	4	13952.45	13952.46
2	2	1	2	2	1	5	1	11735.2	11735.2
2	2	1	1	2	1	5	1	11735.48	11735.48
2	2	1	3	2	1	4	3	11735.75	11735.75
2	2	1	2	2	1	4	2	11736.22	11736.23
2	2	0	2	2	1	6	2	10011.7	10011.71
2	2	0	3	2	1	6	3	10012.61	10012.6
2	2	0	1	2	1	3	1	10013.11	10013.1
5	2	3	6	5	1	3	6	8998.359	8998.356
4	2	2	4	4	1	3	4	9045.578	9045.574
4	2	2	5	4	1	2	5	9045.813	9045.834
3	2	1	3	3	1	2	3	9452.625	9452.627
3	2	1	4	3	1	1	4	9453.188	9453.185
3	2	1	2	3	1	0	2	9453.391	9453.381
4	1	3	3	3	2	0	2	9475.594	9475.592
4	1	3	5	3	2	7	4	9475.813	9475.805
4	1	3	4	3	2	8	3	9476.625	9476.636
6	1	5	5	6	0	8	5	12683.72	12683.7
6	1	5	7	6	0	9	7	12683.97	12683.92
6	1	5	6	6	0	9	6	12685.23	12685.23

Table 4.13: Linelist of *st* 4-pentenenitrile from SPFIT.

J up	Ka up	Kc up	F up	J low	Ka low	Kc low	F low	Observed (MHz)	Calculated (MHz)
3	1	3	3	2	1	2	3	9016.891	9016.88703
3	1	3	3	2	1	2	2	9017.563	9017.55223
3	1	3	4	2	1	2	3	9017.906	9017.90366
3	1	3	2	2	1	2	2	9018.922	9018.92497
3	0	3	3	2	0	2	3	9207.109	9207.09256
3	0	3	2	2	0	2	1	9208.172	9208.1573
3	0	3	4	2	0	2	3	9208.422	9208.39996
3	1	2	3	2	1	1	3	9404.438	9404.42711
3	1	2	3	2	1	1	2	9405.016	9405.02175
3	1	2	4	2	1	1	3	9405.375	9405.37057
3	1	2	2	2	1	1	2	9406.297	9406.2957
4	1	4	4	3	1	3	3	12022.578	12022.54259
4	1	4	5	3	1	3	4	12022.688	12022.69951
4	0	4	4	3	0	3	4	12272.125	12272.10289
4	0	4	5	3	0	3	4	12273.438	12273.44066
4	0	4	3	3	0	3	3	12275.125	12275.09224
4	2	3	5	3	2	2	4	12282.25	12282.23768
4	2	2	4	3	2	1	3	12291.094	12291.1205
4	2	2	5	3	2	1	4	12291.641	12291.65449
5	1	5	6	4	1	4	5	15026.609	15026.60044
5	0	5	6	4	0	4	5	15334.719	15334.73063
5	2	3	5	4	2	2	4	15370.047	15370.07063
5	2	3	6	4	2	2	5	15370.359	15370.34956
5	1	4	6	4	1	3	5	15672.297	15672.29881
6	1	6	6	5	1	5	5	18029.297	18029.32318
6	0	6	7	5	0	5	6	18391.313	18391.3423

Table 4.14: Linelist of *sg*- 4-pentenenitrile from SPFIT.

J up	Ka up	Kc up	F up	J low	Ka low	Kc low	F low	Observed (MHz)	Calculated (MHz)
1	1	1	1	0	0	0	1	7963.547	7963.536
1	1	1	2	0	0	0	1	7963.781	7963.766
2	1	2	2	1	1	1	2	8693.984	8693.995
2	1	2	2	1	1	1	1	8694.203	8694.225
2	1	2	3	1	1	1	2	8694.453	8694.458
4	2	2	5	4	1	3	5	9118.094	9118.109
2	0	2	3	1	0	1	2	9183.125	9183.102
2	0	2	1	1	0	1	1	9183.438	9183.452
3	2	1	4	3	1	2	4	9545.781	9545.8
2	1	1	1	1	1	0	1	9796.875	9796.878
2	1	1	2	1	1	0	1	9797.266	9797.262
2	1	1	3	1	1	0	2	9797.453	9797.447
2	1	1	2	1	1	0	2	9797.688	9797.694
2	1	1	1	1	1	0	0	9797.969	9797.958
3	0	3	4	2	1	2	3	10770.58	10770.63
2	1	2	2	1	0	1	1	12034.97	12034.97
2	1	2	3	1	0	1	2	12035.23	12035.23
2	1	2	1	1	0	1	1	12035.67	12035.69
3	0	3	4	2	0	2	3	13622.73	13622.75
3	2	2	3	2	2	1	2	13868.73	13868.72
3	2	2	4	2	2	1	3	13868.97	13868.94
3	1	3	3	2	0	2	3	15855.84	15855.85
3	1	3	3	2	0	2	2	15856.13	15856.11
3	1	3	4	2	0	2	3	15856.42	15856.4

4.4 Discussion

4.4.1 3-PN and 4-PN as Structural Isomers

In the introduction, we conjectured that 4-PN might be anticipated to form in greater abundance in Titan's atmosphere and in molecule-forming regions in space, as it is the recombination product of two resonance-stabilized radicals: allyl ($\cdot\text{CH}_2\text{-CH}=\text{CH}_2$) and cyanomethyl ($\cdot\text{CH}_2\text{CN}$). However, as a primary alkene, isomerization of 4-PN to the secondary alkene (e.g., 3-PN) is exothermic. This motivated our study of the microwave spectroscopy of this pair of molecules.

3-PN can be formed in both *cis* and *trans* isomers about the double bond. According to the DFT B3LYP-D3BJ/def2TZVP calculations, the *syn* and *eclipsed* conformers of *trans* 3-PN are more stable than the sole conformational minimum (an *eclipsed* structure) in *cis* 3-PN by 631.4 cm^{-1} (7.5 kJ/mol) and 445.1 cm^{-1} (5.3 kJ/mol), respectively. The latter energy difference is similar to the corresponding difference in $\Delta_f\text{H}(0\text{ K})$ of 4.8 kJ/mol between *cis* and *trans* 2-butene,²⁶ indicating that nitrile substitution on the terminal methyl group is only a minor perturbation on the local energy effects of *cis-trans* isomerization about the double bond.

Notably, the corresponding energy difference between primary and secondary alkenes is even larger than the *cis-trans* difference. For instance, the global minimum *trans* 3-PN conformer is calculated to be more stable than the global minimum structure of 4-PN by 11.0 kJ/mol (923.5 cm^{-1}), in good correspondence with the Active Thermochemical Tables best values for $\Delta_f\text{H}^0(0\text{ K})$ that place *trans*-2-butene 11.6 kJ/mol more stable than 1-butene.²⁵ Again, it would appear that substitution of a terminal nitrile group has little effect on these energetics. The primary reason for the relative stabilities of these structural isomers can be attributed to hyperconjugation. In case of 3-PN, partial overlap of the out-of plane C-H/C-C σ bonding orbitals occurs from either side of the vinyl group (making it four in total), whereas for 4-PN it occurs only from one side where partial overlap due to two C-H groups is lost, making it less stable than 3-PN (**Figures 4.2 and 4.3**).

4.4.2 Conformational Preferences of 3-PN and 4-PN

In order to better understand the similarities and differences between the conformational landscapes of 3-PN and 4-PN, we carried out one-dimensional relaxed potential energy scans of the flexible dihedral angles of the two molecules. **Figures 2** and **3** show the optimized conformational structures of the two molecules, keeping the vinyl group fixed in the plane of the page for ready comparison.

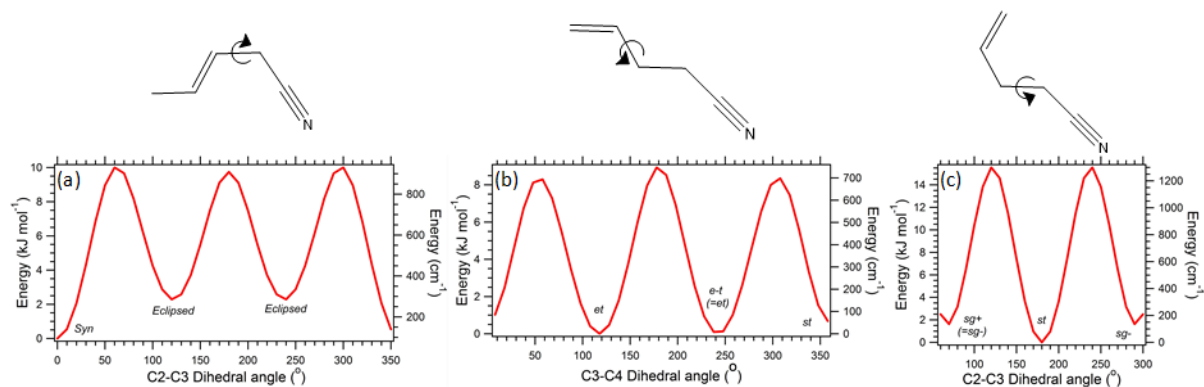


Figure 4.10: Relaxed potential energy scans of the dihedral angle indicated above it, calculated at the dispersion corrected DFT B3LYP-GD3BJ/Def2TZVP level of theory. (a) The C2-C3 dihedral of 3-pentenitrile, (b) the C3-C4 dihedral of 4-PN holding C2-C3 in its trans configuration (*xt*), and (c) the C2-C3 dihedral of 4-PN with C3-C4 held as syn (*sx*). The flexible dihedral angle was rotated in 10° steps. The scan along *sx* includes only dihedral angles from 60 to 300 degrees because the barrier to *sg+* ↔ *sg-* isomerization is too high due to steric constraints.

Figure 4.10 (a) shows the relaxed PE curve for 3-PN, stepping along the C2-C3 dihedral, starting from the optimized *syn* geometry. 3-PN has three energy minima, one at the *syn* geometry (defined as 0°), and a degenerate pair of *eclipsed* minima with C2-C3 dihedrals of ±120°. The energetic preference of *syn* over *eclipsed* is born out in our experiment. Not only are the microwave transitions due to the *syn* conformer several times greater than those for the *eclipsed* conformer, but cooling in Ar increases this ratio still further (to near 10, see **Figure 4.6**), confirming that *syn* is lower in energy than *eclipsed*. This is in keeping with the deduction of Durig and co-workers based on their vibrational spectroscopy in liquid Xe, a non-polar solvent not anticipated to change the gas phase preferences significantly.⁸ They determined a ΔH_{s-e}° (298.15 K) for the *syn*→*eclipsed* isomerization of +2.45 kJ/mol, a value very close to the value predicted by the calculations presented here (ΔH_{s-e}° (298.15 K) = +2.34 kJ/mol).

Note that, due to the presence of two *eclipsed* minima (i.e., a degeneracy of 2), $\Delta G_{s-e}(298.15\text{ K}) = 1.66\text{ kJ/mol}$, predicting equal populations (i.e., [eclipsed]/[syn] = 50/50) at room temperature. This is to be compared with the 18(10):82(10) population ratio of [eclipsed]/[syn] derived from the Boltzmann plots (**Figure 4.11**). This implies that a fraction of the population initially in the *eclipsed* conformational well undergoes collisional cooling over the torsional barrier into the *syn* well during the expansion. The calculated average internal energy of *eclipsed* 3-PN at room temperature is 890 cm^{-1} , while the barrier height for *eclipsed*→*syn* isomerization is 650 cm^{-1} (**Figure 4.10 (a)**), indicating that collision-induced cooling from *eclipsed* to *syn* is energetically feasible. Note that, by comparison, there is no evidence for microwave transitions due to vibrational hot bands of either conformer, consistent with efficient collisional cooling of vibrational energy within a given well.

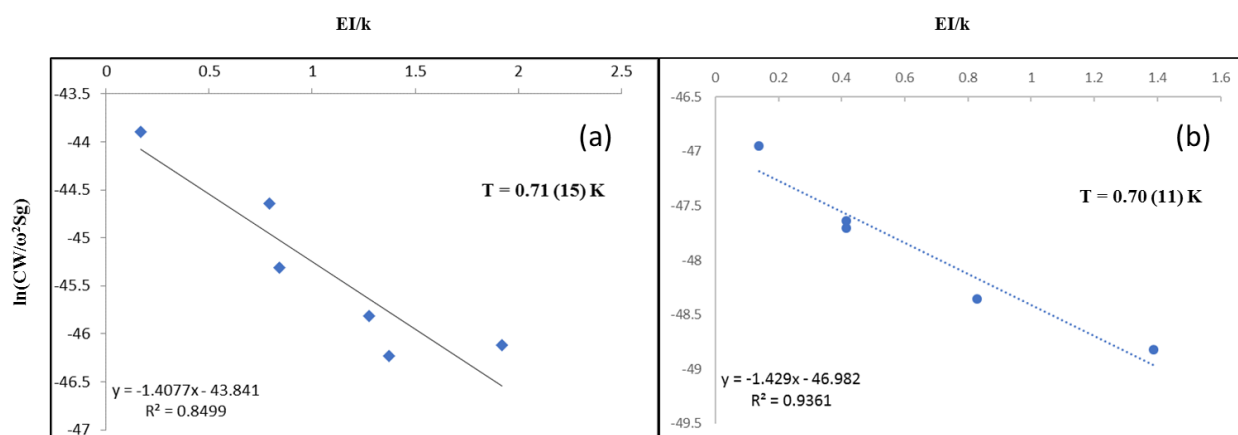


Figure 4.11: The Boltzmann plot for (a) *syn* and (b) *eclipsed* 3-pentenenitrile. The rotational temperature calculated using the equation: $W = \frac{4\pi^2\omega_0^2 S \mu_i^2 g_l g_t \epsilon N_{tot}}{c\sqrt{\alpha} k T Q_{rot}} e^{\frac{-E_l}{kT_{rot}}}$, are shown in the respective plots. The errors on the rotational temperatures were derived from the best-fit plot based on the scatter in the intensities within the set of transitions rather than based on errors from multiple measurements of each rotational transition.

Arguments based on hyperconjugation can be used to rationalize the energetic preference of *syn* over *eclipsed* in 3-PN. Note, first, that the preferred orientation for the methyl group on one side of the double bond, and the CH₂CN group on the other side, is the same. One C-H/C-C bond lies in plane pointing towards the double bond (**Figure 4.2 (a)**), while the other two are above and below the plane. Invoking hyperconjugation, this orientational preference involves partial overlap

of the two filled σ bonding orbitals on the out-of-plane C-H/C-C(N) bonds with the unfilled π^* orbital of the vinyl group.²⁷ The single in-plane C-H/C-C(N) bond has zero overlap with the π^* orbital of the double bond, and thus does not contribute to the stabilization. The *syn* and *eclipsed* conformers differ in the number of out-of-plane C-H and C-C(N) bonds in the CH₂CN group, with *syn* having two out-of-plane C-H bonds, and *eclipsed* one C-H and one C-C(N) bond. But the nitrile group is a strongly electron-withdrawing group, decreasing the electron density in the C-C(N) σ bond, and therefore decreasing its hyperconjugation and stabilization relative to that of a C-H bond. As a result, the *syn* structure is lower in energy than *eclipsed*, as observed and calculated.

The methyl torsional barrier height in 3-PN is also typical of that associated with a C(sp³)-C(sp²) bond. For instance, we have determined a methyl torsional barrier height for *syn* 3-PN of $V_3 = 553 \text{ cm}^{-1}$ (6.61 kJ/mol), a value captured to within 10% by the DFT calculations (**Table 4.7**, $V_3=609 \text{ cm}^{-1} = 7.28 \text{ kJ/mol}$). Previous studies on prototypical molecules like 3-PN, such as acetaldehyde²⁸ and propene²⁹ in which a methyl group is attached to a non-aromatic *sp*² hybridized carbon, have deduced barrier heights for methyl internal rotation of 408 cm^{-1} and $684\text{-}694 \text{ cm}^{-1}$ respectively.

In 4-PN, the two torsionally flexible C-C bonds are adjacent to one another, producing a 2D surface with nine minima, five of which are unique. In our experiment, we have observed all five of these minima, with the most intense transitions (**Figure 4.8**) assigned to the *et* and *eg+* conformers (green and purple), in keeping with their prediction as the two lowest energy conformers. The *eg-* conformer (brown), calculated to be 104 cm^{-1} higher in energy, has transitions that are third most intense, while the two *syn* conformers (blue and red) that are calculated as highest in energy, have strongest transitions less than 10% of the most intense bands in the spectrum.

Interestingly, in 4-PN, it is the *eclipsed* conformations *eg+*, *et*, and *eg-*, that are more stable than their *st* and *sg-/sg+* counterparts (**Table 4.1**) by about $100\text{-}150 \text{ cm}^{-1}$ (1.2-1.8 kJ/mol). This reversal in conformational preference about the C(sp²)-C(sp³) bond is a simple consequence of the fact that the nitrile group is moved one bond further away from the vinyl group; hence, hyperconjugation between the C(sp²) and C(sp³) carbons is to a CH₂-CH₂ bond rather than CH₂-CN. The electron withdrawing properties of the nitrile group are thus mitigated, and the normal circumstance in which an alkyl group C-C bond undergoes stronger hyperconjugation when out-of-plane than C-H bonds holds. As a result, conformations in which that bond is out-of-plane are

preferred, as they are in the *eclipsed* conformers. The experimental rotational temperatures of 4-PN conformers are around 1K (**Figure 4.12**) with population distribution of $eg+ : et : eg- : st = 10 : 7 : 7 : 1$. The $sg-$ conformer has a population smaller than the other four conformers, but could not be quantified.

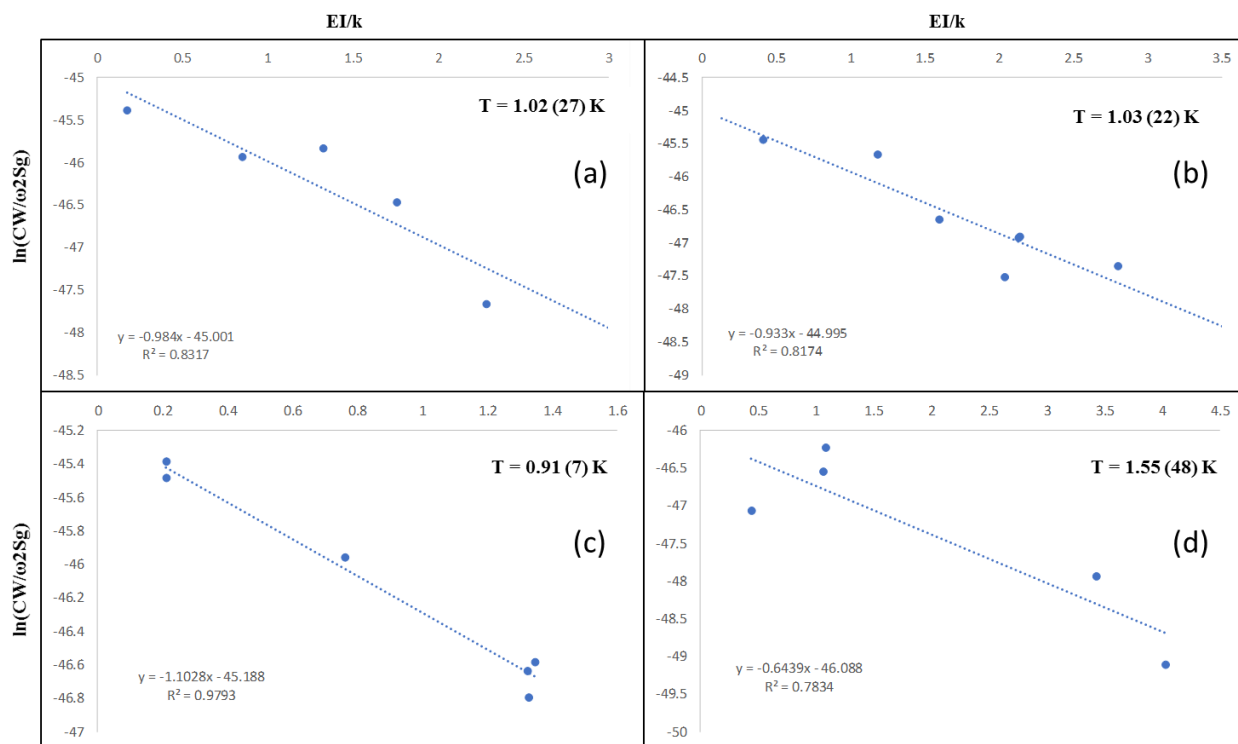


Figure 4.12: The Boltzmann plot for (a) $eg+$, (b) et , (c) $eg-$ and (d) $sg-$ 4-pentenitrile. The rotational temperature calculated using the equation: $W = \frac{4\pi^2 \omega_0^2 S \mu_i^2 g_l g_l \epsilon N_{tot}}{c \sqrt{\alpha} k T Q_{rot}} e^{\frac{-E_l}{kT_{rot}}}$, are shown in the respective plots. The errors on the rotational temperatures were derived from the best-fit plot based on the scatter in the intensities within the set of transitions rather than based on errors from multiple measurements of each rotational transition.

Relaxed PES scans of 4-PN were carried out for torsional motion about the C3-C4 (**Figure 4.10 (b)**) and C2-C3 dihedrals (**Figure 4.10 (c)**). In the relaxed PES scan along C2-C3 (sx), only angles between 60° and 300° were included because the barrier between the $sg+$ and $sg-$ minima was too high due to steric overlap between vinyl and nitrile groups. The PES scans for $xg+$ and ex of 4-PN were also carried out where the corresponding scan for xt and sx were nearly equivalent.

The barrier heights for *syn* ↔ *eclipsed* isomerization along C3(sp³)-C4(sp²) are 8-10 kJ mol⁻¹, very similar to the corresponding barrier in 3-PN. By contrast, *gauche* ↔ *trans* isomerization about

the C2(sp³)-C3(sp³) dihedral has barriers about twice the size (~17 kJ mol⁻¹, **Figure 4.10 (c)**), consistent with a typical torsional barrier in an alkane.³⁰ We surmise on this basis that isomerization during cooling between *gauche* and *trans* will be quite inefficient, while modest conformational redistribution could occur. A comparison of the relative populations derived experimentally from the rotational Boltzmann plots (**Figure 4.12**) with the conformers' relative energies show a good qualitative match-up, consistent with small collisional redistribution with helium as buffer gas.

Finally, in the close analog 4-isocyano-1-butene (H₂C=CHCH₂CH₂NC), which is isoelectronic and isostructural to 4-PN, Samdel *et. al.* found the same three most-abundant conformers as in 4-PN: *et*, *eg+*, and *st* conformers.³¹ However, they did not observe the *eg-* and *sg-* conformers, suggesting some differences in the conformational landscape associated with the change of isonitrile for nitrile.

4.5 Conclusion

Broadband CP-FTMW spectra of 3-PN and 4-PN have been recorded under jet-cooled conditions ($T_{\text{rot}} \sim 1$ K) over the 8-18 GHz range. 3-PN has a simple conformational landscape with just two conformers, but with the possibility for methyl rotor splittings. Microwave transitions due to both conformers (*syn* and *eclipsed*) have been assigned, including the challenging problem of sorting out methyl rotor/nuclear quadrupole splittings when they are similar in magnitude and just larger than the experimental resolution. 4-PN has five conformers located on a two-dimensional torsional surface with barriers of about 10 kJ/mol for hindered rotation about the C(sp²)-C(sp³) and 17 kJ/mol about the C(sp³)-C(sp³) axes. All five conformers were observed experimentally, with relative intensities that in large measure follow the relative energies predicted by calculation. The relative stabilities of the 3-PN and 4-PN structural isomers and the preference of *syn* over *eclipsed* in 3-PN can both be understood in terms of hyperconjugation. Here, the terminal nitrile group has a relatively minor effect on the relative energies of the structural isomers, but a major effect on the conformational preferences within a molecule.

It is hoped that the present data can provide a foundation for future astronomical searches for these molecules. Of the molecules detected to date in space,^{1,2} very few have yet had conformational flexibility to them, with n-propyl cyanide and ethyl formate as two notable

exceptions.³² So far, only the lowest energy conformers of the latter two molecules have been detected; however, molecule-forming regions in space have temperatures that may lead to the detection of multiple conformers, and even provide information from their column densities on the mechanisms by which they are formed, and the extent to which thermal equilibrium is maintained.

4.6 References

- ¹ B. A. McGuire, *Astrophys. J., Suppl. Ser.*, **239**, 17 (2018).
- ² B. A. McGuire, A. M. Burkhardt, S. Kalenskii, C. N. Shingledecker, A. J. Remijan, E. Herbst and M. C. McCarthy, *Science*, **359**, 202 (2018).
- ³ F. Raulin, C. Brasse', O. Poch and P. Coll, *Chem. Soc. Rev.* **41**, 5380 (2012).
- ⁴ M. Morisson, C. Szopa, N. Carrasco, A. Buch and T. Gaurier, *Icarus*, **277**, 442 (2016); M. McGuigan, J. H. Waite, H. Imanaka and R. D. Sacks, *J. Chromatogr. A*, **1132**, 280 (2006).
- ⁵ N. Kitadai and S. Maruyama, *Geosci. Front.*, 2018, 9, 1117.
- ⁶ W. O. George, P. K. Hirani, E. N. Lewis, W. F. Maddams and D. A. Williams, *J. Mol. Struct.*, **141**, 227 (1986).
- ⁷ M. Podzimkova', M. Procha'zka and M. Palec'ek, *Collect. Czech. Chem. Commun.*, **34**, 2101 (1969); M. Podzimkova' and M. Procha'zka, *Collect. Czech. Chem. Commun.*, **35**, 1708 (1970).
- ⁸ J. R. Durig, T. K. Gounev, H. Zhen, A. Drew, S. Shen and G. A. Guirgis, *J. Mol. Struct.* **553**, 221 (2000).
- ⁹ A. O. Hernandez-Castillo, C. Abeysekera, B. M. Hays and T. S. Zwier, *J. Chem. Phys.* **145**, 114203 (2016); S. M. Fritz, A. O. Hernandez-Castillo, C. Abeysekera, B. M. Hays and T. S. Zwier, *J. Mol. Spectrosc.* **349**, 10, (2018).
- ¹⁰ S. M. Fritz, B. M. Hays, A. O. Hernandez-Castillo, C. Abeysekera and T. S. Zwier, *Rev. Sci. Instrum.* **89**, 093101 (2018).
- ¹¹ D. Schmitz, V. A. Shubert, T. Betz and M. Schnell, *J. Mol. Spectrosc.* **280**, 77 (2012).
- ¹² M. Pickett, *J. Mol. Spectrosc.* **148**, 371 (1991).
- ¹³ H. Hartwig and H. Dreizler, *Z. Naturforsch.* **51a**, 923 (1996).
- ¹⁴ PROSPE website: <http://www.ifpan.edu.pl/Bkisiel/prospe.htm>.
- ¹⁵ D. J. Frisch, M. J. Trucks, G. W. Schlegel, H. B. Scuseria, G. E. Robb, M. A. Cheeseman, J. R. Scalmani, G. Barone, V. Mennucci, B. Petersson, G. A. Nakatsuji, H. Caricato, M. Li, X. Hratchian, H. P. Izmaylov, A. F. Bloino, J. Zheng and G. Sonnenb, *GAUSSIAN 09, Revision E.01*, Gaussian, Inc., Wallingford CT (2009).
- ¹⁶ P. Mishra, D. M. Hewett and T. S. Zwier, *J. Chem. Phys.* **148**, 184304 (2018).
- ¹⁷ D. M. Hewett, S. Bocklitz, D. P. Tabor, E. L. Sibert III, M. A. Suhm and T. S. Zwier, *Chem. Sci.* **8**, 5305 (2017).
- ¹⁸ G. P. Moss, *Pure Appl. Chem.*, **68**, 2193 (1996).

- ¹⁹ F. Mohamadi, N. G. J. Richards, W. C. Guida, R. Liskamp, M. Lipton, C. Caufield, G. Chang, T. Hendrickson and W. C. Still, *J. Comput. Chem.*, **11**, 440 (1990).
- ²⁰ C. Peng and H. B. Schlegel, *Isr. J. Chem.*, **33**, 449 (1993).
- ²¹ J. M. Oldham, C. Abeysekera, B. Joalland, L. N. Zack, K. Prozument, I. R. Sims, G. B. Park, R. W. Field and A. G. Suits, *J. Chem. Phys.*, **141**, 154202 (2014); C. H. Townes and A. L. Schawlow, *Microwave Spectroscopy*, Dover Publications, New York (1955).
- ²² K. M. Hotopp, V. V. Vara and B. C. Dian, *J. Mol. Spectrosc.* **280**, 104 (2012).
- ²³ P. J. Mjoberg, W. M. Ralowski and S. O. Ljunggren, *Z. Naturforsch., A: Phys. Sci.* **30**, 1279 (1975).
- ²⁴ W. Jaeger and H. Maeder, *Z. Naturforsch., A: Phys. Sci.*, 1987, 42a, 1405; J.-U. Grabow, H. Hartwig, N. Keineking, W. Jaeger, H. Maeder, H. W. Nicolaisen and W. Stahl, *J. Mol. Struct.* **612**, 349 (2002).
- ²⁵ A. Amirav, U. Even and J. Jortner, *Chem. Phys.* **51**, 31 (1980).
- ²⁶ B. Ruscic and D. H. Bross, *Active Thermochemical Tables (ATcT) values based on ver. 1.122e of the Thermochemical Network*, Argonne National Laboratory, 2019, available at ATcT.anl.gov.
- ²⁷ L. G. Wade, *Organic Chemistry*, Pearson, New Jersey, 4th edn. (1999).
- ²⁸ I. A. Smirnov, E. A. Alekseev, V. V. Ilyushin, L. Margule's, R. A. Motiyenko and B. J. Drouin, *J. Mol. Spectrosc.* **295**, 44 (2014).
- ²⁹ J. R. Durig and G. A. Guirgis, *J. Phys. Chem.* **93**, 3489 (1989); G. Wlodarczak, J. Demaison, N. Heineking and A. G. Csa'sza'r, *J. Mol. Spectrosc.* **167**, 239 (1994); E. Hirota, *J. Chem. Phys.* **45**, 1984 (1966).
- ³⁰ R. G. Ford, *J. Mol. Spectrosc.*, **49**, 117 (1974); A. E. Reed and F. Weinhold, *Isr. J. Chem.*, **31**, 277 (1991).
- ³¹ S. Samdal, T. Gronas, H. Mollendal and J.-C. Guillemin, *J. Phys. Chem. A* **118**, 1413 (2014).
- ³² A. Belloche, R. T. Garrod, H. S. P. Mu'ller, K. M. Menten, C. Comito and P. Schilke, *Astron. Astrophys.* **499**, 215 (2009).

CHAPTER 5. INTERDEPENDENCE BETWEEN THE ALKYL CHAIN AND π H-BOND IN PROPYLBENZENE(WATER)_N, N=2-4 CLUSTERS

5.1 Introduction

Hydrogen bonding is extremely important and fundamental to a very large number of processes. It is responsible for the formation of DNA double helical structure, protein folding, many unique properties of water, which is crucial for the existence of life, just to name a few.^{1,2} A very powerful probe of hydrogen bonding ($Y \cdots HX$) is its effect on the HX vibrational frequency. Upon hydrogen bonding, a blue-shift is observed for the bending mode whereas the stretching mode typically experiences a red-shift, which is more sensitive.² Benzene(Bz)-water clusters possess prototypical π H-bonds, and have received a lot of attention.³⁻⁶ An important conclusion from all these studies is that for the smallest complex Bz(H₂O), large amplitude motion (LAM) is observed, indicating tumbling of water molecule at the zero-point energy (ZPE) level. This is partially quenched for Bz(H₂O)₂, whereas, for all the larger clusters which have more hydrogen bound water framework, there is no evidence for LAM at the ZPE level. As the size of the water cluster increases, the number of bound OH bonds increases with respect to the number of free OH bonds. As was reported by Pribble *et. al.*,^{4,5} the OH stretch is particularly sensitive to the number, strength and type of the hydrogen bonds in such clusters.

Alkylbenzenes are common components of diesel and petroleum-based gasoline.⁷ Detailed studies on propyl and butylbenzene by Curran and co-workers suggest combustion chemistry characteristic of both alkanes and aromatics occurs.⁷ The flexible torsional dihedrals along the alkyl chain increase the conformational complexity when compared with benzene. The low frequency vibrational modes give rise to a rapid increase in density of states that is reflected experimentally in the form of intramolecular vibrational redistribution (IVR), as was probed in detail in the seminal work of Smalley and co-workers.⁸ Conformer-specific IR spectroscopy of ethyl, propyl and butylbenzene in the CH stretch region have been carried out previously in collaboration with Dr. Sibert.⁹

Combustion is a process that takes place in ambient atmosphere in the gas-phase, where water vapor is present beforehand and produced by combustion itself. Post-combustion, when the unreacted molecules are present as aerosols in the atmosphere, they interact with water vapor.

Despite aromatic hydrocarbons being immiscible with water as a solvent, it is interesting that such compounds are bound to water in the gas phase. Understanding the interaction between key fuel components like short-chain alkylbenzenes and solvent such as water, is thus relevant to atmospheric chemistry. The interaction chosen in the present work is the interaction of water with propylbenzene (pBz), where pBz has one flexible dihedral with an sp^2 carbon (θ) and another that is typical of alkyl chain dihedrals connecting two sp^3 carbons (**Figure 5.1**).¹⁰ The chain length in pBz is just long enough that a CH bond can point towards the π aromatic ring and offer two types of dihedrals, but not too long to increase the complexity of the conformational PES when it interacts with the water framework.

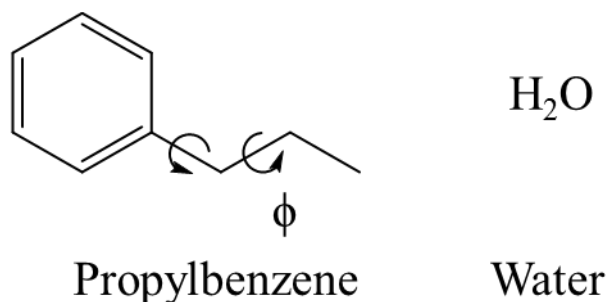


Figure 5.1: Monomer precursors Propylbenzene and water. The flexible dihedral angles with their labels are shown.

As mentioned before, the present study can be seen as an extension of two fundamental pieces of work: (1) π H-bonding in prototypical system of benzene-water clusters, and (2) conformational preferences in short-chain alkylbenzenes. The investigation of pBz-water clusters is aimed at understanding the effect of the presence of the water cluster on the conformational preferences of pBz, and alternatively, the effect of a short alkyl chain on the water cluster. The latter is expected to be a minor perturbation as the interaction of alkyl CH groups with water is much weaker than the hydrogen bonds between the water molecules that make up the water cluster. Experimental studies on gas-phase clusters provides insight to the best solvation mechanisms when the number of solvent molecules is small. Such studies are thus very important as a means to benchmark theoretical modeling, where the clusters studied in the present work are tailor made to be modeled by local mode Hamiltonians.

The potential energy landscape of $\text{pBz}(\text{H}_2\text{O})_n$ clusters is a lot more complex than $\text{Bz}(\text{H}_2\text{O})_n$ clusters, both as a result of the lower symmetry of pBz conformers and the orientation of the propyl chain with respect to the water framework. Broadly speaking, there are four types of $\text{pBz}(\text{H}_2\text{O})_n$ clusters as opposed to one for $\text{Bz}(\text{H}_2\text{O})_n$. We seek to determine (1) whether the chain is on the same side of the aromatic ring as the water cluster or on opposite sides, and (2) the conformation along the propyl chain. The nomenclature is described in the ‘Methods’ section. Despite there being only four classes of structures, the total number of geometric minima is expected to be a lot more due to the propyl chain breaking the D_{6h} symmetry of the benzene ring. These symmetry-based arguments are explained in the results section.

The ideal starting place for the study of propylbenzene-water interactions would be the smallest possible complex, $\text{pBz-H}_2\text{O}$. Yet, despite repeated attempts over a wide range of experimental parameters, we did not experimentally observe this complex. The rationale for this is discussed later. We did, however, observe several larger $(\text{pBz})_m(\text{H}_2\text{O})_n$ clusters and spectroscopically characterized $\text{pBz}(\text{H}_2\text{O})_n$, $n=2-4$ clusters. Henceforth, $\text{pBz}(\text{H}_2\text{O})_n$ refers to those clusters with $n=2-4$. Alternatively, we also use the value of n as a shorthand for a specific sized cluster, for example the ‘ $n=2$ cluster’ or ‘ $1:2$ cluster’ refers to $\text{pBz}(\text{H}_2\text{O})_2$. A combination of complex-specific spectroscopy and *ab initio* calculations were used to study these $\text{pBz}(\text{H}_2\text{O})_n$ clusters. Experimental and spectroscopic similarities are observed between $\text{Bz}(\text{H}_2\text{O})_n$ and $\text{pBz}(\text{H}_2\text{O})_n$ clusters of the same size ‘ n ’, aiding analysis.

5.2 Experimental and Theoretical Methods

Due to the staggering number of stable geometries, the MACROMODEL suite of programs¹¹ was used, following which, the input geometries were subjected to density functional theory (DFT) calculations at the B3LYP/Def2TZVP level of theory, using the GAUSSIAN09 suite of programs¹². 42 starting geometries were obtained for the $n=2$ cluster, whereas for $n=3$ and 4, there were over 100 structures of each. As a result, we limited ourselves to those with low energy geometries obtained via DFT calculations. Obtaining optimized geometries with no imaginary frequency was a challenge, especially for the $n=2$ cluster, as the water molecules moved in very soft potentials on the aromatic ring. ZPE-corrected and basis set superposition error (BSSE)-corrected energies were calculated and the low low energy structures were considered in detail until a relatively large

energy gap was encountered. The specific number of structures and energetic information is in the results section.

The clusters under consideration are weakly bound, and the π H-bond that is favored in the neutral cluster will rearrange its adiabatic geometry when the aromatic species is ionized. As a result, fragmentation upon photoionization occurs with high efficiency by loss of one or more H₂O molecules, as was seen for Bz(H₂O)_n clusters.⁵ For pBz(H₂O)_n, n=2-4, the ionized clusters lose one H₂O molecule, hence they show up in a mass channel 18 m/z units lower than the neutral cluster size from which they originate. RIDIRS, which is an especially powerful technique to study these clusters, is utilized to ensure which neutral carrier is responsible for a given peak in the R2PI spectrum in a given mass channel. R2PI spectra of pBz and pBz(H₂O)_n, n=2-4 clusters are recorded in the molecular beam TOF spectrometer. The spectrum of pBz(H₂O)_n shows up in pBz(H₂O)_{n-1} or pBz(H₂O)_{n-2}. In our experiments we observed the n=2 cluster showing up in the n=1 (m/z=138) mass channel, otherwise referred to as the [1:1]⁺ mass channel. The n=3 cluster showing up in the [1:1]⁺ and [1:2]⁺ (m/z=156) mass channels, and the n=4 cluster showing up in the [1:3]⁺ (m/z=174) mass channel. After obtaining the cluster-specific UV and IR spectra, comparisons were made with calculated vibrational frequencies and IR intensities. The rotational band contour of the S₀-S₁ origin of the n=2 clusters were also scanned, obtaining partially resolved P and R branches, which were not very informative.

The pBz(H₂O)_n clusters can be classified based on (1) the propyl chain conformation (ϕ), and (2) whether the water cluster is on the same side as the chain or on the opposite side. When the ϕ dihedral takes values around 180°, it is labeled *trans* (t), while a value near ±60° is *gauche* (g). When the propyl chain is on the same side of the aromatic ring as the water framework, we label it as (*Syn* or S) and when on opposite sides, (*Anti* or A). This implies that there are broadly four classes of clusters for pBz(H₂O)_n, n=2-4: ‘At’, ‘Ag’, ‘St’ and ‘Sg’. The n=3, 4 clusters have a water framework that is cyclic with one π H-bond. This framework can have either clockwise or anti-clockwise O-H cycles. However, spectroscopically, these types of structures are either mirror images or have very minor differences. This structural aspect is disregarded as we are primarily interested in the nature of the H-bonding and the propyl chain configuration.

The pBz(H₂O)_n clusters are floppy, with the n=2 cluster having several shallow minima. This is to be expected, as the individual H₂O molecules are not tightly held in a particular configuration. Moreover, the water dimer has several shallow orientational minima on the aromatic π cloud.

Calculations and spectral predictions were also performed at M062X/6-311++G(2d,p) for the $n=2$ cluster to be certain of the assignments. In case of $n=3$ and 4 clusters, with their H-bonded water cycles, the individual H_2O molecules are more tightly held together; however, the water clusters still interact with the phenyl ring on shallow minima over the aromatic π cloud. Despite obtaining a large number of cluster minima computationally, we observe only a few experimentally. Previous studies on $\text{Bz}(\text{H}_2\text{O})_n$ clusters suggest that the most stable cluster configuration can be formed in the supersonic expansion via two-body displacement collisions. The results are presented starting from $\text{pBz}(\text{H}_2\text{O})_2$ through $\text{pBz}(\text{H}_2\text{O})_3$ and $\text{pBz}(\text{H}_2\text{O})_4$; although with extensive analysis involving several theoretical structures, we went back and forth between the analysis of $n=2, 3$, and 4 clusters to make consistent assignments. Comparing the $\text{pBz}(\text{H}_2\text{O})_n$ cluster with its close analog $\text{Bz}(\text{H}_2\text{O})_n$ has been an integral part of our analysis.

5.3 Results

R2PI spectra of pBz and $\text{pBz}(\text{H}_2\text{O})_n$, $n=2-4$ clusters in the S_0-S_1 origin region are shown in **Figure 5.2**. R2PI of the pBz monomer is shown in blue for the comparison of electronic shifts. The *gauche* and *trans* conformers of pBz are labeled. The R2PI spectra of the $\text{pBz}(\text{H}_2\text{O})_n$, $n=2-4$ clusters are shown with color-coded labels. The corresponding mass channels used for recording the scans are given in brackets. Recall that neutral clusters undergo fragmentation by loss of one or two H_2O molecules upon photoionization. Dotted lines between the traces connect the peaks belonging to the same cluster fragmenting into multiple mass channels. RIDIR spectra were carried out on all the peaks marked with asterisks.

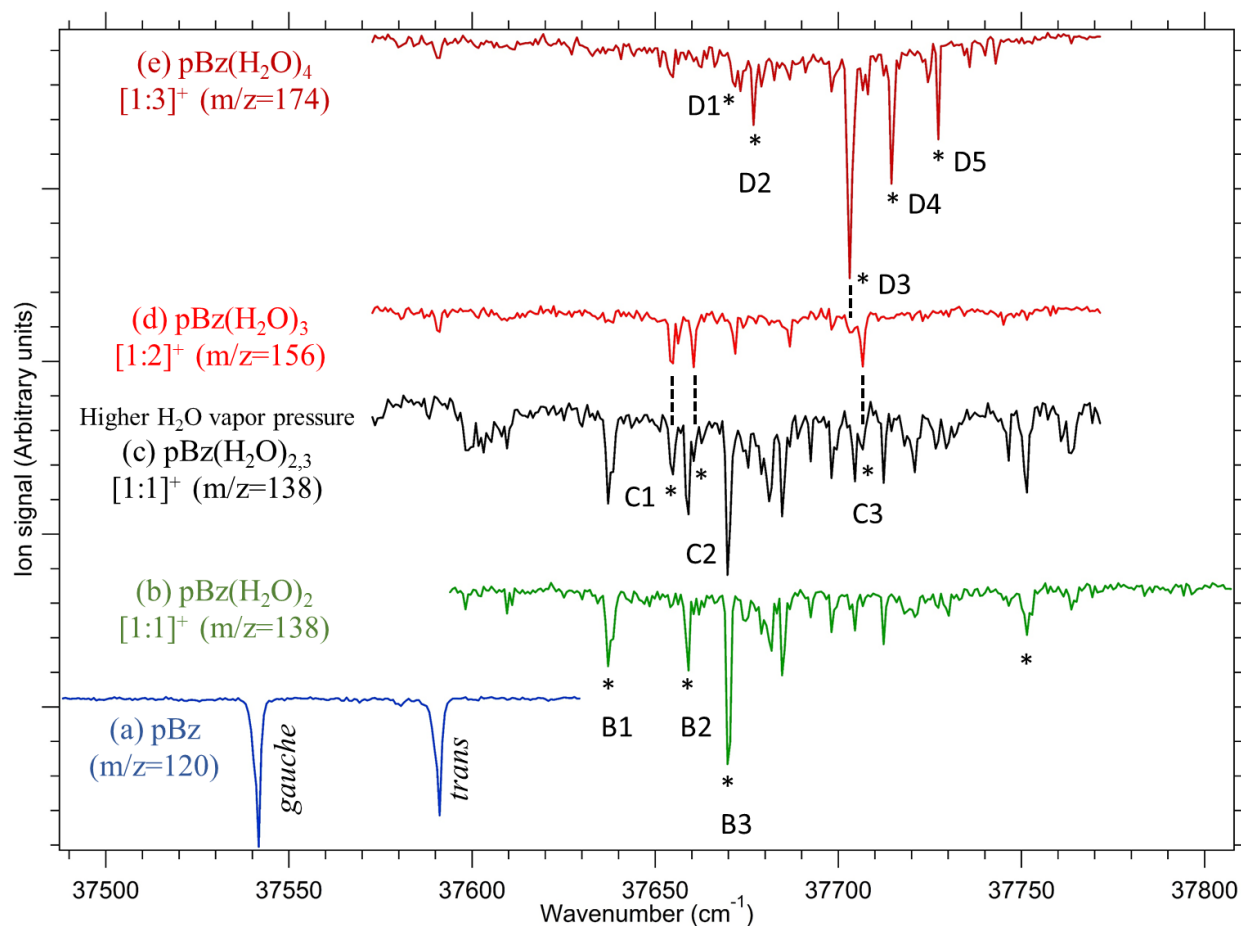


Figure 5.2: R2PI spectra of (a) pBz and (b-e) pBz(H₂O)_n clusters. The mass channels where the spectra was recorded is written in brackets. R2PI spectra of the pBz(H₂O)₂ is shown in (b). With higher water vapor pressure, pBz(H₂O)₃ also shows up in (c) and (d), and pBz(H₂O)₄ shows up in (e). Cluster-specific spectroscopy is performed on the peaks marked with asterisk.

5.3.1 Propylbenzene(H₂O)₂

42 total structures for the n=2 cluster were discovered by force field calculations using Merck Molecular Force Field static (MMFFs). All 42 were subject to geometry optimization using dispersion corrected DFT (B3LYP-GD3BJ/Def2TZVP) calculations. 28 structures were within 6 kJ/mol of the most stable cluster, followed by an energy gap of 4 kJ/mol before the next structure. Of these 28, 15 were unique, while the others were related by symmetry to others in the list. Among the 15 structures, there were 3 ‘St’, 6 ‘Sg’, 2 ‘At’ and 4 ‘Ag’ clusters. These structures and their relative energies, corrected for BSSE and ZPE effects, are collected in **Table 5.1**. The clusters are labeled based on the nomenclature, with numeric labeling according to the order of their relative energy. For example, ‘St(3)’ means an ‘St’ cluster that has third lowest BSSE-corrected energy.

Structures of Bz(H₂O)₂ and a select subset of pBz-(H₂O)₂ clusters that are later assigned are shown in **Figure 5.3**. Given the several possible calculated low energy structures, IR-UVHB, RIDIRS in the OH stretch region and in the CH stretch region were analyzed independent of each other, to see if the complementary information deduced from them was consistent. Furthermore, to corroborate initial assignments made by comparing with B3LYP-GD3BJ/Def2TZVP calculations, we checked these against a similar analysis using DFT M06-2X/6-311++G(2d,p). Many of the low energy structures were common to both these levels of theory.

Table 5.1: BSSE-corrected and ZPE-corrected energies of pBz(H₂O)₂ clusters carried out at B3LYP-GD3BJ/Def2TZVP level of theory. All energies are relative to the most stable structures within their respective column.

Cluster label	BSSE-corrected energy	ZPE-corrected energy
Sg(1)	0	0.51
St(1)	0.28	0
Ag(1)	0.81	1.12
At(1)	1.33	1.18
Ag(2)	2.18	2.60
Sg(2)	2.23	1.875
Sg(3)	3.12	3.13
Sg(4)	3.36	2.91
St(2)	3.53	2.58
Sg(5)	4.62	3.79
St(3)	5.06	3.26
Sg(6)	5.09	4.7
Ag(3)	5.34	5.7
Ag(4)	5.40	5.76
At(2)	5.50	5.29

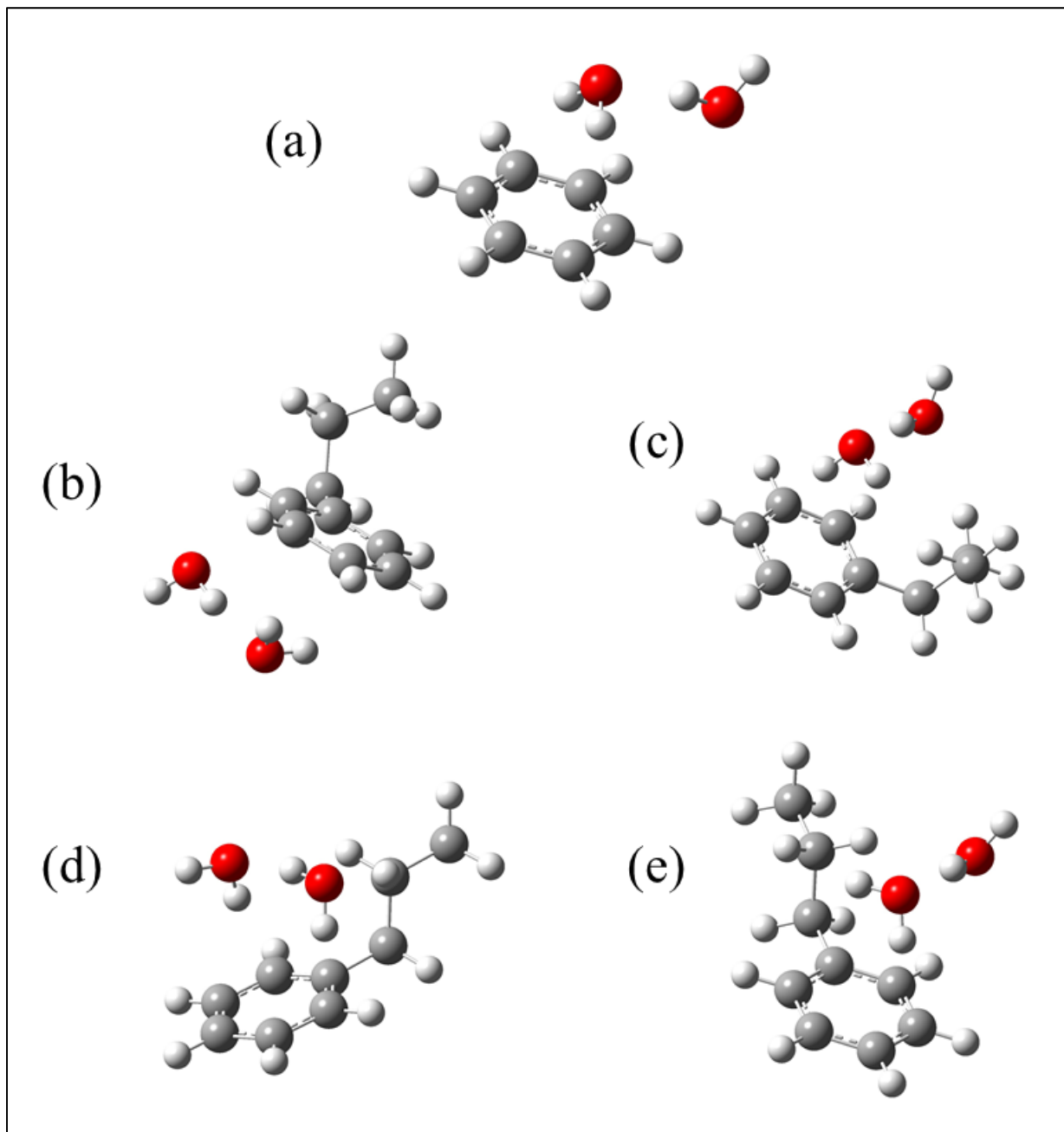


Figure 5.3: Structures of $Bz(H_2O)_2$ and $pBz(H_2O)_2$ clusters along with their labels. (a) $Bz(H_2O)_2$, (b) 'Ag(1)', (c) 'Sg(1)', (d) The double π H-bonded 'St(3)', and (e) 'St(1)'

R2PI spectra recorded in the $[1:1]^+$ mass channel had several peaks, many with FC progressions built off them. RIDIR spectra in the OH stretch region ($3500\text{-}3750\text{ cm}^{-1}$) were recorded for the peaks marked with an asterisk in **Figure 5.2 (b)**. These spectra played an important role in confirming that all transitions in this mass channel belonged to $\text{pBz}(\text{H}_2\text{O})_2$. On the broadened R2PI transition just below 37640 cm^{-1} , RIDIR spectra were recorded both at 37638.56 and 37637.14 cm^{-1} . These spectra and those recorded with UV laser fixed at 37659.11 cm^{-1} and 37670.46 cm^{-1} are all shown in **Figure 5.4**. Three unique IR spectra in the OH stretch region were obtained, implying that there are at least 3 unique clusters of $n=2$ formed. IR-UV HB spectra were recorded at the following IR frequencies: 3591.55 , 3598.00 , 3600.05 , 3705.4 , 3714.98 and 3718.85 cm^{-1} which showed 3 unique UV spectra shown in **Figure 5.5 (a-c)**. The origin (0^0_0) transitions are marked with a pound sign and these spectra corresponding to unique clusters are called B1, B2 and B3 starting from the lowest to highest 0^0_0 frequencies, which are 37609.5 cm^{-1} , 37659.1 cm^{-1} and 37670.5 cm^{-1} respectively. The three IR-UV HB spectra were co-added, resulting in a spectrum virtually indistinguishable from the R2PI scan of **Figure 5.2 (b)**. This confirmed that all the peaks seen in the UV excitation spectrum are from the 1:2 cluster (**Figure 5.5 (d)**). RIDIR spectra of the same three bands were recorded in the CH stretch region ($2800\text{-}3000\text{ cm}^{-1}$), and are shown in **Figure 5.6**.

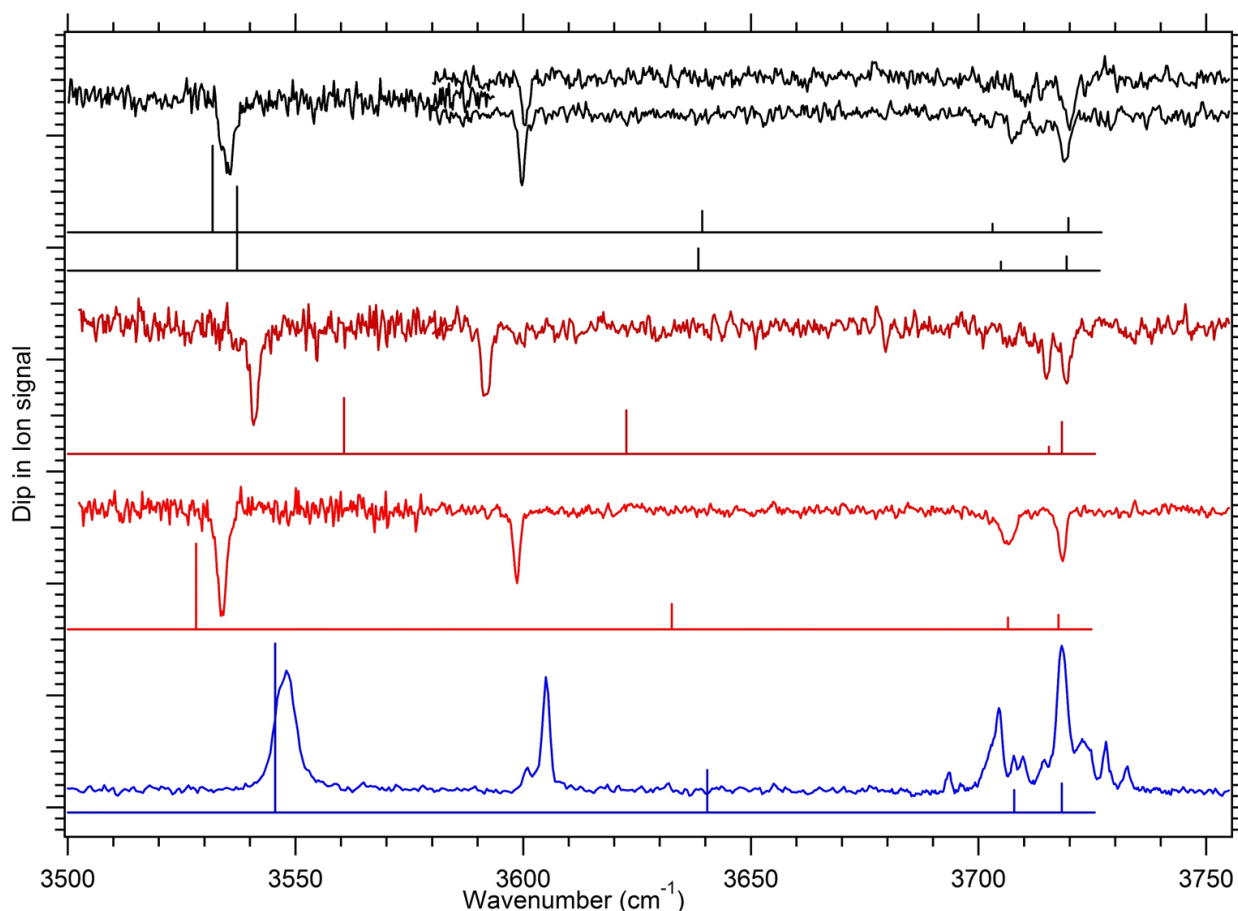


Figure 5.4: RIDIRS of $\text{Bz}(\text{H}_2\text{O})_2$ and $\text{pBz}(\text{H}_2\text{O})_2$ in the OH stretch region. B1, B2 and B3 are labelled along with their best match predictions. The UV frequencies where the RIDIRS were recorded are mentioned. The dotted line goes through the free OH stretch of all the spectra.

The IR-UV HB spectra in **Figure 5.5** provided single-conformer UV spectra of the three types of 1:2 clusters. Three aspects of these spectra can be used to test various hypotheses for the structures responsible for each spectrum: (i) the frequency shift of the electronic origin relative to that in $\text{Bz}(\text{H}_2\text{O})_2$, (ii) the amount of Franck-Condon activity, and (iii) the frequencies of these low-frequency vibrations. The electronic frequency shifts of each cluster's S_0 - S_1 0^0_0 transition from the pBz monomer origins can be used to assign the clusters to *gauche* or *trans* pBz structures. The 0^0_0 peak of $\text{Bz}(\text{H}_2\text{O})_2$ is shifted from the (forbidden) Bz monomer 0^0_0 by $+70 \text{ cm}^{-1}$.⁵ The small B1 0^0_0 (marked by a #) is shifted by $+68 \text{ cm}^{-1}$ from the *gauche* pBz 0^0_0 , whereas B2 and B3 are shifted from *trans* pBz by $+68 \text{ cm}^{-1}$ and $+79 \text{ cm}^{-1}$ respectively. A simple extrapolation implies that B1 is a *gauche* 1:2 cluster, whereas B2 and B3 are *trans* 1:2 clusters.

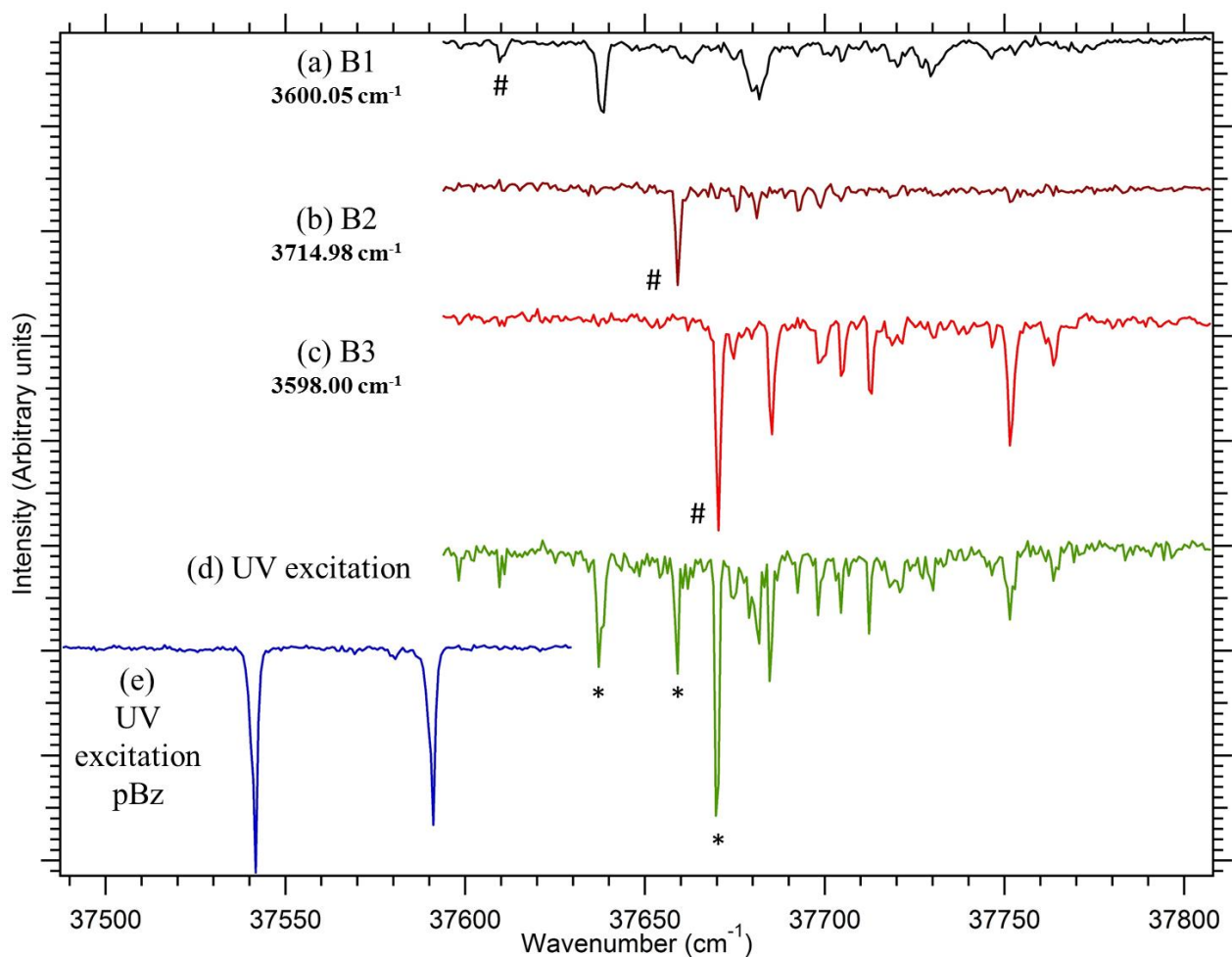


Figure 5.5: IR-UV HB of (a) B1, (b) B2, and (c) B3, UV excitation spectrum of (d) pBz(H₂O)₂, and (e) pBz. The IR frequencies where the IR-UV HB spectra were recorded are mentioned. The electronic origin for each cluster is marked with a pound. RIDIRS are recorded on the peaks marked with asterisks in the UV excitation spectrum.

Second, we hypothesize that, due to the reduced effect of the chain on the water dimer, the electronic frequency shifts of the *anti* clusters from pBz will be closer to those in Bz(H₂O)₂ relative to Bz. While these differences are small, this suggests that B1 and B3 could be *anti* structures, whereas B2 was more consistent with a *syn* structure.

The IR-UV HB spectra also revealed Franck-Condon (FC) progressions present in the pBz(H₂O)₂ clusters. Again, we hypothesized that the FC progressions would be more intense when the chain is interacting with the water cluster. On this basis, the B1 and B3 clusters would be *syn* clusters, whereas B2 is *anti*, at odds with the deductions based on electronic frequency shifts.

Finally, the low-lying frequencies were compared with the predicted frequencies of the S_1 state based on Time-Dependent DFT (TD-DFT) optimizations, carried out at the B3LYP-GD3BJ/Def2TZVP level of theory. The excitation spectra indicated the conformation of the propyl chain in the clusters, but not on whether the clusters were *syn* or *anti*. M062X/6-311++G(2d,p) calculations were also carried out that were equally unsuccessful to the assignment process.

RIDIR spectroscopy in the CH stretch region is another powerful study to characterize the *gauche* vs *trans* clusters of pBz(H₂O)₂, anticipating that the CH stretch spectra of the two pBz conformers will not be changed significantly by water complexation. Scans were recorded at the UV frequencies 37638.00, 37659.11, 37670.46, 37685.36 and 37751.52 cm⁻¹. The unique IR spectra obtained are shown in **Figure 5.6**, where they are compared with the *gauche* and *trans* conformers of pBz monomer. As expected the 2800-2950 cm⁻¹ region was affected significantly by the CH stretch-bend Fermi Resonance (FR), hence our efforts were primarily focused on the shift between the methyl stretch peaks between 2950cm⁻¹ and 2980 cm⁻¹ which is rather sensitive to the conformation of the propyl chain. Here we show four unique IR spectra in the CH stretch region where the B3' spectra is recorded at the UV peak 37751.52 cm⁻¹. Interestingly this peak was obtained in the IR-UV HB when the IR laser was fixed at two OH stretch transitions 3598.0 and 3705.4 cm⁻¹, so it was unlikely that the peak at 37751.52 cm⁻¹ is a different cluster, but the CH stretch region is different from the one recorded at 37670.46 and 37685.36 cm⁻¹.

The methyl CH stretch splitting for *gauche* pBz (8.8 cm⁻¹) is larger than *trans* pBz (7.5 cm⁻¹). For the n=2 clusters, B1 has a splitting of 7.7 cm⁻¹, B2 has 7.5 cm⁻¹, whereas for B3 and B3' with 6.0 cm⁻¹. The trend seen in the methyl CH stretch splitting of B1 and B3 confirm the 0⁰₀ shifts from IR-UV HB scans. RIDIRS in the CH stretch region of B2 has lower S/N when compared with B1 and B3 scans. Harmonic frequency calculations carried out at B3LYP-GD3BJ/Def2TZVP and M062X/6-311++G(2d,p) were used with a linear scaling function obtained by least squared fitting for the pBz conformers for the methyl stretch peaks, which were not very useful to narrow down the assignments due to anharmonic effects. The closest match calculated spectra at B3LYP-GD3BJ/Def2TZVP with a scaling function of $\text{expt}=\text{calc} \times 0.7578 + 625.9$ are shown in **Figure 5.6**. The CH stretch region of the IR spectra is not very illustrative of whether the cluster is *anti* or *syn*, only if they are *gauche* or *trans* on the propyl chain.

The OH stretch frequency shifts are very sensitive to the local environments, including their interactions with the propyl chain. RIDIRS spectroscopy in the OH stretch region was hence

very useful to assign the *syn* vs the *anti* clusters, shown in **Figure 5.4**. We see clear evidence of LAMs in the antisymmetric OH stretch region of Bz(H₂O)₂, which is partially quenched for the pBz(H₂O)₂ clusters. Despite being fundamentally interesting, we have not addressed this issue further, beyond simply noting that the presence of a short alkyl chain partially quenches the LAM of water dimer over the π aromatic ring.

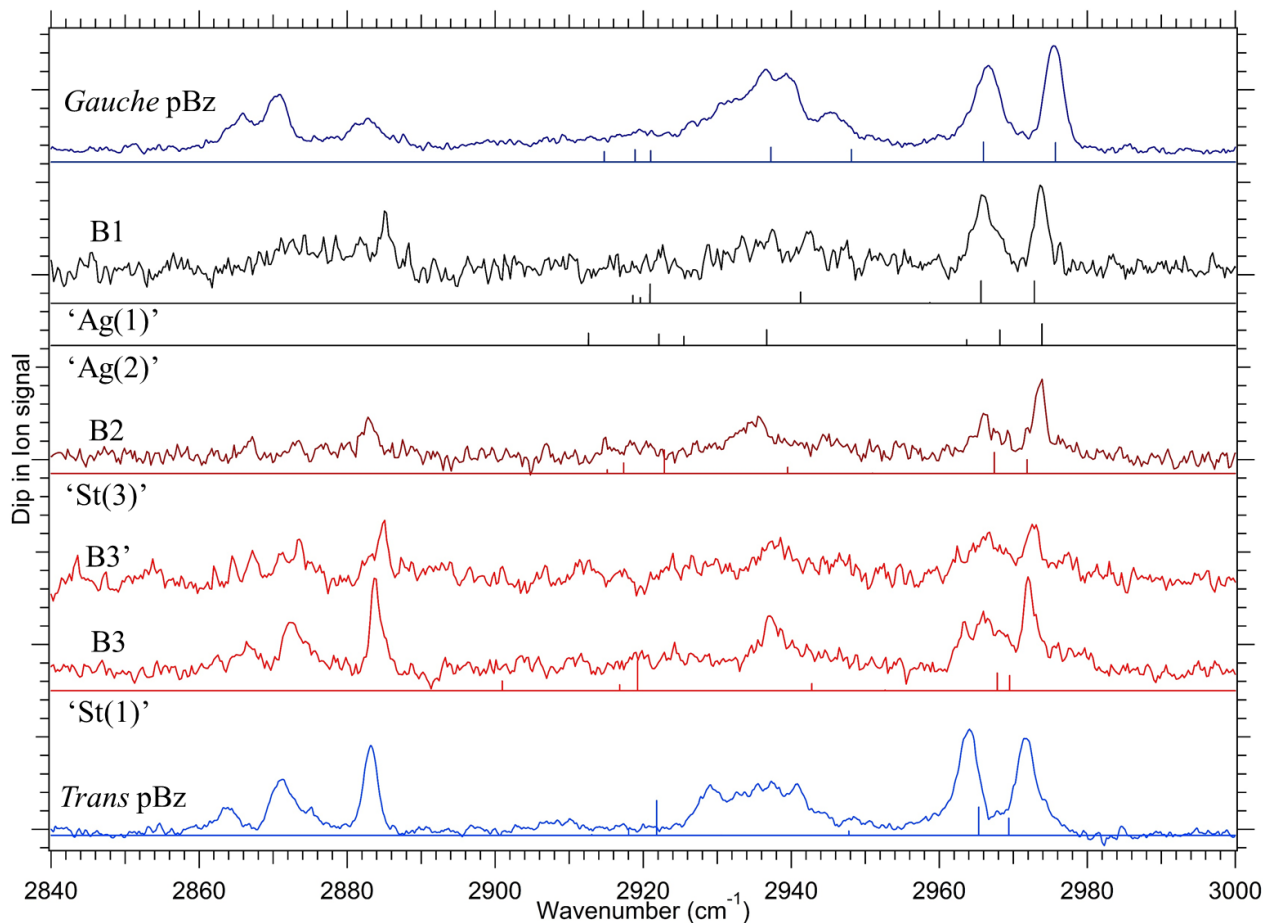


Figure 5.6: RIDIRS of pBz conformers and pBz(H₂O)₂ in the CH stretch region. B1, B2 and B3 are labelled along with their best match predictions. The UV frequencies where the RIDIRS were recorded are mentioned.

The 3500-3750 cm⁻¹ region of the spectrum does not have FR unlike the CH stretch region, which is why harmonic frequency calculations of the clusters were very useful in the assignment process. A linear scaling factor was used which had the least root mean squared value for the Bz(H₂O)₂ IR spectra in the OH stretch region, followed by lining up the free OH stretch by shifting the calculated spectrum (expt=calc*0.7266+917.1). The acceptor water molecule symmetric OH

stretch frequency is clearly overestimated by the calculations. Keeping these deviations in calculated spectrum relative to experiment, we investigate the pBz(H₂O)₂ experimental and the calculated spectra. As expected, the free OH stretch lies at the same frequency for all the n=2 clusters and Bz(H₂O)₂.

We have shown two very similar spectra for B1 recorded at 37638.56 and 37637.14 cm⁻¹ which, as mentioned previously, are shoulders of a broad peak. This could mean that there are 2 very similar clusters with S₀-S₁ origins at nearly identical UV frequencies, possessing similar FC progressions. B1 matches closest to the BSSE-corrected lowest energy structure, namely ‘Sg(1)’, followed by the two ‘Ag’ structures, namely ‘Ag(1)’ and ‘Ag(2)’. It is possible that we are seeing both these gauche clusters but the signal to noise is not high enough to make any clear assignments. B3 has the most intense UV peak which matches the ‘St(1)’ cluster best, followed by ‘At(1)’. There are three St structures below 6 kJ/mol whereas there are two of At. The interconversion between the clusters via collisions during the expansion, might funnel population in the lowest energy ‘St’ structure due to which we would expect ‘St(1)’ in the expansion. The ‘Ag’ and the ‘At’ cluster predictions are very similar, which is expected as the chain conformation will have negligible effect on the water OH stretch frequencies. Following this reasoning, B1 could be an ‘At’ and B3 an ‘Ag’ cluster. Apart from B3LYP-GD3BJ/Def2TZVP, we used the M06-2X/6-311++G(2d,p) harmonic frequency predictions, which basically eliminated ‘Sg(3)’ and ‘St(2)’ as possible structures present in the expansion. This did not further narrow down the possible cluster assignments.

The OH stretch region of B2 has some interesting characteristics. The splitting between the two symmetric and the two antisymmetric OH stretches are smaller than B1 and B3. ‘St(3)’ and ‘Sg(4)’ clusters match up with B2, where the ‘St(3)’ structure has an interesting double π H-bond. In ‘St(3)’, the ordering of the acceptor and donor OH stretch frequencies are switched. M062X/6-311++G(2d,p) calculations predict ‘Sg(4)’ matches with the experimental B2 spectrum, whereas the double π H-bonded ‘St(3)’ could not be converged. The common structural characteristic among these possible cluster assignments is that they are all *syn*, i.e., the propyl chain and the water cluster are on the same side of the phenyl ring.

Considering all of the above studies across UV excitation and IR spectra in both the CH stretch and OH stretch regions, we infer the following assignments. ‘Ag(1)’ and ‘Ag(2)’ match closely with B1, implying the broadened peaks in the UV excitation and the RIDIRS in the OH

stretch region are due to this combination. B3, with the best S/N, corresponds to ‘St(1)’ cluster. Theoretically, the distance between the H-bond distance of the water dimer is shorter for ‘St(1)’ at 190 pm than Bz(H₂O)₂ at 193 pm. The π H-bond however is shorter for Bz(H₂O)₂ than ‘St(1)’. B2 has a very unique IR spectrum in the OH stretch region, which implies a double π H-bonded ‘St(3)’ cluster, although such a structure has not been experimentally observed in Bz(H₂O)₂ or any of the higher water clusters with pBz.

The propyl chain has a small effect on the dimeric water geometry, although the LAM is partially quenched by the presence of this short chain. Both *gauche* and *trans* configurations are seen on the propyl chain while forming the cluster, displaying no clear preference of one over the other. While the calculations suggest the *syn* is preferred over *anti*, the experiments suggest that there are at least 2 clusters with *syn* configuration out of the 3 observed, implying the propyl chain prefers to point towards the same side of the π aromatic ring as the dimeric (H₂O)₂.

5.3.2 Propylbenzene(H₂O)₃

Adding one extra H₂O to the dimeric water in pBz(H₂O)₂ has two clear outcomes: (1) the number of theoretically possible structures for pBz(H₂O)₃ becomes very large, and (2) the flexibility of individual water molecules is constrained by a cyclic trimer of H₂O molecules. There is also a possibility that the propyl chain could break the cyclic water structure and form a chain water structure. At the DFT B3LYP-GD3BJ/Def2TZVP, below 2.5 kJ/mol, there were 33 structures, 25 of which were unique. Theoretically Bz(H₂O)₃ has two unique minima within 0.5 kJ/mol of each other shown in **Figure 5.7 (a)** and **(b)**. First where there is 1 π H-bond and 2 free OH, which is also the experimentally seen Bz(H₂O)₃ structure, and second where there are 2 partial π H-bonds and 1 free OH. Experimentally however, the cluster with 1 π H-bond and 2 free OH bonds is the only one observed for Bz(H₂O)₃. Spectroscopically, there is evidence for only those pBz(H₂O)₃ clusters being formed that have 1 π H-bond, consequently narrowing down the 27 unique clusters to 12 structures. Select few structures of Bz(H₂O)₃ and the n=3 clusters that are later assigned are in **Figure 5.7**.

The cyclic (H₂O)₃ can have a clockwise or an anticlockwise O-H \cdots O H-bonded direction, which cause minor spectral shifts. Moreover, many of such clusters are mirror images of each other, hence their nomenclature have not been differentiated here. The labeling for the n=3 cluster along with their BSSE-corrected and ZPE-corrected energies carried out at the dispersion corrected

DFT B3LYP-GD3BJ/Def2TZVP are shown in **Table 5.2** follows the pBz(H₂O)₂ scheme. The lowest ZPE-corrected cluster has 2 partial π H-bonds and 1 free OH bond, which is why we have not included it in **Table 5.2**. Among the 14 unique structures, there were 4 ‘St’, 4 ‘Sg’, 2 ‘At’ and 2 ‘Ag’ clusters. Like in case of the n=2 cluster analysis, due to several possible calculated low energy structures, IR-UVHB, RIDIRS in the OH stretch region and in the CH region were analyzed independent of each other.

Table 5.2: BSSE-corrected and ZPE-corrected energies of pBz(H₂O)₃ clusters carried out at B3LYP-GD3BJ/Def2TZVP level of theory. All energies are relative to the most stable structures within their respective column.

Cluster label	BSSE-corrected energy	ZPE-corrected energy
Ag(1)	0	1.15
Sg(1)	0.14	0.88
St(1)	0.25	1.77
Sg(2)	0.39	1.53
St(2)	0.51	1.04
Sg(3)	0.67	0.47
Ag(2)	0.76	1.85
Sg(4)	1.18	1.83
At(1)	1.28	1.84
At(2)	1.39	1.91
St(3)	1.42	1.27
St(4)	2.24	0.90

To obtain the spectra of higher pBz-water clusters, the vapor pressure of water was increased by increasing the flow through the water sample chamber. R2PI scans were recorded in the n=1 (m/z=138) and n=2 (m/z=156) mass channels. The presence of pBz(H₂O)₃ cluster was confirmed in both these mass channels by performing RIDIRS in the OH stretch region (**Figure 5.8**). **Figure 5.2 (d)** shows the presence of 5 peaks, 3 of which are fragmenting into the n=1 mass channel, otherwise not present in **Figure 5.2 (b)**, connected by dotted lines. The 3 transitions lie at 37654.86, 37660.53 and 37706.68 cm⁻¹. Despite being resolved in the n=2 mass channel,

RIDIRS was performed on these 3 peaks from the n=1 mass channel due to better S/N. The 3 peaks are marked with an asterisk in **Figure 5.2 (c)**.

Unlike the n=2 cluster, there are no long FC progressions observed for the n=3 cluster. Solely based on the frequency shifts of these 0^0_0 peaks of the pBz conformers, we can make a preliminary assignment of the *gauche* and *trans* clusters. The pBz(H₂O)₃ clusters are labelled C1, C2 and C3 in the increasing order of electronic origin frequencies, which are 37654.86, 37660.53 and 37706.68 cm⁻¹, respectively. The Bz(H₂O)₃ electronic 0^0_0 is shifted from Bz 0^0_0 by 98 cm⁻¹. C1 and C2 are shifted from *gauche* pBz 0^0_0 by 113 cm⁻¹ and 119 cm⁻¹, respectively, whereas C3 is shifted from *trans* pBz by 116 cm⁻¹.

Like in case of the n=2 cluster, the CH region RIDIRS (**Figure 5.8**) is crucial to confirm the *gauche* and *trans* assignments of the three pBz(H₂O)₃ clusters. Only the methyl CH stretch region (2920-3000 cm⁻¹) was recorded as from previous experience with pBz(H₂O)₂, the splitting of these CH stretch frequencies were the most informative with good S/N. *Gauche* pBz has slightly larger methyl CH stretch splitting than *trans* pBz as mentioned in the previous section. The splittings for C1, C2 and C3 are 10.5, 9.0, and 7.2 cm⁻¹ respectively. Based on this observation, C1 is a *gauche* cluster and C3 is a *trans* cluster, as predicted by the electronic origin frequency shifts. As seen in **Figure 5.8**, the C2 has poor S/N in the methyl CH stretch region rendering the RIDIRS in this region non-conclusive.

As mentioned previously, we obtained 25 unique structures within 2.5 kJ/mol. Broadly there were 3 types of trimeric (H₂O)₃ framework: (1) Cyclic structure with 1 π H-bonded OH and 2 free OH bonds, (2) Cyclic structure with 2 partial π H-bonded OH and 1 free OH bond, and (3) bent chain structure. Among these three types, the cyclic structure with 1 π H-bonded OH is observed experimentally as all the n=3 clusters have 2 partially resolved peaks between 3705-3720 cm⁻¹, belonging to 2 free OH stretch frequencies. The closest match of the C1 spectrum is 'Sg(3)' and for C3 it is 'St(1)', followed by 'St(2)'. The spectrum of C2, with broad OH stretch peaks and low S/N CH peaks might be due to 2 unique clusters. This could be best assigned to 'Sg(1)' or 'Sg(2)' which are clockwise and anti-clockwise counterparts with respect to cyclic (H₂O)₃, followed by 'Ag(1)' and 'Ag(2)'.

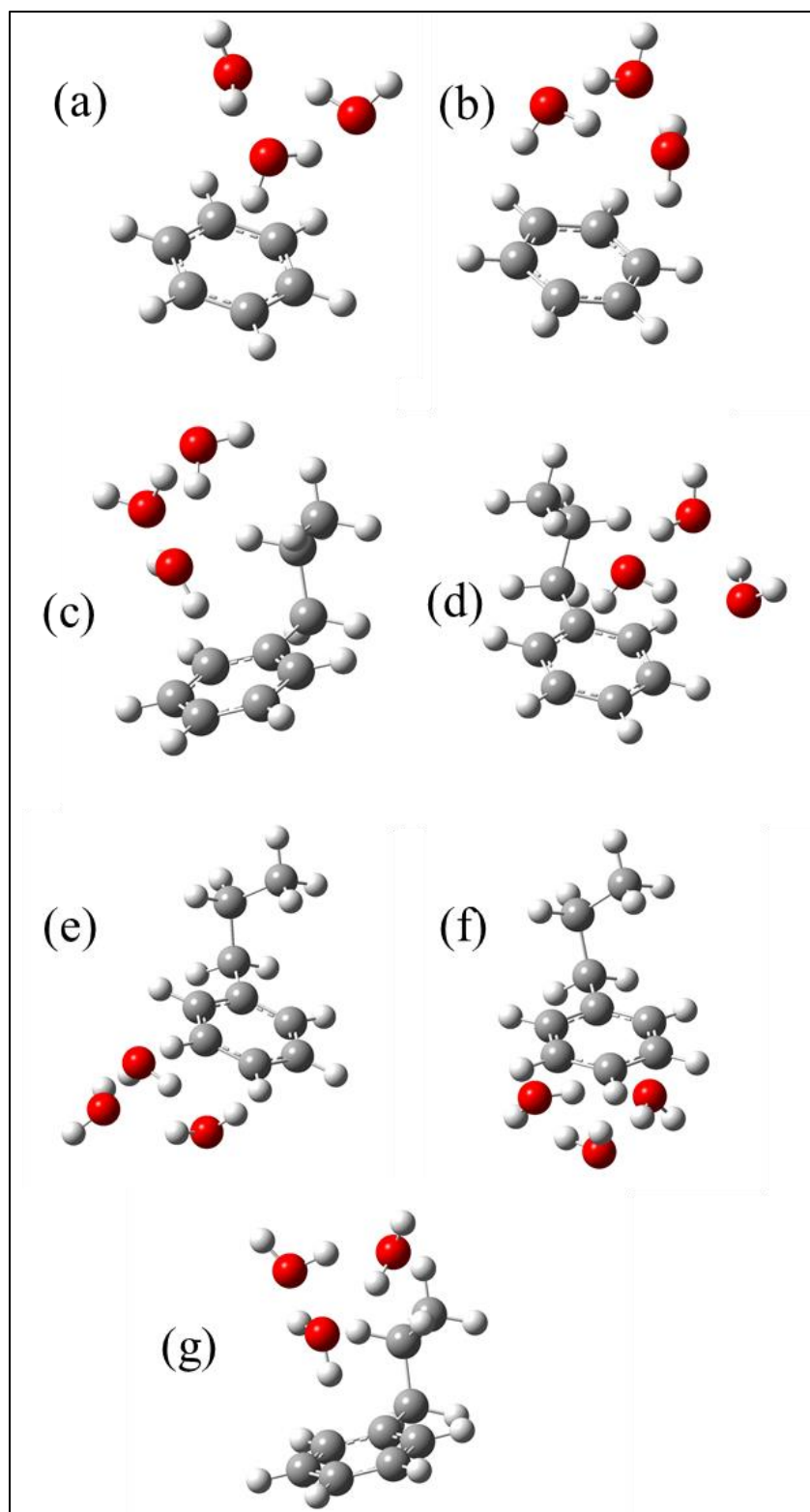


Figure 5.7: Structures of $\text{Bz}(\text{H}_2\text{O})_3$ and $\text{pBz}(\text{H}_2\text{O})_3$ clusters along with their labels. (a) Experimentally observed $\text{Bz}(\text{H}_2\text{O})_3$ structure with 1 π H-bond, (b) $\text{Bz}(\text{H}_2\text{O})_3$ structure with 2 π H-bonds, (c) ‘Sg(3)’, (d) ‘Sg(1)’, (e) ‘Ag(2)’, (f) ‘Ag(1)’, and (g) ‘St(1)’.

The propyl chain has little effect on the cyclic water trimer. Cluster-specific spectroscopy could not be performed on all the observed electronic transitions due to poor S/N. Both *gauche* and *trans* configurations are seen on the propyl chain while forming the cluster. Due to weak excitation peaks, there is not enough evidence to make any statement regarding the preference of *gauche* or *trans* cluster. The calculations suggest that there are many more *syn* clusters than *anti* over the 2.5 kJ/mol energy range. Just like in case of pBz(H₂O)₂ clusters, the experiments suggest that there are at least 2 clusters with *syn* configuration out of the 3 observed, implying the propyl chain prefers to point towards the same side of the π aromatic ring as the cyclic (H₂O)₃.

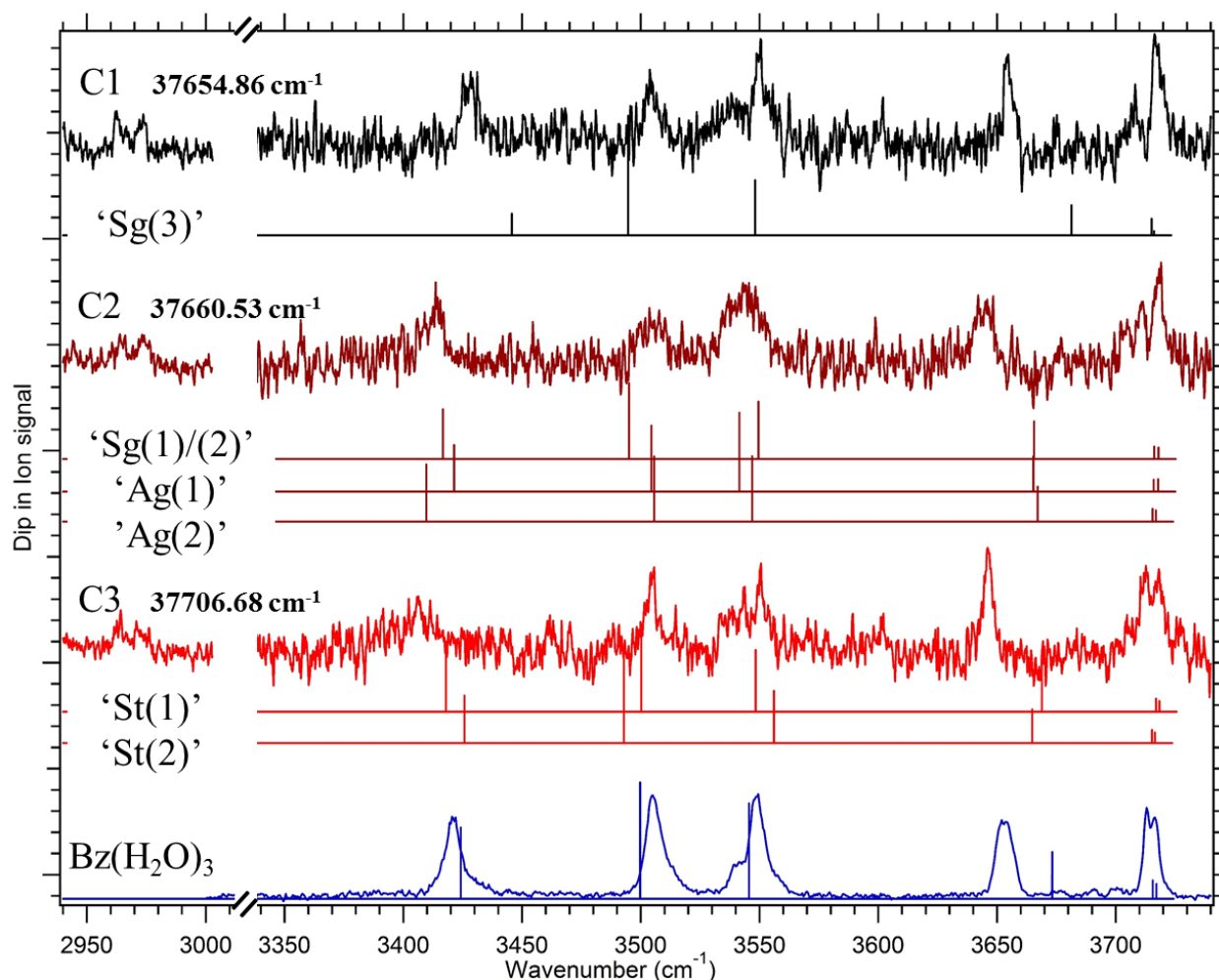


Figure 5.8: RIDIRS of Bz(H₂O)₃ and pBz(H₂O)₃ in the CH and the OH stretch regions. C1, C2 and C3 are labelled along with their best match predictions. The UV frequencies where the RIDIRS were recorded are mentioned.

5.3.3 Propylbenzene(H₂O)₄

Adding one extra H₂O to the cyclic water in pBz(H₂O)₃ further increases the number of theoretically possible structures for pBz(H₂O)₄. There is also a possibility that the propyl chain could break the cyclic water structure and form a chain water structure. At the DFT B3LYP-GD3BJ/Def2TZVP, below 2.5 kJ/mol, there were 21 structures, 12 of which were unique. Theoretically, Bz(H₂O)₄ has two unique minima within 0.1 kJ/mol of each other shown in **Figure 5.9 (a)** and **(b)**. The first of these has free OH bonds alternatively pointing up and down, which is also the experimentally seen Bz(H₂O)₄ structure, and second, where the 2 consecutive free OH bonds point up and the other 2 point down. Experimentally, the cluster of the first type is seen in pBz(H₂O)₄, as seen in **Figure 5.9**. Like in the case of (H₂O)₃, the cyclic (H₂O)₄ can also have a clockwise or anticlockwise O-H···O H-bonded direction with respect to propylbenzene, which causes minor spectral shifts. Moreover, many of such clusters are mirror images of each other, hence their nomenclature has not been differentiated here. The labeling for the n=4 cluster along with their BSSE-corrected and ZPE-corrected energies carried out at the dispersion corrected DFT B3LYP-GD3BJ/Def2TZVP are shown in **Table 5.3** which follows the pBz(H₂O)_{2,3} labeling schemes. Among the 12 unique structures, there were 3 ‘St’, 4 ‘Sg’, 1 ‘At’ and 4 ‘Ag’ clusters. Like in case of the previous two different sized cluster analysis, due to several possible calculated low energy structures, IR-UVHB, RIDIRS in the OH stretch region and in the CH region were analyzed independent of each other.

Table 5.3: BSSE-corrected and ZPE-corrected energies of pBz(H₂O)₄ clusters carried out at B3LYP-GD3BJ/Def2TZVP level of theory. All energies are relative to the most stable structures within their respective column.

Cluster label	BSSE-corrected energy	ZPE-corrected energy
St(1)	0	0
Ag(1)	0.93	1.63
At(1)	1.02	1.03
Ag(2)	1.35	1.88
Sg(1)	1.39	1.52
Sg(2)	1.45	1.65
Sg(3)	1.53	2.48
Ag(3)	1.58	2.52
St(2)	1.70	1.89
Sg(4)	1.74	2.08
Ag(4)	1.86	2.80
St(3)	2.08	1.87

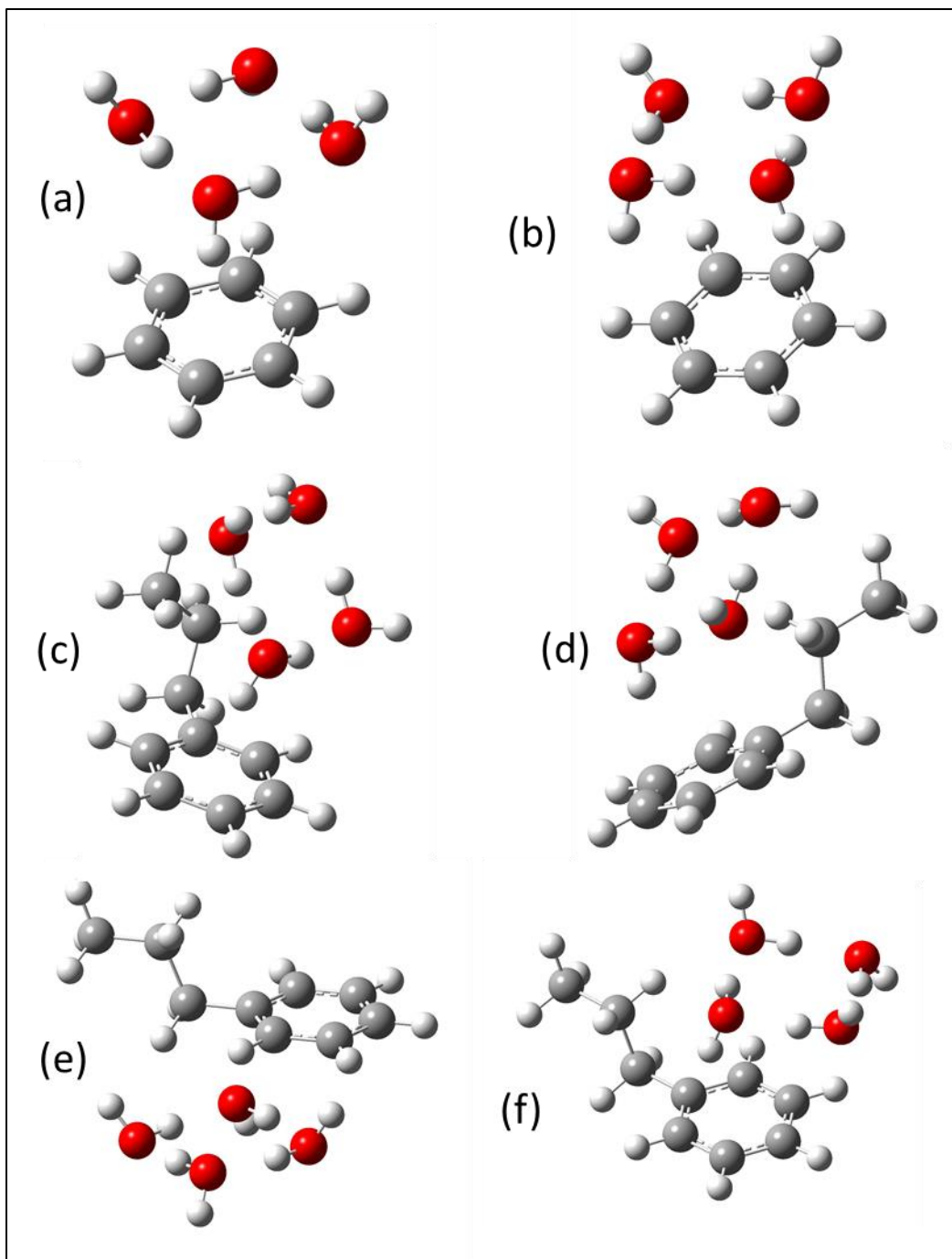


Figure 5.9: Structures of $\text{Bz}(\text{H}_2\text{O})_4$ and $\text{pBz}(\text{H}_2\text{O})_4$ clusters along with their labels. (a) Experimentally observed $\text{Bz}(\text{H}_2\text{O})_4$ with 1 π H-bond, (b) $\text{Bz}(\text{H}_2\text{O})_4$ with 2 π H-bonds, (c) ‘Sg(2)’, (d) ‘St(1)’, (e) ‘At(1)’, and (f) ‘St(2)’.

R2PI scans were recorded in the $[1:3]^+$ ($m/z=174$) mass channel. Transitions due to $pBz(H_2O)_4$ were confirmed by performing RIDIRS in the OH stretch region (**Figure 5.10**). **Figure 5.2 (e)** shows the presence of 5 peaks which are at 37671.88, 37676.85, 37703.13, 37714.50 and 37727.31 cm^{-1} . The peak at 37671.88 cm^{-1} has the poorest S/N and also appears to be a doublet, hence, we have not rigorously characterized it.

There are no long FC progressions observed for the $n=4$ cluster, confirmed by RIDIRS in the OH stretch region (3300-3775 cm^{-1}). Solely based on the frequency shifts of these 0^0_0 peaks from the pBz conformers, we can make a preliminary assignment of the *gauche* and *trans* clusters. The $pBz(H_2O)_4$ clusters are labelled D1, D2, D3 and D4 in the increasing order of electronic origin frequencies, which are 37676.85, 37703.13, 37714.50 and 37727.31 cm^{-1} , respectively. $Bz(H_2O)_4$ electronic 0^0_0 is shifted from $Bz 0^0_0$ by about 100 cm^{-1} . D1 is shifted from *gauche* $pBz 0^0_0$ by 130 cm^{-1} , whereas D2, D3 and D4 are shifted from *trans* pBz by 112, 123 and 136 cm^{-1} , respectively. D2, D3 and D4 might seem to belong to a FC progression, but the OH stretch region suggests otherwise. RIDIRS in the CH stretch region was not recorded as the OH stretch region along with the electronic origin shifts were sufficient to make reliable assignments. As mentioned previously, the cyclic tetrameric $(H_2O)_4$ framework where OH bonds that are not H-bonded to other water molecules, alternatively point up and down, is what is observed in the $pBz(H_2O)_4$ clusters, and which is also the experimentally seen $Bz(H_2O)_4$ structure. The RIDIRS spectra were scanned between 3300-3750 cm^{-1} . There are two more H-bound peaks in the OH stretch region that are unaccounted for below 3300 cm^{-1} , but were not studied as they are split due to FR.⁶ RIDIRS in the OH stretch region showed that the closest match with D1 is ‘Sg(2)’ structure. The 3 remaining *trans* clusters, D2, D3 and D4 were assigned to the ‘St(1), ‘At(1)’ and ‘St(2)’ $n=4$ clusters.

The propyl chain has little effect on the water tetramer’s geometry, like in case of the $n=2,3$ clusters. Both *gauche* and *trans* configurations are seen on the propyl chain while forming the cluster, with preference of *trans* over *gauche*. The experiments suggest that there are at least 3 clusters with *syn* configuration out of the 4 observed, implying the propyl chain clearly prefers to point towards the same side of the π aromatic ring as the dimeric $(H_2O)_2$ and the cyclic $(H_2O)_3$ systems.

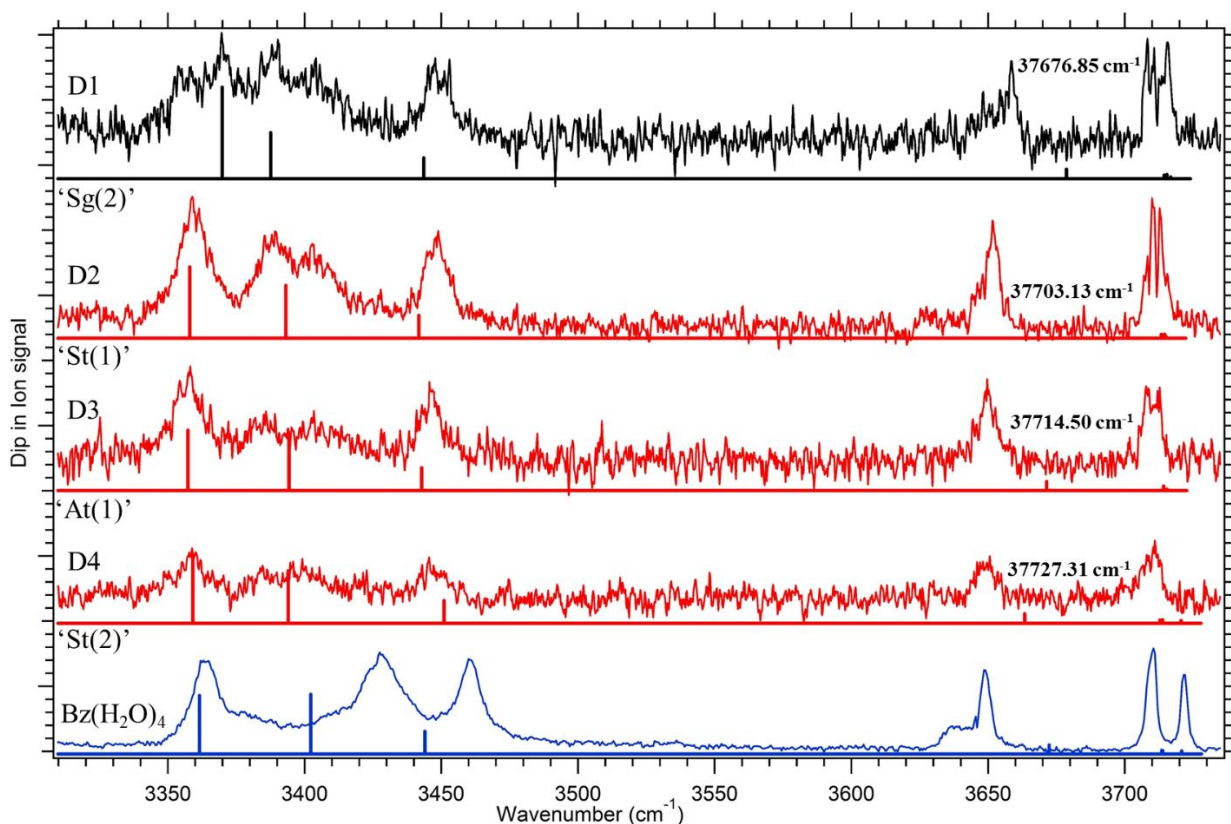


Figure 5.10: Structures of $\text{Bz}(\text{H}_2\text{O})_4$ and $\text{pBz}(\text{H}_2\text{O})_4$ clusters along with the harmonic frequency predictions in the OH stretch region. The UV frequencies where the RIDIRS were recorded are mentioned.

5.4 Discussion and Conclusion

The present work was aimed at understanding the interaction between the short alkyl chain and the water cluster framework that is complexed to the π aromatic ring of propylbenzene. The questions we asked are: (1) How does the water influence the chain conformation or on which side of the aromatic ring does it lie? (2) How does the presence of an aliphatic chain influence the H-bonded water structure? The sizes of the clusters studied are $\text{pBz}(\text{H}_2\text{O})_n$, $n=2-4$. The total vibrational degrees of freedom or the total number of modes are $3N-6$ for an asymmetric molecule. When two molecules form a complex, the $3+3$ translational degrees of freedom of both are reduced down to 3 translational degrees of freedom, whereas the $3+3$ rotational degrees of freedom become just 3 rotational degrees of freedom. The remainder 6 degrees of freedom turn into 6 intermolecular degrees of freedom. Addition of H_2O molecules to the pBz cluster has two outcomes: (1) the number of theoretically possible structures increases, and (2) the flexibility of individual water

molecules is constrained by H-bonded water framework. Due to higher flexibility and lower number of OH frequencies to study, the assignment process of pBz(H₂O)₂ was more challenging than the other 2 cluster sizes.

The experiments designed were very insightful. The UV excitation and IR-UV HB experiments were very useful to determine the propyl chain conformation. Moreover, there is long FC progression in pBz(H₂O)₂ clusters which are not observed in the pBz(H₂O)_{3,4} clusters, something very similar to what was observed for the Bz(H₂O)_n, n=2-4 counterparts. The RIDIRS in the CH stretch region, especially the methyl CH stretch peaks were helpful to confirm the *gauche* vs *trans* propyl chain conformation. After determining the *gauche* and *trans* clusters, the RIDIRS in the OH stretch region was performed to study the π H-bond and the H-bonded structure of the water cluster. A summary of the electronic origin frequency shifts along with their Bz(H₂O)_n counterparts are listed in **Table 5.4**.

Table 5.4: Electronic origin frequency shifts of Bz(H₂O)_n and pBz(H₂O)_n clusters from their respective conformational monomers.

Monomers	(H ₂ O) ₂	(H ₂ O) ₃	(H ₂ O) ₄
Bz	70 cm ⁻¹	98 cm ⁻¹	100 cm ⁻¹
<i>Gauche</i> pBz	B1: 68 cm ⁻¹	C1: 113 cm ⁻¹	D1: 130 cm ⁻¹
		C2: 119 cm ⁻¹	
<i>Trans</i> pBz	B2: 68 cm ⁻¹	C3: 116 cm ⁻¹	D2: 112 cm ⁻¹
	B3: 79 cm ⁻¹		D3: 123 cm ⁻¹
			D4: 136 cm ⁻¹

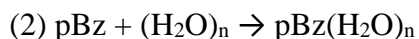
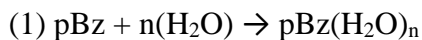
In conclusion, the water framework due to its H-bonded system, is largely unaffected by the presence of a short aliphatic chain, although in pBz(H₂O)₂, we find evidence of an unusual double π H-bonded structure. The presence of a short chain breaks the symmetry of the benzene ring, hence contributing to more number of possible structures. We observe that the water cluster has minor effect on the conformation of the propyl chain in pBz where *trans* clusters are more abundant

than *gauche*. Whereas the *syn* clusters are clearly preferred over *anti*. A summary of the assignments are in **Table 5.5**.

Table 5.5: Summary of the propylbenzene-water cluster assignments.

pBz(H₂O)₂	pBz(H₂O)₃	pBz(H₂O)₄
St	Sg	St
Ag	St	At
St	Sg (or) Ag	St
		Sg

Condensation dynamics does play a role on the clusters that are formed in our expansion. Condensation could occur via a combination of the following two schemes representative of the limiting cases:



This dynamics could affect the conformational preference of the propyl chain between *gauche* or *trans*. It could also affect the *syn* vs *anti* configurations, where the isomerization would be feasible from the energy provided by the enthalpy of condensation. We however have not addressed this issue in our work.

There are two opposing effects influencing the preference of a *syn* or an *anti* configuration of the propyl chain in the cluster. If the propyl chain pushes the water framework via steric repulsion such that the π H-bond formed is not as strong, a *syn* geometry would be destabilized. Conversely, if there are dispersive interactions between the propyl chain and the water cluster, a *syn* cluster would be energetically favored. In summary, we see a small but consistent preference for the water dimer to take up a position on the same side as the propyl chain. However, a *gauche* with *syn* configuration appears to push the water off its preferred position on the aromatic π cloud more than *trans*, consistent with their being a larger number of ‘St’ than ‘Sg’ structures, whereas there is no clear preference of *gauche* vs *trans* in an *anti* configuration.

The smallest alkylbenzene where a stacking of the alkyl chain over the ring, was observed is octylbenzene, in its g1g2g4g5 conformer.¹³ As a potential extension, we carried out

computations on octylbenzene(H₂O) complexes. We identified over 140 low energy structures via force field calculations and performed dispersion corrected DFT optimization and frequency calculations on all the structures. Out of the 4 structures within 1.5 kJ/mol, 3 were stacked structures where the H₂O was sandwiched between the π aromatic ring and the octylbenzene chain. The lowest energy structure within the folded geometries possesses *syn g1g2g4g5* configuration.

5.5 References

- ¹ K. S. Kim, P. Tarakeshwar, and J. Y. Lee, *Chem. Rev.* **100**, 4145 (2000); M. Nishio, *Cryst. Eng. Commun.* **6**, 130 (2004); H. Matsuura, H. Yoshida, M. Hieda, S. Yamanaka, T. Harada, K. Shin-ya, K. Ohno, *J. Am. Chem. Soc.* **125**, 13910 (2003); G. A. Jeffrey, W. Saenger, *Hydrogen Bonding in Biological Structures*, Springer, Berlin (1991).
- ² G. C. Pimentel, A. L. McClellan, *The Hydrogen Bond*, W. H. Freeman: San Francisco CA (1960).
- ³ A. Engdahl and B. Nelander, *J. Phys. Chem.* **89**, 2860 (1985); S. Suzuki, P. G. Green, R. E. Bumgarner, S. Dasgupta, W. A. Goddard III, and G. A. Blake, *Science* **257**, 942 (1992); H. S. Gutowsky, T. Emilsson, and E. Arunan, *J. Chem. Phys.* **99**, 4883 (1993); J. Wanna, J. A. Menapace, and E. R. Bernstein, *J. Chem. Phys.* **85**, 1795 (1986); P. Linse, *J. Comput. Chem.* **9**, 505 (1988); J. D. Augspurger, C. E. Dykstra, and T. S. Zwier, *J. Phys. Chem.* **96**, 7257 (1992); J. D. Augspurger, C. E. Dykstra, and T. S. Zwier, *J. Phys. Chem.* **97**, 980 (1993); G. Karlstrom, P. Linse, A. Wallqvist, and B. Jonsson, *J. Am. Chem. Soc.* **105**, 3777 (1983); P. Linse, *J. Chem. Phys.* **86**, 4177 (1987); S. Li, V. R. Cooper, T. Thonhauser, A. Puzder, and D. C. Langreth, *J. Chem. Phys.* **112**, 9031 (2008).
- ⁴ R. N. Pribble, A. W. Garrett, K. Haber, and T. S. Zwier, *J. Chem. Phys.* **103**, 531 (1995).
- ⁵ R. N. Pribble, and T. S. Zwier, *Science*. **265**, 75 (1994); R. N. Pribble, and T. S. Zwier, *Faraday Discuss.* **97**, 229 (1994).
- ⁶ D. P. Tabor, R. Kusaka, P. S. Walsh, T. S. Zwier, and E. L. Sibert III, *J. Phys. Chem. A.* **119**, 9917 (2015).
- ⁷ F. Battin-Leclerc, *Prog. Energy Combust. Sci.* **34**, 440 (2008); D. Darcy, C. J. Tobin, K. Yasunaga, J. M. Simmie, J. Wurmel, W. K. Metcalfe, T. Niass, S. S. Ahmed, C. K. Westbrook, and H. J. Curran, *Combust. Flame* **159**, 2219 (2012).
- ⁸ J. B. Hopkins, D. E. Powers, and R. E. Smalley, *J. Chem. Phys.* **72**, 5039 (1980); J. B. Hopkins, D. E. Powers, S. Mukamel, and R. E. Smalley, *J. Chem. Phys.* **72**, 5049 (1980).
- ⁹ D. P. Tabor, D. M. Hewett, S. Bocklitz, J. A. Korn, A. J. Tomaine, A. K. Ghosh, T. S. Zwier, and E. L. Sibert III, *J. Chem. Phys.* **144**, 224310 (2016).
- ¹⁰ P. Mishra, D. M. Hewett, and T. S. Zwier, *J. Chem. Phys.* **148**, 184304 (2018).
- ¹¹ F. Mohamadi, N. G. J. Richards, W. C. Guida, R. Liskamp, M. Lipton, C. Caufield, G. Chang, T. Hendrickson, and W. C. Still, *J. Comput. Chem.* **11**, 440 (1990).

- ¹² M. J. Frisch, G. W. Trucks, H. B. Schlegel, G. E. Scuseria, M. A. Robb, J. R. Cheeseman, G. Scalmani, V. Barone, B. Mennucci, G. A. Petersson, H. Nakatsuji, M. Caricato, X. Li, H. P. Hratchian, A. F. Izmaylov, J. Bloino, G. Zheng, J. L. Sonnenberg, M. Hada, M. Ehara, K. Toyota, R. Fukuda, J. Hasegawa, M. Ishida, T. Nakajima, Y. Honda, O. Kitao, H. Nakai, T. Vreven, J. A. Montgomery, Jr., J. E. Peralta, F. Ogliaro, M. Bearpark, J. J. Heyd, E. Brothers, K. N. Kudin, V. N. Staroverov, T. Keith, R. Kobayashi, J. Normand, K. Raghavachari, A. Rendell, J. C. Burant, S. S. Iyengar, J. Tomasi, M. Cossi, N. Rega, J. M. Millam, M. Klene, J. E. Knox, J. B. Cross, V. Bakken, C. Adamo, J. Jaramillo, R. Gomperts, R. E. Stratmann, O. Yazyev, A. J. Austin, R. Cammi, C. Pomelli, J. W. Ochterski, R. L. Martin, K. Morokuma, V. G. Zakrzewski, G. A. Voth, P. Salvador, J. J. Dannenberg, S. Dapprich, A. D. Daniels, O. Farkas, J. B. Foresman, J. V. Ortiz, J. Cioslowski, and D. J. Fox, gaussian 09, Revision C.01, Gaussian, Inc., Wallingford, CT, 2010.
- ¹³ D. M. Hewett, S. Bocklitz, D. P. Tabor, E. L. Sibert III, M. A. Suhm, and T. S. Zwier, *Chem. Sci.* **8**, 5305 (2017).

CHAPTER 6. **LOOKING AHEAD**

In this chapter, we describe research projects that have been carried out, but more work is warranted. We also include collaborative projects where a part of the projects has been carried out in the Zwieter lab at Purdue University. We start with the laser spectroscopy projects and then move to the chirped-pulse projects. We discuss Ethylanthracene (EA) and dianthrylethane (dAE) series of molecules, and projects carried out in collaboration with (1) Dr. Stephen Drucker (University of Wisconsin, Eau Claire) on Laser Induced Phosphorescence (LIP) studies of 4-H-pyran-4-one, and (2) Dr. Vasilios Stavros (University of Warwick) on LIF studies of Homosalate, a sunscreen candidate. Next, we discuss the pyrolysis reaction studies on 3-Pentenenitrile (3-PN).

6.1 Ethylanthracenes

6.1.1 Introduction

Soot formation is a field that has been an important area of research, but it still lacks in accurate modeling of the early stages of PAH and soot formation.¹ Until recently, there has been a conundrum in understanding how the first stages of soot formation occur. Stacking of polycyclic aromatic hydrocarbons (PAH) is considered an important first step towards soot formation.² The current model of the inception of soot requires PAHs to come together, and stack to form dimers at sizes of pentacene, it also involves radical recombination forming PAH dimers with an ethyl linker.³

We study this through logical set of experiments starting from alkylaromatics and small fused aromatic molecules to larger aromatic molecules with a chemical link. Specifically, our research is aimed towards understanding of the stacking tendency of diarylethane molecules with the ethyl chain linking the various unique positions on the fused aromatic ring. The structures where 2 π aromatic rings are stacked, are dispersion mediated. Work was carried out by Hewett in our lab on dinaphthylethane and ethyl naphthalene series. Series of dianthrylethanes would be the logical next step towards understanding stacking of PAHs. Ethyl chain substituted at unique positions on anthracene giving rise to a series of ethylanthracenes are studied as preliminary experiments to better understand the spectroscopic signatures of the stacking structures of dianthrylethanes and its stability with respect to the unstacked structures.

Here, we present computational studies of the entire series of ethylanthracenes and dianthrylethanes. Anthracene is a fused three 6-member aromatic ring with 3 unique positions for an ethyl chain or linker. Examples of such chemical structures are in **Figure 6.1** along with the numbering of C atoms on the molecule. The experimental electronic spectroscopy of 2-ethylanthracene (2-EA), which is a single conformation molecule is also discussed here, where $S_1 \leftarrow S_0$ UV excitation spectrum is obtained in the LIF chamber. This helps us understand the change in geometry in the excited electronic state through vibronic transitions and FC progressions. DFL was performed to study the ground state low-lying vibrational modes.

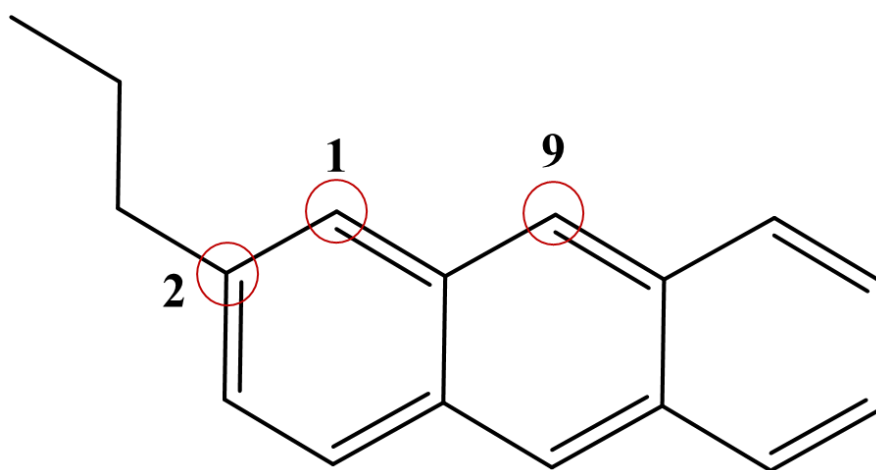


Figure 6.1: 2-Ethylanthracene with the unique positions on anthracyl ring rounded.

6.1.2 Methods

The series of ethylanthracenes are single conformation molecules and dianthrylethanes are anthracene rings connected to each other by an ethyl linker, which have multiple isomers and several conformers within each isomer. The dianthrylethanes were subjected to a conformational search utilizing MACROMODEL suite of program⁴ to ensure all stable starting geometries are accounted for at MMFFs through torsional dihedral rotations, followed by dispersion-corrected DFT calculations using Gaussian09 suite of program⁵.

A commercially available sample of 2-EA (98%, Sigma-Aldrich) was taken without further purification. Helium backing gas was flown over the sample and supersonically expanded into the LIF chamber. Experiments were carried out with 1.4 bar of He while the sample was maintained at 140°C. We also performed experiments at He backing pressures of up to 7 bar to ensure no hot

bands were observed in our spectrum. UV excitation was performed in the range 27341-28110 cm^{-1} (365.75-355.75 nm) using the dye LDS-722 (Pyridine 2, Exciton Laser Dyes). DFL was carried out on multiple excitation transitions for which 0.1-0.2 mm slitwidths were used. The UV excitation peaks have 2.5 cm^{-1} FWHM, whereas the DFL peaks are about 10 cm^{-1} , because (1) the monochromator slitwidths used were 0.2 mm to allow more light entering, and (2) the UV enhanced steering optics before the monochromator loses its reflectivity above 400 nm.

6.1.3 Theoretical Results and Discussion

6.1.3.1 Ethylanthracene

The molecules studied here have extended π cloud system along with short aliphatic chain, a dispersion corrected DFT is hence crucial to obtain accurate predictions. Calculations were carried out at B3LYP-GD3BJ/Def2TZVP, which have been reliable for very similar systems.^{6,7} Symmetry constrained optimization was carried out on anthracene which has a D_{2h} point group. Ethylanthracenes are a series of 3 single conformational molecules. From **Figure 6.1 (a)**, the three unique positions to attach an ethyl chain are 2, 1 and 9, giving rise to 2-, 1-, and 9-ethylanthracene, respectively. Due to the high symmetry of this fused ring system, all the other positions are mirror images of 2-, 1-, or 9-ethylanthracene.

In the Zwier lab, molecules with alkyl chains attached to aromatic rings have been an important theme of research.⁶⁻⁸ From the conformations studied, we know that the ethyl chain has low energy structures when pointing out of the plane of the aromatic ring, and have high energy and shallow minima, when the C atoms on the ethyl chain are in the plane of the aromatic ring. PES of such dihedral scans are shown in **Figure 3.10 (a)**.⁶ Such 'planar' conformations are not considered for the EAs, as they are not expected to have populations trapped in their shallow minima. The most stable molecule is 2-EA (**Figure 6.2 (a)**), followed by 1-EA with 4.39 kJ/mol and 9-EA with 13.45 kJ/mol higher energy.

When compared with the vibrational modes of anthracene, EAs have several extra low frequency torsional modes due to the ethyl chain. In aromatic ring systems, upon a $S_1 \leftarrow S_0$ transition, which is typically a $\pi\pi^*$ excitation, a ring expansion is the accompanied geometric change. In case of EAs, a ring expansion would involve a displacement of the ethyl chain. The affected ethyl torsional modes would depend on the position of the C atom where the chain is

attached. Hence, we anticipate to observe several ethyl torsional modes built off the aromatic ring expansion modes.

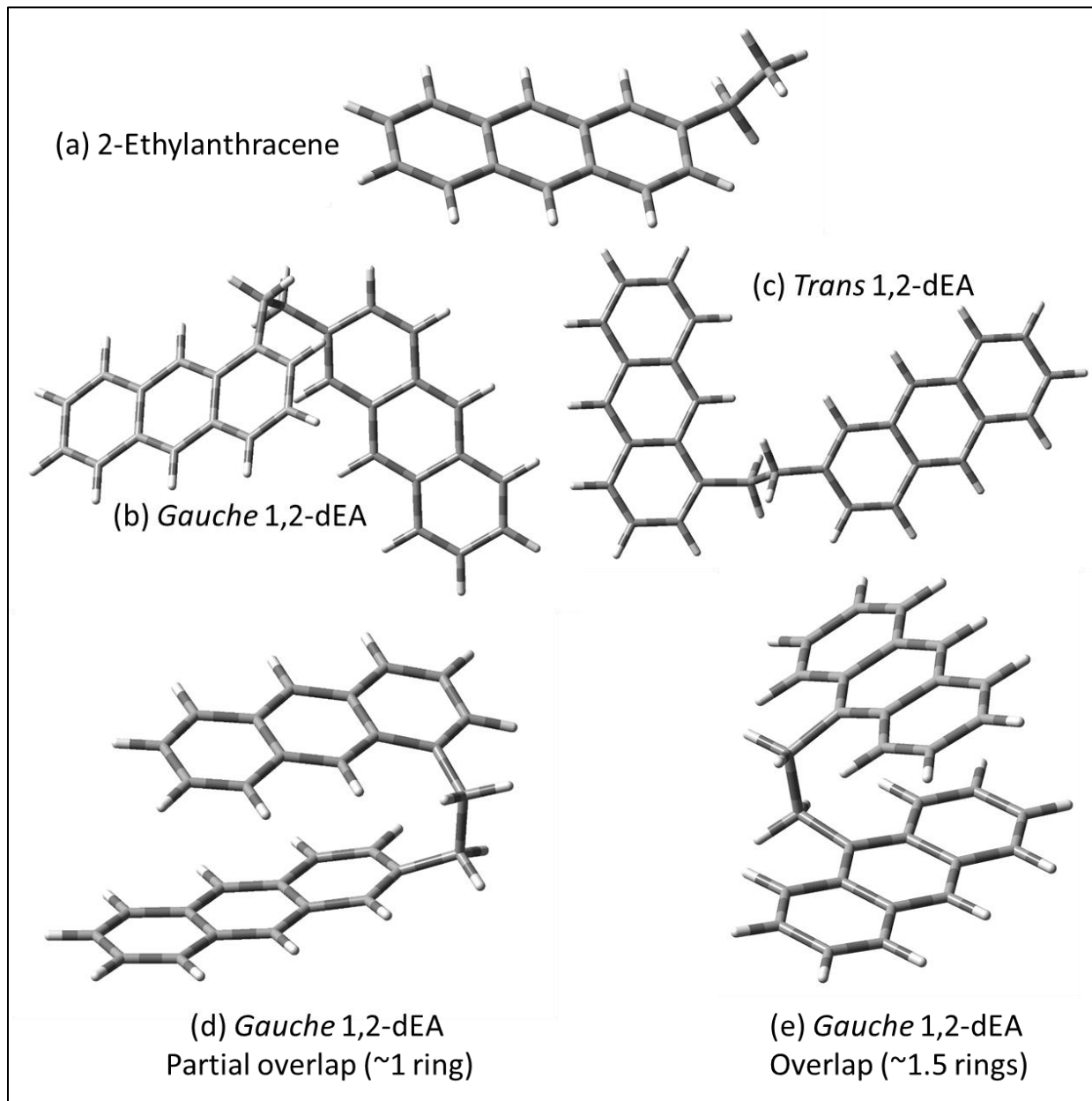


Figure 6.2: Structures of (a) 2-ethylanthracene, and (b)-(e) dianthrylethanes.

6.1.3.2 Dianthrylethane

As mentioned before, there are several possible combinations of positions on the anthracene ring that give rise to unique isomers. With 3 unique C atom positions, there are $3 \times 3 = 9$ possibilities,

3 of which are redundant. The unique isomers are 1,1-dianthrylethane (1,1-dEA), 1,2-dianthrylethane (1,2-dEA), 1,9-dianthrylethane (1,9-dEA), 2,2-dianthrylethane (2,2-dEA), 2,9-dianthrylethane (2,9-EA), and 9,9-dianthrylethane (9,9-EA). The number of unique structures are listed in **Table 6.1**.

Table 6.1: List of dianthrylethane isomers and the number of unique conformations in each.

Isomer	1,1-dEA	1,2-dEA	1,9-dEA	2,2-dEA	2,9-dEA	9,9-dEA
Number of conformers	10	13	4	5	4	2

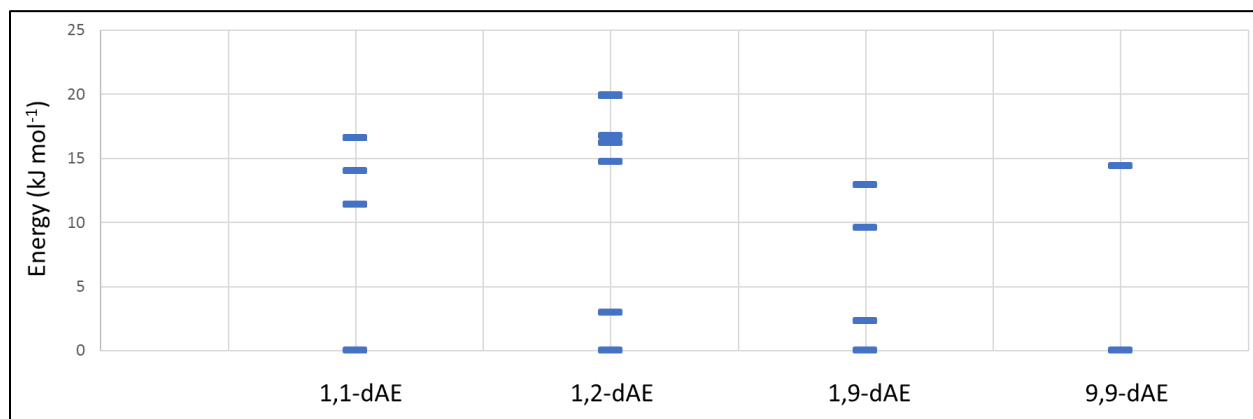


Figure 6.3: Energy level diagram of dianthrylethanes.

Due to the presence of two aromatic rings, there can be up to 2 ‘planar’ configurations which have high energy shallow minima. Such structures typically have energies above 20 kJ/mol relative to the most stable structure within their respective isomers, hence these have not been considered here. Due to the added asymmetry of the terminal methyl group of this ethyl linker, the ethyl chain dihedral can take conformations of *trans* (180°) or *gauche* ($\pm 60^\circ$). We are interested in the stacking tendency of these diarylethane systems, which is why, apart from the nomenclature of the ethyl linker, we differentiate the structures based on the extent of stacking. Broadly, in the increasing order of relative energies, there are stacked, partially stacked, and unstacked structures (**Figure 6.2 (d)-(e)**).

Figure 6.3 shows the energy level diagrams of select dEA molecules. The lowest energy structures have stacked aromatic rings with ring overlap of ~ 1.5 . The structures with partially

stacked rings lie 2-3 kJ/mol higher in energy, have an overlap of ~ 1 . Structures with no ring overlap are typically >10 kJ/mol relative to the stacked structures. 1,2-dEA and 9,9-dEA would be the best molecular candidates to observe the tendency of the stacking of anthracyl rings, as the possible low energy structures are stacked and partially stacked.

The vibrational analysis from the excitation spectrum of dEA conformers would be very informative. As mentioned before, the affected ethyl torsional modes would depend on the position of the C atom where the linker is attached. Moreover, the stacked vs partially stacked structures would have signature differences in the low frequency modes and the ethyl C-C/C-H stretch modes. Hence, we anticipate experimental spectroscopic studies can characterize the structures conclusively.

6.1.4 Experimental Results and Discussion of 2-ethylanthracene

2-EA, which is the most stable molecule among the 3 EAs, has been studied experimentally. As this molecule belongs to the asymmetric C_1 point group, the UV excitation spectrum and the obtained DFL spectra would not be symmetry governed, unlike *para*-diethylbenzene.⁶ Several important spectroscopic research, both experimental and theoretical, have been carried out on anthracene.^{9,10} Most notably, the experimental spectroscopy by Zewail and co-workers⁹, where UV excitation (up to 6000 cm^{-1} from the 0^0_0) and DFL (up to 3500 cm^{-1} from 0^0_0) have been performed, is compared with our work. We scanned our UV excitation spectrum up to 1230 cm^{-1} above the 0^0_0 , but signal was observed only up to 650 cm^{-1} . UV excitation has been recorded up to 750 cm^{-1} from the 0^0_0 and DFL up to 850 cm^{-1} from the 0^0_0 of 2-EA (**Figure 6.4**). Ground state and excited state vibrational frequencies were used to analyze both UV excitation spectrum and DFL spectra.

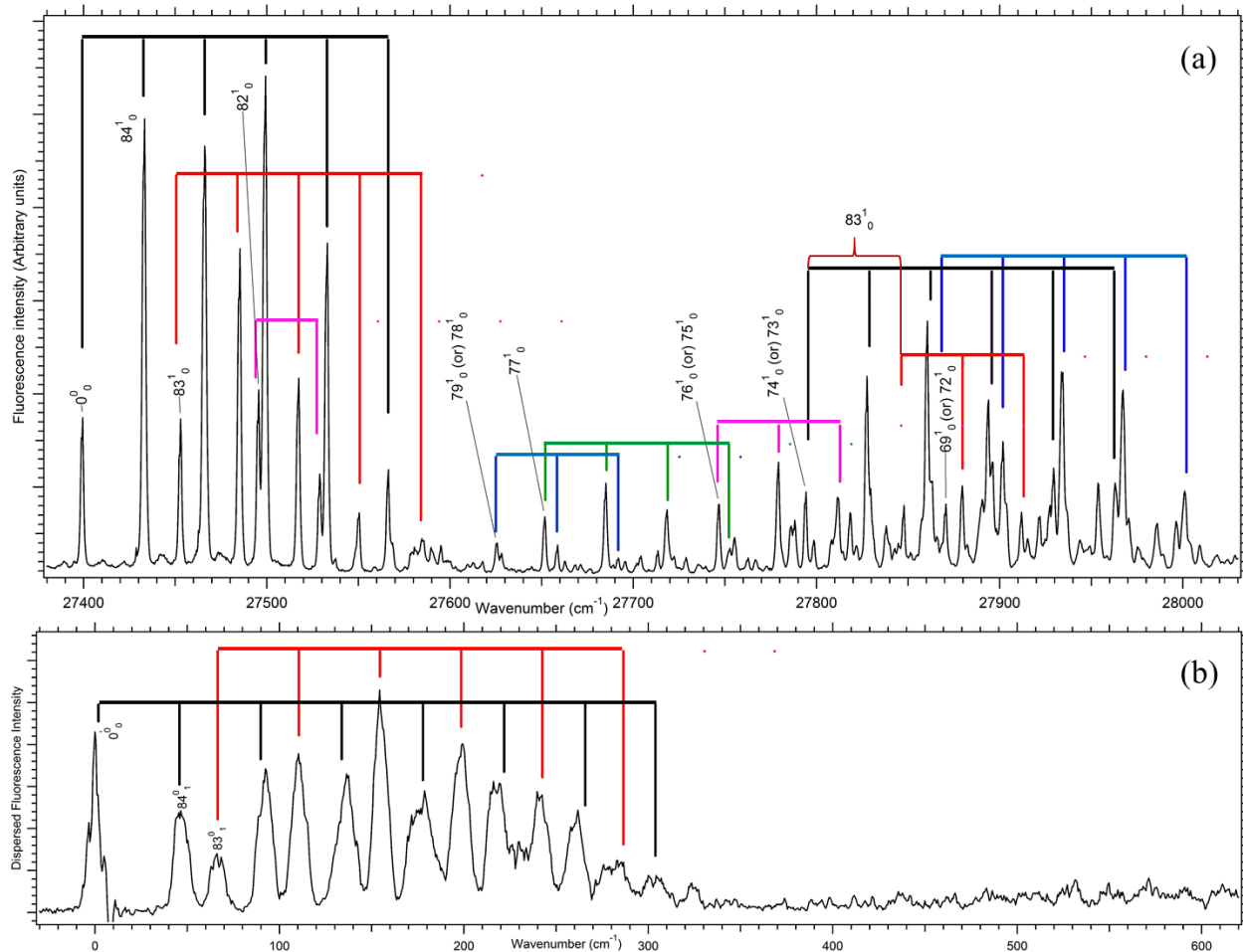


Figure 6.4: Electronic spectra of 2-ethylanthracene. (a) UV excitation spectrum, and (b) DFL spectra at 0^0_0 . Long FC progressions of ethyl torsional mode are connected by tie lines.

In the UV excitation spectrum of anthracene, the electronic origin is the strongest peak, which suggests that the geometry change upon $S_1 \leftarrow S_0$ excitation is not very large. Within the first 1000 cm^{-1} of the electronic origin, the most intense vibronic mode, apart from 0^0_0 , was assigned to mode 12^1_0 (Mulliken notation¹¹) belonging to a_g symmetry which had a 385 cm^{-1} shift,^{9,10} involving elongation of the fused ring system along its a -axis (long axis, passing through the centers of the aromatic rings). In benzene, there are 2 planar vibrations of the ring that contribute to ring expansion upon a $\pi\pi^*$ excitation: (1) symmetric and (2) antisymmetric along the mirror plane perpendicular to the aromatic ring. These modes are popularly called the $6a$ and the $6b$ mode, following Varsanyi labelling scheme.¹² Drawing an analogy to anthracene, the 12^1_0 mode corresponds to $6a$ vibration of all three phenyl rings. The antisymmetric counterpart of this planar ring distortion mode, which is symmetry forbidden, belongs to b_{3g} symmetry; here, the $6b$ vibration

is localized on the central phenyl ring. Other strong vibronic transitions of anthracene were observed beyond 1000 cm^{-1} .

As seen in Chapter 3, the most distinct vibronic modes in a $\pi\pi^*$ excitation are the symmetric ($6a$ type mode) and the antisymmetric ($6b$ type mode) ring distortion transitions contributing to the overall ring expansion in the excited state. Symmetry constrained optimization in the S_0 and S_1 states of anthracene predict an elongation along the a-axis, instead of ring ‘expansion’. This ring elongation is also predicted for 2-EA. A noticeably large geometry change along the ethyl torsional co-ordinate was predicted between S_0 (105°) and S_1 (75°) states. When compared with anthracene, 2-EA has a broken symmetry due to the presence of an ethyl chain, hence we anticipate to see the in-plane ring distortion vibronic transitions as well as modes involving ethyl group displacement, in the excitation spectrum.

Unlike anthracene, the UV excitation spectrum of 2-EA (**Figure 6.4 (a)**) exhibited several low frequency modes within 200 cm^{-1} built off 0^0_0 , 83^1_0 , and 82^1_0 transitions. This comprised primarily of the ethyl torsional mode 84 (Mulliken notation) up to $v=5$ (84^5_0) with a uniform spacing of 33.5 cm^{-1} . Contrary to popular notion regarding a $\pi\pi^*$ transition, the out-of-plane geometry of the ethyl group is making out-of-plane ring modes, such as mode 83 and 82, active.

Closely spaced peaks with patterns very similar to the ones seen around 0^0_0 ($27395\text{--}27595\text{ cm}^{-1}$) were also observed in the $27725\text{--}28025\text{ cm}^{-1}$ range, primarily comprising of mode 84 with a long FC progression built off the transition at $0^0_0+394.9$ and $0^0_0+671.2\text{ cm}^{-1}$. Unlike in case of anthracene, which is a symmetric molecule, 2-EA does not possess clear $6a$ or $6b$ type modes, but instead, has planar ring distortion modes that contribute to the elongation of the fused ring system, which are modes 76, 72, and 69. Other combinations of alkyl torsion and ring distortion modes are 77, 75, 74, and 73. A large geometry change between the ground and the excited electronic state suggests a possibility of Duschinsky mixing, which originates due to mixing of ground state normal modes in the excited state. Several modes above 0^0_0+200 cm^{-1} (27600 cm^{-1}) are tentatively assigned to modes involving a combination of alkyl torsions and ring distortion, as the excited state harmonic frequencies do not capture the experimental frequencies well. The assignments and FC progressions marked with tie-lines are shown in **Figure 6.4 (a)**.

The DFL spectra records fluorescence emission from the excited state, which maps the low lying vibrational modes of the S_0 electronic state. DFL spectrum recorded at the electronic origin is shown in **Figure 6.4(b)**, below the UV excitation spectrum for a ready comparison. The peak

widths have a FWHM of 10 cm^{-1} due to reasons stated in the methods section. Here, we discuss the DFL spectrum recorded by exciting the 0^0_0 peak, where incomplete subtraction is seen at the scatter peak (0 cm^{-1}). The pattern and assignments of the DFL spectrum are very similar to that observed in the UV excitation spectrum. The tie-lines connecting the low frequency torsions show a slightly longer FC progression (**Figure 6.4 (b)**). As we can see, the most active modes are 84 and 83. One major difference is that the spacing between the peaks are greater in DFL as opposed to the UV excitation peaks, which is a typically expected behavior. The S_0 state has deep potential wells, whereas the S_1 has a π^* antibonding molecular orbital occupied, hence, having a shallower potential. DFL spectra was recorded for multiple excitation peaks shown in **Figure 6.5**. DFL was also recorded on peaks beyond 200 cm^{-1} from the electronic origin, which are weaker. These are not shown here due to their low S/N, and lack of conclusive assignments.

As mentioned before, the UV excitation spectrum suggests there is a large geometry change upon $S_1 \leftarrow S_0$ excitation, as the 0^0_0 is not the strongest transition. The strong vibronic modes showing up have strong overlap with their ground state modes, and the modes having long FC progressions have large geometric changes along those modal co-ordinates. The ethyl torsional mode has long FC progression built off the electronic origin as well as the $6a$ and $6b$ type ring distortion modes. The symmetric ring distortion $6a$ mode contributes to the expansion of the fused aromatic system that is localized on the central phenyl ring. Hence, 2-EA experiences largest geometry changes along the ethyl torsional and the fused ring expansion modes.

There is a reduction in symmetry from anthracene (D_{2h}), through 2-methylantracene (2-MA) (C_s) and 2-EA (C_1), due to which fewer transitions will be symmetry forbidden with decreasing symmetry. From the work by Lin *et. al.*¹³, 0^0_0 is not the strongest transition in 2-MA, suggesting large geometry change, just like in case of 2-EA. The longest FC progression belongs to methyl torsion, suggesting that alkyl torsion is the co-ordinate along which the geometry change is the largest between the S_0 and the S_1 states. Modes that are active in 2-MA with methyl FC progressions built off, all are in-plane vibrations, whereas in case of 2-EA, there are modes 83 and 82, that are clearly out-of-plane vibrations. An important conclusion to be drawn is that as an out-of-plane functionality is added to a fused ring system, contrary to a $\pi\pi^*$ transition, out-of-plane vibrational modes become active.

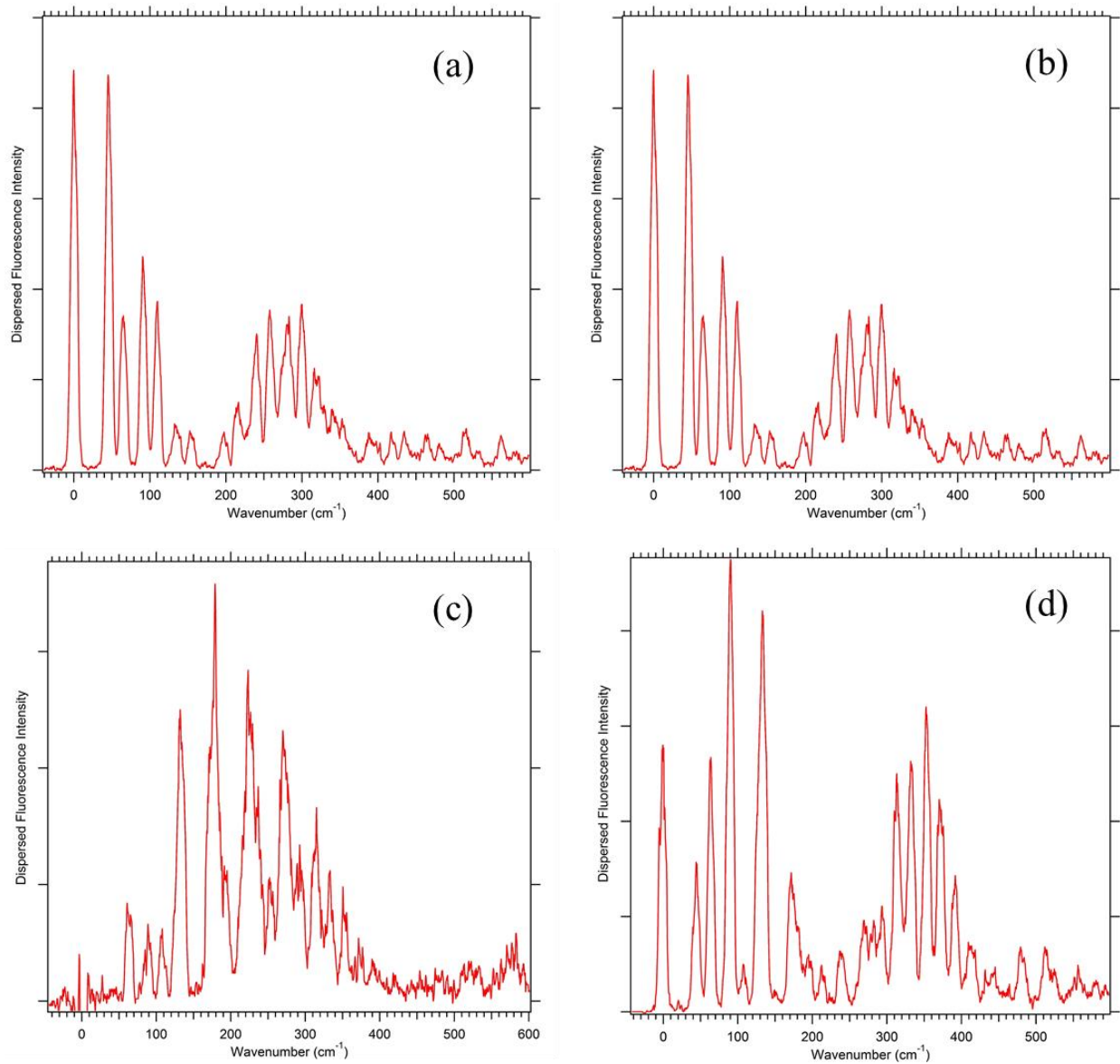


Figure 6.5: DFL spectra of 2-ethylanthracene at (a) 84^1_0 (b) 84^2_0 (c) 83^1_0 (d) $83^1_0 84^1_0$.

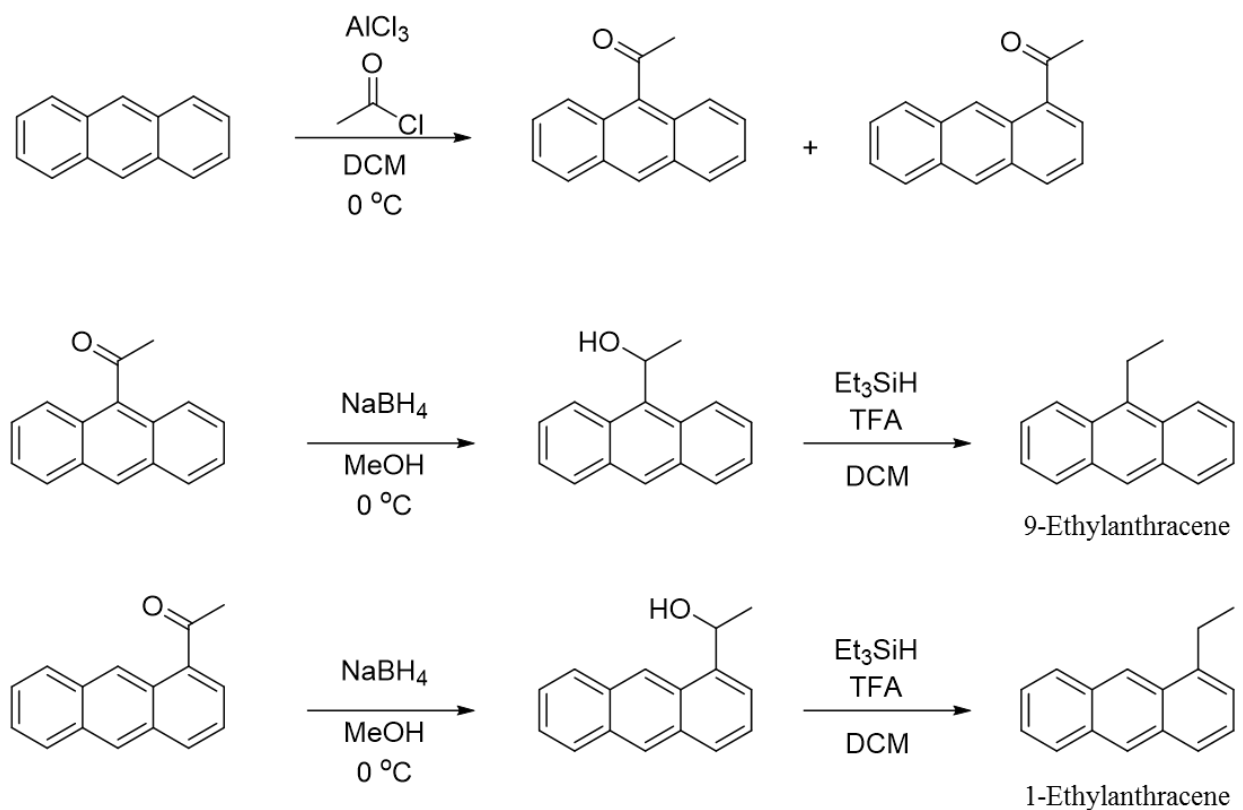


Figure 6.6: Synthetic scheme of 9- and 2-ethylantracene.

As mentioned in an earlier section, we will study the series of ethylantracenes in order to better understand the spectroscopy of dianthrylethanes. Joseph Bungard, from the Ghosh group, our synthetic collaborator in Purdue University, followed the scheme outlined in **Figure 6.6** to provide us with a complete series of ethylantracenes. 9- and 1-ethylantracenes would offer rich spectroscopic information regarding how the torsional activity changes with change in the ring position, and in turn how the out-of-plane modes are affected. We would also see the effects of symmetry in case of 9-ethylantracene.

6.2 Phosphorescence of 4-H-pyran-4-one

Laser spectroscopy was carried out on 4-H-pyran-4-one (4HP) in collaboration with Dr. Stephen Drucker, University of Wisconsin, Eau Claire. 4HP is a conjugated enone with a planar C_{2v} geometry. Access to the triplet state from singlet ground state upon excitation is inherently spin forbidden, making its experimental spectroscopy rather challenging. The $n\pi^*$ $T_1 \leftarrow S_0$ excitation of 4HP at 40°C has been studied in Cavity Ringdown Spectrometer by Drucker et. al.¹⁴ The spectrum hence obtained had several hot band contaminations, reducing the accuracy in the rotational band contour fit of the triplet state and raising the chance of misassignments.

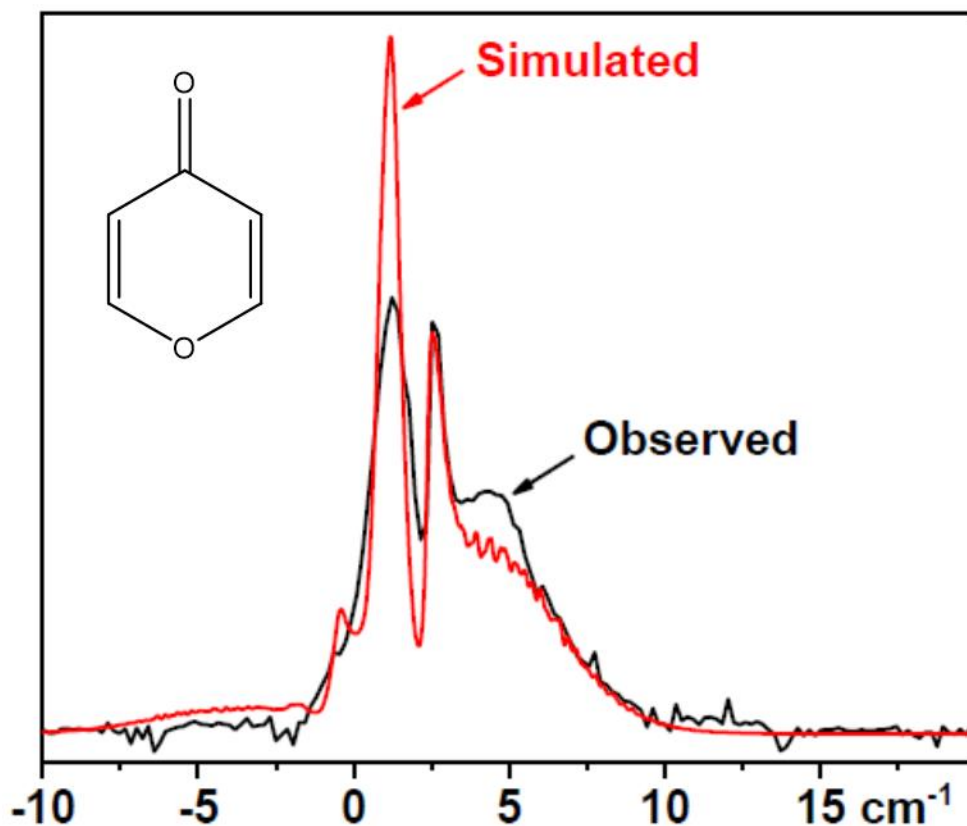


Figure 6.7: Jet-cooled LIP spectrum of the $T_1(n\pi^*) \leftarrow S_0$ origin band in 4-H-pyran-4-one, compared to a simulation generated using the STROTA program. The simulation used a rotational temperature of 20 K. The chemical structure of 4-H-pyran-4-one is in the top right corner.

The LIF chamber described in Chapter 2 was utilized for collecting Laser Induced Phosphorescence (LIP) spectrum of 4HP. The data-taking process was modified as we were

probing a spin forbidden transition with a very low signal. Sample of 4HP was placed in the sample chamber and maintained at 110°C and the PMT voltage was raised upto 1600 V. At such high sensitivity of the PMT, artifacts could be seen on the spectrum obtained, which were carefully identified. The lights in the lab were turned off to reduce ambient light entering the LIF chamber. Phosphorescence is very long lived, hence we gated after the scattered peak and PMT recoil time, which was in the range 1.20-4.00 μ s. We recorded the 0^0_0 peak of the $T_1(n\pi^*)\leftarrow S_0$ transition, which was about 10 cm^{-1} wide (**Figure 6.7**). The selection rules state that $\Delta J=0,\pm 2$ is allowed, implying that we would observe the O, Q and S rotational branches.

The 0^0_0 peak of the $T_1(n\pi^*)\leftarrow S_0$ transition of 4HP centered around 27298.5 cm^{-1} was recorded with 0.2 cm^{-1} step-size. Higher resolution spectrum at 0.04 cm^{-1} step-size is not shown here. STROTA suite of program¹⁵ was utilized to generate a simulation of the spectrum at 20 K rotational temperatures. Efforts are being made to obtain a better spectral simulation, hence, accurately determining the rotational constants of the T_1 state of 4HP.

6.3 Electronic Spectroscopy of Homosalate

Electronic spectroscopy of homosalate was carried out in collaboration with Dr. Vasilios Stavros, University of Warwick, Coventry. Homosalate, a member of the salicylate family of molecules, is a potential candidate for sunscreen, particularly against the effects of solar ultraviolet radiation. The Stavros lab specializes in studying ultrafast dynamics in the gas phase as well as in solution phase. Previous members of the Zwier group have studied the spectroscopy of plant sunscreen molecules. Due to their application, such compounds absorb over a very broad spectral range. The two viewpoints are (1) stationary state and the (2) wavepacket dynamics. Using ultrafast spectroscopy alongside complementary electronic spectroscopy, we piece together the photoprotection mechanism of homosalate. In the present thesis we briefly discuss the research carried out in the Zwier lab, Purdue University.

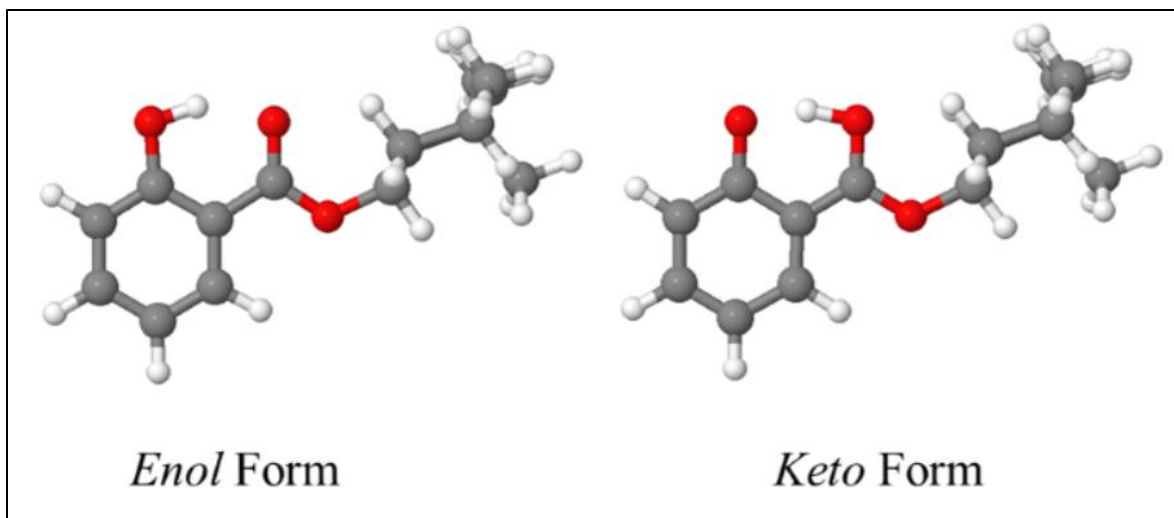


Figure 6.8: The tautomers of homosalate

Upon photoexcitation, an ideal sunscreen compound non-radiatively comes to the ground electronic state via a conical intersection, so that photodegradation does not occur. Homosalate can exist as *keto* and *enol* tautomers. It exists as the *enol* state in S_0 whereas in the S_1 state it exists as *keto* homosalate (**Figure 6.8**). Computationally the *enol*→*keto* is a barrierless process. The present collaborative project is aimed at determining if homosalate is a promising sunscreen candidate. Homosalate has two chiral centers, implying, there are four possible isomers. Due to the presence of two flexible dihedral angles, each isomer could potentially have four conformations, raising the total number of unique structures to 16. We, however, have not made attempts to characterize the different species present in our expansion due to two reasons: (1) the ultrafast spectroscopy does not have the resolution to differentiate various species spectroscopically, and (2) the sunscreen used will be present in all its isomeric and conformational forms.

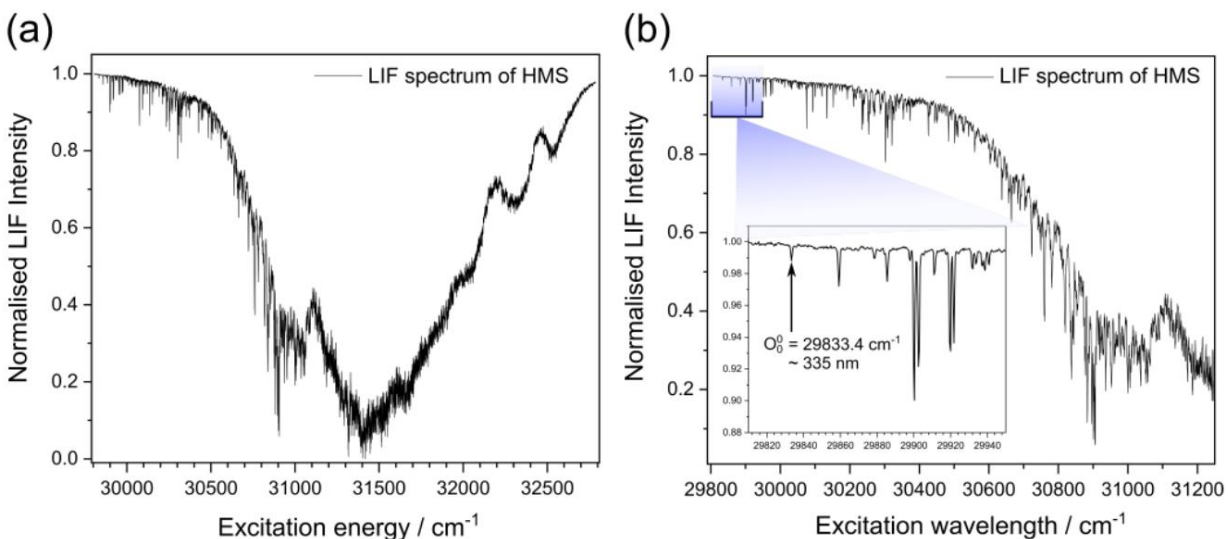


Figure 6.9: (a) LIF spectrum of vaporized HMS upon photoexcitation in the 29806.26 – 32786.89 cm⁻¹ energy region; the same spectrum is shown in more detail in (b), with the inset showing the peak and energy corresponding to the 0⁰₀ of HMS.

The UV excitation in the LIF is carried out as mentioned in Chapter 2. Solid sample of homosalate (TCI, *cis*: 12.2 % and *trans*: 87.0%) was maintained at 110°C to produce sufficient vapor pressure. The tunable dye laser (Exciton laser dye: DCM) was scanned in the 335.5-305.0 nm range. While recording the DFL spectra, a modified procedure was followed due to two reasons: (1) The signal was spread over a very large range, and (2) The UV enhanced steering optics were nearing their spectral edge of efficiency. DFL spectra were obtained by fixing the laser wavelength resonant with selected transitions in the excitation spectrum, and imaging the fluorescence onto the entrance slit of a ¾-m monochromator. Since the fluorescence was spread over a large range red-shifted from the excitation frequency, distinct peaks were not observed in the DFL spectrum. In order to obtain the shape of the broad DFL spectra, the slit width was set at 1 mm and an intensified CCD camera (Andor SOLIS iStar) collected the total dispersed emission signal impinging on the CCD at a fixed grating position. The grating position was tuned point-by-point and the entire spectrum for a given central grating position was integrated.

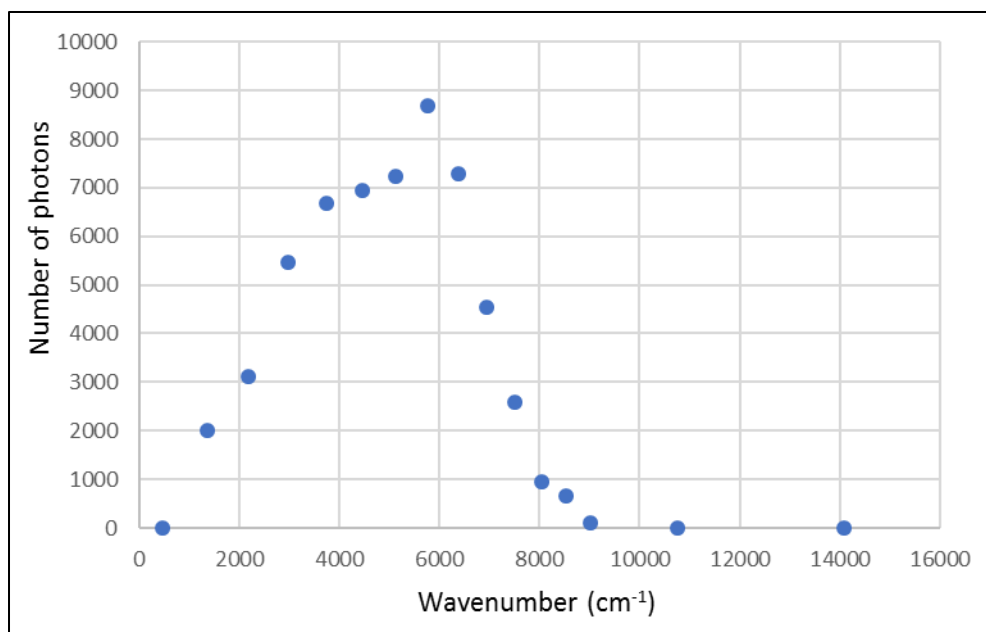


Figure 6.10: Dispersed fluorescence plot of homosalate exciting at 30761.19 cm^{-1} . X-axis is the shift from the exciting frequency. Maximum is $\sim 5750\text{ cm}^{-1}$.

The UV spectrum (**Figure 6.9**) as expected of a sunscreen candidate molecule, is a very dense and broad spectrum, spanning $\sim 3000\text{ cm}^{-1}$. Consistent with a large geometry change, the electronic origin is extremely weak compared to the rest of the spectrum (**Figure 6.9 (b)**). Within the first 500 cm^{-1} , the most active modes with long FC activity are those that move the OH bond relative to the C=O group, facilitating the H atom transfer, which lie between $\sim 350\text{ cm}^{-1}$ and $\sim 450\text{ cm}^{-1}$. The ring expansion modes that occur due to a $\pi\pi^*$ excitation, are predicted to lie $\sim 650\text{ cm}^{-1}$. Due to the sudden rise in congestion $\sim 30400\text{ cm}^{-1}$, it is hard to determine the experimental mode frequency corresponding to the in-plane ring distortion. Although, we hypothesize such modes to be the primary cause of the rise in congestion of the UV excitation spectrum, we also found evidence of the existence of at least one other conformer within our spectrum by photoexciting the molecule at different pulse times. We did not explore to characterize it any further as the sunscreen we would use exist in all their isomeric and conformational forms. The evidence of chiral isomeric species present in our expansion can be seen due to several closely spaced peaks (**Figure 6.9 (b)**).

The main reason to carry out DFL spectroscopy (**Figure 6.10**) on homosalate was to determine how large is the geometry change between the S_0 and the S_1 state. Species specific spectroscopy was not performed as the complementary ultrafast spectroscopy cannot distinguish between the various isomers and conformers. The maxima of the DFL distribution plot was

determined to be at least 5750 cm^{-1} from the 0^0_0 . The reason we reported a lower limit is because the efficiency of the UV enhanced mirrors used as steering optics decreases rapidly beyond 400 nm.

We also tried to recreate these results by recording the total signal intensity from the oscilloscope while changing the filters before the PMT. Increasing the wavelength of the low-pass filter would provide us with the integrated signal over the range the filters were ‘scanned’. We could see evidence even after $10,000\text{ cm}^{-1}$ shift from the peak being excited, suggesting the geometry change is very large. These results are not shown here as the DFL spectrum generated is more concrete. Fluorescence lifetime traces were also recorded by exciting selected transitions, and directly recording the time profile of the fluorescence signal from the PMT on the digital oscilloscope, which are not shown here. The fluorescence decay profile suggested that closer to the electronic origin, the lifetime was $\sim 14\text{ ns}$, whereas about $0^0_0 + 1400\text{ cm}^{-1}$, the lifetimes were $\sim 19\text{ ns}$.

The sharp transitions towards the beginning of our UV excitation spectrum suggests that the *enol*→*keto* is not a barrierless process, contrary to the calculations. Due to the timescales of ultrafast spectroscopy, the spectral resolution of the laser is very broad, hence state selectivity is not possible. Further analysis of the ultrafast time-resolved spectroscopy is underway to understand the photophysical processes following excitation of homosalate to the S_1 state.

6.4 Pyrolysis of *Trans* 3-Pentenenitrile

6.4.1 Introduction

Titan, a moon of Saturn, has a nitrogen- and methane-rich atmosphere that is similar to prebiotic earth, and is replete with organic nitriles. These nitriles are also present in interstellar and circumstellar medium, which comprise of about 18% of the compounds detected so far in space.¹⁶ Pentenenitriles (C_5H_7N) have not yet been detected in Titan’s atmosphere or in molecular clouds, but are potential precursors to hetero-aromatic compounds such as pyridine. the pentenenitriles are also worthy of attention as potential intermediates along the pathway to heteroaromatics such as pyridine (C_5H_5N). Absorption in the deep UV could provide the energy needed to dissociate them by loss of $2H$ or H_2 , rearrange its backbone, and cyclize to pyridine, either in a single step or in sequence. As the prototypical nitrogen heteroaromatic, establishing pathways to its formation

could be important for understanding initial steps along the pathway to nitrogen-rich aromatics present in the nucleic acid bases that are among the fundamental building blocks of life.¹⁷

There are multiple ways to initiate a radical reaction of pentenenitriles, such as utilizing a discharge source, laser photolysis or flash pyrolysis. We have performed flash pyrolysis using the mass-correlated CP-FTMW instrument to study *trans* 3-pentenenitrile (3-PN), where we could identify the reaction intermediates and products of both radical and molecular nature. We obtained very informative mass spectra at various pyrolytic nozzle temperatures, showing several peaks, including signal at $m/z=79$, which implies that this peak corresponds to a species with C_5H_5N chemical formula. Over 150 new microwave transitions were obtained, most of which were assigned to ^{13}C isotopologues of 3-PN. We have a few assignments of the mass spectrum and a few interesting features in the broadband rotational spectrum.

6.4.2 Results and Discussion

The Mass-correlated CP-FTMW spectrometer used in the study of pyrolysis of *trans* 3-pentenenitrile (3-PN) has been described previously. Argon was the chosen carrier gas to achieve a more efficient cooling. The temperature of the source was scanned up to 950°C and the signal of the products were optimized at 830°C. Evidence for a pyrolysis reaction was seen at 625°C in the mass spectrum. Mass spectra were collected at 625°C, 685°C, 770°C, 830°C and 950°C. We have shown mass spectra recorded at 685°C and 830°C in **Figure 6.11**. 1 million FID average scans were recorded at 25°C, 770°C, and 3 million FID average scan at 830°C was recorded to get a better S/N in the small MW peaks, that showed up only at pyrolytic temperatures. MW spectrum of the pyrolysis reaction at 830°C is shown in **Figure 6.12**. The mass spectrum was first analyzed, followed by the MW spectrum.

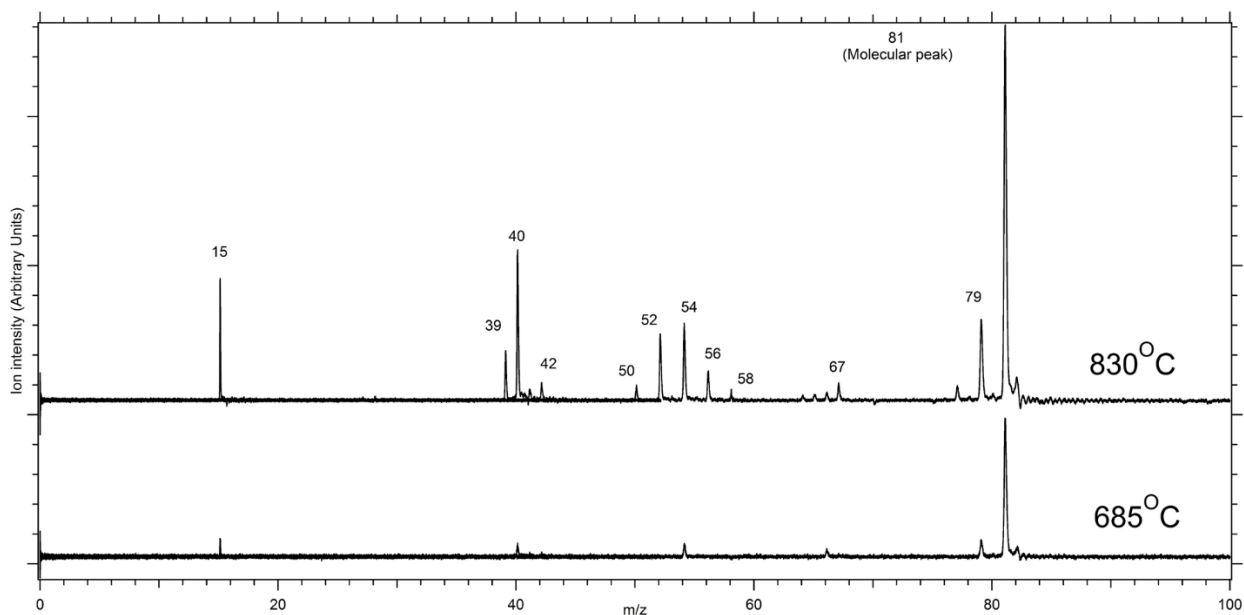


Figure 6.11: Mass spectrum of pyrolysis of 3-pentenenitrile at 830°C and 685°C.

The mass spectrometer is a very important tool when performed with broadband rotational spectrometry, especially when studying reactions. Due to the high resolution and the number of transitions observed, knowing the m/z of the species present in the expansion narrows down the number of structures we need to look for in the MW spectrum. We utilize a VUV source to ionize the species in the expansion via a single photon process, which is a soft ionization technique with an energy of 10.5 eV (118 nm). All the species ionized that show up in **Figure 6.11** have an ionization threshold of <10.5 eV. This means that smaller molecules, that generally have higher ionization potential, might evade our mass spectrum.

3-PN has a mass of 81 which is labelled as the molecular peak. The other signals at various m/z are listed along with the potential species in **Figure 6.13**. We see signal at $m/z=79$, which forms after 3-PN loses 2 H atoms or a H_2 . This could belong to multiple structures with chemical formula of C_5H_5N , including pyridine. This could also belong to conjugated chain nitriles such as E and Z 2,4-pentadienenitriles, which have 2 conformers each owing to one flexible dihedral. Other less likely candidates are 3,4-pentadienenitriles, 2-cyano-1,3-butadiene. The peak at $m/z=15$ belongs to methyl radical. Other m/z are listed in **Figure 6.13** correspond to species of both molecular and radical nature. Detecting species such as HCN, C_2H_2 , CH_3CN , $H_2C=CH_2$, $H_2C=CHCN$, and C_2H_5CN would have given us an insight into the pyrolytic processes, but unfortunately, their ionization potential is higher than 10.5 eV. Multiple reaction schemes have

been worked out explaining the various m/z peaks in the mass spectrum, but without any spectroscopic evidence as backup.

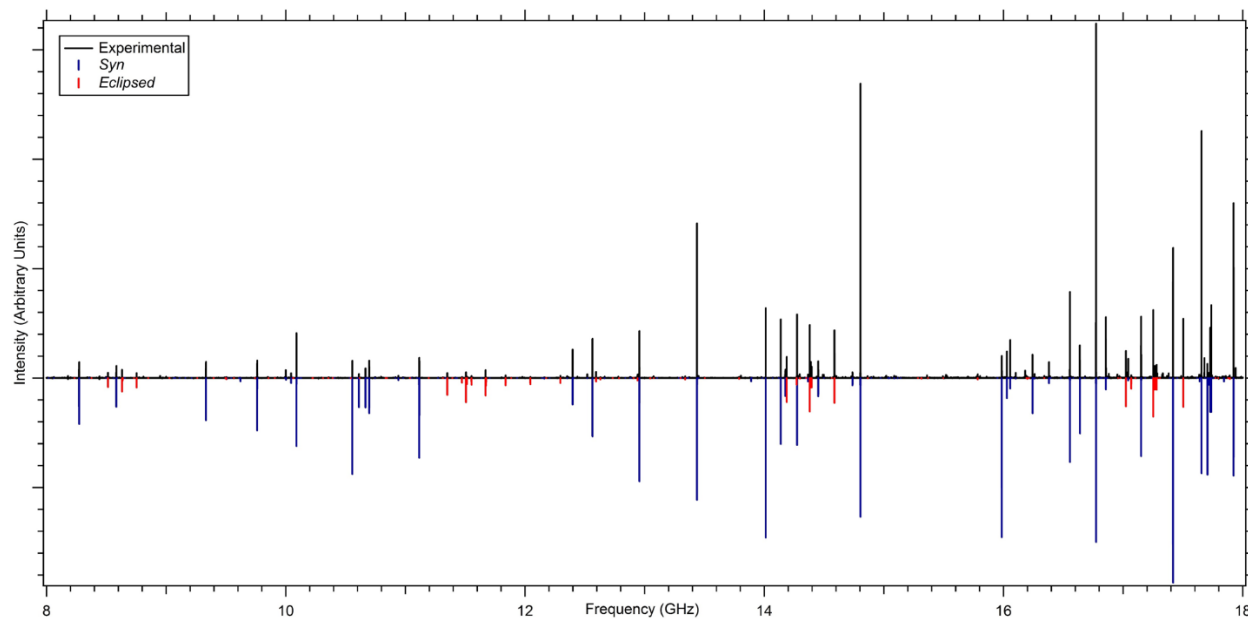


Figure 6.12: Broadband microwave spectrum of pyrolysis of 3-pentenenitrile at 830°C.

Despite having a mass spectrum collected simultaneously with the MW spectrum at 830°C, the assignment process of the MW spectrum was challenging. Over 150 new transitions were found that are not present in the MW spectrum recorded at room temperature. Efforts were made to look for signatures of pyridine within our MW spectrum, but could not be found. The E and Z 2,4-pentadienenitriles have not been studied previously. Moreover, these compounds are not commercially available as they are unstable. Species such as HCN and CH₃CN that are probably formed, cannot be detected in the mass spectrum or in the MW spectrum, as their signatures do not lie within the 8-18 GHz range. Aliphatic species with low dipole moments have been studied in rotational spectrometers, but could not be identified here, due to very low populations.

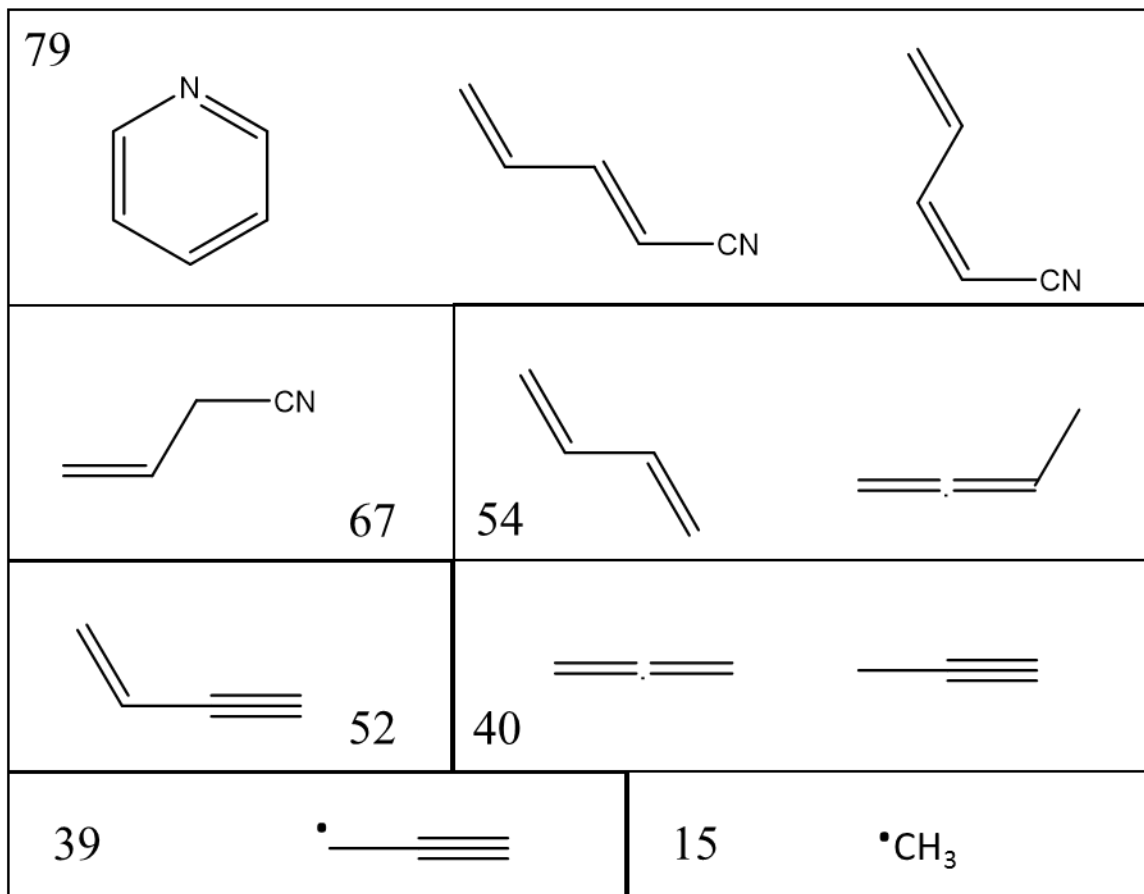


Figure 6.13: The species with the same mass corresponding to the m/z seen in the mass spectrum. The m/z values are in the respective boxes.

Signal observed in the pyrolysis MW spectrum was higher and warmer than the one recorded at room temperature, hence we looked for rotational transitions corresponding to vibrationally excited states of 3-PN, and due to ^{13}C isotopologues of 3-PN. No transitions due to vibrationally excited states could be identified, probably because the lowest modes of vibration in *syn* 3-PN were $> 100\text{ cm}^{-1}$, whereas all five ^{13}C isotopologues of *syn* 3-PN were identified and fit. The above mentioned analysis was not performed for the *eclipsed* conformer of 3-PN as the S/N was too low to observe the minor conformation.

To fit the vibrationally excited states of *syn* 3-PN, we start by performing anharmonic frequency predictions using the dispersion corrected DFT B3LYP/Def2TZVP. The predicted rotational constants correspond to the equilibrium geometry, labelled A_e , B_e , and C_e , and vibrational zero-point energy state, labelled A_0 , B_0 , and C_0 in the table ‘Rotational Constants (in

MHz)’ within the Gaussian output file. We also have the experimental A_0 , B_0 , and C_0 , from our ground vibrational state fits. The ‘Vibro-Rot alpha Matrix (in MHz)’ (**Table 6.2**) from the calculated output file lists the coupling between the rotational constants and the corresponding vibrational mode. Vibrational mode assignments to the α_i ’s could also be confirmed by inspecting the vibration and its effect over the inertial axes. For example, the vibrational mode frequency 1437.016 cm^{-1} has the highest $\alpha_{A,i}$, implying, this vibration is primarily along the A inertial axis.

Table 6.2: α along with the corresponding i^{th} vibrational mode.

$\alpha_{A,i}$	$\alpha_{B,i}$	$\alpha_{C,i}$	Vibrational mode frequency
-3.40995	2.80596	1.77293	149.075
-3.68552	3.20436	2.01165	128.079
0.00876	0.40339	0.19944	220.931
5.56682	-0.46312	-0.1947	241.737
-9.4367	1.7931	0.83823	292.338
4.40075	0.08059	0.02848	373.261
-4.2125	1.42019	0.58195	432.555
30.30481	2.14441	2.5775	673.866
23.74138	0.92025	1.57666	743.547
-67.6891	-0.38762	-1.41882	837.031
74.26156	-2.55024	-0.11017	936.187
-2.2529	0.53326	-1.06944	952.233
1.08064	3.35404	1.92887	989.07
5.50546	-0.98951	0.97837	1032.583
-0.43155	-0.42071	0.36827	1053.493
9.6067	-1.70946	0.69677	1101.625
25.21405	-3.31536	-2.33988	1210.856
-11.932	2.25505	2.45238	1283.697
7.01331	2.08339	0.49632	1336.784
34.164	-1.45868	0.39507	1342.872

Table 6.2 continued.

10.5327	-1.04906	-0.97954	1382.876
-67.9412	3.25592	1.65463	1422.443
75.90597	2.18154	1.84222	1437.016
-12.0761	6.22368	4.56789	1450.668
10.34386	0.20569	-0.10648	1705.391
2.86076	0.34069	1.11335	2330.356
-35.221	2.32783	2.51712	2908.028
-9.13638	1.28033	-1.05012	2930.497
-70.967	-1.25018	-0.56342	2891.42
52.08521	1.27884	-0.37004	2922.716
15.68952	0.51028	-0.40245	2948.751
-71.0843	-0.44373	2.2935	2979.761
2.00319	6.4789	0.58668	3022.156

Applying the following equation, we predicted the rotational constants corresponding to a specified vibrational state¹⁸:

$$B_v = B_e - \sum \alpha_i \left(v_i + \frac{1}{2} \right)$$

Where B refers to rotational constant, v corresponds to a specified vibrational state, e corresponds to equilibrium, and i corresponds to a particular vibrational mode. Hence, when $v_i=0$ for all i's, $B_v=B_0$. As a check, if all v_i 's are set to -0.5, then $B_v=B_e$. After obtaining the vibrationally excited state rotational constant, we add the difference between the predicted and experimental A_0 , B_0 , and C_0 to get rotational constants that are more accurate. These 'updated' rotational constant predictions are typically accurate to within 1% of the experimental rotational constants. The distortion coefficients were taken from the fit of *syn* 3-PN for the initial assessment. No rotational transitions were found around the predicted lines, implying, there was no evidence for vibrationally excited rotational transitions in our expansion.

The next step is looking for rotational transitions due to ^{13}C isotopologues. We start by performing dispersion corrected DFT calculations and using the following formula to obtain a more accurate rotational constant prediction:

$$\text{Accurate pred. } (^{13}\text{C}) = \frac{\text{expt. } (^{12}\text{C})}{\text{pred. } (^{12}\text{C})} \times \text{pred. } (^{13}\text{C})$$

Pred. refers to predicted and expt. refers to experimental rotational constants. Using these ‘updated’ predictions, we looked for the ^{13}C isotopologue peaks, all five of which were found within our spectrum. Following the C atom numbering from **Figure 4.1 (b)**, the ^{13}C isotopologues for *syn* 3-PN are $^{13}\text{C}(1)$, $^{13}\text{C}(2)$, $^{13}\text{C}(3)$, $^{13}\text{C}(4)$, and $^{13}\text{C}(5)$ with the C atom numbers written in brackets. Nuclear quadrupolar coupling and methyl internal rotation were not considered in our fitting process as the number of lines were very few and we could not resolve the hyperfine and A/E state splittings. SPFIT¹⁹ rotational constants (**Table 6.3**) and the experimental line list (**Table 6.4**) of all the ^{13}C isotopologues are listed here.

Table 6.3: SPFIT parameters of the ^{13}C isotopologues of *syn* 3-PN.

Rotational parameters	$^{13}\text{C}(1)$	$^{13}\text{C}(2)$	$^{13}\text{C}(3)$	$^{13}\text{C}(4)$	$^{13}\text{C}(5)$
A (MHz)	8161.52(21)	7998.32(35)	8064.010(16)	8149.6(21)	8124.42(17)
B (MHz)	1919.3310(15)	1934.2305(28)	1936.91120(13)	1929.356(16)	1888.2331(13)
C (MHz)	1583.6245(15)	1587.4046(27)	1591.81350(12)	1589.946(15)	1561.01630(99)
RMS (kHz)	7	12	5	68	23
Number of lines	6	6	5	6	4

Table 6.4: Line list of the ^{13}C isotopologues of *syn* 3-PN.

Isotopologue label	J up	Ka up	Kc up	J low	Ka low	Kc low	Observed (MHz)
$^{13}\text{C}(1)$	4	1	3	3	1	2	14655.6875
	5	1	5	4	1	4	16621.0000
	5	0	5	4	0	4	17256.8750
	5	2	4	4	2	3	17485.4375
	5	2	3	4	2	2	17742.8750
	4	0	4	3	0	3	13881.1250
$^{13}\text{C}(2)$	4	1	3	3	1	2	14749.9375
	5	1	5	4	1	4	16681.5625
	5	0	5	4	0	4	17326.1250
	5	2	4	4	2	3	17576.0000
	5	2	3	4	2	2	17857.5625
	4	0	4	3	0	3	13943.3750
$^{13}\text{C}(3)$	4	1	3	3	1	2	14775.4375
	5	1	5	4	1	4	16722.4375
	5	0	5	4	0	4	17366.9375
	5	2	3	4	2	2	17888.3125
	4	0	4	3	0	3	13974.5000
$^{13}\text{C}(4)$	4	1	3	3	1	2	14727.7500
	5	1	5	4	1	4	16692.1250
	5	0	5	4	0	4	17332.1875
	5	2	4	4	2	3	17566.3750
	5	2	3	4	2	2	17830.2500
	4	0	4	3	0	3	13943.3750
$^{13}\text{C}(5)$	5	1	5	4	1	4	16376.2500
	5	2	4	4	2	3	17218.3125
	5	2	3	4	2	2	17463.5625
	4	0	4	3	0	3	13672.5625

6.4.3 Conclusion

The flash pyrolysis of *trans* 3-pentenenitrile formed species of both molecular and radical nature. The mass spectrum showed several peaks including one at $m/z=79$, which would be a nitrogen containing molecule. Unfortunately, we could not identify any species beyond reasonable doubt as the S/N was low and the background literature for the probable structures was not available. We could however fit all five ^{13}C isotopologues of *syn* 3-PN and ensured no vibrationally hot precursor was observed.

The combination of a soft ionization mass spectrometer and broadband rotational spectrometer is a very powerful technique to study reactions. Due to our limitations of the VUV ionization source of 10.5 eV and the MW spectrometer range of 8-18 GHz, we are not very well equipped to handle small molecules, such as majority of the products that we are forming. With our experimental results, along with computations and searches of linelists, identifying the new transitions are underway.

6.5 References

- ¹ C. J. Mueller, W. J. Cannella, T. J. Bruno, B. Bunting, H. D. Dettman, J. A. Franz, M. L. Huber, M. Natarajan, W. J. Pitz, M. A. Ratclif, and K. Wright, *Energy Fuels* **26**, 3284 (2012).
- ² M. R. Kholghy, A. Veshkini, and M. J. Thomson, *Carbon* **100**, 508 (2016).
- ³ M. Frenklach, *Phys. Chem. Chem. Phys.* **4**, 2028 (2002). H. Sabbah, L. Biennier, S. J. Klippenstein, I. R. Sims, B. R. Rowe, *J. Phys. Chem. Lett.* **1**, 2962 (2010).
- ⁴ F. Mohamadi, N.G.J. Richards, W. C. Guida, R. Liskamp, M. Lipton, C. Caufield, G. Chang, T. Hendrickson, and W. C. Still, *J. Comput. Chem.* **11**, 440 (1990).
- ⁵ M. J. Frisch, G. W. Trucks, H. B. Schlegel, G. E. Scuseria, M. A. Robb, J. R. Cheeseman, G. Scalmani, V. Barone, B. Mennucci, G. A. Petersson, H. Nakatsuji, M. Caricato, X. Li, H. P. Hratchian, A. F. Izmaylov, J. Bloino, G. Zheng, J. L. Sonnenberg, M. Hada, M. Ehara, K. Toyota, R. Fukuda, J. Hasegawa, M. Ishida, T. Nakajima, Y. Honda, O. Kitao, H. Nakai, T. Vreven, J. A. Montgomery, Jr., J. E. Peralta, F. Ogliaro, M. Bearpark, J. J. Heyd, E. Brothers, K. N. Kudin, V. N. Staroverov, T. Keith, R. Kobayashi, J. Normand, K. Raghavachari, A. Rendell, J. C. Burant, S. S. Iyengar, J. Tomasi, M. Cossi, N. Rega, J. M. Millam, M. Klene, J. E. Knox, J. B. Cross, V. Bakken, C. Adamo, J. Jaramillo, R. Gomperts, R. E. Stratmann, O. Yazyev, A. J. Austin, R. Cammi, C. Pomelli, J. W. Ochterski, R. L. Martin, K. Morokuma, V. G. Zakrzewski, G. A. Voth, P. Salvador, J. J. Dannenberg, S. Dapprich, A. D. Daniels, O. Farkas, J. B. Foresman, J. V. Ortiz, J. Cioslowski, and D. J. Fox, *Gaussian 09, Revision C.01 Gaussian, Inc, Wallingford, CT, 2010.*
- ⁶ P. Mishra, D. M. Hewett and T. S. Zwier, *J. Chem. Phys.*, **148**, 184304 (2018).
- ⁷ D. M. Hewett, S. Bocklitz, D. P. Tabor, E. L. Sibert III, M. A. Suhm and T. S. Zwier, *Chem. Sci.*, **8**, 5305 (2017).
- ⁸ D. P. Tabor, D. M. Hewett, S. Bocklitz, J. A. Korn, A. J. Tomaine, A. K. Ghosh, T. S. Zwier, and E. L. Sibert III, *J. Chem. Phys.* **144**, 224310 (2016).
- ⁹ W. R. Lambert, P. M. Felker, J. A. Syage, and A. H. Zewail, *J. Chem. Phys.* **81**, 2195 (1984).
- ¹⁰ D. Gruner, A. Nguyen, and P. Brumer, *J. Chem. Phys.* **101**, 10366 (1994); B. W. Keelan, and A. H. Zewail, *J. Chem. Phys.* **82**, 3011 (1985); S. Rashev, *Chem. Phys. Lett.* **167**, 320 (1990); M. Baba, T. Katori, M. Kawabata, S. Kunishige, and T. Yamanaka, *J. Phys. Chem. A.* **117**, 13524 (2013).
- ¹¹ R. S. Mulliken, *J. Chem. Phys.* **23**, 1997 (1955).
- ¹² G. Varsanyi, *Assignments for Vibrational Spectra of 700 Benzene Derivatives* (Wiley, New York, 1974).
- ¹³ H. Lin, J. A. Hunter, and J. Pfab, *Chem. Phys. Lett.* **210**, 38 (1993).

- ¹⁴ A. Sessions, M. McDonnell, D. Christianson, and S. Drucker, *J. Phys. Chem. A*. **123**, 6269 (2019).
- ¹⁵ R. Judge, A. Korale, J. York, D. Joo, D. Clouthier, and D. Moule, *J. Chem. Phys.* **103**, 5343 (1995).
- ¹⁶ B. A. McGuire, *Astrophys. J., Suppl. Ser.* **239**, 17 (2018).
- ¹⁷ N. Kitadai and S. Maruyama, *Geosci. Front.* **9**, 1117 (2018).
- ¹⁸ P. F. Bernath, *Spectra of Atoms and Molecules*, Oxford University Press, New York (1995).
- ¹⁹ M. Pickett, *J. Mol. Spectrosc.* **148**, 371 (1991).

VITA

PIYUSH MISHRA

- Date of birth** 15 September 1992
- Nationality** Indian
- Educational career**
- 1) Secondary School: 83.4 % marks
 - 2) Higher Secondary School: 82.6 % marks
 - 3) Five Year BS/MS Program at IISER-Mohali, Punjab: 8.5 (10 point scale), final year research in the Viswanathan lab.
 - 4) Purdue University Coursework: 4 (4 point scale)
- Currently pursuing graduate studies in Purdue University in the Zwier lab.
- Awards and achievements**
- 1) 39th rank in the 10th Junior Mathematics Olympiad (JMO) (2007-08).
 - 2) KVPY (Kishore Vaigyanik Protsahan Yojana) fellow (A Government of India Fellowship to encourage young scientists) (2008).
 - 3) Purdue University International Student Travel Award (2015).
 - 4) Member of the Chemistry Honorary Club: Phi Lambda Upsilon (PLU)- Nu chapter (2016).
 - 5) Student Awards for discounted registration DMC (2019).
- Research experience**
- 1) Conformer specific spectroscopy of jet cooled molecules.
 - 2) Laser spectroscopy (vibrational and electronic) – Laser Induced Fluorescence (LIF), Dispersed Fluorescence, Resonance 2-photon ionization (R2PI), Laser Induced Phosphorescence, Double resonance techniques.
 - 3) Chirp-pulse broadband microwave spectroscopy (rotational). Strong-field coherence breaking (SFCB).
 - 4) Matrix isolation infrared spectroscopy.
 - 5) Basic computational techniques.
- Career goal** To excel in doctoral and postdoctoral studies from a leading laboratory working in the general area of molecular spectroscopy and reaction dynamics studies, both experimental and theoretical. Starting a lab in the same field in academia.
- Conferences**
- 1) International Symposium on Molecular Spectroscopy (ISMS-2016)- Attended
 - 2) International Symposium on Molecular Spectroscopy (ISMS-2017)- Delivered talk (Conformational explosion: Understanding the complexity of short chain *para*-dialkylbenzene potential energy surfaces).
 - 3) International Symposium on Molecular Spectroscopy (ISMS-2018)- Delivered talk (Propylbenzene-(H₂O)_n clusters: Effect of the alkyl chain on the π H-bond).
 - 4) International Symposium on Molecular Spectroscopy (ISMS-2019)- Delivered talk (*Trans* 3-pentenenitrile, 4-pentenenitrile and their pyrolysis products)
 - 5) Dynamics of Molecular Collisions XXVII (DMC-2019)- Presented poster (Broadband microwave spectroscopy of *trans* 3-pentenenitrile, its pyrolysis products and 4-pentenenitrile)
- Publications**
- 1) Does borazine-water behave like benzene-water? A matrix isolation infrared and *ab initio* study. Mishra, P.; Verma, K.; Bawari, D.; Viswanathan, K. S., *J. Chem. Phys.* 2016, 144, 234307.

- 2) Conformational explosion: Understanding the complexity of short chain *para*-dialkylbenzene potential energy surfaces.
Mishra, P.; Hewett, D. M.; Zwier, T. S., *J. Chem. Phys.* 2018, 148, 184304.
- 3) Strong Field Coherence Breaking as a tool for identifying methyl rotor states in microwave spectra: 2-hexanone.
Fritz, S. M.; Mishra, P.; Zwier, T. S., *J. Chem. Phys. Comm.* 2019, 151, 041104. (Featured article)
- 4) Broadband rotational spectroscopy of *trans* 3-pentenenitrile and 4-pentenenitrile.
Mishra, P.; Fritz, S. M.; Hays, B. M.; Mehta-Hurt, D. N.; Jawad, K. M.; Zwier, T. S., *Phys. Chem. Chem. Phys.* 2019, 21, 23651.
- 5) Unimolecular decomposition of novel high nitrogen content energetic molecules following electronic state excitation: BTATz and DATz.
Sylvinson, D. M. R.; Bera, A.; Mishra, P.; Bhattacharya, A.; Bernstein, E. R., *J. Chem. Phys.* (Manuscript submitted).
- 6) Measuring combustion intermediates via broadband chirped-pulse microwave spectroscopy.
Fritz, S. M.; Mishra, P.; Wullenkord, J.; Fugazzi, P. G.; Kohse-Hinghaus, K.; Zwier, T. S.; Hansen, N., *Proceedings of the Combustion Institute* (Manuscript submitted).
- 7) Insights into the photoprotection mechanism of the UV filter homosalate.
Holt, E. L.; Krokidi, K. M.; Turner, M. A. P.; Rodrigues, N. d. N.; Mishra, P.; Zwier, T. S.; Stavros, V. G. . (Manuscript in preparation).
- 8) The unusual symmetry of 1,2-bis(trifluoromethyl)benzene and its broadband rotational spectroscopy.
Herbers, S.; Fritz, S. M.; Mishra, P.; Zwier, T. S. (Manuscript in preparation).
- 9) Broadband rotational spectroscopy of pentanal and 2-pentenal.
Fritz, S. M.; Mishra, P.; Zwier, T. S. (Manuscript in preparation).
- 10) Broadband rotational spectroscopy of 4-methylacetophenone.
Herbers, S.; Fritz, S. M.; Mishra, P.; Nguyen, H. V. L.; Zwier, T. S. (Manuscript in preparation).

Current projects

- 1) Studying propylbenzene-water clusters through mass-resolved laser double resonance spectroscopy. (Experiments completed)
- 2) Studying broadband rotational spectrum of pyrolysis intermediates and products of pentenenitrile molecules. (Experiments completed)
- 3) Studying electronic and vibrational spectra ethylanthracene series of molecules. (Experiments started)
- 4) Studying the stacking tendency of dianthrylethanes.
- 5) Studying phosphorescence of pyrone under jet-cooled conditions. (Collaboration with Dr. Stephen Drucker, UW-Eau Claire)

Teaching experience

- 1) Served as a teaching assistant (TA) in an undergraduate physical chemistry lab for 1 semester at IISER Mohali.
- 2) Served as a teaching assistant (TA) in an undergraduate analytical chemistry lab for 1 semester at IISER Mohali.
- 3) Served as a teaching assistant (TA) in freshman general chemistry lab for engineers for 3 semesters at Purdue University.
- 4) Served as a teaching assistant (TA) in an undergraduate physical chemistry lab for 1 semester at Purdue University.

Post-doc

- 1) Prof. Robert W. Field, Massachusetts Institute of Technology (MIT), Cambridge, Massachusetts, USA.

PUBLICATIONS

- 1) ‘Conformational explosion: Understanding the complexity of short chain *para*-dialkylbenzene potential energy surfaces.’ Mishra, P.; Hewett, D. M.; Zwier, T. S., *J. Chem. Phys.* **148**, 184304 (2018).
- 2) ‘Strong Field Coherence Breaking as a tool for identifying methyl rotor states in microwave spectra: 2-hexanone.’ Fritz, S. M.; Mishra, P.; Zwier, T. S., *J. Chem. Phys. Comm.* **151**, 041104.(2019) (Featured article)
- 3) ‘Broadband rotational spectroscopy of *trans* 3-pentenenitrile and 4-pentenenitrile.’ Mishra, P.; Fritz, S. M.; Hays, B. M.; Mehta-Hurt, D. N.; Jawad, K. M.; Zwier, T. S., *Phys. Chem. Chem. Phys.* **21**, 23651 (2019).
- 4) ‘Does borazine-water behave like benzene-water? A matrix isolation infrared and *ab initio* study.’ Mishra, P.; Verma, K.; Bawari, D.; Viswanathan, K. S., *J. Chem. Phys.* **144**, 234307 (2016).